IUSS
Scuola Universitaria Superiore Pavia

Scuola Universitaria Superiore IUSS Pavia

3D numerical investigation of nonlinear seismic soil-structure interaction in shallow-founded masonry towers with mixed implicit-explicit integration for improved solution stability

A Thesis Submitted in Partial Fulfilment of the Requirements
for the Degree of Doctor of Philosophy in

EARTHQUAKE ENGINEERING AND ENGINEERING SEISMOLOGY

Obtained in the framework of the Doctoral Programme in
Understanding and Managing Extremes

by

Onur Deniz Akan

September 2024

Scuola Universitaria Superiore IUSS Pavia

3D numerical investigation of nonlinear seismic soil-structure interaction in shallow-founded masonry towers with mixed implicit-explicit integration for improved solution stability

A Thesis Submitted in Partial Fulfilment of the Requirements
for the Degree of Doctor of Philosophy in

EARTHQUAKE ENGINEERING AND ENGINEERING SEISMOLOGY

Obtained in the framework of the Doctoral Programme in
Understanding and Managing Extremes

by

Onur Deniz Akan

Supervisors:
Prof. Carlo G. Lai
Prof. Guido Camata
Prof. Enrico Spacone
Prof. Claudio Tamagnini

September 2024

ABSTRACT

This thesis explores the intricate dynamics of soil-structure interaction, particularly in the seismic analysis of masonry structures. The rigid and brittle nature of masonry, in conjunction with the nonlinear soil beneath, presents a challenge in identifying the weakest link that could result in a failure mechanism. This study provides novel insights by simultaneously addressing structural and soil nonlinearities, staying faithful to the characteristics of masonry and soil behaviour.

The primary objective is to comprehend the potential inelastic mechanisms and identify sources of hysteretic energy dissipation in the seismic analysis of soil-structure interaction of shallow-founded masonry structures. Furthermore, recognizing the substantial computational cost of incorporating material nonlinearity in the solution of solid finite element models, the thesis introduces the advantages of employing a computationally efficient implicit-explicit integration scheme to solve constitutive equations. The implicit-explicit integration method poses significant computational advantages over the explicit solution, providing larger time steps for efficient time history analyses. The intricacies of the IMPL-EX method, including the possible error accumulation, are carefully addressed here to ensure robust and accurate solutions.

Within the scope of the thesis, new OpenSees source code has been developed in C++ to include additional implicit-explicit tools to solve soil-structure interaction problems. First, a novel, highly stable contact-friction element is implemented. Second, the implicit-explicit (IMPL-EX) versions of the well-known Pressure-dependent (PDMY02) (Yang et al., 2003) and Pressure-independent (PIMY) (Gu et al., 2011) multi-yield-surface materials are implemented. During impl-ex integration, the material internal parameters are extrapolated at the beginning of each step and then corrected via a single implicit iteration after convergence. Hence, a solution with controlled amount of error is guaranteed.

In the application part of the thesis, a virtual laboratory is developed in OpenSees using the STKO preprocessor to study the nonlinear soil-structure interaction of shallow-founded masonry towers. The bell tower of Guardiagrele and the hill structure underneath it is modelled using 3D 8-node brick elements. A state-of-the-art implicit-explicit damage-plasticity material is used to model the masonry behaviour, whereas the soil behaviour is modelled with the multi-yield surface kinematic hardening model.

The input ground motions are selected for bedrock conditions using the Conditional Spectrum (CS) (Lin et al., 2013) conditioned on AvgSA as the target spectrum. The deconvolved motions are used in the SSI model, whereas the free surface accelerations are computed via nonlinear 1D site response analysis to be used in the fixed base analyses. The free filed soil behaviour is considered in two cases. First, the soil profile is assumed to consist of fine-grained material, leading to analyses based on total stresses, which is consistent with the in-situ soil investigations. Effects of the 2D and 3D topographic features on the free surface accelerations are discussed. Alternatively, the second soil layer is replaced with a clean sand layer. In this case, the possibility of liquefaction of the clean sand layer is assessed based on effective stress analyses. As the pore pressure builds up, the sand layer becomes softer, resulting in reduced amplifications and higher deformations.

The fixed-base dynamic response of the tower is studied under 3-component free surface acceleration. A sensitivity analysis is performed to find the permissible time step to be used in the impl-ex seismic analyses of the tower. The orthotropic features of the masonry model are shown to affect the seismic response of the tower. The dynamic response of the bell tower as well studied. It is observed that the pounding interaction between the adjacent walls and the tower amplifies the damage observed in the tower due to strong shaking. Furthermore, the detrimental effects of including the vertical component in the analysis are discussed over the dynamic response of the tower.

Then, the seismic response of the bell tower SSI system is studied systematically through time history analyses. As input motion, the 3-component deconvolved acceleration history is applied at the base of the model. It is observed that the seismic response of the bell tower is strongly affected by the foundation rotations. Furthermore, it is shown that the rocking isolation mechanism discussed by Gazetas (2015) for RC frame structures, also exists in the bell tower SSI system. The removal of pounding interaction led to a stronger isolation mechanism. Additionally, it is observed that the rocking isolation mechanism in the bell tower is sensitive to the shear stiffness reduction characteristics of the foundation soil. A softer soil response in the small strain ranges led to beneficial effects in the tower, reducing the observed cracking damage, and vice versa. Unlike the fixed base model, the detrimental effect of including the vertical motion in the analysis is not observed in the SSI model. Future studies might investigate the effect of synchronized vertical and horizontal peak accelerations on the bell tower SSI model.

Finally, leveraging the computational efficiency of the implicit-explicit solution, the record-to-record variability in the SSI system response is studied using seven records. It is observed that ground motions with longer durations or higher frequency content might lead to increased foundation damage.

SOMMARIO

Questa tesi esplora le complesse dinamiche dell'interazione suolo-struttura, con particolare riferimento all'analisi sismica delle strutture in muratura. La natura rigida e fragile della muratura, in combinazione con il comportamento non lineare del terreno sottostante, rappresenta una sfida nell'individuazione dell'anello debole che potrebbe innescare un meccanismo di collasso. Questo studio offre nuove informazioni affrontando contemporaneamente le non linearità strutturali e del terreno, mantenendo un'aderenza fedele alle caratteristiche del comportamento della muratura e del suolo.

L'obiettivo principale è comprendere i potenziali meccanismi inelastici e identificare le fonti di dissipazione di energia isteretica nell'analisi sismica dell'interazione suolo-struttura di edifici in muratura a fondazione superficiale. Inoltre, riconoscendo l'elevato costo computazionale dell'inclusione della non linearità dei materiali nella soluzione di modelli a elementi finiti solidi, la tesi introduce i vantaggi derivanti dall'impiego di uno schema di integrazione implicito-esplicito computazionalmente efficiente per risolvere le equazioni costitutive. Il metodo di integrazione implicito-esplicito (IMPL-EX) offre vantaggi computazionali significativi rispetto alla soluzione esplicita, consentendo l'uso di passi temporali più ampi per analisi efficienti di time history. Le complessità del metodo IMPL-EX, inclusa la possibile accumulazione di errori, sono accuratamente esaminate in questo lavoro per garantire soluzioni robuste e precise.

Nell'ambito della tesi, è stato sviluppato un nuovo codice sorgente in OpenSees in C++ per includere strumenti implicito-espliciti aggiuntivi per la risoluzione di problemi di interazione suolo-struttura. In primo luogo, è stato implementato un nuovo elemento di contatto-attrito altamente stabile. In secondo luogo, sono state implementate le versioni implicito-esplicite dei noti materiali a multi-superfici di snervamento dipendenti dalla pressione (PDMY02) (Yang et al., 2003) e indipendenti dalla pressione (PIMY) (Gu et al., 2011). Durante l'integrazione IMPL-EX, i parametri interni del materiale vengono estrapolati all'inizio di ciascun passo e poi corretti attraverso una singola iterazione implicita dopo la convergenza, garantendo così una soluzione con un livello controllato di errore.

Nella parte applicativa della tesi, è stato sviluppato un laboratorio virtuale in OpenSees utilizzando il preprocessore STKO per studiare l'interazione suolo-struttura non lineare di torri in muratura a fondazione superficiale. Il campanile di Guardiagrele e la struttura collinare sottostante sono modellati utilizzando elementi solidi in muratura 3D a 8 nodi.

Per modellare il comportamento della muratura viene utilizzato un avanzato modello di plasticità-danno implicito-esplicito, mentre il comportamento del suolo è modellato tramite un modello cinematico di incrudimento con multi-superfici di snervamento.

I moti del terreno in ingresso sono selezionati per le condizioni di substrato roccioso utilizzando lo Conditional Spectrum (CS) (Lin et al., 2013), condizionato su AvgSA come spettro di riferimento. I moti deconvoluti sono utilizzati nel modello SSI, mentre le accelerazioni della superficie libera sono calcolate attraverso un'analisi non lineare della risposta sismica 1D, da utilizzare nelle analisi a base fissa. Il comportamento del suolo in condizioni di campo libero è considerato in due scenari. Nel primo, si presume che il profilo del suolo sia costituito da materiale a grana fine, portando ad analisi total stress, in linea con le indagini geotecniche in situ. Vengono discussi gli effetti delle caratteristiche topografiche 2D e 3D sulle accelerazioni della superficie libera. In alternativa, il secondo strato di terreno è sostituito con uno strato di sabbia pulita, valutando la possibilità di liquefazione tramite analisi delle effective stresses.

La risposta dinamica della torre con base fissa è studiata sotto l'accelerazione a 3 componenti della superficie libera. Viene effettuata un'analisi di sensibilità per determinare il passo temporale ottimale da utilizzare nelle analisi sismiche IMPL-EX della torre. Si osserva che le caratteristiche ortotrope del modello di muratura influenzano la risposta sismica della torre. La risposta dinamica del campanile è ulteriormente studiata. Si nota che l'interazione di impatto tra le pareti adiacenti e la torre amplifica il danno subito dalla torre a causa di forti sollecitazioni sismiche. Inoltre, vengono discussi gli effetti negativi dell'inclusione della componente verticale nell'analisi sulla risposta dinamica della torre.

Successivamente, la risposta sismica del sistema SSI del campanile viene studiata sistematicamente attraverso analisi di time history. La storia di accelerazione deconvoluta a 3 componenti viene applicata alla base del modello. Si osserva che la risposta sismica del campanile è fortemente influenzata dalle rotazioni della fondazione. Inoltre, si dimostra che il meccanismo di "rocking isolation" discusso da Gazetas (2015) per le strutture in cemento armato (RC), esiste anche nel sistema SSI del campanile. La rimozione dell'interazione di schiacciamento ha portato a un meccanismo di isolamento più efficace. Si osserva inoltre che il meccanismo di "rocking isolation" del campanile è sensibile alla riduzione della rigidezza a taglio del terreno di fondazione. Una risposta del suolo più morbida per piccole deformazioni ha prodotto effetti benefici per la torre, riducendo i danni da fessurazione osservati, e viceversa. Diversamente dal modello a base fissa, l'effetto negativo dell'inclusione della componente verticale non è osservato nel modello. Infine, sfruttando l'efficienza computazionale della soluzione implicito-esplicita, la variabilità del sistema SSI da record a record viene studiata utilizzando sette registrazioni sismiche. Si osserva che moti del suolo con durate più lunghe o contenuti di alta frequenza potrebbero portare a un aumento dei danni alla fondazione.

ACKNOWLEDGEMENTS

I wish to extend my deepest gratitude to my supervisors, Professor Guido Camata, Professor Carlo Lai, Professor Enrico Spacone, and Professor Claudio Tamagnini, for their unwavering support and guidance throughout this journey. Their expertise and the resources they provided have been instrumental in making this work possible. I am profoundly grateful to Dr Massimo Petracca for his insights into modelling and C++ coding, particularly in using and developing OpenSees. The knowledge I gained from each member of our team has been invaluable. I also thank the Italian Ministry of Education for providing the funding that made this PhD research possible.

My heartfelt appreciation and love go to my beloved parents, Belgin Gul, Turgay Akan, and Ozlem Askin Akan, for their unwavering support and encouragement throughout this journey.

In the face of technical challenges, a company of curious friends to brainstorm with is all one needs. I am indebted to them for the fruitful discussions over numerous pizzas, drinks, and countless cups of coffee. A special thanks go to Dr Ali Guney Özcebe, who introduced me to site response analysis and geotechnical modelling. His insatiable curiosity and willingness to engage in technical discussions whenever he had time were greatly appreciated. I also want to express my gratitude to Ricardo Plata Rodriguez, Du Fangqing, Maithree Kurukulasuriya, Enes Veliu, Besim Yukselen, Volkan Ozsarac, and Numan Eren for the technical discussions we had. Here is to many more "technical committees," hopefully next time at a taverna in Istanbul or by the Aegean coast, where the meze, fish, music, and drinks are abundant.

I am also grateful to Mr. Oykun Gurkan for his psychological support, guidance in work and time management, and for offering alternative perspectives on life and science. The COVID-19 pandemic presented many challenges but also opportunities for personal growth, reflection, and a deeper understanding of gratitude.

A wise mentor once told me, “A PhD is thirty per cent work and seventy per cent psychology—and by thirty per cent, I mean a lot of work.” This observation proved remarkably accurate. In addition to hard work, I also found great friendships, unique experiences, and countless stories to cherish. Later, in my PhD journey, Professor Guney

Özcebe and I had the opportunity to teach a course on Reinforced Concrete together in Pavia, making him a part of my story.

I am also grateful to Professor Cem Akguner and Professor Zehra Cagnan for imparting fundamental civil engineering knowledge at TEDU and exemplifying the master-apprentice relationship in engineering education. Additionally, I thank Ms. Sevgi Basbayraktar for helping me overcome my insecurities with mathematics during high school, which inspired me to embrace the mathematical challenges presented in this thesis.

Many thanks go to Mr Andrea Rosato and Bentley for providing access to the Plaxis 2D suite during the advanced constitutive modelling course at Imperial College London, which greatly enhanced my knowledge of geotechnical modelling. I am indebted to Ms. Hannah Cartwright, Mr. Maurizio Bottini, and the ASDEA team for their software and technical support. I also thank Professor Daniela Giretti and Professor Vincenzo Fioravante for providing cyclic triaxial test results of Ticino sand specimens and Dr Igor Tomic and the SERA-AIMS team for making their experimental data on shake table tests available.

I also wish to thank my friends Satyadhrik Sharma, William Galik, Bryan Chalarca Echeverri, Bishvabhanu Puhan, Sevgi Özcebe, Bulut Özcebe, Al Mouayed Bellah Nafeh, Rita Couto, Basar Yucel, Derek Rodriguez, Lana Todorovic, Nevena Sipcic, Alessandra Miliziano, Karim Aljawhari, Carlos Grajales, Naveen Ragu Ramalingam, Maud Bonzi, Madalena Ponte, Sebastian Maluje, Andres Abarca, Carlos Mesta, Savvinos Aristeidou, Jose Poveda, Serkan Hasanoglu, Stelios Kallioras, Alejandro Calderon, and Simona Baroni. During times when I felt that being a brain in a jar connected to a high-performance computer might be more efficient, they reminded me of the value of staying human. In an environment where knowledge is everything, they showed me that the capacity to love and trust is what truly makes life meaningful. For that, I am eternally grateful.

Finally, I express my deepest thanks to my dear friends in Ankara—Mert Kumbasar, Murat Aytemiz, Yasemin Doganci, Sahin Kuranel, Mesut Ozer and Meric Goker—for sharing countless experiences and supporting me through the challenges of the past five years. They have become the large family I always dreamed of, gathering around a warm, festive table to celebrate both joys and sorrows.

Sweet summer zephyr,
Squirrel finds mother on branch,
Leaves rustle in peace.

Onur Deniz Akan
24 August 2024, Pavia

TABLE OF CONTENTS

LIST OF FIGURES

LIST OF TABLES

LIST OF SYMBOLS

Scalars

$ijkl$	= Iterators or free indices	f_t	= Peak elastic tensile strength
f_{cp}	= Peak compressive strength	f_{c0}	= Elastic compressive limit
d_c^+	= Compressive cracking damage	d_c^-	= Tensile cracking damage
d_{pl}^+	= Compressive plastic damage	d_{pl}^-	= Tensile plastic damage
$\breve{\tau}^+$	= Compressive equivalent stress	$\breve{\tau}^-$	= Tensile equivalent stress
$\breve{I}_1$	= First invariant of the trial effective stress tensor	$\breve{J}_2$	= Second invariant of the trial effective stress deviator tensor
k_b	= Ratio of the compressive bi-axial strength to the uniaxial compressive strength	k_1	= Parameter to control the dilatancy behaviour of compressive damage surface
r^+	= Tensile damage threshold	r^-	= Compressive damage threshold
q^+	= Tensile hardening variable	q^-	= Compressive hardening variable
λ^+	= Tensile equivalent plastic strain	λ^-	= Compressive equivalent plastic strain
K_n	= Contact normal stiffness	K_f	= Contact friction stiffness
μ	= Contact friction coefficient	N	= Contact normal weight
Δu_N	= Contact displacement jump	ξ	= Residual shear stress
σ_N	= Contact nominal stress	pc	= Compressive projector
λ	= Equivalent plastic strain (total slip multiplier)	d_a	= Apparent plastic damage
r	= Damage threshold	$\hat{r}$	= Effective damage threshold
$\breve{\tau}$	= Equivalent shear stress	δ	= Small perturbation (delta)

K	= Bulk modulus	ε_{vol}	= Volumetric strain
K_{ref}	= Reference bulk modulus	$\dot{\varepsilon}_{vol}^{p}$	= Plastic volumetric strain increment
G	= Shear modulus	p	= Mean effective stress
G_{ref}	= Reference shear modulus	p_{ref}	= Reference mean effective stress
ς	= Pressure dependent modulus update factor	np	= Modulus update power
H'	= Plastic shear modulus	$\acute{p}$	= Modified mean effective stress
H'_{ref}	= Reference plastic shear modulus		
Ψ	= Plastic potential function	f	= Yield function
β	= Plastic dilatancy	R	= Yield radius
P"	= Volumetric part of the unit normal tensor to the plastic potential	Q"	= Volumetric part of the unit normal tensor to the yield surface
m	= Active yield surface number	η	= Stress ratio
p_{atm}	= Atmospheric pressure	$\dot{\eta}$	= Stress ratio increment
Λ	= Direction of the contraction increment (dot product)	η_{PT}	= Phase transformation stress ratio
c_1	= Contraction parameter 1	η_{CS}	= Critical state stress ratio
c_2	= Contraction parameter 2	d_1	= Dilation parameter 1
c_3	= Contraction parameter 3	d_2	= Dilation parameter 1
ε_c	= Accumulated volumetric plastic strain over contraction phase	d_3	= Dilation parameter 3
$\Delta\lambda$	= Step plastic multiplier	γ_d	= Accumulated octahedral shear strain over dilation cycle
$\dot{\lambda}$	= Plastic multiplier increment within a return-mapping iteration	$\bar{G}$	= Extrapolated shear modulus
$\Delta\bar{\lambda}$	= Extrapolated step plastic multiplier	$\bar{K}$	= Extrapolated bulk modulus

χ	= Extrapolated deviatoric impl-ex state variable	κ	= Extrapolated volumetric impl-ex state variable

Vectors

$\boldsymbol{F}$	= Force vector	$\boldsymbol{u}$	= Displacement vector
$\dot{\boldsymbol{u}}$	= Velocity vector	$\ddot{\boldsymbol{u}}$	= Acceleration vector

Second order tensors

$\boldsymbol{m}$	= Mass matrix	$\boldsymbol{C}$	= Viscous damping matrix
$\boldsymbol{K}$	= Stiffness matrix	$\boldsymbol{\Omega}$	= Nodal coordinates of body in the reference configuration
$\boldsymbol{\varepsilon}$	= Strain	$\boldsymbol{\sigma}$	= Stress (also Nominal stress)
$\boldsymbol{\varepsilon^p}$	= Plastic strain	$\boldsymbol{\sigma^{tr}}$	= Trial stress
$\widehat{\boldsymbol{\sigma}}^{+}$	= Compressive effective stress	$\widehat{\boldsymbol{\sigma}}^{-}$	= Tensile effective stress
$\breve{\boldsymbol{\sigma}}^{+}$	= Compressive trial effective stress tensor	$\breve{\boldsymbol{\sigma}}^{-}$	= Tensile trial effective stress tensor
$\Delta\boldsymbol{u}$	= Displacement jump	$\Delta\boldsymbol{u_T}$	= Tangential displacement jump
$\boldsymbol{\sigma}$	= Nominal stress	$\boldsymbol{\sigma_T}$	= Tangential nominal stress
$\boldsymbol{e}$	= Strain deviator	$\boldsymbol{\tau}$	= Stress deviator
$\boldsymbol{\varepsilon_{vol}}$	= Volumetric part of the stress tensor	$\boldsymbol{\sigma^{vol}}$	= Volumetric part of the stress tensor
$\boldsymbol{e^p}$	= Plastic strain deviator	$\boldsymbol{\zeta}$	Reduced stress deviator (i.e., backstress removed)
$\dot{\boldsymbol{\varepsilon}}$	= Strain increment	$\boldsymbol{\alpha}$	= Backstress
$\dot{\boldsymbol{\varepsilon}}^{\boldsymbol{e}}$	= Elastic strain increment	$\boldsymbol{\delta}$	= Kronecker delta function
$\dot{\boldsymbol{\varepsilon}}^{\boldsymbol{p}}$	= Plastic strain increment	$\boldsymbol{Q}$	= Outwards unit normal tensor to the yield surface

$\dot{\boldsymbol{e}}^{\boldsymbol{p}}$ = Plastic strain deviator increment

$\dot{\boldsymbol{\varepsilon}}^{\boldsymbol{p}}_{\boldsymbol{vol}}$ = Plastic volumetric strain increment

$\overline{\boldsymbol{\sigma}}$ = Rephrased (impl-ex) stress

$\overline{\boldsymbol{\tau}}$ = Rephrased stress deviator

$\overline{\boldsymbol{a}}$ = Rephrased backstress

$\widetilde{\boldsymbol{\sigma}}$ = Linearized (impl-ex) stress

$\boldsymbol{\tau}^{*}$ = Contact stress deviator

$\boldsymbol{Q}'$ = Deviatoric part of the unit normal tensor to yield surface

$\boldsymbol{P}$ = Outwards unit normal tensor to plastic potential

$\boldsymbol{P}'$ = Deviatoric part of the unit normal tensor plastic potential

$\overline{\boldsymbol{Q}}$ = Rephrased unit normal tensor to yield surface

$\overline{\boldsymbol{P}}$ = Rephrased unit normal tensor to plastic potential

$\widetilde{\boldsymbol{Q}}$ = Linearized unit normal tensor to yield surface

$\widetilde{\boldsymbol{P}}$ = Linearized unit normal tensor to plastic potential

Fourth order tensors

$\mathbb{E}$ = Elastic coefficients tensor

$\mathbb{H}$ = Elastoplastic tangent operator

$\mathbb{C}$ = Consistent tangent operator

$\mathbb{A}$ = Stress derivative of the flow rule

$\overline{\mathbb{E}}$ = Extrapolated elastic coefficients tensor

$\overline{\mathbb{A}}$ = Stress derivative of the rephrased flow rule

$\mathbb{P}^{+}$ = Positive projector tensor

$\mathbb{P}^{-}$ = Negative projector tensor

$\mathbb{I}$ = Symmetric operator

$\mathbb{I}^{vol}$ = Volumetric operator

$\mathbb{I}^{dev}$ = Deviatoric operator

1 INTRODUCTION

In this chapter, the background information leading to the research question of the thesis is presented. Subsequently, a virtual laboratory, involving a prototype shallow-founded masonry tower is defined. Various modelling assumptions commonly employed in seismic assessment of structures and the methodology followed in addressing the research question is presented, setting the stage for the following chapters where the effects of different assumptions on the model's response are comprehensively investigated. Finally, the chapter concludes by presenting a detailed outline of the goals addressed in each chapter of this thesis.

Keywords: Seismic soil-structure interaction, Finite element method, Shallow-founded masonry towers, Nonlinear soil response, Implicit-explicit integration

1.1 OPENING AND MOTIVATION

Unreinforced masonry (URM) towers are part of the historical heritage and were often constructed as security structures or bell towers during the Renaissance period. They can be found as standalone edifices or as components of larger architectural complexes. The inherent brittleness of masonry renders tower structures particularly hazardous, as collapses can occur without warning and lead to catastrophic results. Historical records provide numerous URM tower failures, whether under gravity loading (e.g., "Torre civica" in Pavia) or due to seismic activity, such as the destruction caused by the Emilia-Romagna earthquake in 2012. Such catastrophic events underscore the need for a detailed understanding of how these structures respond under seismic loading.

The mechanisms that lead to the damage and collapse of masonry towers are still an open research question and require studying complex material, geometric, and interaction nonlinearities. Over the years, the numerical investigation of various URM tower systems has received increasing attention from researchers. In the literature, there is a recent effort to study the structure level dynamic response of stone masonry structures for assessment or retrofit purposes. These studies focus on either the fixed-base structural response or the soil-structure interaction response considering that SSI effects might be important.

Soil-structure interaction may play a crucial role in the seismic analysis of masonry structures. The rigid yet brittle nature of masonry coupled with softer soil poses a challenge in identifying the so-called "weakest link" that might lead to the failure of the whole chain

of members. A discussion that has lately become integral to the seismic assessment and retrofit of structures. Each component in a soil-structure system has strong nonlinear characteristics; however, the governing inelastic mechanism of the whole system may emerge due to the interplay between material and geometric features.

The foundation flexibility and the energy dissipation provided by the hysteretic response are essential factors. Furthermore, kinematic interaction (i.e. mismatch between the stiffness of the foundation and that of the surrounding soil) which causes wave scattering and diffraction may significantly affect the structural response. At the same time, there are aspects of wave propagation, such as the wave amplitude. Depending on the soil profile and stiffness the accelerations acting at the structure's foundation may be amplified or de-amplified.

With the advancement of computational resources, the modelling of direct soil-structure interaction (SSI) for large structures and foundation size effects, indicates that SSI effects may significantly alter the response of stiff structures due to the modification of strong motion, kinematic effects, or the inertial effects of an oscillating heavy body. However, further research is needed on the role of soil and structural material nonlinearities in large soil-structure interaction problems.

Modelling the seismic behaviour of masonry towers accurately, especially when considering soil-structure interaction (SSI) can become a challenging a task. Masonry, as a material, exhibits complex behaviour under dynamic loading, including nonlinear elasticity and progressive cracking. These complexities are amplified when towers are part of an aggregate structure, where interactions between neighbouring buildings can further modify seismic behaviour. Therefore, realistic models must incorporate both the nonlinear material behaviour of masonry, soil and the dynamic contact between bodies.

Finite element (FE) models are commonly used in simulating the seismic response of masonry towers, but they come with substantial computational costs. The behaviour of masonry involves softening, where cracking leads to a reduction in stiffness, and capturing this accurately requires advanced constitutive models that are robust, stable, and don't suffer from convergence problems. Additionally, when modelling large systems, the possible dynamic contact-friction conditions between the masonry blocks in an aggregate might further complicate the simulations. Traditional implicit schemes often struggle with convergence, particularly in dynamic analysis. Explicit schemes, on the other hand, can be prohibitively expensive due to the extremely small-time steps required to ensure stability. A more efficient approach involves using an implicit-explicit integration scheme, which can provide larger time steps while controlling numerical error, but this method requires careful calibration to avoid error accumulation over time.

Meanwhile, the recent work done by Professor Gazetas and colleagues offers valuable insights into potential solutions for managing the challenges of SSI in seismic analysis. Their research on reinforced concrete (RC) frames has demonstrated the benefits of allowing controlled foundation rocking during seismic events. Rocking isolation allows for energy dissipation through foundation motion, which reduces the forces transmitted to the superstructure. Gazetas' findings on the seismic resilience provided by controlled foundation motions open new possibilities for better understanding the seismic demands acting on masonry towers.

This thesis seeks to address a fundamental research question: how does the stiffness degradation and strength of the soil around the foundation affect the predicted cracking damage in masonry towers? While Gazetas and others have explored rocking isolation mechanisms in RC frames, there remains a gap in understanding how such mechanisms might apply to more fragile and brittle structures like masonry towers. Given the susceptibility of masonry to cracking and the importance of the foundation's response during seismic events, it is crucial to explore whether controlled foundation motions can offer the same protective benefits to these heritage structures. This research delves into the effects of soil-structure interaction on the seismic response of masonry towers, focusing specifically on how the nonlinearity of both the soil and the masonry can influence the overall behaviour of the structure.

1.2 OBJECTIVES AND METHODOLOGY

To achieve the research objectives, a comprehensive virtual laboratory is developed in OpenSees using the STKO pre-processor. The bell tower and the adjacent cathedral of Guardiagrele are modelled as a prototype masonry tower structure, incorporating both the superstructure and the underlying soil layers extending to the bedrock. The model captures the essential nonlinear characteristics of both masonry and soil, ensuring that key phenomena such as cracking, stiffness degradation, and soil nonlinearity are accurately represented. Furthermore, the model includes novel, highly stable dynamic contact-friction elements between the tower and adjacent church that can model the dynamic pounding interactions without convergence issues.

The modelling of soil and masonry materials is performed using advanced constitutive laws that reflect their kinematic hardening and damage-plasticity behaviour, respectively. A state-of-the-art implicit-explicit (IMPL-EX) integration scheme is employed to improve computational efficiency. This scheme allows for the extrapolation of internal parameters at the beginning of each time step, followed by a single implicit correction after convergence. This approach significantly reduces the computational cost compared to traditional fully implicit or explicit methods, which either suffer from slow convergence or require extremely small-time steps. The IMPL-EX version of the pressure-independent and

pressure-dependent soil materials are also implemented in OpenSees, reducing the time and computational resources required to simulate the complex soil-structure interaction mechanisms.

The seismic input for the analyses consists of ground motions selected based on the Conditional Spectrum (CS) method, targeting bedrock conditions. The deconvolved motions are used as input for the soil-structure interaction model, while free surface accelerations are computed through nonlinear 1D site response analysis for the fixed-base cases. The analyses explore two soil scenarios: one assuming fine-grained soil profile and the other involving a clean sand layer to assess the potential for liquefaction.

The fixed base response of the tower is studied as a reference. A sensitivity analysis is performed to assess the optimal time steps for the IMPL-EX method. Since the fixed base assumption triggers the most plastic response in the structure, the permissible time step identified in the fixed base conditions is expected to accurately model the structural behaviour in the remaining SSI analyses.

In the 3D direct SSI analyses, the pressure-independent multi-yield surface material is used to model the nonlinear behaviour of the soil. This is crucial for simulating the effects of stiffness degradation in the foundation soil during seismic events. The integration of soil nonlinearities allows for an exploration of the impact of soil stiffness degradation on the seismic response of the bell tower, especially in relation to foundation rotations and rocking isolation mechanisms. The impact of soil nonlinearity, foundation rocking, and the interaction between soil layers is studied systematically to determine the role of soil stiffness in modifying the seismic demand on the bell tower.

Finally, a series of time history analyses is conducted to assess the bell tower's seismic response under various conditions, including the effects of pounding interaction with the adjacent cathedral and the contribution of vertical seismic accelerations. The role of the soil's stiffness degradation in the observed cracking patterns is closely examined, alongside the rocking isolation mechanism, which has been previously suggested as a beneficial feature for reinforced concrete structures. The computational efficiency of the IMPL-EX scheme allows for multiple simulations with varying ground motions, enabling a robust statistical analysis of the record-to-record variability in the tower’s seismic response. This approach ensures that both the localised damage mechanisms in the masonry and the global SSI effects are adequately captured and analysed.

1.3 OUTLINE OF THE THESIS

This thesis is organized into nine chapters, each addressing a key aspect of the material and boundary nonlinearities in the finite element modelling of masonry structures and soil-structure interaction effects.

- Chapter 2: Literature review

Chapter 2 provides a comprehensive review of the relevant literature. A few critical gaps in the existing research are identified, including the effect of nonlinear soil response on the cracking damage of masonry structures, the discussion of potential failure mechanisms in masonry tower-soil interaction systems, the impact of pounding between adjacent structures on the dynamic response of masonry towers, and the implicit-explicit (impl-ex) solution for kinematic hardening soil models. These gaps underscore the need for more advanced modelling techniques to accurately capture the complex SSI behaviour of masonry towers, which this thesis aims to address.

- Chapter 3: IMPL-EX contact mechanics

This chapter begins with a discussion of the contact-friction mechanics. It then introduces the formulation of a new implicit-explicit contact element, developed and implemented in OpenSees as part of this thesis. The performance and validation of this contact element are demonstrated through the numerical modelling of a sliding block. The chapter concludes with the application of the contact elements in modelling the experimental cyclic loading of a stone masonry pier.

- Chapter 4: IMPL-EX kinematic hardening soil model

Chapter 4 introduces the formulation of the pressure-dependent multi-yield (PDMY02) surface model currently available in OpenSees. The chapter discusses relevant constitutive equations crucial for the implicit-explicit implementation of the PDMY02 model. It proceeds with the derivation of linearised flow rules for both pressure-independent and pressure-dependent behaviours. Then, an implicit-explicit return-mapping algorithm is presented, utilising the linearized flow formulation to enhance computational efficiency. Finally, the implicit-explicit pressure-dependent model is calibrated to match cyclic triaxial testing data from a Ticino sand specimen. The model is validated by comparing the impl-ex solution with the traditional implicit solution.

- Chapter 5: Modelling of a virtual laboratory

This chapter defines a virtual laboratory to study the effects of nonlinear soil-structure interaction on masonry towers. The laboratory includes detailed models of the bell tower and the church of St. Maria Maggiore in Guardiagrele. The modelling process for the structure and the underlying soil layers is discussed. Two distinct soil profiles are defined for total and effective stress analyses. An optimal strategy for coupling the structural and soil models is discussed, ensuring an accurate representation of the soil-structure interaction. Finally, the chapter addresses the solution to the resulting large-scale boundary value problem, leveraging parallelisation algorithms available in OpenSees to efficiently handle computational demands.

- Chapter 6: Ground motion selection and site response

Chapter 6 presents the one-dimensional (1D) ground response analysis of the bell tower. The chapter discusses AvgSA (Average Spectral Acceleration) as a suitable intensity measure for seismic record selection, given its ability to represent a range of frequencies relevant to the tower's dynamic response. Then, a set of eleven ground motion records is selected at the bedrock level using the conditional spectrum approach, ensuring that the selected records represent the seismic hazard. The chapter concludes with a comparative discussion of the 1D, 2D, and 3D free-surface responses, analysing both total and effective stress soil profiles to provide insights into the seismic behaviour of the site.

- Chapter 7: Fixed-base response of the bell tower

This chapter begins by determining a permissible time step for the implicit-explicit (impl-ex) damage model, identified as one-fourth of the sampling interval of the input motion. The significance of accurately modelling strength anisotropy is then demonstrated, showing its critical role in capturing a more realistic cracking behaviour of the masonry tower under seismic loading. The analysis reveals that adjacent structures can induce cracking damage in the tower. Finally, the chapter explores the effects of including the vertical component of seismic motion, noting that in some cases where the peak vertical acceleration arrives later than the peak horizontal accelerations, the cracking response might intensify.

- Chapter 8: Nonlinear SSI response of the bell tower

This chapter explores the crucial role of foundation rocking in the soil-structure interaction (SSI) response of the bell tower. It identifies the presence of a rocking isolation mechanism, which becomes even more pronounced when adjacent walls are removed. The analysis reveals that the cracking damage response intensifies as a function of the stiffness reduction in the foundation soil. In contrast to the fixed-base model, the vertical seismic motion in the SSI model does not lead to strong amplifications due to the foundation's filtering of high-frequency accelerations. Finally, it is observed that short, burst-like motions with

strong, high frequencies tend to trigger the primary cracking mechanism, while longer motions with strong, low frequencies are more likely to result in foundation failure.

- Chapter 9: Conclusions

The final chapter summarises the key contributions of the research, including the development of a robust numerical model for studying the nonlinear soil-structure interaction in masonry towers. The formulation of impl-ex integration of contact and kinematic hardening mechanics. It discusses the limitations of the current study and proposes directions for future research.

Finally, the references and appendices are placed at the end of the thesis, where some figures that are referenced in the text are presented.

2 LITERATURE REVIEW

This chapter presents a comprehensive review of the relevant literature within the scope of the thesis. Initially, fundamental works in seismic-soil structure interaction are surveyed, providing a broad understanding. Next, an in-depth review of the widely used numerical solution approaches in seismic-soil structure interaction (SSI) boundary value problems is provided. This review highlights the details and emergence of the implicit-explicit (impl-ex) numerical integration technique. Then, the formulation of the *ASDConcrete3D* material for concrete and masonry is presented. *ASDConcrete3D* material is employed throughout the thesis to model masonry behaviour.

Following, a brief evaluation of some of the most popular models used in the cyclic analysis of soils is presented. A gap in the literature for an impl-ex cyclic constitutive model to conduct a fully imp-lex SSI analysis is recognised.

For the application part of the thesis, the prior experience found in the literature on the modelling and assessing masonry towers is discussed. Methodologies, results, and engineering demand parameters (EDPs) highlighted by these studies for studying the seismic response are thoroughly examined. A critical discussion on challenges authors face in modelling nonlinear masonry behaviour is provided, emphasising the relevance of an impl-ex solution.

The literature review concludes by focusing on the direct soil-structure interaction studies of masonry towers and engineering structures. A gap in the literature for SSI studies is identified, particularly those considering soil and structure material nonlinearities. Lessons learned and numerical challenges these studies face are discussed, highlighting the potential advantages of adopting a mixed impl-ex solution in direct SSI analyses.

Keywords: Seismic Soil-Structure Interaction, Nonlinear Analysis, Mixed Implicit-Explicit Integration, Constitutive Modelling, Masonry Towers

2.1 SHALLOW-FOUNDED SOIL-STRUCTURE INTERACTION PROBLEMS

Soil-structure interaction has been the focus of research for a long time. It covers a wide range of subjects, such as soil mechanics, structural mechanics, computational mechanics, and mathematics; hence, it is an interdisciplinary field requiring input from engineers, physicists, and mathematicians. The beginning and early development of soil-structure

interaction, including seminal works in the fields, have been reviewed in a recent work by Kausel (2010), who is a key figure in SSI research.

Kausel (2010) summarised some of the key research topics that received attention from the researchers in SSI and referenced seminal studies as follows:

- **Fundamental solutions:** These involve the response of an elastic soil domain to external dynamic or static disturbances, such as those addressed in Stokes', Boussinesq's, Cerruti's, Chao's and Lamb's problems (Kausel, 2006; Poulos & Davis, 1974).
- **Free-field (or site-response) problems:** These studies determine the response of a soil stratum under earthquake excitations or vibrations.
- **Kinematic interaction problems:** These analyse the oscillatory response of rigid or semi-rigid foundations due to seismic waves passing beneath them.
- **Inertial interaction problems:** These focus on soil deformations induced by structural movements in the vicinity of a foundation.
- **Development of numerical techniques:** This includes advancements in finite element models, transmitting boundaries, boundary elements, interface elements, constitutive models, and nonlinear solution schemes (Arduino, 2014).

Some of the findings of early works, especially concerning the interaction between the foundation and the soil, are still relevant. As summarised by Kausel (2010), breakthroughs were made in foundation filtering, kinematic interaction, and structural response, considering fixed versus compliant base assumptions. Some of the relevant studies are mentioned here.

For instance, Sezawa and Kanai (1935) focused on the energy dissipation of an idealistic rod structure with a hemispherical foundation embedded in a half-space. The structure is subjected to vertically propagating P waves. They analytically demonstrated that considering SSI limits the structural vibrations partly due to the scattering of the incoming wave in all directions upon hitting the foundation and partly due to loss of energy in the form of waves returning to the ground from the structure (Kausel, 2010).

Later, Merritt and Housner (1954) studied the effect of foundation flexibility and rocking response on the structural response. They analytically solved the model of a single-story wall structure attached to a flexible rotational spring at its base. Then, the same exercise was repeated for 5, 10, and 15-storey structures during the shaking induced by the "El Centro" earthquake ground motion record. The solution was obtained with the help of an "Electric Analog Computer", a novel technology at the time. They observed that the system response strongly depends on the seismic excitation, and buildings with different height-to-width ratios might suffer different damage even if they have similar compliance ratios.

Housner (1957) revisited the topic and analysed the motions of a building with a considerably elongated shape in the plan view. Housner observed that the frequency content of the waves propagating in the long direction of the building was significantly filtered (Kausel, 2010). In contrast, the waves propagated in the short direction seem unaware of any filtering effect. Housner (1957) concluded that the passing waves are influenced by the deformations of the building in the two directions. The short side behaved relatively in a flexible way and deformed easily, complying with the passing wave motion, whereas the long side was stiffer, hence forcing the ground to comply with the rigid motions of the foundation. (Kausel, 2010).

Kausel (2010) also explained the "tau effect," a concept first described by Nathan M. Newmark, which relates to the torsional response of symmetric structures due to seismic waves travelling beneath the foundation. This effect results from the time delay between the arrival of seismic waves on different sides of the structure, quantifiable by the speed of horizontally propagating shear waves.

On the other hand, numerical SSI analysis methods have developed increasingly as computational resources become more available. Currently, three popular methods of analysis are used in industry and research to evaluate SSI response.

2.1.1 The Sub-Structure Method

Sometimes called the indirect method, this approach divided a complex structural system into kinematic and inertial components, which were analysed separately (Kausel et al., 1978). According to the superposition theorem by Kausel et al. (1978), the responses of these substructures were combined to determine the overall response of the complete system. However, as superposition suggests, this approach was only applicable to linear or equivalent linear systems (Lai & Martinelli, 2013).

Kinematic interaction involved modifying seismic waves as they passed through the soil and interacting with a massless foundation, resulting in a "foundation input motion" that differed from the free-field motion, particularly for embedded foundations. Inertial interaction, meanwhile, focused on the dynamic response of the soil-foundation-structure system under seismic loads, which involved calculating foundation impedance, including dynamic stiffness (springs) and damping effects (dashpots) for each mode of vibration. (Gutierrez & Chopra, 1978; Huang et al., 2015; Kausel et al., 1978; Mylonakis et al., 2006; Wolf, 1998)

2.1.2 The Macro-Element Method

In the macro-element method, the soil-foundation system was modelled as a single element incorporating the soil and foundation's stiffness and damping characteristics. Macro

elements were typically calibrated using results from more detailed analyses or experiments and could capture complex nonlinear behaviours, such as plasticity and large deformations. Since the nonlinear characteristics of the system were modelled, the macro-element approach was suitable for simulating the performance of foundations under strong seismic events. However, calibrating these elements could be strenuous, as representing all the nonlinearities associated with soils and foundations within a single element was challenging. (Chatzigogos et al., 2009; Cremer et al., 2001, 2001, 2002; Einav & Cassidy, 2005; Gajan & Kutter, 2007; Paolucci, 1997; Taciroglu et al., 2006; Veletsos & Nair, 1975; Veletsos & Wei, 1971).

2.1.3 The Direct Method

The Direct approach involved a comprehensive modelling strategy where the soil, foundation, and structure are modelled together within a large finite element model (Lai & Martinelli, 2013). It allowed for the detailed simulation of the interaction between soil and structure, capturing the complexities of SSI without relying on simplifying assumptions. This method was particularly useful for analysing complex geometries and materials, although it was computationally more intensive compared to other methods.

2.2 SEISMIC DIRECT SSI BOUNDARY VALUE PROBLEMS

Soil-structure interaction (SSI) problems are numerically complex due to the coupled nature of the interacting systems, which involve multiple physical phenomena (Lai & Martinelli, 2013). Lai & Martinelli (2013) summarised various approaches available in the literature to tackle such problems. Among these approaches, direct modelling was the only method that maintained the coupled nature of the differential equation system at each step in the time-discretized solution. Lai & Martinelli (2013) stated that due to its precision, many authors and industry professionals prefer the direct method for solving SSI problems while considering various complexities, and the fact that several software packages, such as FLAC, Abaqus, Plaxis, DIANA, and OpenSees, offer robust frameworks and capabilities for effectively modelling and solving SSI problems was noted.

Three-dimensional modelling of shallow-founded structures is a significant area of interest in the literature, especially for seismic assessment and liquefaction-induced settlement analysis. Bray & Dashti (2014) and Dashti et al. (2010a) proposed a decomposition of the expected deformations of foundations over liquefiable soils based on centrifuge experiments. The identified modes of deformation are classified into volumetric and deviatoric types. Volumetric deformations were due to rapid drainage ($\boldsymbol{\varepsilon}_{DR}^{\boldsymbol{p}}$), sedimentation ($\boldsymbol{\varepsilon}_{SED}^{\boldsymbol{p}}$), and consolidation ($\boldsymbol{\varepsilon}_{CON}^{\boldsymbol{p}}$). Deviatoric deformations resulted from partial bearing capacity loss ($\boldsymbol{e}_{BC}$) and induced building ratcheting ($\boldsymbol{e}_{SSI}$).

Bullock et al. (2019) focused on devising novel design strategies for shallow-founded structures by considering vertical settlements and foundation rotations. The effect of the foundation aspect ratio on foundation rotation and settlements was noted. Furthermore several studies, including Bullock et al. (2018), Dashti & Karimi (2017), and Karimi & Dashti (2017), examined the efficiency, sufficiency, and practicality of various intensity measures for shallow-founded structures. These studies found that pseudo-spectral velocity (PSV) best correlated with foundation rotations, settlements correlated most effectively with cumulative absolute velocity (CAV), and the structural response was best captured with spectral acceleration (SA).

A similar effort Bray & Macedo (2017) presented a 2D numerical model of a medium-sized shallow-founded structure on liquefiable soil. The authors observed partial or total vertical settlements driven by the rocking motion of the structure over softer soil. The authors attributed the triggering of this phenomenon to the softening of soil immediately below the foundation due to liquefaction. Local liquefaction of these areas was observed due to momentary increases and decreases in pore water pressures as the foundation rocks, leading to ratcheting settlements.

Studies by Conte et al. (2002) and Zhang et al. (2003; 2004; 2008) modelled a 330 m bridge using a 2D plane-strain model, focusing on nonlinear soil behaviour. The study included a probabilistic analysis to determine the return period of events that would generate different failure modes of the structure. Elgamal et al. (2008) expanded upon this work by incorporating a 3D soil model, allowing for the inclusion of the bridge's transverse behaviour.

Su et al. (2019) introduced a 2D solid-fluid fully coupled nonlinear finite element model for seismic fragility analysis of a pile-supported wharf in OpenSees. In their study, they highlighted the significant impact of dike permeability on the seismic fragility of the wharf, particularly at higher damage states.

Ucci et al. (2011) studied the nonlinear soil-structure interaction (SSI) of a curved bridge on the Italian Tollway A25, focusing on the effects of seismic wave amplification in superficial soil layers and the complexities involved in the computational modelling of SSI problems. The study introduced a detailed finite element model that follows the direct SSI approach, highlighting the importance of soil and boundary conditions in evaluating the seismic response of a reinforced concrete bridge.

Solberg et al. (2016) developed a generalised nonlinear time-domain method for soil-structure interaction (SSI) analysis based on an extension of the DRM. The method was applied to model an embedded small modular reactor subjected to earthquake loads. The

study demonstrated that this approach could effectively capture the nonlinear behaviour of soils and structural responses under seismic conditions, providing a more accurate alternative to traditional frequency-domain methods like SASSI.

Kanellopoulos et al. (2023) investigated the dynamic structure-soil-structure interaction (SSSI) effects for nuclear power plants (NPPs) using high-fidelity 3D finite element models. The study focused on the interaction between the reactor and auxiliary buildings under seismic loading, accounting for nonlinear soil and soil-foundation interface behaviours. The findings demonstrated that nonlinear soil response could significantly mitigate detrimental out-of-phase rotational interactions.

Abell et al. (2018) investigated the effects of directional wave propagation on the seismic response of NPPs by explicitly modelling the source and the SSI system in the ESSI simulator. In their simulation, they used DRM boundaries to apply the wave field occurring at the boundaries due to a point source in the distance. Recently, Abell et al. (2022) implemented the DRM boundaries in OpenSees, allowing users to model spatial variability in the incoming wavefield.

2.2.1 Direct SSI response of shallow-founded RC frame structures

On the other hand, Professor Gazetas and colleagues studied the beneficial effects of SSI-induced foundation deformations on RC frame structures. In his paper for the 4th Ishihara Lecture, Gazetas (2015) and during the 59th Rankine Lecture, Gazetas (2019) discussed seismic foundation design methods, particularly focusing on rocking foundations. The studies emphasised the potential benefits of allowing foundations to undergo controlled rocking motion during seismic events rather than following traditional capacity design principles. The study demonstrated that this approach could reduce residual displacements and enhance the overall seismic resilience of structures.

Mylonakis & Gazetas (2000), examined whether soil-structure interaction (SSI) effects are beneficial or detrimental during seismic events. Through analytical and numerical studies, they demonstrated that SSI could reduce seismic forces transmitted to a structure, thereby providing a protective effect in certain conditions, particularly when rocking and uplift are allowed to occur.

Anastasopoulos et al. (2010) proposed that soil failure mechanisms, traditionally viewed as detrimental, could be intentionally used as a form of seismic protection. By designing foundations that allow for controlled soil failure, they showed that structures could dissipate seismic energy more effectively, reducing the demand on the superstructure and enhancing overall seismic performance.

Gelagoti et al. (2012a) explored rocking isolation for low-rise frame structures on isolated footings. They demonstrated that allowing controlled rocking motion of the foundation can serve as an effective seismic isolation mechanism, reducing the forces transmitted to the superstructure and mitigating potential damage during earthquakes.

Gazetas (2013) argued that, under seismic loading, achieving a factor of safety greater than one is not always feasible or necessary for geotechnical structures. The study provided several examples demonstrating that an apparent seismic factor of safety below one does not necessarily indicate failure but can still result in acceptable performance due to the cyclic nature of seismic loads and the inherent ductility of the soil-structure system.

Gazetas et al. (2013) investigated the nonlinear stiffness characteristics of foundations that undergo rocking motion during seismic events. It provided a detailed analysis of how rocking affects the dynamic response of structures, emphasizing the importance of considering nonlinear behaviour in seismic design and assessment of foundations.

In summary, the literature highlights the critical role of SSI in seismic analysis. Research on rocking isolation and controlled foundation motions has demonstrated significant potential in reducing seismic demands on structures, particularly for low-rise buildings. However, there is still room for discussing the SSI effects on structures such as masonry towers, where both soil and structural nonlinearities play a crucial role. The findings in the literature align well with the results presented in Sections 8.3, 8.4 and 8.5 of this work, which similarly shows that rocking isolation can significantly benefit squat masonry towers, both in the presence and absence of adjacent structures, by reducing seismic demands.

2.3 MODELLING AND SEISMIC ANALYSIS OF MASONRY STRUCTURES

Modelling masonry behaviour presents significant challenges due to its composite nature, comprising brick and mortar, and its anisotropic characteristics resulting from the method of bricklaying. Furthermore, the mechanical properties of historical masonry structures often involve a high degree of uncertainty, complicating the accurate characterisation of mechanical properties. Historically, architects and engineers have relied on empirical methods and prior experience when designing and constructing masonry structures, primarily due to the limited availability of experimental data and computational tools (Drysdale et al., 1994; Hendry, 1990).

As more experimental data became available, engineers developed various computational strategies to better understand and predict masonry behaviour. Macro-modelling techniques simplified the representation of masonry by treating it as a homogeneous continuum. This technique was computationally efficient and suitable for large-scale structures but struggled to capture microstructural variations and strain localisation effects

accurately (Pelà et al., 2011, 2013; Petracca, 2015; Roca et al., 2010). In contrast, micro-modelling approaches offered a detailed representation of the heterogeneous microstructure of masonry, providing a more realistic simulation of its behaviour. However, these methods were computationally intensive, making them less feasible for large-scale applications (Abdulla et al., 2017; Di Trapani et al., 2024; Petracca et al., 2017, 2021; Zucchini & Lourenço, 2009).

An emerging solution was using computational homogenisation techniques, which aim to combine the advantages of both macro- and micro-modelling by treating the structure as an equivalent homogeneous medium at the macro scale while solving the micro-scale problem separately on a representative volume element (RVE). Although promising, these methods require adaptation to handle strain localisation and accurately model the brittle behaviour of masonry materials, highlighting the ongoing need for advancements in this field (Addessi et al., 2010; Oliver et al., 2014; Otero et al., 2018; Petracca, 2015; Petracca et al., 2016).

2.3.1 Micro-modelling

Micro-modelling of masonry structures involves representing the detailed geometry and material properties of the individual components, such as brick units and mortar joints. This approach captured the heterogeneous nature of masonry by explicitly modelling the distinct materials and their interactions. Micro-modelling techniques were broadly classified into detailed micro-modelling (DMM), simplified micro-modelling (SMM), and continuous micro-modelling (CMM) (Lourenço, 1996; Lourenço & Rots, 1997; Oktiovan et al., 2023; Petracca, 2015; Petracca et al., 2022). DMM provided the most accurate representation using continuum elements for both units and joints and interface elements to simulate friction and cohesion. SMM simplified the model by treating brick units as linear elastic elements and mortar joints as nonlinear interfaces, reducing computational costs while still capturing essential mechanical behaviour, but it often compromised the accuracy and detail of the simulation, limiting their ability to predict complex failure mechanisms such as cracking and crushing accurately (Kalkbrenner, 2021).

2.3.2 Multi-scale modelling

Multiscale modelling combined the strengths of micro and macro modelling by linking analyses at different scales to provide a comprehensive understanding of masonry behaviour. This approach used detailed micro models to capture the material behaviour at the scale of individual components and macro models to represent the overall structure. The computational homogenisation technique, also known as FE^2, was commonly used in multiscale modelling, where the behaviour at the macro scale was derived from the response of a representative volume element (RVE) modelled at the micro-scale (Kalkbrenner, 2021; Schröder & Hackl, 2014).

The primary challenge of multiscale modelling was its computational demand, as it requires solving coupled problems at both the micro and macro scales. This complexity made the approach computationally expensive, particularly for large-scale structures where the number of RVEs and the associated calculations were vast. Moreover, accurate multiscale modelling necessitated a precise definition of boundary conditions and material properties at the micro-scale, which were difficult to determine (Kalkbrenner, 2021; Mercatoris et al., 2009; Mercatoris & Massart, 2011; Petracca et al., 2016).

To address these challenges, recent developments in multiscale modelling have focused on improving the efficiency and accuracy of the homogenisation process. Techniques such as off-line computation of RVE responses and machine learning-based homogenisation have been proposed to reduce computational costs by decoupling the micro and macro analyses (Zaghi et al., 2018). These approaches allowed for the rapid extraction of precomputed RVE responses during macro-scale analysis, significantly enhancing computational efficiency while maintaining the accuracy of the multiscale model (Petracca et al., 2017; Zaghi et al., 2018).

Machine learning-based (data-driven) homogenisation and off-line techniques have also been explored to reduce the computational burden of micro-modelling, enabling more extensive and detailed analyses without prohibitive computational costs (Kalkbrenner, 2021; Zaghi et al., 2018).

2.3.3 Macro-modelling

Macro modelling simplified the representation of masonry by treating it as a homogeneous material with averaged properties. This approach did not distinguish between the brick units and mortar joints but instead used a single continuum model to represent the entire structure. Macro modelling was particularly useful for analysing large-scale masonry structures, such as bridges, towers, and cathedrals, where detailed micro-modelling would be computationally impractical. The models typically employed smeared damage or plasticity formulations to simulate the nonlinear behaviour of masonry, accounting for differences in tensile and compressive strengths and capturing the material's orthotropic characteristics (Lourenco, 1995; Lourenço & Rots, 1997; Pelà et al., 2013).

One of the primary challenges in macro modelling was the accurate representation of masonry's anisotropic and brittle behaviour. Since the method did not explicitly model the individual components, it struggled to capture localised effects such as cracking and stress redistribution, which were crucial for understanding failure mechanisms. Hence, developing suitable constitutive models that can adequately represent the complex behaviour of masonry under different loading conditions remains an ongoing area of research (Kalkbrenner, 2021; Petracca, 2015; Petracca et al., 2022).

2.3.4 Seismic analysis of masonry towers

Seismic analysis of masonry towers was essential due to their intrinsic vulnerabilities, such as slenderness, anisotropic material properties, and irregular geometries. These factors make towers susceptible to seismic forces, necessitating comprehensive analysis methods that integrate static and dynamic approaches.

Abruzzese et al. (2009) focused on the static pushover behaviour of medieval masonry towers, emphasising the importance of vibration measurements for modal characterisation. Their study underscored how natural frequencies and mode shapes influence the response of towers to seismic loads. Similarly, Peña et al. (2010) demonstrated through finite element (FE) analysis that the upper sections of masonry towers were particularly vulnerable to seismic forces due to higher mode vibrations. Their work highlighted that seismic effects were often more intense at the top of the structure.

D'Ambrisi et al. (2012) provided a comprehensive seismic assessment of a historical masonry tower using nonlinear static (pushover) analyses. They found that while pushover analysis was helpful for identifying overall structural weaknesses, it often underestimates the seismic response compared to dynamic vibration analyses, which capture the effect of higher modes.

Valente & Milani (2016) conducted nonlinear dynamic and static analyses on eight historical towers in Italy. They observed that factors such as slenderness, wall thickness, and openings significantly influence the seismic performance of towers. Their study showed that the damage distribution and displacement demand under seismic loads were strongly affected by local irregularities. Bartoli et al., (2017) further reinforced these findings by computing seismic risk metrics and using them as a quantitative understanding of the potential damage scenarios. Similarly, Salvatori et al. (2015) introduced a probabilistic seismic assessment framework that combined nonlinear static analysis with damage probability distributions, which provided a method for predicting potential damage under various earthquake intensities.

Despite the significant advancements in the seismic analysis of masonry towers, there remains a notable gap in the application of dynamic transient analysis. While many studies focus on nonlinear static (pushover) and modal combination analyses, these approaches often fail to capture the full complexity of a structure's response under real-time seismic loads. Dynamic transient analysis, which models the time-dependent behaviour of structures during an earthquake, is underutilised, even though it is critical for understanding how towers respond to varying seismic inputs over time.

Additionally, there is a pressing need to incorporate the nonlinear behaviour of the masonry towers and the underlying soil in these analyses. Most existing studies treat the soil-structure interaction either simplistically or ignore it, leading to an incomplete understanding of how the foundation's behaviour influences the overall seismic response. Addressing these gaps through transient dynamic analysis and fully accounting for the nonlinear interactions between the soil and masonry structures would significantly enhance the accuracy of seismic vulnerability assessments and improve the strategies for preserving these historic towers.

2.4 RETURN-MAPPING SCHEMES FOR HIGHLY NONLINEAR MATERIALS

The robust treatment of material nonlinearities within the Finite Element Method (FEM) has been a significant area of focus in research. In conventional FEM, the material response at a Gauss point is generally described by a phenomenological law, which is calibrated against experimental data to ensure accuracy. In damage mechanics and plasticity, internal material computations—such as the evaluation of flow rules, updates of internal variables, and stress calculations—often require complex calculations. These intricate processes are managed through the return mapping procedure, which may involve solving a multivariable optimisation problem or a set of differential equations using numerical integration methods (Simo & Hughes, 1998).

2.4.1 Implicit methods

Implicit integration methods are extensively utilised in computational plasticity due to their stability and robustness, mainly to solve highly non-linear material behaviour in larger time steps. The backward Euler scheme was one of the most employed among these methods. The state variables were solved at each subsequent time step, t_{n+1}, through an iterative process for non-linear material equations (Simo & Hughes, 1998).

The integration process began with an elastic predictor step, where a trial elastic stress state was calculated under the assumption of purely elastic behaviour. If this state exceeded the yield condition, a plastic corrector step was triggered, projecting the stress back onto the yield surface. During this plastic corrector step, the equations governing plastic flow were iteratively solved using Newton's method, enforcing yield and consistency conditions. Critical to this method was the calculation of the consistent tangent stiffness matrix, which facilitates quadratic convergence of the Newton iterations by accurately representing material stiffness in the plastic regime (Simo & Hughes, 1998; Tamagnini et al., 2002).

Several studies have employed implicit integration techniques for specific applications. Genna & Pandolfi (1994) developed a two-step integration scheme for the rate plasticity equations of the Drucker-Prager model using a non-radial return mapping approach. Jeremić & Sture (1997) introduced a fully implicit algorithm for the direct integration of

material equations of geomaterials, enhancing convergence and stability using a consistent tangent stiffness tensor. Rouainia & Muir Wood (2001) achieved a computationally efficient solution for cyclic loading in soils with an implicit integration scheme for kinematic hardening. Borja et al. (2003) implemented an implicit integration method for three-invariant elastoplastic models to capture complex pressure-dependent behaviours.

Further enhancements were made by Pérez-Foguet & Armero (2002), who demonstrated the performance of closest-point projection algorithms in a variational framework of material thermodynamics equations, and Seifert & Schmidt (2008), who introduced line-search methods to return mapping algorithms to boost convergence in porous plasticity models. Motamedi & Foster (2015) improved the handling of plastic flow in three-invariant models, and finally, a robust return-map algorithm for multi-surface plasticity was proposed by Adhikary et al. (2017), and Gu et al. (2011).

2.4.2 Explicit methods

In e***xplicit schemes,*** the solution at the next time step was determined solely based on the current state, without the need for solving simultaneous equations. This characteristic made explicit methods particularly appealing for highly nonlinear problems, where obtaining an implicit solution was computationally expensive. The simplicity of explicit solutions allowed for straightforward implementation, which was advantageous in certain contexts (Simo & Hughes, 1998).

However, explicit methods have several drawbacks, especially when applied to nonlinear problems. These disadvantages included stability constraints that often require small time steps to maintain numerical stability, which can significantly increase computational cost. Additionally, explicit methods suffered from constraint violations, accuracy limitations, and difficulties in handling inertia effects, which limited their applicability in some scenarios (Tu et al., 2009).

Various researchers have extensively studied the explicit integration of material equations and the associated error quantification. For example, Andrianopoulos et al. (2010) and Zhao et al. (2005) utilised explicit methods to solve well-known plasticity models and advanced soil models. A notable application of explicit integration in material return mapping was the cutting plane algorithm (Simo & Hughes, 1998; Simo & Taylor, 1985). This algorithm was particularly relevant in the solution of the multi-yield-surface material model proposed by Prevost (1982, 1989) and in solving the non-smooth kinematic hardening equations developed by Mróz (1967) and Mróz & Pietruszczak (1983).

Despite their benefits, explicit methods were limited by their computational cost due to the necessity of small-time steps, potential violations of thermodynamic constraints, stability issues, accuracy limitations, and challenges in managing inertia effects (Tu et al., 2009).

2.4.3 Mixed implicit-explicit methods

Mixed methods combined various numerical approaches, such as explicit sub-stepping, implicit-to-explicit switching, implicit-explicit partitioning, operator splitting, and semi-implicit methods. The development of these mixed solution methods, including partitioned solution and operator splitting approaches, was first introduced by Belytschko & Mullen (1978) and Hughes et al. (1979).

Partitioned implicit-explicit approaches involved the simultaneous use of both implicit and explicit integration schemes within different parts of the same finite element mesh. This methodology was applied by Belytschko et al. (1979) and subsequently by Liu & Belytschko (1982) to address computationally intensive fluid-structure interaction problems, where the structure's behaviour was often linear. They employed various combinations such as implicit-explicit, explicit-explicit with different time steps, and implicit-implicit with different time steps in their partitioned solutions. Similarly, Kunar, (1982) demonstrated an implicit-explicit partitioned soil-structure interaction model, where the structural behaviour was assumed linear and handled using an explicit scheme, while the nonlinear soil behaviour was modelled using an implicit return-mapping algorithm.

More recently, Lv & Chen (2022) introduced a partitioned asynchronous parallel partitioning algorithm to solve the dynamic soil-structure interaction (SSI) of a nuclear power plant. In their approach, the linear structure and nonlinear soil were treated in separate domains, each with different solution algorithms. As one domain was updated in time, synchronization occurred over shared nodes, and the solution iterated between domains until convergence was achieved.

In contrast, the ***operator splitting approach*** separated the governing equations into distinct components that were solved independently, allowing for efficient computation and better stability in nonlinear problems. Plesha & Belytschko (1985) introduced an approach in which they divided the material's constitutive law into an implicit, history-independent portion and an explicit, history-dependent portion. They efficiently integrated a strain-softening material, demonstrating unconditional stability and accurate solutions to dynamic problems.

Later, Jacob & Ebecken (1994) applied operator splitting within hybrid time integration schemes for structural dynamics. Their work leveraged both explicit and implicit algorithms

to improve computational efficiency in solving complex non-linear problems, particularly for dynamic analysis of structures.

Implicit-to-explicit switching method involved switching between implicit and explicit schemes depending on the problem's requirements at a particular step, optimizing both stability and computational efficiency. Jung & Yang (1998) introduced a stepwise combined implicit-explicit scheme for the finite element analysis of sheet metal forming. The method switched from implicit to explicit time integration when convergence difficulties occurred, enabling more efficient handling of complex geometries and contact conditions without sacrificing accuracy.

Noels et al. (2004) presented a combined implicit-explicit algorithm to simulate sheet metal forming processes. In this method, the stamping process, characterized by rapid, highly non-linear dynamics, was handled by an explicit scheme. Meanwhile, the slower spring-back process, which benefits from stability over larger time steps, was managed by an implicit scheme.

Curiel-sosa et al. (2013) applied the implicit-explicit switching technique to snap-through and snap-back buckling problems. In their work, the implicit method was used until the solution began to diverge; after this point, the explicit method was activated to overcome convergence issues. After passing the instability point, the solver switched back to the implicit method.

Semi-implicit methods combined explicit and implicit solutions within a single time step to achieve a balance between computational efficiency and stability. The implicit-explicit (IMPL-EX) method was first introduced by Oliver et al. (2008), and the free-continue approach, introduced by Tu et al. (2009), were examples of such a technique.

The freeze-continue approach, proposed by Tu et al. (2009), offered an efficient methodology for computationally demanding multi-scale problems, such as finite element method-discrete element method (FEMxDEM) simulations of geomaterials. At the beginning of a Newton-Raphson step, the plastic internal variables of the material are "frozen," and previously converged values were used to achieve stress and stiffness during the predictor step. Therefore, this approach led to a constant consistent tangent by evaluating the flow rule based on the stress from the previous step, avoiding the linearisation of the flow rule. After convergence, the frozen plastic internal variables are updated by solving a single implicit step (Figure 2.1).

The freeze-continue method differed from the IMPL-EX approach because it used previous step variables in the tangent calculation instead of explicit extrapolation. Tu et al. (2009) omitted the explicit extrapolation step due to the potential for yield surface drifting

associated with explicit algorithms, where the consistency condition was infinitesimally violated due to extrapolation.

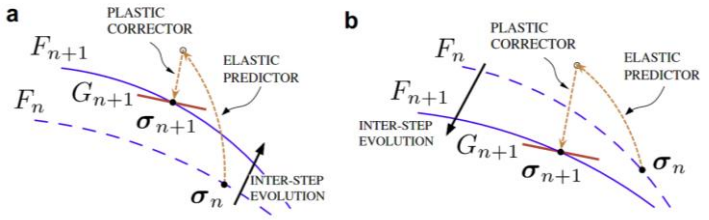

Figure 2.1. Elastic predictor-plastic corrector steps of the freeze-continue approach. (a) Strain hardening case and (b) Strain softening case. Figure adapted from Tu et al. (2009)

2.4.4 The implicit-explicit method

The mixed implicit-explicit (IMPL-EX) integration method was a numerical technique designed to enhance stability and computational efficiency in non-linear problems. By combining explicit extrapolation of internal variables with implicit stress updates, IMPL-EX balances robustness and accuracy, allowing for larger time steps without compromising stability. This approach was particularly useful in handling complex material behaviours, such as strain softening and contact-friction scenarios, where traditional implicit methods may be less efficient or fail to converge (Oliver et al., 2008).

Mathematically, the IMPL-EX method results in a symmetric and semi-positive definite algorithmic tangent constitutive tensor, improving solution robustness even when negative tangent stiffness could cause non-convergence in implicit methods. Computationally, it reduced the solution cost by converting non-linear problems into a series of linear problems, significantly decreasing computational time and resources, especially in large-scale simulations. However, the method's reliance on extrapolation can introduce errors in highly non-linear situations, requiring careful calibration and adaptive time-stepping to maintain accuracy (Oliver et al., 2008; Petracca et al., 2022).

2.4.4.1 *Implicit-explicit engineering problems*

The impl-ex method has been effectively utilized in various engineering applications to address complex material behaviours. Gimenes et al. (2020) and Rodrigues et al. (2020) applied the impl-ex method in multiscale finite element method (FEMxFEM) crack propagation analysis in plain concrete. In their studies, the elastic parameters of a linear elastic constitutive material were actively updated by upscaling the response of a double-scale model, which allowed for a more accurate simulation of crack propagation.

Maedo et al. (2021) extended the impl-ex method to model crack propagation in porous media within the coupled thermo-hydro-mechanical processes associated with hydraulic fracturing. They adapted the Mesh Fragmentation Technique to incorporate thermal effects, demonstrating the flexibility of the IMPL-EX method in handling complex, multi-physics problems.

Oliynyk et al. (2021) implemented the impl-ex integration scheme with an extension proposed by Monforte et al. (2019) to develop a finite deformation isotropic hardening non-associative elastic-plastic constitutive model, known as the FD_Milan model. In this model, the correction stage was achieved using an explicit return mapping strategy, continuing iteratively until the consistency condition was satisfied within a specified tolerance. This approach essentially created an explicit-explicit (EXPL-EX) variant of the IMPL-EX method. To further enhance the model, a non-local hardening law was applied to ensure mesh-independent solutions, which was crucial in scenarios where strain softening occurs. The robustness and effectiveness of this model were demonstrated through simulations of a bi-axial compression test and a 2D cone penetration test (CPTu), showcasing its ability to handle complex deformations and maintain stability across different mesh sizes.

Petracca et al., (2022) utilised the impl-ex method in a continuum damage-plasticity model designed for masonry and concrete behaviour. To address the strain localisation problem, they employed a fracture energy-based regularization technique. The impl-ex integration scheme was then applied to efficiently simulate a dynamic shake table test of a 3D, two-story masonry structure, highlighting the method's capability in dynamic applications.

Despite these successful applications, the literature still has a notable gap regarding the performance of semi-implicit models in the context of kinematic hardening materials and liquefaction models.

2.4.4.2 *Implicit-explicit contact problems*

The impl-ex method has also been applied to challenging contact problems, such as those involving frictional interactions and rolling contacts, to assess its effectiveness in handling complex boundary conditions and non-linearities typical of these scenarios. In their study, Oliver et al. (2008) developed a 2D contact model involving two cylinders rolling over each other, which represents a typical contact problem with significant non-linear behaviour due to friction and deformation.

The impl-ex method was used to simulate the contact interactions by combining explicit extrapolation for internal variables with implicit stress updates. This approach was particularly advantageous in managing the computational difficulties associated with

contact problems, which often require very fine time steps and robust convergence criteria when using traditional implicit methods. By allowing for larger time steps, the impl-ex method significantly reduced computational costs while maintaining the accuracy and stability of the solution (Oliver et al., 2008).

2.5 IMPLICIT-EXPLICIT DAMAGE-PLASTICITY FORMULATION FOR MASONRY

Damage continuum materials were often used in the numerical modelling of masonry behaviour. The damage approach differed from the elastoplastic material theory at the irrecoverable straining process. In the elastoplastic process, the plastic work was assumed to be spent modifying the internal crystalline structure, causing dislocations in the crystal lattice and progressive collapse-formation cycles of defects. In return, the material accommodated large plastic deformation without fracturing. On the other hand, the damage process assumed that the plastic work was spent on forming microcracks or increasing crack length and causing new surfaces to form within the material structure, modelling the internal process of a progressively fracturing solid (Lubliner et al., 1989). As a result, the material did not accumulate permanent deformations. Instead, the characteristic feature of the damage assumption was the reduction in the unloading-reloading stiffness with increased straining.

From a mathematical perspective, analogous to the plastic multiplier in elastoplastic materials, the history of the plastic process in damage materials was considered through the evolution of the damage ratio. The damage ratio was a rational number within the domain of [0, 1]. It was a function of the damage surface and was only allowed to increase as a threshold value determined by the stress history (Petracca et al., 2022).

The experimental stress-strain response of masonry brick and mortar and behaviour at the member level, such as masonry walls, was reasonably captured using a combination of damage and elastoplastic material theory (Oller et al., 2003; Petracca et al., 2022; Wu et al., 2006). This hinted at the possibility of having a complex internal behaviour at the microscale in which the plastic process was controlled by both fracturing and dislocation of the microstructure (Kalkbrenner, 2021; Petracca et al., 2017). The fracturing behaviour was further decomposed into three essential modes of cracking: tensile, compressive and shear (Petracca, 2015). The state-of-the-art models provide parallel formulations to govern each cracking mode, offering distinct stress-strain and damaging behaviour as a function of the stress path.

Standard damage models worked in total strains, and the damage surface evolution was only possible with monotonic loading. Furthermore, damage models available in OpenSees and Abaqus worked with a single damage variable for both tension and compression. This caused issues in the structural response, leading to premature tensile failure due to high

compression loading cycles identified by Rosell (2010). Employing individual damage variables in compression and tension required formulating two sets of damage surfaces and state parameter evolution equations accordingly. However, the advantage of doing so was significant in cyclic loading. Petracca et al. (2022) showed a remarkable match in crack patterns observed in the cyclic laboratory testing and numerical modelling of masonry walls when a tension-compression damage anisotropic formulation was employed.

Strain softening response was a fundamental aspect of masonry structure behaviour. As a brittle material, masonry dissipated energy primarily through cracking. As the straining progressed, the micro-cracks started to orient and widen along the maximum and minimum principal stress directions, forming larger-scale cracks that propagated at the structural member level. The relationship between microscale cracking and macroscale crack propagation is well-known and has been studied extensively through multi-scale methods (using FEMxFEM or FEMxDEM coupled analysis) by various authors (Kalkbrenner, 2021; Oliver et al., 2014).

At the structure scale, the strain softening capability of the material model was essential in capturing the crack propagation in the structure and realistically computing inelastic failure mechanisms (Rosell, 2010). Most damage models (Pelà et al., 2011; Petracca et al., 2022; Wu et al., 2006) included strain-softening expressions in their tensile and compressive hardening functions.

2.5.1 DamageTC3D and ASDConcrete3D material formulation

Recently, a particular damage-plasticity model was developed and implemented in OpenSees by Petracca et al. (2022) combined many of the advanced features preferred in masonry modelling that were identified by various studies (Pelà et al., 2011, 2013; Wu et al., 2006).

The formulation of the tension-compression anisotropic, impl-ex damage-plasticity model was given as follows (Petracca, 2015; Petracca et al., 2017, 2022). The boldface letters denote tensors, whereas the $\otimes$ and : signs define tensor multiplication resulting in higher order tensor and contraction operations. All variables without subscripts refer to the current step, while subscripts n and $n-1$ refer to the previously converged time steps. The positive and negative parts of a mentioned tensor can be additively (linearly) composed to obtain the full tensor. The nominal stress tensor, $\boldsymbol{\sigma}$ is defined as

$$\boldsymbol{\sigma} = (1 - d_c^+)\hat{\boldsymbol{\sigma}}^+ + (1 - d_c^-)\hat{\boldsymbol{\sigma}}^- \qquad \textbf{2.1}$$

where $\hat{\boldsymbol{\sigma}}^+$ and $\hat{\boldsymbol{\sigma}}^-$ were the negative and positive parts of the effective stress tensor, $\hat{\boldsymbol{\sigma}}$. The nominal stress was related to the effective stress through the scalar positive and negative cracking damage variables, d_c^+ and d_c^-. The damage variables were initially 0, indicating an

intact material, and can increase up to 1, representing a completely fractured material as the straining progresses. Hence, the material stress and stiffness were reduced as a function of the cracking damage. Furthermore, the positive and negative parts of the effective stress tensor were related to the trial effective stress tensor, $\breve{\boldsymbol{\sigma}}^{\pm}$ (i.e. elastic prediction), through the scalar positive and negative plastic damage variables, $d_{pl}^{\pm}$, respectively.

$$\hat{\boldsymbol{\sigma}} = \hat{\boldsymbol{\sigma}}^{+} + \hat{\boldsymbol{\sigma}}^{-} \tag{2.2}$$

$$\hat{\boldsymbol{\sigma}}^{\pm} = (1 - d_{pl}^{\pm})\breve{\boldsymbol{\sigma}}^{\pm} \tag{2.3}$$

The trial effective stress tensor, $\breve{\boldsymbol{\sigma}}$ was found by multiplying the strain increment tensor with the initial elastic coefficient tensor, $\mathbb{E}_0$ to compute the trial stress increment and sum with the committed effective stress at the previous time step, $\hat{\boldsymbol{\sigma}}_{\boldsymbol{n}}$. The positive part of the trial effective stress tensor was equal to the spectral decomposition of trial effective stress tensor. In contrast, the negative part was computed by subtracting the positive part from the trial effective stress tensor, itself.

$$\breve{\boldsymbol{\sigma}} = \hat{\boldsymbol{\sigma}}_{\boldsymbol{n}} + \mathbb{E}_0 : (\boldsymbol{\varepsilon} - \boldsymbol{\varepsilon}_{\boldsymbol{n}}) \tag{2.4}$$

$$\breve{\boldsymbol{\sigma}}^{+} = \sum_{i=1}^{3} \langle \breve{\sigma}_i \rangle \, \boldsymbol{p}_i \otimes \boldsymbol{p}_i \tag{2.5}$$

Petracca et al. (2022), drawn attention to a fundamental discrepancy between the formulated damage-plasticity model and the preceding formulations by Wu et al. (2006) in the computation of the trial stress. Unlike pure damage models, the plastic dissipation was split between damage and elastoplastic modes. Hence, the formulation featured a plastic strain tensor. This meant that the trial stress could not be computed in total strain and must be the function of the strain increment.

The loading and un/re-loading conditions were assessed via two scalar variables named the positive and negative equivalent stresses, $\breve{\tau}^{\pm}$. The equivalent stresses were a function of the positive and negative Lubliner-type (Lubliner et al., 1989) damage surfaces and computed as follows:

$$\breve{\tau}^{-} = H(-\breve{\sigma}_{min}) \left[\frac{1}{1-\varrho} \left(\varrho \breve{I}_1 + \sqrt{3\breve{J}_2} + k_1 \varphi \langle \breve{\sigma}_{max} \rangle \right) \right] \tag{2.6}$$

$$\breve{\tau}^{+} = H(\breve{\sigma}_{max}) \left[\frac{1}{1-\varrho} \left(\varrho \breve{I}_1 + \sqrt{3\breve{J}_2} + \varphi \langle \breve{\sigma}_{max} \rangle \right) \frac{f_t}{f_{cp}} \right] \tag{2.7}$$

$$\varphi = \frac{f_{cp}}{f_t}(1-\varrho) - (1+\varrho) \quad \textbf{2.8}$$

$$\varrho = \frac{k_b - 1}{2k_b - 1} \quad \textbf{2.9}$$

where the I_1 and J_2 were the invariants of the trial effective stress tensor obtained in the previous step. k_b was the ratio of the compressive bi-axial strength to the uniaxial compressive strength. k_1 was introduced (Petracca, 2015; Petracca et al., 2017) to provide some control over the dilative response. In Equation 2.6, a k_1 value that was equal to 1 resulted in a Drucker-Prager surface, whereas a 0 value led to a Lubliner-like (Lubliner et al., 1989) surface. Finally, f_t and f_{cp} were the tensile and compressive peak stresses, respectively. It was noted that, due to the consideration of plasticity, the equivalent stresses calculated differ from those derived using traditional continuum models. Regardless, comparable stress values were obtained by Petracca et al. (2022) by incorporating the contribution of plastic strains, calculated as the product of the elastic modulus and plastic strain.

Petracca et al. (2022) provided a formula to transform the equivalent stresses from Equations 2.6 and 2.7 into values compatible with the standard damage theory framework. Cyclic loading was considered using Heaviside functions applied to the damage surfaces. Specifically, the Heaviside functions ensured that (1) the compressive surface evolved only when at least one principal stress was negative, and (2) the tensile surface evolved only when at least one principal stress was positive.

The irreversible damaging history was kept track of via two scalar variables called the positive and negative damage thresholds, r^+ and r^-, respectively. Essentially, the damage thresholds keep the largest values reached by the corresponding equivalent stress values as a function of time throughout the analysis (Petracca et al., 2022).

$$r^+(t) = \max\left(\left(\max_{s \in [0,t]} \breve{\tau}^+(s)\right), f_t\right) \quad \textbf{2.10}$$

$$r^-(t) = \max\left(\left(\max_{s \in [0,t]} \breve{\tau}^-(s)\right), f_{c0}\right) \quad \textbf{2.11}$$

f_{c0} and f_t were the elastic compressive and tensile limits. As in a classical damage model, the hardening behaviour was obtained through a hardening law which was a function of total strains. In Petracca et al. (2022) r^+ and r^- were converted to total strains by diving the corresponding damage threshold with the elastic modulus. Then, positive and negative total stresses were plugged into distinct tension and compression hardening laws. For more information regarding the formulation of the hardening functions and the shapes,

interested readers are referred to the original publications (Petracca, 2015; Petracca et al., 2017).

In summary, strain hardening and softening response are considered in both tension and compression laws, and the mathematical form of the curves were obtained through custom Bezier curves, in which the user can calibrate the coefficients of each Bezier curve to fit experimental material response accurately with relative ease.

$$q^{\pm} = f^{\mp}(\varepsilon_{tot}^{\mp}) \quad \textbf{2.12}$$

$$\varepsilon_{tot}^{\mp} = \frac{r^{\mp}}{E} \quad \textbf{2.13}$$

$q^{\pm}$ included the effect of both plastic and cracking damage. Positive and negative and damage variables are calculated as follows:

$$d_{pl}^{\mp} = 1 - \frac{q_{pl}^{\mp}}{\check{r}^{\mp}} \quad \textbf{2.14}$$

$$\check{r}^{\mp} = E(\varepsilon_{tot}^{\mp} - \lambda_n^{\mp}) \quad \textbf{2.15}$$

$$q_{pl}^{\mp} = q^{\pm} + (1 - w^{\mp})(r^{\mp} - q^{\pm}) \quad \textbf{2.16}$$

$w^{\mp}$was the positive and negative damage factors. The cracking damage:

$$d_c^{\mp} = 1 - \frac{q^{\pm}}{q_{pl}^{\mp}} \quad \textbf{2.17}$$

Finally, knowing the plastic and cracking damage variables, the nominal stress was computed as shown in Equation 2.1. The equivalent plastic strain was updated as follows:

$$\lambda^{\mp} = \varepsilon_{tot}^{\mp} - \frac{q_{pl}^{\mp}}{E} \quad \textbf{2.18}$$

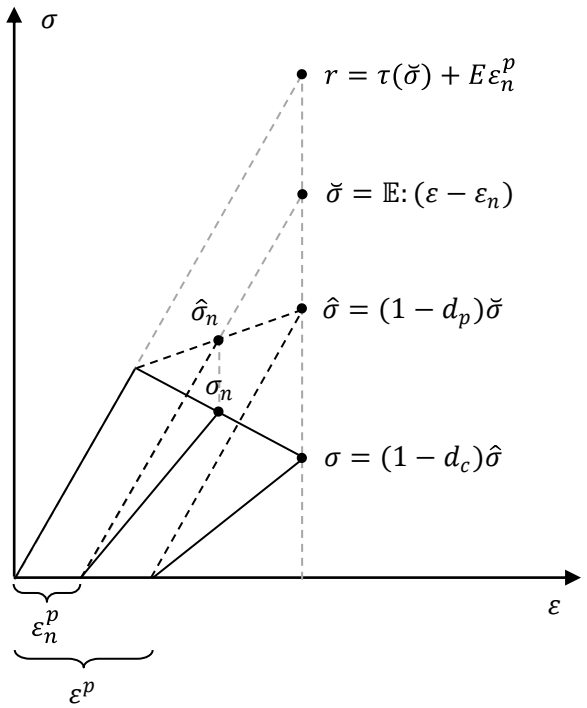

Figure 2.2. Elastic prediction (trial stress) and correction process. After Petracca et al., (2022).

2.5.1.1 *The crack plane or orthotropic yield surface assumption*

Many real-world materials, such as masonry, composites, ceramics, and polymers, exhibit orthotropic behaviour due to their inherent micro-structure or manufacturing process. The traditional isotropic yield criteria, which assumed uniform properties in all directions, failed to capture the directional dependence of these materials. Therefore, an orthotropic yield surface was crucial for developing more precise and reliable models that could predict the behaviour of materials under different loading conditions and orientations (Lourénço, 1995; Lourénço et al., 1997; Oller et al., 2003; Pelà et al., 2013).

The isotropic yield criteria, such as the von Mises or Drucker-Prager criteria, assumed uniform material properties and stress responses in all directions. In contrast, the orthotropic yield criterion assumed different criteria for the two main directions of the material. Oller et al. (2003) defined an orthotropic yield criterion, which enables the adaptation of classical isotropic yield criteria to the behaviour of anisotropic materials. This method involved defining an isotropic yield criterion in a fictitious space and then transforming it into an orthotropic criterion in the real stress space using a fourth-rank

transformation tensor. This tensor embodied the material's directional properties and allowed the isotropic function to be mapped to an orthotropic one, capturing the anisotropic nature of the material.

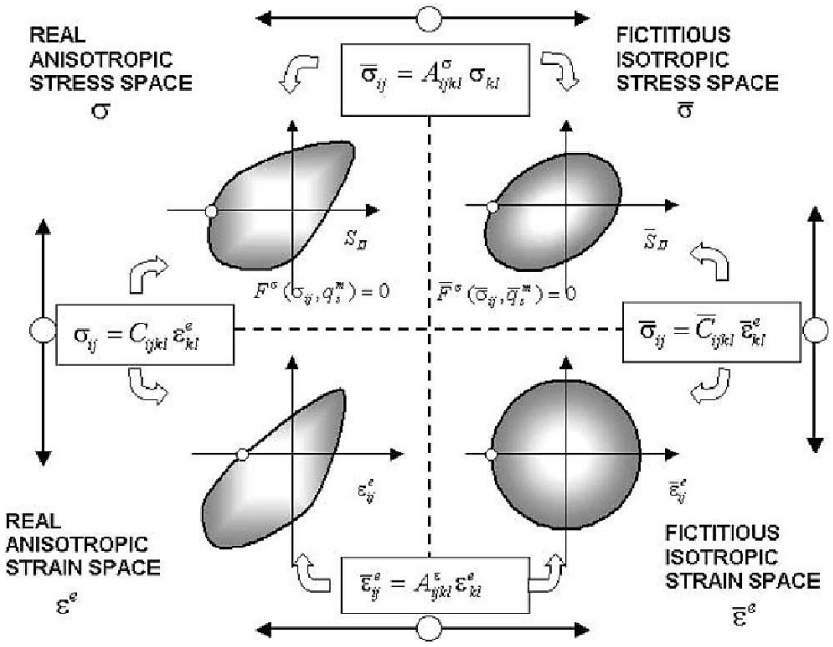

Figure 2.3. Relationship between the anisotropic and isotropic yield surfaces. Tensor $\mathbb{A}$ is the rotation tensor as explained in Oller et al. (2003).

In Figure 2.3, the fictitious isotropic space was a conceptual space where the material was assumed to behave isotopically, meaning its properties were the same in all directions. The real anisotropic space, on the other hand, represented the actual material behaviour where properties differ depending on the direction due to anisotropy (Oller et al., 2003).

Following this technique, Petracca et al., (2022) proposed a user input cracking angle, in which the directional nature of the cracking process was included through the transformation tensor that reflected the principal material directions. By defining yield criteria in the principal stress space and applying the transformation tensors, it was possible to adjust the model to accommodate specific cracking angles as input parameters. This flexibility allowed for the customisation of the yield surface to reflect the onset of damage and crack propagation in preferred orientations, aligning with the anisotropic characteristics of the material.

2.5.1.2 *Fracture energy-based regularisation*

In finite element analysis, material behaviour in the post-peak ranges often suffers from mesh bias. When Drucker's stability postulate is violated, strain increments tend to localise within a narrow band of elements while the rest of the model begins to unload. This concentration of strain in a limited number of elements can lead to inaccuracies in the simulation, as the energy dissipation associated with fracture can be either overestimated or underestimated, depending on the size of the elements where the strain localises.

To mitigate this issue, fracture energy-based regularisation was employed. This approach helped prevent mesh dependency and allowed for the correct dissipation of fracture energy, resulting in a more physically consistent simulation of crack growth and propagation, particularly in materials like masonry, where strain localisation plays a dominant role (Petracca et al., 2022). Petracca et al. (2022) proposed a significantly more flexible evolution law for the compressive and tensile damage parameters $d^{\pm}$ compared to conventional formulations. In this approach, the control points of the Bezier curves used to define the compressive damage evolution were calibrated to match the experimental response from uniaxial compressive tests. To ensure a consistent representation of the material's fracture energy, the compressive and tensile curves, as shown in Figure 2.4, were regularised. In terms of compression, the area under the stress-strain curve was equated to G_c/l_{dis}, where G_c was the compressive fracture energy and l_{dis} was the characteristic length related to the finite element discretisation.

This regularisation was achieved by applying a "stretching" technique to the strain abscissas ε_j, ε_k, ε_r and ε_u shown in Figure 2.4. These strain values were scaled by a stretching factor S, computed to maintain the integrity of the fracture energy dissipation. The stretching factor S, derived as $S = G_c/A_c l_{dis}$, where A_c represents the area under the unregularised stress-strain curve.

$$g_f l_{dis} = G_f \tag{2.19}$$

$$g_f = \left(1 + \frac{1}{H_{dis}}\right)\frac{f_t^2}{2E} \tag{2.20}$$

$$H_{dis} = \frac{l_{dis}}{l_{mat} - l_{dis}} \tag{2.21}$$

where $l_{mat} = 2EG_f/f_t^2$ and $l_{dis} = l_{ch}$ was assumed to be equal to the characteristic length of the finite element. The resulting compressive and tensile stress-strain laws are shown in Figure 2.4.

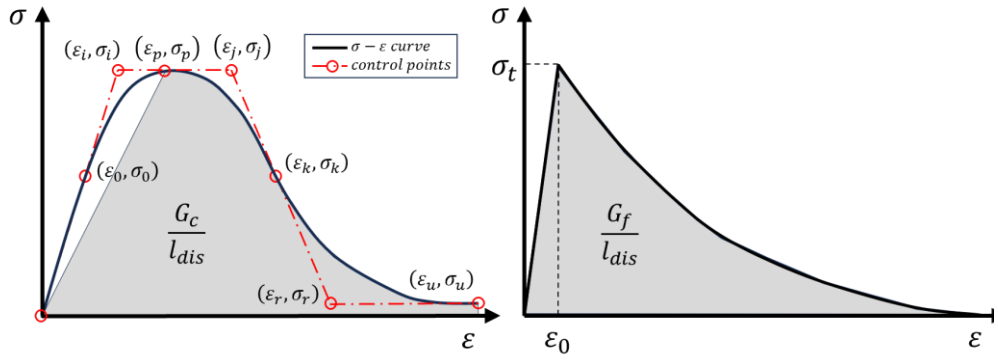

Figure 2.4. Definition of tensile and compressive fracture energies. Material response in tension and compression is regularised by scaling fracture energies by the element's characteristic length. Figure taken from Petracca et al. (2022).

The condition $S > -1.0$ was imposed to prevent constitutive snap-back, a phenomenon where the post-peak response collapses into a single strain value at the peak strain ε_p. To avoid this, the characteristic length l_{dis} , which governs the regularisation process, must satisfy a specific condition to ensure a stable and physically realistic post-peak behaviour.

$$l_{dis} < \frac{2G_c}{\sigma_p \varepsilon_p} \qquad \textbf{2.22}$$

This regularisation framework, therefore, allows the numerical model to maintain accuracy in energy dissipation and avoid mesh sensitivity.

2.5.1.3 *Implicit-explicit (IMPL-EX) integration*

The IMPL-EX integration scheme, originally formulated by Oliver et al. (2008), has been adopted by Petracca et al. (2022) to enhance the stability and efficiency of the damage-plasticity model with strain-softening behaviour. In their formulation, Petracca et al. (2022) ensured that the internal variables remained linearly dependent on the current strain tensor during the explicit phase. This led to a computationally efficient solution by keeping the global problem linear at each time step and providing a positive definite stiffness matrix.

In the standard integration scheme, there were two sources of nonlinearities breaking the linear dependence of current stresses on the current trial strain tensor. First, the internal variables $r^{\mp}$weree nonlinear functions of the trial effective stress tensor, as per Equations 2.10 and 2.11, and second, the tension-compression split of the stress tensor as per Equation 2.5 introduced a nonlinearity (Petracca et al., 2022).

Petracca et al. (2022) handled the nonlinear dependence of internal variables by introducing an explicit extrapolation step. At each time step $n+1$, the internal variables were explicitly extrapolated from their known values at previous time steps n and $n-1$ according to the Equation 2.23:

$$r_{n+1}^{\mp} = r_n^{\mp} + \frac{\Delta t_{n+1}}{\Delta t_n}(r_n^{\mp} - r_{n-1}^{\mp}) \qquad \textbf{2.23}$$

Meanwhile, to handle the nonlinear dependence on the tension-compression split of the stress tensor, Petracca et al. (2022) employed rank-four projection tensors $\mathbb{P}^{+}$ and $\mathbb{P}^{-}$ which were defined using Heaviside functions as shown in Equation 2.24:

$$\mathbb{P}^{+} = \sum_{i=3}^{3} H(\breve{\sigma}_i)\boldsymbol{p}_i \otimes \boldsymbol{p}_i \otimes \boldsymbol{p}_i \otimes \boldsymbol{p}_i \qquad \textbf{2.24}$$

$$\mathbb{P}^{-} = \mathbb{I} - \mathbb{P}^{+} \qquad \textbf{2.25}$$

Here, $H(\breve{\sigma}_i)$ was the Heaviside function applied to the principal stresses, ensuring that the tensile surface evolved only when at least one principal stress was positive, and the compressive surface evolved only when at least one principal stress was negative. The effective stress tensors $\breve{\sigma}^{\pm}$ were computed as:

$$\breve{\sigma}^{\pm} = \mathbb{P}^{\pm} : \breve{\sigma} \qquad \textbf{2.26}$$

During the explicit stage, the projectors $\mathbb{P}^{\pm}$ were held constant, using their values from the previous time step:

$$\mathbb{P}^{\pm} = \mathbb{P}_n^{\pm} \qquad \textbf{2.27}$$

This stepwise linearisation enabled larger time steps without compromising numerical stability. Once equilibrium was achieved at the time $n+1$, the internal variables were implicitly corrected to reduce the error introduced during the explicit extrapolation phase.

The stiffness matrix, which incorporates both the tensile and compressive damage and plasticity contributions, was computed as:

$$\mathbb{C} = \left((1-d_c^{+})(1-d_{pl}^{+})\mathbb{P}^{+} + (1-d_c^{-})(1-d_{pl}^{-})\mathbb{P}^{-}\right) : \mathbb{E} \qquad \textbf{2.28}$$

This mixed implicit-explicit scheme, therefore, balances computational efficiency with the accuracy required to model the complex cyclic response of masonry under cyclic loading.

2.6 CONSTITUTIVE MODELLING OF SOILS FOR SEISMIC SSI ANALYSIS

Several well-established approaches in the literature exist for cyclic dynamic modelling of soils in seismic soil-structure interaction problems. The most notable were the bounding surface plasticity model, the multi-yield surface plasticity model, and the hypoplastic models. Multi-yield surface plasticity was highly effective in scenarios requiring precise control of shear modulus degradation, and simulations in which multiple loading cycles were anticipated. On the other hand, bounding surface plasticity was better suited for modelling scenarios where ultimate strength and large deformation behaviour were critical, such as in the assessment of liquefaction induced deformations (Feng, 2017).

2.6.1 Bounding surface plasticity

As explained by Dafalias & Manzari (2004) the bounding surface plasticity relied on a single bounding surface that controlled the ultimate strength. The material behaviour was governed by the distance of the current state to the outer surface as a function of the stress ratio. Dilatancy components were also incorporated in a similar manner to simulate pore pressure changes and volumetric strain, which were crucial for modelling liquefaction.

The concept of bounding surface plasticity was introduced by Dafalias, (1986), designed to model materials undergoing cyclic loading. This framework enabled more realistic simulations of large deformations, particularly useful for phenomena such as liquefaction and post-liquefaction behaviour in soils.

A significant advancement came from Dafalias & Manzari (2004), who incorporated a critical state soil mechanics approach that considered the effects of fabric changes in granular soils. The SANISAND model effectively simulated both monotonic and cyclic loading, making it particularly valuable for assessing liquefaction potential during seismic events. Furthermore, the introduction of the state parameter allowed the model to account for the dilatant and contractive behaviour of sands in an intuitive manner.

Building on this work, Cheng et al. (2013) implemented the SANISAND model into the FLAC3D software, validating it with experimental triaxial tests. Their work demonstrated the model's ability to capture cyclic stress-strain behaviour, including shear modulus degradation and excess pore pressure accumulation. This made bounding surface plasticity more accessible for practical dynamic simulations in seismic design.

Boulanger & Ziotopoulou (2022) further refined the model by publishing the PM4Sand model, which was specifically developed for liquefaction assessment. This version includes features to account for fabric changes and nonlinear stress-strain behaviour under cyclic loading, enhancing the model's accuracy in simulating the cyclic degradation and stiffness reduction in sands.

Jefferies (1993) contributed to the field with the Nor-Sand model, a simplified critical state model for sands utilising the state parameter for the first time in a constitutive model. This model allows consistent simulation of sand behaviour across different densities and stress conditions, balancing computational simplicity with accuracy.

Cubrinovski & Ishihara (1998b) proposed incorporating the state index and focusing on the stress-strain-dilatancy of the soil structure under cyclic loading as an interconnected process. They related the dilatancy behaviour of their model to the stress-dilatancy equation, which led to a near-complete description of the granular soil behaviour observed in the laboratory tests.

Taborda et al. (2014) modified the original bounding surface model to improve numerical stability and performance under large deformations, making the model more suitable for cyclic loading scenarios involving significant strain and structural changes in the soil.

2.6.2 Multi-yield surface plasticity

Multi-yield surface plasticity utilised multiple yield surfaces to represent the gradual degradation of material stiffness under increasing stresses. These surfaces were arranged in a nested fashion within the deviatoric stress space and allowed to interact with each other following the translation rule proposed by Mróz (1967). This approach was developed to address the limitations of single-yield surface models, particularly in representing complex loading paths such as cyclic and seismic conditions.

Later, Mróz & Pietruszczak (1983) expanded the model to account for anisotropic hardening, allowing it to capture directional dependence in material behaviour under complex stress states. This extension made the model particularly suitable for granular materials, such as sands, by integrating anisotropic effects and irreversible strain accumulation during active and reverse loading. The model's flexibility in handling stress reversals was critical for accurately simulating cyclic loading and hysteresis.

Prevost (1989) associated each yield surface with a specific shear modulus to model the evolution of the material with stress and strain history. When stress states exceed a given yield surface, the shear modulus reduces to match the characteristics defined by the next yield surface. The yield surfaces were allowed to be von-Mises, Drucker-Prager, or rounded Mohr-Coulomb, depending on the specific material properties and modelling requirements. The plastic flow rule employed an associative flow rule for deviatoric plastic flow, while the volumetric component followed a non-associative rule. The modelling approach required storing the back-stress and other parameters for each yield surface, leading to significant computational memory usage.

The Prevost (1989)formulation contributed significantly to the practical application of the multi-yield surface model by introducing a numerical implementation that could handle monotonic and cyclic loading in clays and sands. This extension further validated the model's use in dynamic soil-structure interaction problems, where precise control over shear modulus degradation is crucial.

More recently, Elgamal et al. (2003), Yang et al. (2003) and Yang & Elgamal (2008) applied the multi-yield surface approach to model liquefaction-induced ground deformations. Their models captured the complex interaction between pore pressure changes and soil stiffness degradation during seismic events, making the multi-yield surface model a robust tool for liquefaction analysis.

In more recent work, Gu et al. (2009, 2011, 2015) have refined the multi-yield surface plasticity model by introducing consistent tangent moduli and improved numerical integration schemes. These enhancements were designed to improve the model's efficiency in finite element simulations, reducing computational costs while maintaining accuracy during large-scale dynamic analyses.

Finally, Qiu et al. (2023a, 2023b) and Qiu & Elgamal (2020) implemented strain softening in the kinematic hardening framework. Their contributions helped solidify the multi-yield surface model as a critical tool for simulating soil behaviour under a wide range of loading conditions.

2.6.3 Other approaches

The hypoplastic model was formulated to simulate the nonlinear behaviour of granular soils without relying on the traditional decomposition of strains into elastic and plastic components. Unlike elastoplastic models, hypoplasticity did not employ predefined yield surfaces or hardening rules. Instead, it used a rate equation that captures the incremental response of materials as a function of current stress and deformation states (von Wolffersdorff, 1996). One of the significant advances in hypoplastic modelling was the incorporation of the intergranular strain concept by Niemunis & Herle (1997)The intergranular strain variable tracks the direction and magnitude of the previous loading, allowing the model to handle strain accumulation and reversal with improved accuracy. This extension enabled the model to better capture cyclic loading behaviour and path dependence. Herle & Gudehus (1999) presented a systematic method for determining the model's parameters based on grain assembly properties. This calibration framework helps capture essential soil characteristics like barotropy (pressure dependency) and pyknotropy (density dependency). Recent developments in hypoplasticity, such as those proposed by Mašín (2013), have enhanced its performance in simulating small-strain behaviour and showed applications in tunnelling and foundation problems.

2.7 SUMMARY AND DISCUSSION

The literature review highlights several challenges in the seismic SSI analysis of masonry towers. One major challenge is the accurate modelling of nonlinear behaviour in both soils and masonry structures. Many existing models, such as those discussed by Camata et al. (2008) and Rosell (2010) either oversimplify soil behaviour by assuming linear elasticity or fail to capture the complex interaction between soil and masonry. These limitations can lead to overestimations of plastic responses in structures like the bell tower in Guardiagrele, as linear soil models do not fully account for energy dissipation during seismic events.

Potential avenues for future research include developing more efficient constitutive models for the kinematic hardening modelling of soils and contact-friction behaviour. Specifically, incorporating the mixed implicit-explicit (IMPL-EX) numerical method alongside existing damage-plasticity models could enhance the stability and accuracy of SSI simulations. Such an efficient model can focus on capturing the coupled nonlinear behaviour of the structure and the soil during seismic shaking without suffering from numerical instabilities.

This thesis might fill the identified gaps, particularly in understanding the direct SSI behaviour of historical masonry structures subjected to seismic loading. By demonstrating the benefits of employing high-fidelity numerical models, this research could lead to more reliable tools for the seismic vulnerability assessment of masonry towers and enhance preservation strategies.

3 IMPLEMENTATION OF AN IMPL-EX CONTACT ELEMENT IN OPENSEES

Dynamic contact problems are highly nonlinear due to the alternating contact conditions and the tangential stick-slip when in contact. Such problems are often solved with explicit schemes that require small time steps in the order of microseconds which might not be favourable for large seismic boundary value problems. As a practical solution, the implementation of a novel zero-length node-to-node contact element in OpenSees is presented. The element is compatible with a variety of possible d.o.f. settings in 2D and 3D, including nodes with mismatching d.o.f.s. The contact axis can be arbitrarily oriented along a direction vector. The two nodes can separate, whereas a penalty stiffness prevents penetration. In contact, the tangential friction follows a Drucker-Prager yield surface that provides an elastic-perfectly-plastic stick-slip behaviour. The integration of the material internal variables is offered in implicit or implicit-explicit (impl-ex) mode to increase the solution's stability. During Newton-Raphson iterations, the material equations are stepwise linearized, and the material response is achieved by explicitly extrapolating the internal variables. Before committing the history, these variables are corrected by an implicit step. Hence, a solution with a controlled error is guaranteed. The accuracy of the contact element is demonstrated via a patch test. Finally, the characteristics of the dynamic solution using the newly implemented implicit-explicit element is investigated through studying the motions of an oscillating s.d.o.f. friction damper attached to an elastic horizontal spring. To conclude, the effect of the chosen time step on the analysis results is discussed.

Keywords: new OpenSees element, Dynamic contact nonlinearity, Implicit-explicit integration, Mohr-Coulomb friction, Frictional damping

3.1 MODELLING OF CONTACT-FRICTION MECHANICS

Numerical modelling of discontinuities can become quite complex, particularly in dynamic settings. Since discontinuities are inherently nonlinear, they add significant complexity to finite element (FE) solutions (Frohne et al., 2016; Schellekens & De Borst, 1993). In FEM, discontinuities are often represented using specialized contact (gap) elements, which handle all the contact-related nonlinearities. These contact elements typically involve both material and geometric nonlinearities, often interacting in a coupled manner—geometric nonlinearity influences material nonlinearity and vice versa.

One approach involves modelling the discontinuity as material nonlinearity within an otherwise continuous domain. In a penalty-based contact element, the contact condition between two nodes is managed by allowing node separation while preventing node penetration. Along the local normal axis of the element, nodes are constrained from experiencing negative displacement jumps by a high stiffness, while positive displacements are permitted with no stiffness. In the simplest formulations, no plastic work is generated along the normal axis, though some formulations do consider this aspect (Muthukumar & DesRoches, 2006).

During contact, nodes can move relative to each other along the tangential axes. In a 3D continuum, the dynamic linear momentum balance (Equation 3.1) equation of a contact-friction problem writes as:

$$\boldsymbol{m_{\Omega} \cdot \ddot{u}_{\Omega} + C_{\Omega} \cdot \dot{u}_{\Omega} + K_{\Omega} \cdot u_{\Omega} + F_{contact} = F_{seismic}} \qquad \textbf{3.1}$$

$\boldsymbol{K_{\Omega}}$ and $\boldsymbol{u_{\Omega}}$ are the stiffness and the displacement vectors related to the body, $\boldsymbol{\Omega}$ in motion. $\boldsymbol{F_{contact}}$, represents the force vector generated by the contact. Within the scope of the thesis $\boldsymbol{\Omega}$, is always the nodal coordinates of the body of interest in the reference configuration (i.e., small strain assumption). Even in cases where $\boldsymbol{K_{\Omega}}$ linearly depends on the $\boldsymbol{u_{\Omega}}$, Equation 3.1 is a system of nonlinear equations because of $\boldsymbol{F_{contact}}$. Obtaining an analytical solution to Equation 3.1 is not feasible due to the discontinuous nature of $\boldsymbol{F_{contact}}$, therefore a numerical solution technique such as the Newton's approach is necessary. The term $\boldsymbol{F_{contact}}$ is nonlinear regardless of the contact formulation whether its Hertzian, Coulomb-friction or Kelvin-Voigt type. The nonlinearity simply comes from the alternation of the contact condition. Considering an Hertzian contact in which only the contact or no-contact cases along the normal axis are considered (i.e., only the normal component of the contact force is non-zero), the normal component F_n becomes:

$$F_n = H(-u_n) \cdot K_n \cdot u_n = \begin{cases} 0, & u_n > 0 \\ K_n \cdot u_n, & u_n \leq 0 \end{cases} \qquad \textbf{3.2}$$

K_n is the contact normal penalty stiffness. The function H is the Heaviside step function which is discontinuous over the values of u_n. Due to dependence of F_n on u_n which is the computed displacement jump along the local normal axis of the contact, the contact force is nonlinear. As in all geometric nonlinearities, the displacement jump across the element (projection of the current element length on the contact axis), u_n is updated at the beginning of each iteration.

Further nonlinearity can be incorporated through allowing stick or slip conditions in the tangential axes only when the contact condition is achieved (i.e., Coulomb friction). Additionally, the amount of the friction force can be a function of the normal stress on the contact surface, leading to a Mohr-Colomb friction formulation:

$$\boldsymbol{F_t} = H(-u_n) \cdot \begin{cases} \mu \cdot (\boldsymbol{m_\Omega}|\Omega = \mathrm{i}) \cdot \ddot{u}_n \cdot \dfrac{\dot{\boldsymbol{u}}_t}{\|\dot{\boldsymbol{u}}_t\|}, & f(\boldsymbol{F_t^{trial}}) > 0 \\ K_f \cdot \boldsymbol{u_t}, & f(\boldsymbol{F_t^{trial}}) \leq 0 \end{cases} \quad \textbf{3.3}$$

The tangential displacement jump, $\boldsymbol{u_t}$, and the tangential force, $\boldsymbol{F_t}$, are 2-by-1 vectors. μ is the friction coefficient of the surface, $(\boldsymbol{m_\Omega}|\Omega = \mathrm{i})$ is the total mass along the contact normal within the influence zone of the ith contact element, $\ddot{u}_n$ is the normal component of the acceleration acting on the body, $\ddot{\boldsymbol{u}}_{\boldsymbol{\Omega}}$ (e.g., gravitational acceleration), and $\dot{\boldsymbol{u}}_{\boldsymbol{t}}$ is the tangential component of $\ddot{\boldsymbol{u}}_{\boldsymbol{\Omega}}$. Finally, K_f is the frictional penalty stiffness. The velocity term corresponds to the unit direction vector that acts against the applied tangential force. Studying $\boldsymbol{F_t}$, reveals the present geometric nonlinearity due to the contact condition and the material nonlinearity due to the possibility of slip. It is worth noting that, in case of stick, the contact element terms contribute to the global stiffness matrix, whereas when slip happens the element generates a constant damping force. In the dynamic balance equation, even though the frictional damping is tied to the velocity term, trough unit vector, it results in a characteristic constant (rate-independent) decay in the displacements. On the contrary, the viscous damping is related to the velocity term directly and results in a linear (rate-dependent) decay in the displacements. Hence, in seismic analysis, a friction damper is expected to generate frequency independent energy dissipation which may not be captured using viscous dashpot elements.

The function f defines a yield locus, where if the trial tangential force, $\boldsymbol{F_t^{trial}}$ is larger than the Mohr-Coulomb friction, some plastic work is done by generating slip to relax the tangential force. For a physical rough surface mathematically described through a smooth conical Drucker-Prager surface, f becomes:

$$f = \|K_f \cdot \boldsymbol{u_t}\| - \mu \cdot mass \cdot \ddot{u}_n \quad \textbf{3.4}$$

A similar relation can be found by starting from the energy balance equation and showing that the Helmholtz free energy in the system can be separated into elastic and plastic components, then which the plastic component can be further decomposed into the plastic free energy and the irrecoverable (entropy) component as illustrated by Yang et al. (2018).

In FEM, various approaches are used to numerically impose the discontinuity introduced by contact mechanics. Prominent methods include the use of Lagrange multipliers and the Penalty method (Bathe, 2016; Belytschko et al., 2014). For the contact element presented, the Penalty method was selected due to its simplicity and suitability for implicit-explicit integration. The Penalty approach involves applying a penalty to enforce contact constraints.

A Mohr-Coulomb type friction material is implemented using a damage-plasticity material formulation, which offers significant potential for future development. The implicit-explicit integration of state variables is also available as an alternative to the standard backward-Euler approach. Upcoming versions could incorporate a damage-dependent reduction in friction stiffness to model the progressive smoothing of the contact surface, a feature observed experimentally (Lourenco, 1998). Additionally, the effect of cohesion and its progressive degradation along the contact surface, particularly between mortar and brick in masonry, could be improved. This aspect was recently addressed in OpenSees by Tomić & Beyer (2023).

However, the Penalty method has limitations, as it only approximates the enforcement of the impenetrability condition. Its effectiveness is highly dependent on the chosen penalty parameters. Small penalty parameters can lead to excessive interpenetration and, in impact problems, can result in underestimations of maximum stresses. Choosing the appropriate penalty parameter remains a challenging task (Belytschko et al., 2014).

To sum up, the exploration above clearly shows that the nonlinearity of the analysis comes from not only the material and geometric nonlinearities but the contact condition as well (Bathe, 2016). Hence, the solution of contact behaviour can become a particularly challenging problem in static or dynamic analysis. In seismic analysis the convergence issues may become worse since separated bodies by contact elements can pound at each repetitively while the maintaining a cyclic frictional interaction at times of contact.

Convergence issues resulting from the contact elements often are a reason to stop the analysis before the desired structural nonlinearities are achieved in the model. As an example, the convergence issues experienced at the implicit contact elements between the bell tower and the masonry sidewalls during the dynamic analysis of the bell tower discussed in Chapter 7, led to the implementation of the mixed implicit-explicit element discussed in this chapter. On the other hand, the explicit integration of material equations requires significantly smaller time steps to control the error build-up leading to lengthy analysis durations unfavourable for long seismic analysis.

In this chapter, observing the drawbacks of implicit contact elements in nonlinear SSI problems, an implicit-explicit contact element is implemented to achieve a highly stable contact mechanics solution during dynamic analysis.

3.2 IMPLICIT-EXPLICIT INTERFACE ELEMENT FORMULATION

The contact element behaviour discussed in Section 3.1 is implemented in a two-node element. The initial length of the two-node element is allowed to be either zero or a positive value i.e., coordinates of the 2nd node, Ω_2 subtracted from the coordinates of the 1st node,

Ω_1 must result in a positive distance along the element local contact axis (Figure 3.1). The contact axis can be defined uniquely by the user for each element by signifying the direction of the local x axis (the contact axis) as a vector in the global coordinate system. The direction vector can be defined arbitrarily. Then, the element internally computes the tangential axes corresponding to the defined contact axis automatically (Figure 3.2). This is especially useful for problems with complicated contact geometries such as sloped sliding surfaces or pile-friction problems.

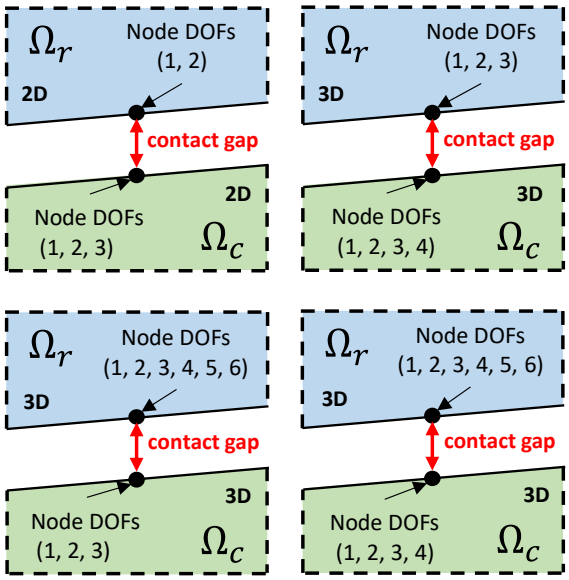

Figure 3.1. Example (2D & 3D) permitted d.o.f. configurations at the restrained and constrained end nodes of the impl-ex contact element.

Furthermore, the contact element can be defined between two nodes with incompatible d.o.f.s. The element stiffness matrix and force vector are adjusted automatically for every possible node combination available in OpenSees (Figure 3.1). Node compatibility can become a challenge in soil-structure-interaction problems in which the structural element nodes (often with 6 d.o.f.s) are in contact with solid element nodes (often with 3 or 4 d.o.f.s). The interaction between the nodes of brick elements modelling a pile member, and the nodes of soil brick elements with pressure d.o.f. can be an example (Saqib et al., 2023).

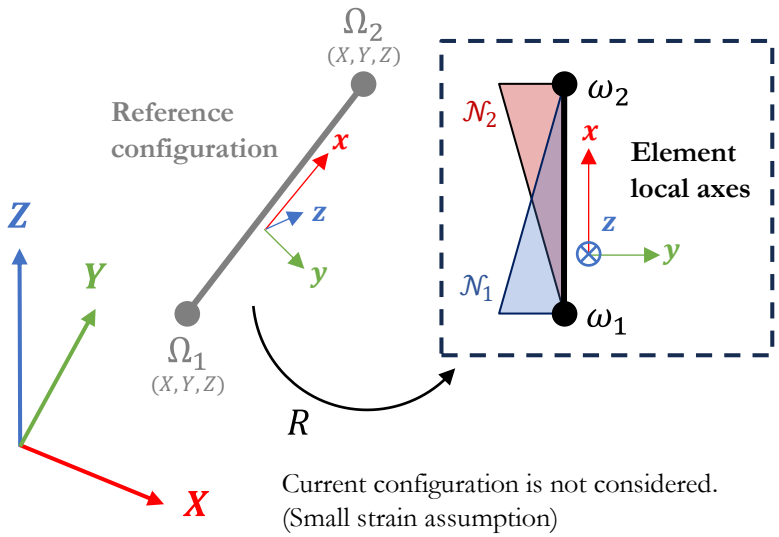

Figure 3.2. Reference configuration in the global coordinate system and contact element local axes. R matrix defines a rotation from the reference configuration to local coordinate system.

The formulation of the element in 3D is discussed below. Formulation in 2D is omitted for brevity. In OpenSees, after the step trial displacements are computed at each node, the element analysis cycle is triggered by the solver through calling the *update* method of each element. The *update* first triggers computation of the displacement jump, then triggers the material internal update. In this function, depending on the user choice, the internal update can be triggered in implicit or impl-ex mode. Then in each contact element, the step displacement jump, $\boldsymbol{\Delta u}$ (equivalent to strain in solid elements) is computed as a first step as shown in Equations 3.5 to 3.8.

$$\boldsymbol{u}_{global} = \mathcal{M}(\boldsymbol{u}) \tag{3.5}$$

$$\boldsymbol{u}_{local} = \boldsymbol{R} \cdot \boldsymbol{u}_{global} \tag{3.6}$$

$$\Delta\boldsymbol{u} = \boldsymbol{B} \cdot \boldsymbol{u}_{local} + \Delta\boldsymbol{u}_{initial} \tag{3.7}$$

$$where\ \boldsymbol{u}_{global}^{T} = [u_{1_X} \quad u_{1_Y} \quad u_{1_Z} \quad u_{2_X} \quad u_{2_Y} \quad u_{2_Z}] \tag{3.8}$$

The cycle starts with mapping the translational nodal displacements in the global d.o.f. set to the local d.o.f. set of the interface element (Equation 3.5). $\mathcal{M}$ is a mapping function that picks the translational d.o.f.s among a set of arbitrary number of d.o.f.s and arranges them in a 6 d.o.f. vector as shown in Equation 3.8. In Equation 3.6, $\boldsymbol{u}_{global}$ and $\boldsymbol{u}_{local}$ are the nodal displacements in the global and local coordinate systems, respectively. $\boldsymbol{R}$ is the 6-by-6 transformation matrix and defines a rotation from the reference configuration in the

global coordinate system to the local coordinate system (Figure 3.2). The '·' symbol defines dot product operation (or contraction over single index) between a matrix and a vector. In Equation 3.7, $\boldsymbol{\Delta u}$ and $\boldsymbol{\Delta u_{initial}}$ are the step displacement jump, and the initial displacement jump at the reference configuration. In Equation 3.8, the displacements at the end nodes, Ω_i are denoted as u_i.

The $\boldsymbol{B}$ matrix is the strain-displacement transformation matrix, well-known in finite elements. It is obtained by differentiating and combining the rows of the displacement interpolation matrix $\boldsymbol{H}$ (K.-J. Bathe, 2016). The interpolation matrix of the contact element is composed of linear functions, $\mathcal{N}_i$ for each d.o.f. and like that of a two-node truss element in each d.o.f. (Figure 3.2). Hence, the $\boldsymbol{B}$ matrix, as the derivative of $\boldsymbol{H}$, is composed of ones and minus ones at the corresponding d.o.f.s, as in Equation 3.9.

$$\boldsymbol{B} = \begin{bmatrix} -1 & 0 & 0 & 1 & 0 & 0 \\ 0 & -1 & 0 & 0 & 1 & 0 \\ 0 & 0 & -1 & 0 & 0 & 1 \end{bmatrix} \qquad \textbf{3.9}$$

Furthermore, the rotation matrix $\boldsymbol{R}$ defines a rotation from the global to local coordinate system and it is computed at the beginning of the analysis. Since the current configuration of the element is out of scope (small strain analysis), $\boldsymbol{R}$ is kept constant throughout the analysis. To compute $\boldsymbol{R}$, the basis of local axes in the global coordinate system needs to be determined. The orientation of the local x (contact) axis in the global coordinate system, X_{orient} is a user input. The rest of $\boldsymbol{R}$ is computed automatically following the Algorithm 3.1. Then the rotation matrix is assembled as shown in Equation 3.11.

$$\boldsymbol{R_3} = \begin{bmatrix} \mathbf{X}_{orient} \\ \boldsymbol{Y}_{orient} \\ \boldsymbol{Z}_{orient} \end{bmatrix} \text{ where } \boldsymbol{R_3} \text{ is a (3-by-3) matrix} \qquad \textbf{3.10}$$

$$\boldsymbol{R} = \begin{bmatrix} \boldsymbol{R_3} & \mathbf{0} \\ \mathbf{0} & \boldsymbol{R_3} \end{bmatrix} \text{ where } \boldsymbol{R} \text{ is a (6-by-6) matrix} \qquad \textbf{3.11}$$

After the step displacement jump is evaluated, the contact-friction material update process is invoked (Section 3.2.2). Depending on the mode of integration chosen by the user (i.e., impl-ex or implicit), the element force vector, $\boldsymbol{F}$ and stiffness matrix, $\boldsymbol{K}$ are computed. The dimensions of $\boldsymbol{F}$ and $\boldsymbol{K}$ depend on the total number of d.o.f. owned by the element nodes which might be arbitrary. However, the contact element only works in the translational d.o.f.s. To overcome the incompatibility between the element and attached node d.o.f.s, an extra step is included in the assembly process in which the local d.o.f. set is mapped to the global d.o.f. set. First, the force and stiffness are assembled in the local d.o.f. set. Then the translation d.o.f.s of the element are mapped to the corresponding translational d.o.f.s of

the nodes and the remaining rows and columns of $\boldsymbol{F}$ and $\boldsymbol{K}$ are filled with zeros. This way compatibility with various combinations of attached node sets is provided.

According to zero-length element approach, single gauss point is assigned at the centre of the contact element. Therefore, the stress field along the element is assumed to be constant. Then the force vector, $\boldsymbol{F}$ is assembled as shown in Equations 3.12 to 3.14.

$$\boldsymbol{F}_{local} = \boldsymbol{B} \cdot \boldsymbol{\sigma} \quad \textbf{3.12}$$

$$\boldsymbol{F}_{global} = \boldsymbol{R} \cdot \boldsymbol{F}_{local} \quad \textbf{3.13}$$

$$\boldsymbol{F} = \mathcal{M}^{-1}(\boldsymbol{F}_{global}) \quad \textbf{3.14}$$

$$\boldsymbol{K}_{local} = \boldsymbol{B}^{\boldsymbol{T}} \cdot \mathbb{C} \cdot \boldsymbol{B} \quad \textbf{3.15}$$

$$\boldsymbol{K}_{global} = \boldsymbol{R}^{\boldsymbol{T}} \cdot \boldsymbol{K}_{local} \cdot \boldsymbol{R} \quad \textbf{3.16}$$

$$\boldsymbol{K} = \mathcal{M}^{-1}(\boldsymbol{K}_{global}) \quad \textbf{3.17}$$

Algorithm 3.1. Calculation of rotation matrix from the user input orientation vector.

Input: Orientation vector X_{orient}
Output: Rotation matrix $\boldsymbol{R}$

START
if ($\mathbf{X}_{orient}$ and $\boldsymbol{Y}_{global}$ are **not** parallel) **then**
cross multiply vectors $\boldsymbol{Z}_{orient} = \mathbf{X}_{orient} \times \boldsymbol{Y}_{global}$
normalize vector $\boldsymbol{Z}_{orient}$
cross multiply vectors $\boldsymbol{Y}_{orient} = \mathbf{X}_{orient} \times \boldsymbol{Z}_{orient}$
normalize vector $\boldsymbol{Y}_{orient}$

else
cross multiply vectors $\boldsymbol{Y}_{orient} = \mathbf{X}_{orient} \times \boldsymbol{Z}_{global}$
normalize vector $\boldsymbol{Y}_{orient}$
cross multiply vectors $\boldsymbol{Z}_{orient} = \mathbf{X}_{orient} \times \boldsymbol{Y}_{orient}$
normalize vector $\boldsymbol{Z}_{orient}$

assemble matrix $\boldsymbol{R}$, knowing X_{orient}, Y_{orient} and Z_{orient} (Equation 3.11)

END

3.2.1 The contact-friction material

Following the penalty contact approach, the nonlinear contact process within the element is considered via a built-in contact-friction material. The contact material simulates the contact condition and shear slip as a result of plastic dissipation process and it can be considered as a regularization of the contact conditions (Belytschko et al., 2014).

When the contact condition is satisfied, the material models a rough surface between two nodes. The compatibility between nodes is enforced by applying a user input penalty stiffness in normal and tangential stress directions. For practicality, the contact element deformations can be decomposed into normal and tangential components which are both nonlinear. In the normal axis, the two nodes are allowed to move away from each other freely along the positive contact (normal) axis whereas penetration (negative displacement jump) is prevented with positive stresses depending on the normal penalty stiffness and the amount of penetration.

Similarly, any tangential displacement is free to occur in case there is no contact between the two nodes. During contact, the relative deformation between nodes can be elastic (fully recoverable) or if the friction strength is surpassed, slipping (irrecoverable) occurs in the tangential axes. The amount of elastic deformation is a function of the tangential penalty stiffness.

The contact material formulation is implemented following the damage-plasticity material approach and variables. In Section 2.5.1, the formulation of the *DamageTC3D* damage-plasticity material used as an example for the contact material is given. Such an approach is useful since the state variables associated with plasticity and damage can be implemented in a coupled manner. The current version of the contact element, presented here, only considers the plasticity variables such as the plastic strain (slip) and the slip multiplier trough the plastic damage variable and does not include cracking damage. Hence the contact material only differs from the traditional plasticity formulation by using the damage material variables and style in capturing the plastic process (Table 3.1).

The damage-plasticity formulation has been found to be advantageous over the traditional plasticity for the contact element considering the future expansion of the formulation. By simply adding the cracking damage and the effect of contact cohesion in the next versions, the contact element can be upgraded to capture cases where progressive degradation of the

friction stiffness as increasing amounts of slip, or the behaviour of a progressively softening cohesive connection might be important. Such type of nonlinear behaviour can be important in modelling brick-mortar interfaces(Sacco & Lebon, 2012), adjacent structures attached with mortar joints (Tomić & Beyer, 2023), degradation of pile skin friction due to increasing cyclic loading (Li et al., 2023; Tabucanon et al., 1995) or rock-structure interfaces (Leong & Randolph, 1992).

Table 3.1. List of scalar and tensor quantities and their corresponding matrix representation for compressed tensor operations

Tensor quantity	Tensor notation	Matrix form (representation)	Einstein notation
Displacement jump	$\Delta \boldsymbol{u}$	Strain-like	Δu_{ij}
Contact displacement jump	Δu_N	Scalar	Δu_N
Tangential displacement jump	$\Delta \boldsymbol{u_T}$	Strain-like	$\Delta u_{T\,ij}$
Nominal stress	$\boldsymbol{\sigma}$	Stress-like	σ^{ij}
Contact nominal stress	σ_N	Scalar	σ_N
Tangential nominal stress	$\boldsymbol{\sigma_T}$	Stress-like	${\sigma_T}^{ij}$
Trial effective stress	$\breve{\boldsymbol{\sigma}}$	Stress-like	$\breve{\sigma}^{ij}$
Elastic modulus	$\mathbb{E}$	Stress-like	E^{ijkl}
Consistent tangent operator	$\mathbb{C}$	Stress-like	C^{ijkl}
Residual shear stress	ξ	Scalar	ξ
Compressive projector	pc	Scalar	pc
Equivalent plastic strain (total slip multiplier)	λ	Scalar	λ
Apparent plastic damage	d_a	Scalar	d_a
Damage threshold	r	Scalar	r
Effective damage threshold	$\hat{r}$	Scalar	$\hat{r}$

Equivalent shear stress	$\check{\tau}$	Scalar	$\check{\tau}$

3.2.2 Mixed implicit-explicit return mapping

The contact element material algorithm is relatively straightforward and many of the steps computed during the explicit extrapolation stage are repeated in the implicit correction stage. Hence, a unified step-by-step return-mapping is given below for both stages. At those steps in which the explicit stage differs from the implicit stage, a decision box is given, and both operations are stated. Hence, each stage can be read by separating the return-mapping into explicit and implicit phases and keep following the corresponding explicit or implicit formulation from start to end. The independent variable of the return-mapping process is the displacement jump tensor, $\boldsymbol{\Delta u}$ and it is computed as a part of the contact element analysis cycle (see Section 3.2). In the following equations, the displacement jump tensor is decomposed into its normal, Δu_N and tangential, $\boldsymbol{\Delta u_T}$ parts for the sake of practical documentation. The stored material internal variables are shown in Table 3.2.

Table 3.2. List of material internal variables stored in the contact element.

Independent variables	Dependent variables		State (history) variables	
$\Delta \boldsymbol{u}$	$\boldsymbol{\sigma_T}$	$\boldsymbol{\sigma_{T(n)}}$	λ	r
$\boldsymbol{\Delta u_{(n)}}$	pc	ξ	$\lambda_{(n)}$	$r_{(n)}$
	$pc_{(n)}$	$\xi_{(n)}$		$r_{(n-1)}$
		$\xi_{(n-1)}$		

The formulation of the damage-plasticity-like contact-friction model is as follows. Variables without subscript belong to the current step (n+1)th, whereas (n) and (n-1) indicate the last and previous committed steps, respectively. The return-mapping begins with the elastic trial as shown in Equations 3.18 and 3.19. The contact trial effective stress, $\breve{\sigma}_N$ is computed in total terms whereas the tangential trial effective stresses, $\breve{\boldsymbol{\sigma}}_{\boldsymbol{T}}$ are computed incrementally. Hence the tangential displacement jumps computed at the previous, nth step, $\boldsymbol{\Delta u_{T(n)}}$ and the nominal tangential stresses at the previous step, $\boldsymbol{\sigma_{T(n)}}$ are kept as internal variables.

$$\breve{\sigma}_N = K_n \cdot \Delta u_N \qquad \textbf{3.18}$$

$$\breve{\boldsymbol{\sigma}}_{\boldsymbol{T}} = K_f \cdot \left(\Delta \boldsymbol{u}_{\boldsymbol{T}} - \Delta \boldsymbol{u}_{\boldsymbol{T}_{(n)}}\right) + \boldsymbol{\sigma}_{\boldsymbol{T}_{(n)}} \qquad \textbf{3.19}$$

The material behaviour is decomposed into normal and tangential parts. The normal part is fairly straightforward and only includes the contact condition. The contact condition is satisfied if the trial effective contact stress, $\breve{\sigma}_N$ is less than zero, indicating an infinitesimal penetration. In this case an opposite force is computed to counteract the small penetration. Otherwise, no stress is computed (Equation 3.21). The state of the contact is tracked over the compressive projector, pc variable. Furthermore, compressive projector, pc is an impl-ex variable, hence required to be extrapolated at the beginning of the step (Equation 3.20). In this case, since a decision variable need to be extrapolated, the committed value is kept.

explicit stage:
$$pc = pc_{(n)} \qquad \textbf{3.20}$$

implicit stage:
$$pc = \begin{cases} 1.0, & \breve{\sigma}_N < 0 \\ 0.0, & \breve{\sigma}_N \geq 0 \end{cases} \qquad \textbf{3.21}$$

In the following step the residual shear stress, ξ is computed. Since ξ is introduced as an impl-ex variable, it is extrapolated in the explicit stage and computed from the material equaitons in the implicit stage as shown in Equations 3.22and 3.23. $\langle\odot\rangle$ is the Macaulay bracket function applied to ξ, since the residual shear stress (i.e., the friction strength) cannot be less than zero. $\Delta t_{n+1}/\Delta t_n$ is the time factor associated with the step and can be taken as unity for most problems, including this thesis (Oliver et al., 2008).

explicit stage:
$$\xi = \langle \xi_n + \frac{\Delta t_{n+1}}{\Delta t_n} \cdot (\xi_n - \xi_{n-1}) \rangle \qquad \textbf{3.22}$$

implicit stage:
$$\xi = \langle -\mu \cdot \breve{\sigma}_N \rangle \qquad \textbf{3.23}$$

Then the damage threshold, r is computed. The damage threshold, r is an impl-ex variable hence it is required to be extrapolated based on its historical values in the explicit stage and computed from the material equations during the implicit stage as shown in Equations 3.24 to 3.26. Hence, in the implicit stage the equivalent shear stress, $\breve{\tau}$ that is exceeding the residual shear stress should be computed as an intermediate step. The damage threshold is the maximum equivalent shear stress, $\breve{\tau}$ value observed until the current time step (n+1).

explicit stage:
$$r = r_n + \frac{\Delta t_{n+1}}{\Delta t_n} \cdot (r_n - r_{n-1}) \qquad \textbf{3.24}$$

It is worth noting that, in traditional damage formulation the equivalent shear stress, $\breve{\tau}$ is computed in total stress terms. Whereas in damage-plasticity, the plastic straining is additionally accounted for, therefore the stress relaxed due to slip should be added (Equation 3.25) to obtain the equivalent metric in pure damage mechanics (Petracca et al.,

2022). Further clarification is offered in Figure 2.2, in which the relationship between plastic strain, damage and total stresses in a damage-plasticity context is illustrated.

implicit stage:

$$\breve{\tau} = \sqrt{\breve{\boldsymbol{\sigma}}_{\boldsymbol{T}} : \breve{\boldsymbol{\sigma}}_{\boldsymbol{T}}} + \lambda \cdot K_f - \xi \quad \textbf{3.25}$$

$$r = \max(r_n, \quad \breve{\tau}) \quad \textbf{3.26}$$

The next steps are computed in both integration stages the same, however the corresponding impl-ex or implicit versions of the input variables are used depending on the stage. The equivalent plastic strain (equivalent to slip multiplier in plasticity terms), λ is updated according to Equation 3.27, and the apparent plastic damage d_a variable is updated.

$$\lambda = \frac{r}{K_f} \quad \textbf{3.27}$$

$$\hat{r} = (\lambda - \lambda_n) \cdot K_f + \xi \quad \textbf{3.28}$$

$$d_a = \begin{cases} \begin{cases} 1.0, & \hat{r} \leq 0 \\ 1.0 - \dfrac{\xi}{\hat{r}}, & \hat{r} > 0 \end{cases}, & \lambda > 0 \\ 0.0, & \lambda = 0 \end{cases} \quad \textbf{3.29}$$

The operator, $H(\odot)$ is the Heaviside step function. It is worth noting that, since model does not include the friction stiffness degradation capability implemented yet, in Equation 3.29, the apparent plastic damage d_a is set to zero in case the plastic multiplier, λ is computed as zero, leading to the full recovery of the initial frictional stiffness. Essentially this corresponds to a full plasticity behaviour unlike the adjustable damage-plasticity material described in Section 2.5.1 through calibration coefficients. However, with further development of Equation 3.29, effects such as the degradation of the frictional stiffness can be also captured in future versions. In cases where some plastic dissipation exists, apparent plastic damage is computed as a function of the effective damage threshold, $\hat{r}$. As $\hat{r}$ increases, the apparent plastic damage decreases yielding a softer frictional stiffness. If $\hat{r}$ is significantly larger than the residual shear stress, ξ the apparent plastic damage reaches to unity, leading to zero frictional stiffness. Therefore, a smooth transition from the elastic to plastic frictional behaviour is provided (Equation 3.31).

$$\sigma_N = pc \cdot \breve{\sigma}_N \quad \textbf{3.30}$$

$$\boldsymbol{\sigma}_{\boldsymbol{T}} = (1 - d_a) \cdot \breve{\boldsymbol{\sigma}}_{\boldsymbol{T}} \quad \textbf{3.31}$$

Finally, in Voigt notation the nominal stress tensor can be assembled as follows. The stress vector resulting from Equation 3.32 is returned to the element analysis cycle for the assembly of the residual vector.

$$\boldsymbol{\sigma_{voigt}} = \begin{bmatrix} \sigma_N \\ \sigma_{T_{11}} \\ \sigma_{T_{22}} \end{bmatrix} \qquad \textbf{3.32}$$

Algorithm 3.2. Implemented IMPL-EX integration scheme for the damage-plasticity contact material

Input: Displacement jump $\Delta\boldsymbol{u}$
Output: Nominal stress $\boldsymbol{\sigma}$, and Algorithmic tangent $\mathbb{C}$

START
step $n + 1$
get displacement jump $\Delta\boldsymbol{u}$.
initialize internal parameters:
$r = r_n$, $\lambda = \lambda_n$, $\boldsymbol{\sigma} = \boldsymbol{\sigma}_n$, and $\xi = \xi_n$.
do elastic trial $\breve{\boldsymbol{\sigma}}$ (Equations 3.18 and 3.19)
Compute the norm of the tangential stress component
if (explicit stage **and** impl-ex integration option is chosen) **then**
do explicit extrapolation for r, ξ, and pc (Equations 3.20, 3.22 and 3.24)
else
Compute r, ξ, and pc (Equations 3.21, 3.23, 3.25 and 3.26)

Update equivalent plastic strain, λ (Equation 3.27)
Compute effective damage threshold, $\hat{r}$ (Equation 3.28)
Assume no plastic damage, $d_a = 0.0$
if ($\lambda > 0$) **then**
Assume full plastic damage, $d_a = 1.0$
if ($\hat{r} > 0$) **then**
Compute plastic damage, d_a (Equation 3.29)

Update effective normal and shear stresses (Equations 3.30 and 3.31)
Assemble nominal stress vector (Equation 3.32)
if (consistent tangent, C^{alg} is required) **then**
Compute the impl-ex tangent, $C^{alg} = C^{implex}$ (Equation 3.35)

if (user wants implicit) **then**
if (plastic loading: i.e. $\chi > \chi_n$) **then**
Compute the consistent tangent, $C^{implicit}$ (Equation 3.34)

END

3.2.3 Consistent tangent operator

When in contact, the elastic tangent operator becomes as follows (Equation 3.33) whereas, in cases which the contact condition is not satisfied, the stiffness matrix is zero. However, such a description is insufficient to capture slipping behaviour, since it does not account for the reduction in computed shear stresses due to the stress relaxion process.

$$\mathbb{E} = \begin{bmatrix} K_c & 0 & 0 \\ 0 & K_f & 0 \\ 0 & 0 & K_f \end{bmatrix} \qquad \textbf{3.33}$$

To represent the effect of return-mapping on the material stiffness, the concept of consistent tangent was introduced (Simo & Hughes, 1998; Simo & Taylor, 1985) which involves the computation of the material stiffness matrix through step-wise derivation of the material equations. Unlike the elastoplastic tangent, the consistent tangent requires the differentiation of the resulting stress increment with respect to the strain increment measure. A stiffness matrix that is consistent with the return-mapping ensures quadratic rate of convergence during Newton-Raphson iterations. Following the chain rule, all the material equations that relates strain to stress needs to be differentiated (Equation 3.34).

$$\mathbb{C}^{implicit} = \frac{\partial \boldsymbol{\sigma}}{\partial \Delta \boldsymbol{u}} = \begin{bmatrix} \frac{\partial \sigma_N}{\partial \Delta u_N} & \frac{\partial \sigma_N}{\partial \Delta u_{T_{11}}} & \frac{\partial \sigma_N}{\partial \Delta u_{T_{22}}} \\ \frac{\partial \sigma_{T_{11}}}{\partial \Delta u_N} & \frac{\partial \sigma_{T_{11}}}{\partial \Delta u_{T_{11}}} & \frac{\partial \sigma_{T_{11}}}{\Delta u_{T_{22}}} \\ \frac{\partial \sigma_{T_{22}}}{\partial \Delta u_N} & \frac{\partial \sigma_{T_{22}}}{\partial \Delta u_{T_{11}}} & \frac{\partial \sigma_{T_{22}}}{\Delta u_{T_{22}}} \end{bmatrix} =$$

$$\begin{bmatrix} pc \cdot K_n & 0 & 0 \\ -\breve{\sigma}_1 \cdot \frac{K_n \cdot \|\breve{\boldsymbol{\sigma}}_{\boldsymbol{T}}\| \cdot \mu}{(\breve{\sigma}_N \cdot \mu + \|\tilde{\tau}\|)^2} & -\breve{\sigma}_1 \cdot \frac{\|\breve{\boldsymbol{\sigma}}_{\boldsymbol{T}}\| \cdot \xi \cdot \frac{\Delta u_{T_{11}}}{\|\Delta \boldsymbol{u}_{\boldsymbol{T}}\|}}{(\|\breve{\boldsymbol{\sigma}}_{\boldsymbol{T}}\| - \xi)^2} & -\breve{\sigma}_1 \cdot \frac{\|\breve{\boldsymbol{\sigma}}_{\boldsymbol{T}}\| \cdot \xi \cdot \frac{\Delta u_{T_{22}}}{\|\Delta \boldsymbol{u}_{\boldsymbol{T}}\|}}{(\|\breve{\boldsymbol{\sigma}}_{\boldsymbol{T}}\| - \xi)^2} \\ -\breve{\sigma}_2 \cdot \frac{K_n \cdot \|\breve{\boldsymbol{\sigma}}_{\boldsymbol{T}}\| \cdot \mu}{(\breve{\sigma}_N \cdot \mu + \|\breve{\boldsymbol{\sigma}}_{\boldsymbol{T}}\|)^2} & -\breve{\sigma}_2 \cdot \frac{\|\breve{\boldsymbol{\sigma}}_{\boldsymbol{T}}\| \cdot \xi \cdot \frac{\Delta u_{T_{11}}}{\|\Delta \boldsymbol{u}_{\boldsymbol{T}}\|}}{(\|\breve{\boldsymbol{\sigma}}_{\boldsymbol{T}}\| - \xi)^2} & -\breve{\sigma}_2 \cdot \frac{\|\breve{\boldsymbol{\sigma}}_{\boldsymbol{T}}\| \cdot \xi \cdot \frac{\Delta u_{T_{22}}}{\|\Delta \boldsymbol{u}_{\boldsymbol{T}}\|}}{(\|\breve{\boldsymbol{\sigma}}_{\boldsymbol{T}}\| - \xi)^2} \end{bmatrix} \qquad \textbf{3.34}$$

At a first glance to Equation 3.34, one can see that, the derivative terms at the 2nd and 3rd columns of the 1st row evaluates to zero, since the contact normal stress does not relate to the tangential displacement jumps. On the other hand, the same statement is not true for the derivative terms at the 2nd and 3rd row of the 1st column, since the tangential shear stresses are related to the normal contact stress through the scalar residual shear stress, ξ. Hence, the $\mathbb{C}^{implicit}$ in Equation 3.34 becomes asymmetrical when the residual shear stress is not zero. Furthermore, additional asymmetry may arise from derivative terms located at row-2-column-3 and column-3-row-2, due to the dependence of these terms on the frictional displacement jump increment unit direction vector (Equation 3.34).

Whereas the IMPL-EX tangent operator computes as shown in Equation 3.35. Like the elastic stiffness matrix, the impl-ex tangent is nonzero when the contact condition is satisfied. Furthermore, the impl-ex tangent operator is always positive definite.

$$\mathbb{C}^{implex} = \frac{\partial \boldsymbol{\sigma}}{\partial \Delta \boldsymbol{u}} = \begin{bmatrix} pc \cdot K_c & 0 & 0 \\ 0 & (1-d_a)\cdot K_f & 0 \\ 0 & 0 & (1-d_a)\cdot K_f \end{bmatrix} \qquad \textbf{3.35}$$

As an alternative, numerical tangent operator involves the completion of the return-mapping process six times. In each return-mapping, one member of the displacement jump vector is perturbed first with a positive delta, δ and then a second time with a negative delta, δ. Then for each column of the stiffness matrix the slope between computed stress vectors is computed by dividing the resulting stress vector by two times the delta increment (Equation 3.36).

$$\mathbb{C}^{num.} = \left[\aleph\left(\Delta \boldsymbol{u}, \begin{bmatrix}\delta\\0\\0\end{bmatrix}\right) \quad \aleph\left(\Delta \boldsymbol{u}, \begin{bmatrix}0\\\delta\\0\end{bmatrix}\right) \quad \aleph\left(\Delta \boldsymbol{u}, \begin{bmatrix}0\\0\\\delta\end{bmatrix}\right) \right] \qquad \textbf{3.36}$$

$$where\ vector\ function\ \aleph(\boldsymbol{x},\boldsymbol{y}) = \frac{\boldsymbol{\sigma}(\boldsymbol{x}+\boldsymbol{y}) - \boldsymbol{\sigma}(\boldsymbol{x}-\boldsymbol{y})}{2\|\boldsymbol{y}\|} \qquad \textbf{3.37}$$

$\aleph(\boldsymbol{x},\boldsymbol{y})$ describes a numerical differentiation calculation operation by taking two vectors $\boldsymbol{x}$ and $\boldsymbol{y}$ as input. Then does return-mapping to compute stress vector for $\boldsymbol{x}+\boldsymbol{y}$ and then for $\boldsymbol{x}-\boldsymbol{y}$. Finally, computes the slope elementwise between the resulting stress vector (Equation 3.37). In only implicit solution, using the numerical tangent found to yield more robust calculations than that of the implicit consistent tangent. It is observed that the averaging effect of the numerical derivation operation around the altering contact condition results in the smoothing of the stress tensor between steps. Furthermore, since the return-mapping process is fairly fast for the presented contact element, the computational cost of computing the numerical tangent is not found to increase significantly in the implicit

solution. However, it is worth noting that the most computationally efficient solution is obtained through the use of impl-ex consistent tangent (see Section 3.4, Chapters 7 and 8).

3.3 PATCH TEST

A patch test is performed to validate the accuracy of the implemented contact element. The goal of the test is to compare the contact element solution with an independent result to make sure first the implicit formulation correctly works, second impl-ex formulation results in the same response that of implicit. Hence, a check of element internal computations was done by imposing a known closed form displacement history at the end nodes of the contact element and compare the computed forces in the element to an independent calculation. Obtaining the friction force for a monotonic loading case is relatively simple, since the friction force linearly relates to slip through the friction stiffness, K_f and capped at the friction force, $F_t = \mu N$. On the other hand, in the introduction (Section 3.1), the partial differential equations governing a dynamic contact system were reviewed. It was shown that due to the presence of discontinuous functions such as the Heaviside step function and the velocity unit (direction) vector in a dynamic setting, having an analytical solution to the balance equation is not feasible. However, for a simple case with single contact element, obtaining a numerical solution by hand is an attainable goal. A straightforward example is a single element model of a body sliding on a rough surface shown in Figure 3.3.

In OpenSees, a body with a known mass is simply modelled as a node that is allowed to move in three-dimensions. The surface is modelled by another node located at the same coordinates, fixed in all directions, whereas the contact between over a rough surface roughness is modelled using the zero-length contact element presented in Section 3.2. A constant downward force (along the contact normal axis) is applied to model the normal force acting on the contact surface originating from the mass of the body and the gravitational acceleration. The friction coefficient, μ, contact stiffness, K_c, and friction stiffness, K_f are taken as 0.5, 1e10 kPa, and 100 kPa respectively, whereas the normal force is 80 kN. The contact stiffness is chosen to be eight orders of magnitude higher than the frictional stiffness to provide a stiff constraint condition when in contact.

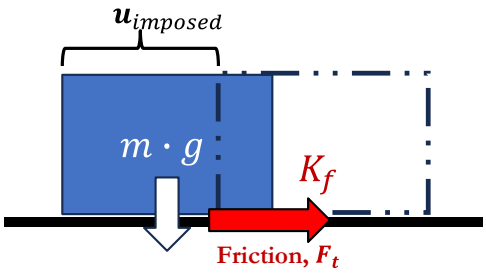

Figure 3.3. The patch test model. A body with a mass allowed to slip on a rough surface. Free node displacement is imposed, and the friction force is calculated: 1) in the contact element and 2) by hand.

A known harmonic displacement, u is imposed as a function of time. u is chosen to be a sinusoidal oscillation with an increasing amplitude at each cycle. The coefficients c_1 and c_2 are simply the values that results in a meter of maximum displacement in 5 cycles. The time step is chosen reasonably small as 0.0005 sec to prevent possible step size effects in the impl-ex version. A detailed discussion of the effect of time step on the results in a similar model is covered in Section 3.4.

$$\boldsymbol{imposed} \rightarrow u(t) = sin(c_1 \pi t) \cdot c_2 t \qquad \textbf{3.38}$$

$$c_1 = 10.0$$

$$c_2 = 1.05204383095388$$

$$t = [0, 1.0]\ second$$

$$dt = 0.0005\ second$$

The results of the patch test can be seen in Figure 3.4. For the shown displacement history, the forces computed by the contact element via implicit, and impl-ex integration schemes are compared to an independent solution. To obtain an independent result, the uniaxial Mohr-Coulomb plasticity equations (Section 3.1) are integrated incrementally with a time-step of 5e-6 second. The solution at a given time t is obtained in Python programming language by integrating the imposed analytical displacement history for the friction force and updating the plastic strain along the way. The matching friction forces are displayed in Figure 3.4. The error versus time plot shows the percent difference between the contact element and the Mohr-Coulomb plasticity solution. The error is usually insignificantly low, except for the times when the direction of loading changes. The error instantaneously rises about 1%, due to the time-step difference between the OpenSees and independent solutions. The discrepancy is because of the difference in the number of points used to approximate the sharp corners in the force-displacement plot, which is a feature of the elastic perfectly plastic response. Studying the friction versus normal force response of the material plotted against the Mohr-Coulomb envelope reveals that, the material response is indeed pressure-dependent. Overall, the contact element displays an expected frictional behaviour with little to no difference between implicit and impl-ex integration techniques. This means that, the element formulation together with the impl-ex friction material works without problems and the final response is as intended.

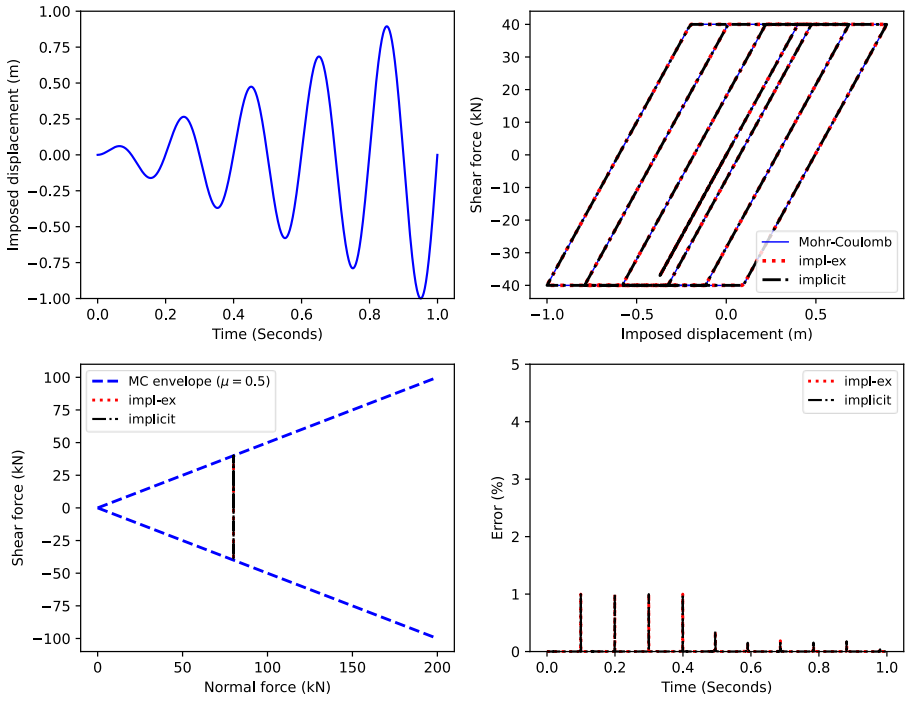

Figure 3.4. Results of the patch test. A sinusoidal displacement history is applied. The resulting stress history (implicit and impl-ex) is compared to numerical solution by hand (Mohr-Coulomb)

The element formulation is tested via a patch test. Figure 3.4 indicates that the element can simulate the frictional physics of a rough surface through both implicit and impl-ex formulations. It is observed that, with a sufficiently small time-step, the impl-ex solution can recover the results obtained with implicit solution. Next, the characteristics of the impl-ex solution is studied in detail.

3.4 DYNAMIC ENERGY DISSIPATION ANALYSIS OF A FRICTION DAMPER

Characteristics of an impl-ex solution might differ from the one obtained through the implicit or explicit approach. Since the implicit solution requires the stiffness matrix and residual vector computed at the next time step, a convergence criterion is checked, and multiple iterations might be necessary to obtain convergence. Consequently, the obtained solution is unconditionally stable. On the other hand, explicit time-stepping uses the current tangent and stress to extrapolate the material state at the next step. Hence, there is no need for iterations or check of convergence, ensuring a significantly faster solution. However, since an accurate solution is not guaranteed, small time steps in the order of

micro-seconds might be necessary for achieving accuracy or to prevent the divergence of state variables integrated within the contact element.

As an alternative, the implicit-explicit integration aims to strike a balance between the efficient solution characteristics of the explicit solution and the stability of the implicit integration. At the beginning of a step, the state variables at the next step are extrapolated using the history of these variables, independently from the strain increment vector. The stiffness and stress obtained using the extrapolated variables are used in the global Newton-Raphson solution. After convergence, the extrapolated state variables are corrected by solving a single implicit iteration, leading to an extrapolation through corrected variables at the beginning of the next solution step. Such a solution strategy is anticipated to improve the computational efficiency by ensuring convergence and not compromising the stability of the solution. In Section 3.2 the formulation of a mixed implicit-explicit contact element, implemented in OpenSees is presented. The characteristics and the anticipated efficacy of the impl-ex solution is studied through a simple theoretical model with only contact nonlinearity.

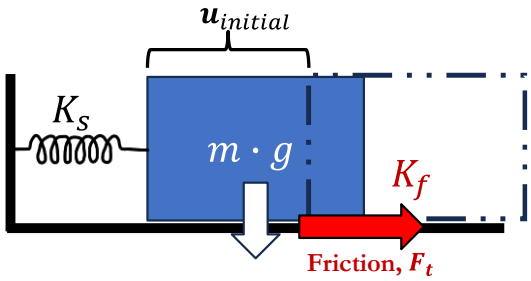

Figure 3.5. S.d.o.f. oscillator with a friction damping mechanism.

The s.d.o.f. oscillator is obtained by attaching a linear horizontal string to a box that can slide over a rough surface, shown in Figure 3.5. The box is initially displaced off-centre and let go at the start of the analysis to induce a harmonic motion. Over time, some energy in the system is converted to heat through friction interact at the rough surface. No additional damping (e.g. viscous or hysteretic) is considered. In OpenSees, the box is modelled as a free node with mass of 20 tonnes. The free node is attached to another fixed node using the proposed contact element to model the rough surface having a friction coefficient, μ, of 0.15, contact stiffness, K_c, of 1e10 kPa, and friction stiffness, K_f of 2e3 kPa. Finally, the free node is further attached to a third node using a zero-length element with an embedded elastic material having a Young's modulus, K_s, of 2.2e4 kPa in the horizonal d.o.f. to model the spring. Before the dynamic analysis, the free node is displaced 0.1 m off-centre in 10 incremental static analysis steps. The static analysis is done with the Newton-Raphson method, whereas the transient analysis is solved using the implicit Newmark approach with a time-step of 0.0005 seconds.

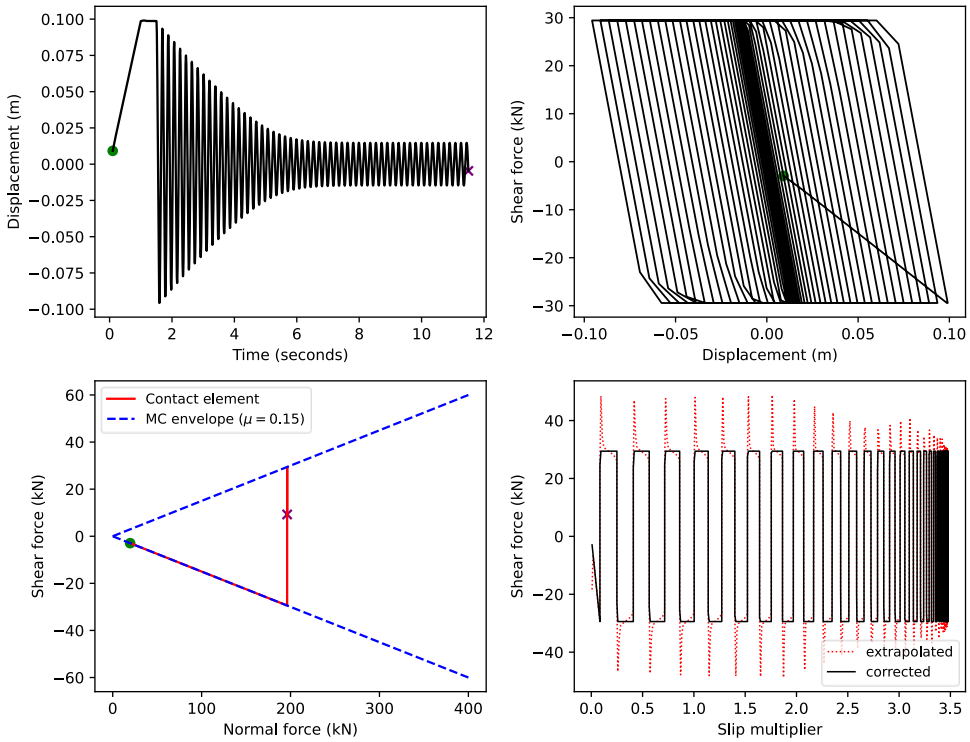

Figure 3.6. Soft impl-ex friction damper (K_f = 2e3 kPa). The discrepancy between the extrapolated and corrected stresses. (dt = 0.005 seconds)

At the same time, the weight of the node is applied along the contact axis incrementally in a linearly increasing fashion. In impl-ex solution, the application of weight incrementally over multiple steps is fundamental since the contact stress is not computed correctly for a few steps at the beginning of the analysis. The first step incorrectly results in zero contact stress and stiffness, and it is spent to update the state variables which were zero before. The second step results in non-zero contact stress and stiffness, though the magnitudes are incorrect due to the error committed in the previous step. Over the following steps, the error gradually starts to decrease, and the contact stress converges to the correct value following the final weight increment. The number of required steps depends on the contact stiffness and the magnitude of the load increment. A steeper stiffness would lead to high initial contact forces during the extrapolation requiring more steps to correct or equivalently, requiring a smaller weight increment. It is observed that, usually, 5 to 10 iterations are enough to control the error accumulation and obtain accurate self-weight analysis. Following, the dynamic analysis might be started. Similarly, at the beginning of the time-history analysis, the material is biased towards the latest action. Hence, 2-3 steps of

steady-state analysis in which the impl-ex materials are allowed to update state variables might be necessary before starting the dynamic analysis.

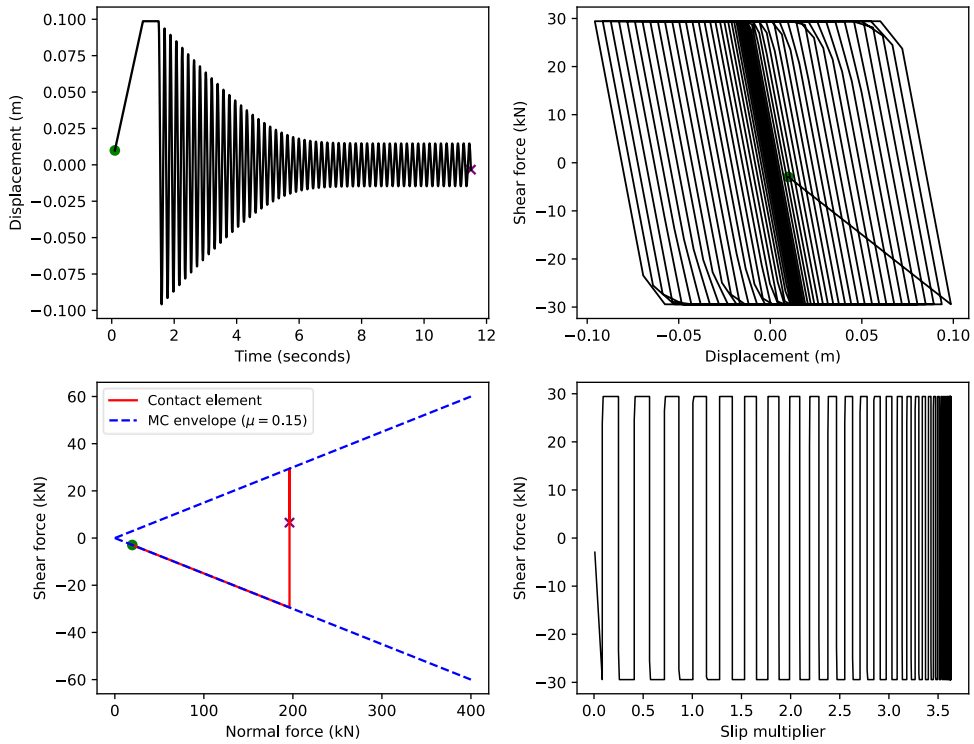

Figure 3.7. Soft implicit friction damper (K_f = 2e3 kPa). The implicit and the impl-ex solution results in a similar stress-strain response. (dt = 0.005 seconds)

In Figure 3.6, the impl-ex dynamic solution of the s.d.o.f. oscillator can be seen. In the displacement-time plot, the path of the model, beginning at the green dot and terminating at the purple cross, is plotted. As deduced by studying the governing balance equation (Section 3.1), unlike viscous damping, the frictional damper leads to a linear damping in the maximum displacement over time. This is a fundamental characteristic of the friction physics. As the maximum displacement falls below the permissible elastic displacement, the friction damping vanishes, and the problem turns in to the undamped free-vibration case. This can be confirmed in the force-displacement plot in which the hysteretic cycles become smaller and smaller with time until the loop turns into a straight line. It is worth noting the creases at the edge of hysteresis loops. These are artefacts of the large time-step used in the solution and are unrelated to the impl-ex solution. In fact, they also exist in Figure 3.7, in which the implicit solution of the same model is presented. Due to the sharp

turns in the hysteresis loops at these points (i.e., idealised plasticity), the chosen time-step is not small enough to precisely approximate the edges. On the other hand, comparing Figure 3.6 and Figure 3.7, the impl-ex solution matches the implicit solution.

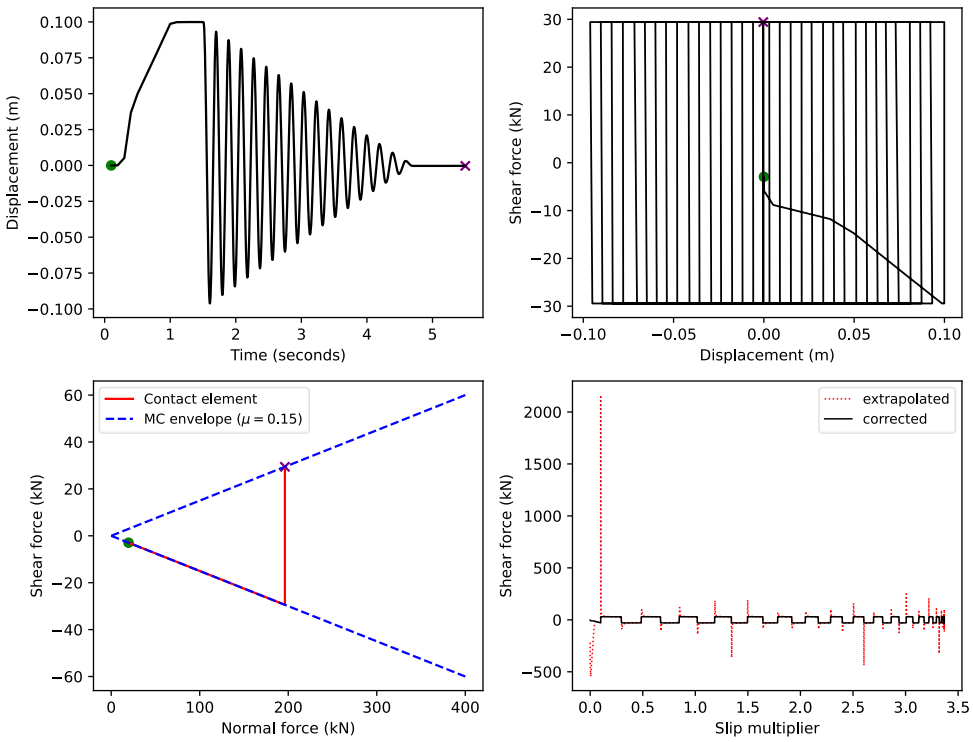

Figure 3.8. Stiff impl-ex friction damper (K_f = 2e8 kPa). Diverging extrapolated stress due to high K_f is controlled after the correction step. (dt = 0.005 seconds)

The characteristic of the impl-ex solution can be seen by studying the shear force versus slip multiplier plots. The slip multiplier is one state variable that is extrapolated during the explicit stage and corrected at the explicit stage. As per the impl-ex contact formulation presented in Section 3.2, the shear force linearly depends on the slip multiplier during the Newmark solution. Figure 3.6 shows the evolution of the shear force at each step during extrapolation and after correction. The corrected shear force matches that of the implicit solution shown in Figure 3.7. It is noted that after each slip direction change, the extrapolated force starts with a high peak due to the steepness of the slip multiplier history. The discrepancy between the extrapolated and corrected force reduces over a few iterations until the slip direction abruptly changes again. This behaviour results in a relatively smoother approximation of the saw-tooth shape of the friction force.

The accuracy of the approximation depends on the number of solution points between each change of slip direction. This observation shows that, for the s.d.o.f. oscillator, the proper time step to obtain reliable results is a function of the fundamental vibration period of the system. The accuracy of the solution can be improved by increasing the density of solution points between each oscillation or relaxing the frictional stiffness, which leads to a smaller discrepancy between the forces after extrapolation. In Figure 3.8, the same model is solved again by increasing the frictional stiffness, K_f to 2e8 kPa to obtain a stiff damper. As expected, increasing the frictional stiffness leads to significantly higher extrapolated forces. However, it is worth noting that after the correction step, the friction force is effectively stabilized and brought down to the implicit solution value. This exercise offers an insight into the robustness of the impl-ex solution, even when the time-step is sufficiently large to trigger the divergence of the solution during explicit solution.

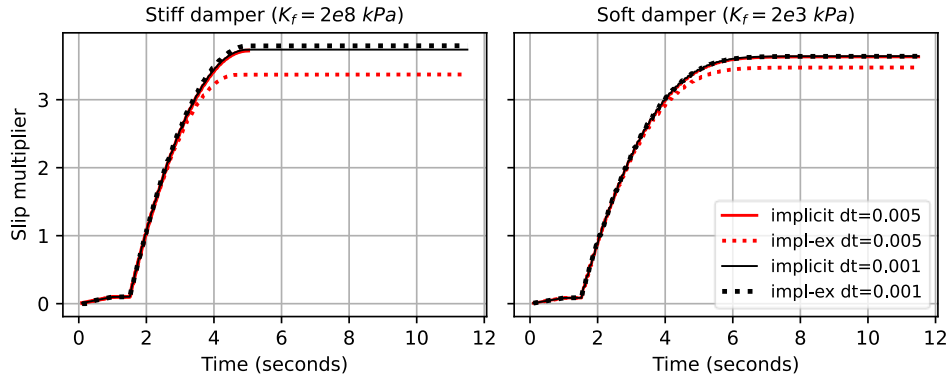

Figure 3.9.The comparison of the irreversible deformation (dissipation) computed using implicit and impl-ex integration approaches.

Figure 3.9 plots the evolution of irreversible deformations computed by the contact element for the stiff and soft frictional stiffness. First, increased plastic behaviour is computed when the damper is stiff observed from the higher final value of the slip multiplier in the stiff case than the soft case. This is confirmed by studying the displacement-time plots of each damper. At the end of analysis, the stiff damper stops completely, whereas the soft damper oscillates in a free undamped manner. Since each model's initial potential energy is the same, the stiff damper generates faster and increased energy dissipation.

The final aspect to consider is the error accumulation characteristics of the impl-ex solution. Figure 3.9 shows the directly proportional relation between the discrepancy in the computed dissipation and the time step. The impl-ex and implicit solutions coincide when the time step is appropriately chosen. However, the stiff case displayed in Figure 3.8, the

chosen time-step of 0.005 seconds results in the underestimation of irreversible plastic response. The total slip found by integrating the slip multiplier over the analysis time relates to the cumulative area covered by the hysteretic loops generated by the material. At the infliction point between the elastic and plastic response, approaching from the elastic domain, a steeper frictional stiffness results in a more deviated force, resulting in the overestimation of the elastic response. The same effect is present while transitioning from plastic to elastic response. However, the studied element is insensitive to the changes in the plastic stiffness since the plastic stiffness is always zero (perfectly plastic).

In conclusion, the characteristic of having an impl-ex solution to the contact mechanics equations is investigated thoroughly over a simple example of an s.d.o.f. oscillator. It is established that the impl-ex solution is sensitive to the chosen time step, specifically the number of solution points used to approximate the solution. Experience suggests that 5-10 points yield acceptable results in approximating rough solutions, such as the force generated by a friction damper, as shown here. On the other hand, convergence is guaranteed with the impl-ex solution and the correction step, making the approach robust enough to prevent divergence problems even when the time step is large.

3.5 CYCLIC SHEAR TEST MODEL OF A HISTORICAL STONE MASONRY PIER

Historical stone masonry structures are common throughout the cities in Europe. The unreinforced masonry structures in high seismicity zones in Europe, such as Italy and parts of Switzerland, are at risk of heavy damage or collapse. On the other hand, structures are threatened by the induced seismicity in places such as Groningen, where fracking is used as a standard way of extracting natural resources. Given the complex behaviour of stone masonry under seismic loads and its inherent variability, experimental data are crucial to understanding and predicting structural responses. To address this problem, researchers showed increased interest in full or half-scale shake table testing of historical masonry structures (Angiolilli & Gregori, 2020; Magenes et al., 2010; Milosevic et al., 2013; Penna et al., 2016; Petry & Beyer, 2015; Restrepo Vélez et al., 2014; Senaldi et al., 2014; Tomić et al., 2023; Uranjek et al., 2012; Vaculik et al., 2014; Vasconcelos & Lourenço, 2009). Among these tests, the SERA-AIMS shake table tests conducted in Lausanne by Tomić et al. (2023) are highly relevant to this study. In their shake table test, Tomić et al. (2023) tested the behaviour of a half-scale historical stone masonry aggregate composed of two separate structures. The two adjacent structures were in contact with each other through a dry joint. Their study used scaling laws and the masonry characteristics previously proposed and tested by Senaldi et al. (2018), which considered the same typology of masonry structures.

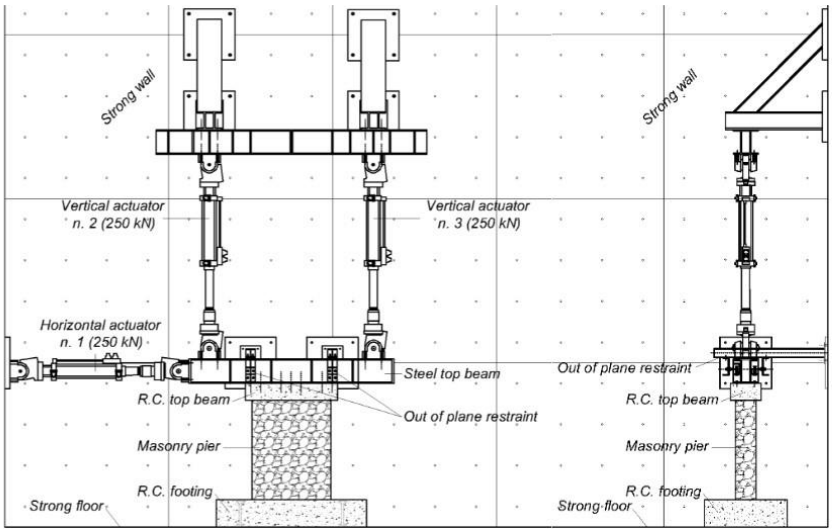

a) Front view **b) Side view**

Figure 3.10. The pseudo-static cyclic tests done by Senaldi et al. on historical masonry piers with various geometries. The a) front view and b) side view of the testing rig at the Eucentre. (Senaldi et al., 2018)

Senaldi et al. (2018) was also motivated by the need to assess the seismic vulnerability of natural stone masonry buildings, particularly those prevalent in historical centres like Basel, Switzerland. The research aimed to provide a detailed analysis of stone masonry's mechanical properties and failure mechanisms to inform effective seismic retrofit strategies.

They conducted in-plane cyclic shear-compression tests on four half-scale unreinforced stone masonry piers to evaluate their behaviour under cyclic horizontal loads. These tests aimed to assess the masonry piers' lateral strength, stiffness, deformation capacity, and energy dissipation under different axial compression levels and aspect ratios. The piers were constructed using the same materials and techniques as the half-scale masonry aggregate used in the shake-table tests by Tomić et al. (2023)Two different aspect ratios were considered: squat piers with an aspect ratio of 1.26 (CT01 and CT02) and slender piers with an aspect ratio of 3.0 (CS01 and CS02). Additionally, the axial compression levels at the pier base varied between 0.2 and 0.3 for the squat piers and between 0.3 and 0.45 for the slender piers.

Similitude relationships governed the scaling of the masonry piers for the in-plane cyclic shear-compression tests, which are essential for ensuring that the half-scale model accurately represents the behaviour of a full-scale structure under dynamic loading conditions. Key mechanical properties such as strength, stiffness, and density had to be scaled accordingly to maintain these similitude relationships—one critical adjustment

involved modifying the mortar mix by incorporating expanded polystyrene (EPS) beads. The EPS beads were added to reduce the stiffness and strength of the mortar, aligning the mechanical properties of the scaled masonry with those expected from full-scale natural stone masonry. This approach resulted in a half-scale masonry compressive strength of approximately 1.3 MPa, consistent with the requirements for dynamic testing. In contrast, full-scale tests on similar masonry showed a compressive strength of around 2.5 MPa. The masonry density was approximately 1,980 kg/m³.

The CT01 pier had a height of 1,580 mm and a length of 1,260 mm. The pier was subjected to an axial compression level defined by the ratio of the uniform normal stress at the base to the masonry compressive strength. For CT01, this ratio was set at 0.3 (approximately 135 kN), representing a higher axial load condition than other test specimens.

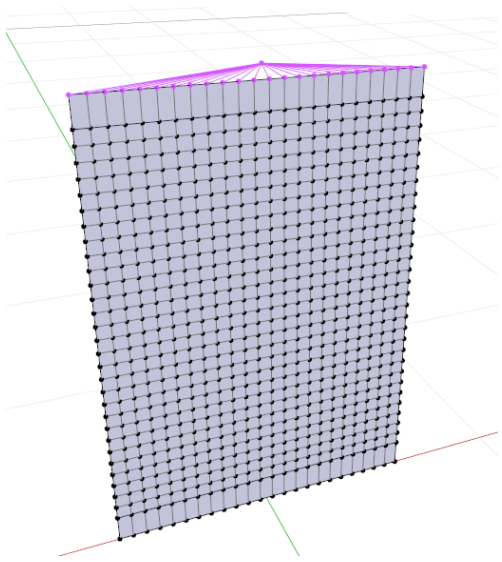

Figure 3.11. The finite element (FE) model of the pier CT01 in STKO.

The pier exhibited a complex hybrid failure mechanism during testing. The initial response was dominated by flexural rocking, with horizontal cracks forming at the base and below the top stone course at a drift ratio of 0.2%. However, as the testing progressed, diagonal and vertical cracks began to appear, indicating the onset of a shear mechanism. Ultimately, the pier experienced shear failure triggered by diagonal strut crushing, which was reflected in the degrading cyclic force-displacement response observed in the test. The maximum drift ratio reached by CT01 was 1.75%, beyond which extensive toe crushing and bulging led to the termination of testing.

The finite element model of CT01, is prepared in OpenSees with the help of the STKO pre-processor (Figure 3.11). The *ASDShellQ4* (Petracca, 2022) shell elements are used for the modelling of the masonry pier as well as the rigid top and bottom beams. The bottom beam is fixed at the bottom side, whereas the rotation of the top beam is fixed by forcing equal vertical displacements for all the rigid beam nodes taking a master node slightly above the specimen as a reference. The self-weight is applied as face forces and the vertical load is applied as a point load acting on the master node. In each element, the thickness of the shell element is provided by eight fibres. This is done by assigning a *LayeredShell* section to each Gauss point. Then, the plate fibre stress conditions are enforced on the material by using a wrapping material called the *PlateFiber* material. The geometric nonlinearities are considered by activating the corotational kinematics offered by the *ASDShellQ4* element.

Finally, the opening and closing of the gap between the pier and the rigid beams are modelled with the impl-ex contact element formulated in Section 3.2. The effect of considering or ignoring the modelling of the gap is studied here by comparing the results of the FE model with and without the contact elements which are called the smooth boundaries and rough boundaries in this section, respectively.

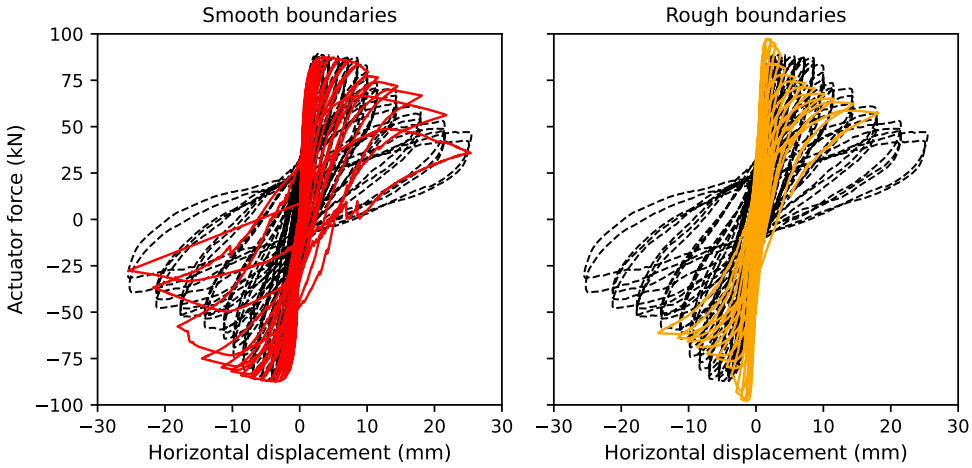

Figure 3.12. The cyclic analysis of the pier CT01 FE model. The analysis with rough boundaries terminated earlier due to the loss of fixities as the model separated into four pieces through the crack planes.

The masonry material is modelled with the *ASDConcrete3D* material since it offers a user input crack angle (Table 3.3). The principal strain planes and the crack propagation direction is guided via an orthotropic hardening rule (Section 2.5.1). It is worth noting that, the accurate modelling of the pier behaviour under shear loading is only possible due to the orthotropic failure assumption. The orthotropic behaviour leads to the rotation of the failure plane along an assumed angle which otherwise would be vertical in a homogeneous

isotropic material. The angle of failure is closely related to the micromechanics of the brick-mortar fabric and the crack propagation through mortar joints in the stone masonry.

Table 3.3. Parameters of the ASDConcrete3D material calibrated for the stone masonry pier CT01 (units in kPa)

Parameter	Masonry	Definition
rho	1.98	Density in tons per cubic meter
E	2,800,000	Young's modulus
v	0.14	Poisson's ratio
ft	185	Tensile strength
Gt	0.3	Tensile fracture energy
fc0	10	Compressive elastic limit
fcp	1500	Compressive peak strength
fcr	300	Compressive residual strength
ep	0.0035	Compressive strain at peak strength
Gc	17	Compressive fracture energy
PSc_T	0.70	Plastic-Damage factor for tensile response [0: full damage ... mixed ... 1: full plasticity]
PSc_C	0.40	Plastic-Damage factor for comp. response [0: full damage ... mixed ... 1: full plasticity]
autoReg.	active	Option to scale Gt and Gc by the element characteristic length

Figure 3.12 shows force-displacement curves obtained with both FE models. Notably, the model with the smooth boundaries (with the contact elements) performs better in capturing the initial stiffness, the peak strength and the post peak behaviour of the masonry pier. Furthermore, the rough boundary model does not seem to capture the toe crushing mechanism at the end of the analysis. Both models miss the initial anisotropic stiffness of the pier since stiffness anisotropy is not a feature in either model.

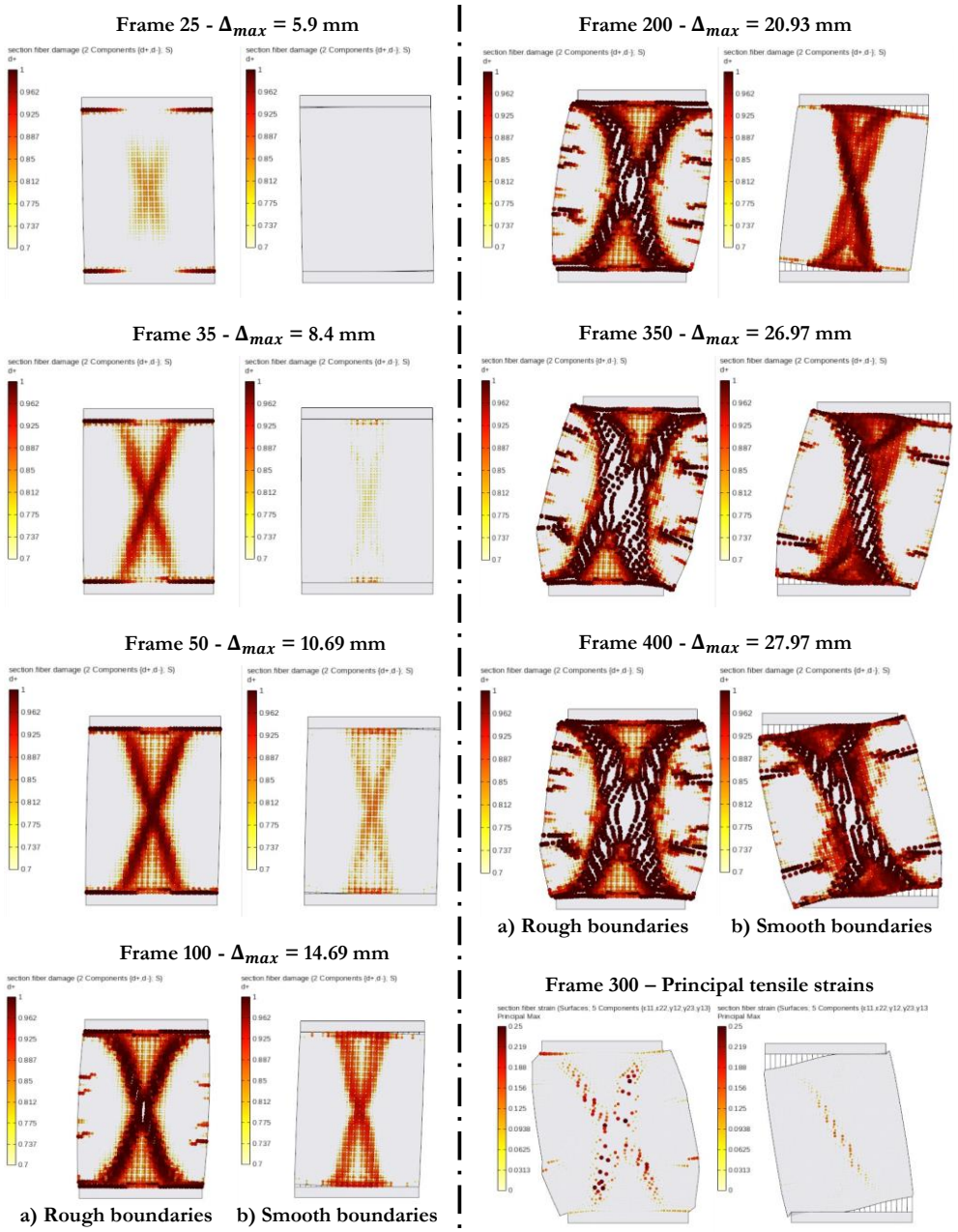

Figure 3.13. The step-by-step evolution of the cracking damage with increasing displacement cycles. The comparison between the tensile damage observed in the rough and smooth boundary models.

The frame-by-frame evolution of the cracking damage during the analyses can be seen in Figure 3.13. The effect of modelling the closing and opening of the gap becomes apparent from the early stages of the analysis. In the rough boundary model, the joint between the masonry pier and the rigid beams starts to crack as soon as the top beam horizontally displaces. This is expected since the beams are significantly stiffer than the masonry pier. A cross-shape damage zone starts to appear in the model because of some tensile stress transfer to the pier. On the other hand, no failure mechanism is observed in the smooth boundary model at this stage since the beams and the pier are allowed to separate without inducing tensile cracking at the interface.

As the cyclic displacement grows, the initial cracking at the interfaces trigger a distinguishable cross shape failure in the rough boundary model, where the pier gradually separates into several independent pieces. On the other hand, the damage zone appears much later in the smooth boundary model. Unlike the rough boundary model, the damage mechanism is triggered by the shear induced by compression strut, which is mechanically more accurate. The most prominent outcome of the compression strut mechanism is the asymmetric failure of the pier under shear, which is also observed in the masonry specimen. Even though the compression strut appears in a symmetrical manner initially, due to reaching the peak strength first along the primary direction of loading, the corresponding compression strut fails first around the 300th frame. Then, secondary compression struts form in the opposite direction and eventually a shallower second failure is observed at the frame 400.

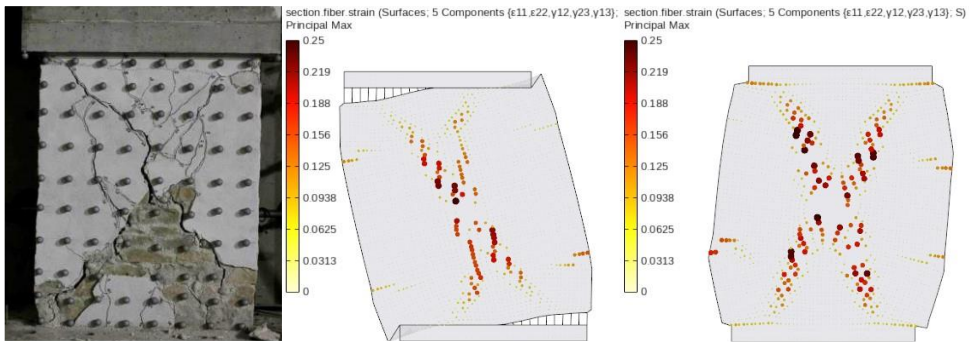

a) Specimen CT01 **b) Smooth boundaries** **c) Rough boundaries**

Figure 3.14. The a) cracking of the specimen CT01, the tensile principal strain plots of the b) smooth boundary, and c) rough boundary models.

Finally, as observed in the experiment a toe crushing mode appears, which leads to the abrupt cyclic degradation of the of the force-displacement response as shown in Figure 3.12. Such a mechanism is not captured by the rough boundary model, since the masonry at the interfaces are already heavily damaged due to cracking early in the analysis.

The final crack composition of the pier at the point of failure is displayed in Figure 3.14. The asymmetric failure mechanism composed of a failed primary and secondary compression struts can be seen in the photograph of the specimen CT01. The smooth boundary model fails in a similar fashion. Furthermore, the dislocation at the four corners of the pier due to toe crushing is visible in the smooth boundary model. Meanwhile, the rough boundary model, exhibits an outward bulging at sides due to the cross-shape failure at its centre. This is because the tensile strain generates a large plastic strain component following the failure. The amount of damage-plasticity component to be generated is controlled by the model parameter, PSc_T, shown in Table 3.3. Even though the force-displacement response of the rough boundary model is not extremely far off from the experimental response, the predicted mechanism does not represent an accurate picture of the experimentally observed response.

Overall, the smooth boundary model in which the contact elements are employed to model interface separation predicts results that are more compatible with the experimental observations. The smooth boundary model captures

1. The initial stiffness of the pier,
2. The asymmetric failure of the compression struts, and
3. The toe crushing mechanism

efficiently, whereas the failure mechanism of the rough boundary model is biased by the initial cracking of the interfaces. This phenomenon might not result in such a powerful outcome in the micro modelling approach, in which the mortar and the stones are explicitly modelled. Unlike in a macro model in which the underlying micro-mechanics are homogenized, the observed cracking of the interface would translate to the localized failure of the mortar between the stones and the rigid beam in a micro model. Therefore, the importance of modelling the opening and closing of the gap between the pier-beam interfaces in a cyclic experiment is shown. Furthermore, such a solution is shown to be possible and numerically stable thanks to the robustness of the implicit-explicit integration.

3.6 SUMMARY AND DISCUSSION

Contact problems are highly nonlinear due to the alternating contact conditions and the tangential stick-slip behaviour present at the contact interfaces. Explicit methods that are typically used for solving such problems require small time steps, which may be impractical for large-scale seismic simulations. This chapter has introduced the formulation of a mixed implicit-explicit (impl-ex) contact element in OpenSees to address the challenges of dynamic contact problems with frictional interactions. The newly developed penalty-based zero-length node-to-node contact element offers arbitrary degrees of freedom configurations. The frictional interaction is modelled using a Drucker-Prager yield surface to provide an elastic-perfectly-plastic stick-slip response. The element supports both

implicit and implicit-explicit (impl-ex) modes for material internal variable integration, enhancing solution stability during dynamic analysis.

The element's accuracy has been validated through a patch test, which confirms the consistency of the impl-ex formulation with the theory. The dynamic behaviour of the element was further explored through the analysis of a single-degree-of-freedom (s.d.o.f.) friction damper model, which demonstrated the impl-ex element's ability to produce accurate and stable results comparable to those obtained using implicit integration, with the added benefit of reduced computational cost.

However, the results also highlight the sensitivity of the impl-ex method to time step selection, especially for cases with high penalty stiffness. Future extensions could include the implementation of friction degradation and cohesion loss mechanisms, which are crucial for accurately simulating the behaviour of masonry structures subjected to seismic loads.

4 IMPLEMENTATION OF AN IMPL-EX MULTI-YIELD SURFACE KINEMATIC HARDENING MATERIAL IN OPENSEES

Numerical handling of soil nonlinearity can be challenging. The desired soil response in seismic assessment is often nonlinear from the beginning with having little or no elastic domain of behaviour as in the case of multi-yield surface model. This nonlinearity is useful when the hysteretic damping provided by the material is a point of interest; however, it brings cost in the numerical solution by requiring multiple iterations to achieve convergence. Furthermore, convergence issues might be faced during the solution of a pressure-dependent model with built-up pore water pressures due to non-coaxial and extreme straining characteristics of a liquefying model. Many authors reported numerical challenges in the solution of 3D FE models with liquefying soil or other material nonlinearities. In the case of DamageTC3D model, an impl-ex integration at the material level helps controlling the computational demand of a multi-axial softening material. In this chapter, the implicit-explicit integration scheme is extended to the Pressure-dependent (PDMY02) and Pressure-independent (PIMY) multi-yield surface materials available in OpenSees. These models are widely used in the soil-structure interaction studies available in the literature and well-known by researchers.

Initially, a comprehensive review and formulation of the PDMY02 material is given with special comments on the implementation in OpenSees. The Pressure-independent case is omitted for brevity. Additionally, it is noted that significantly more resources were made available on the pressure-independent case by the implementors of the models. Then, details of the novel implemented implicit-explicit internal integration strategy is given. First, the linearization of the nonlinear flow rule is discussed. Two flavours of linearized formulation are tested: rephrased-flow and linearized-flow. The linearized flow is observed to be in line with the computation of a consistent tangent since it involves the stress derivative of the flow rule. The rephrased flow is found to be mathematically much simpler. The implementation and the solution timing studies show that even though linearized flow is mathematically superior, rephrased flow offers a much faster calculation, and more compatible formulation with the OpenSees implementation of the PIMY and PDMY02 materials.

The validity and the performance of the implementation is shown by means of single element modelling of a cyclic triaxial test. Then, examples of two 1D soil response column

tests, one total stress (*freeFieldIndepend.tcl*) and one effective stress (*freeFieldEffective.tcl*) is presented. The behaviour of these models is well-known since they are the example models in the OpenSees manual. The comparisons show a good match between the impl-ex and implicit versions with significant reduction in the analysis time. The effect of error build-up becomes pronounced in records with longer duration. However, the error build-up can be controlled via increasing the number of steps or adopting adaptive time-stepping approaches.

Keywords: Pressure-dependent multi yield, Pressure-independent multi yield, Finite Elements, Implicit-explicit integration, Linearized flow, Single element tests

4.1 THE PRESSURE-DEPENDENT MULTI-YIELD SURFACE MODEL

The philosophy behind the multi-yield surface models is discussed in Section 2.6. Consequently, the focus of this section shifts towards elucidating the formulation of the PDMY02 material in OpenSees, as implemented by Yang et al. (2003) and later extended by Yang & Elgamal (2008), excluding the lode angle effects. The formulation of the PIMY material is given by Gu et al. (2009, 2011). Within the scope of this thesis the PDMY02 and PIMY materials are extended to impl-ex integration scheme. To achieve this task a detailed mathematical description of these models is required. Hence, this section is dedicated to document the complete formulation and the algorithm of the most recent multi-yield surface model, combining various sources from the literature.

A bold-faced letter notation is employed to represent tensors, with 2nd order tensors, such as strain or stress tensors, denoted by small letters. Conversely, 4th order tensors, such as the stiffness tensor, are distinguished using double-struck letters. Operator ':' define a double tensor contraction operation, whereas '$\otimes$' defines a tensor multiplication resulting in an increase in the order of the output tensor. Einstein notation is used in conjunction with tensor notation to elucidate the mathematical structure of certain crucial tensors. Although the formulation is presented with a 3D generic case in mind, references to the 2D plane-strain special case are incorporated in the text when deemed necessary. It is important to note that all stress terms referred to in this context are effective stresses, and for the sake of convenience, the prime symbol is omitted from stress terms.

In accordance with Equation 4.1, plasticity is introduced in the model through computing a plastic strain tensor and removing the plastic component of the strain from the total strain increment tensor based on the linear decomposition of the strain tensor into elastic and plastic parts.

$$\dot{\boldsymbol{\varepsilon}} = \dot{\boldsymbol{\varepsilon}}^{\boldsymbol{e}} + \dot{\boldsymbol{\varepsilon}}^{\boldsymbol{p}} \qquad \textbf{4.1}$$

The non-coaxial nature of the strain increment tensor is a well-established characteristic of granular materials (Roscoe, 1970) (i.e., the strain increment is not always along the stress increment vector on the contrary of a pure-shear deformation behaviour). In the presented model, the orientation of the principal strain axes is allowed to rotate through the accumulation of plastic strain (Jefferies et al., 2015). The plastic strain increment is assumed to be a linear composition of a deviatoric, and a volumetric component as shown in Equation 4.2.

$$\dot{\boldsymbol{\varepsilon}}^{\boldsymbol{p}} = \dot{\boldsymbol{e}}^{\boldsymbol{p}} + \dot{\boldsymbol{\varepsilon}}^{\boldsymbol{p}}_{\boldsymbol{vol}} \qquad \textbf{4.2}$$

The presented simplification holds practical significance as it facilitates the treatment of deviatoric and volumetric responses through distinct sets of equations and state variables. In classical elastoplasticity, the prevalent adoption of the linear decomposition of the plastic strain increment tensor is a well-established convention. Moreover, some of the widely-used models often assume that the overall plastic behaviour is driven by the plastic, with volumetric deformation being a consequence of such shearing (Dafalias & Manzari, 2004; Jefferies, 1993). Empirical evidence substantiates this assumption and underscores its significance in the framework of Critical State Soil Mechanics (CSSM), aligning with experimental findings (Jefferies & Been, 2015). It is imperative to acknowledge, however, that relying solely on the plastic shear strain-driven plastic response assumption may prove inadequate for capturing certain fundamental soil behaviour such as the observed irreversible volumetric straining under increasing isotropic consolidation pressure (Dafalias & Manzari, 2004).

Table 4.1. List of tensor quantities and their corresponding matrix representation for compressed tensor operations

Tensor quantity	Tensor notation	Matrix form (representation)	Einstein notation
Strain	$\boldsymbol{\varepsilon}$	Strain-like	ε_{ij}
Plastic strain	$\boldsymbol{\varepsilon^p}$	Strain-like	ε^p_{ij}
Strain deviator	$\boldsymbol{e}$	Strain-like	e_{ij}
Plastic strain deviator	$\boldsymbol{e^p}$	Strain-like	e^p_{ij}
Stress	$\boldsymbol{\sigma}$	Stress-like	σ^{ij}
Trial stress	$\boldsymbol{\sigma^{tr}}$	Stress-like	$\sigma^{tr\,ij}$
Stress deviator	$\boldsymbol{\tau}$	Stress-like	τ^{ij}

Reduced stress deviator	$\boldsymbol{\zeta}$	Stress-like	ζ^{ij}
Volumetric stress	σ^{vol}	Scalar	σ^{vol}
Stress ratio	$\boldsymbol{\eta}$	Stress-like	η^{ij}
Back-stress	$\boldsymbol{\alpha}$	Stress-like	α^{ij}
Elastic modulus	$\mathbb{E}$	Stress-like	E^{ijkl}
Elastoplastic modulus	$\mathbb{H}$	Stress-like	H^{ijkl}
Consistent tangent operator	$\mathbb{C}$	Stress-like	C^{ijkl}
4th order volumetric operator	$\boldsymbol{I}\otimes\boldsymbol{I}$	Stress-like	$\delta^{ij}\delta^{kl}$
4th order symmetric operator	$\mathbb{I}$	Stress-like	$^1/_2\left(\delta^{ik}\delta^{lj}+\delta^{il}\delta^{jk}\right)$

The volumetric and deviatoric strain components are computed as follows. The incremental tensor quantities are computed in a similar fashion. Notably, in the context of a 2D plane strain scenario, the third strain component is assumed to be zero, resulting in a 2-by-2 strain tensor. Nevertheless, when computing the strain deviator, it is essential to divide the volumetric strain by 3, regardless.

$$\varepsilon_{vol} = \varepsilon_{xx} + \varepsilon_{yy} + \varepsilon_{zz} \tag{4.3}$$

$$\boldsymbol{e} = \boldsymbol{\varepsilon} - \frac{\varepsilon_{vol}}{3}\boldsymbol{I} = \begin{bmatrix} \varepsilon_{xx} - \frac{\varepsilon_{vol}}{3} & \varepsilon_{xy} & \varepsilon_{xz} \\ \varepsilon_{xy} & \varepsilon_{yy} - \frac{\varepsilon_{vol}}{3} & \varepsilon_{yz} \\ \varepsilon_{zx} & \varepsilon_{zy} & \varepsilon_{zz} - \frac{\varepsilon_{vol}}{3} \end{bmatrix} \tag{4.4}$$

By decomposing the strain increment tensor into deviatoric and volumetric components, it becomes possible to compute the corresponding deviatoric and volumetric stress increments. The determination of the stress increment, as shown in Equation 4.5, necessitates the computation of the plastic strain increment. The plastic strain increment is a function of the material characteristics and especially strength. In single surface plasticity, the material strength is assumed to be limited by a yield surface existing in the six-dimensional stress space. Fundamentally, the stress state of the material cannot exceed or exist outside of the region wrapped by the yield surface. For a stress demand that exceeds the yield surfaces, the material must dissipate the excessive energy by generating plastic

strain and return the stress state back to the surface of the yield surface in the process. This process is called stress relaxation.

$$\dot{\boldsymbol{\sigma}} = \mathbb{E}: (\dot{\boldsymbol{\varepsilon}} - \dot{\boldsymbol{\varepsilon}}^{\boldsymbol{p}}) \tag{4.5}$$

In case of a single surface the failure response of the material is a bi-linear stress-strain response. However bi-linear behaviour is not elaborate enough to model the hysteretic behaviour that is desired in this thesis. Multi-yield surface approach suggests adding multiple yield surfaces before the failure surface (Mróz, 1967; Prévost, 1977). This way the hysteretic response as well as a cyclic response memory is provided to the material. The amount of plastic strain, and consequently stress reduction, is contingent upon the active yield surface. Furthermore, surfaces are allowed to move in the stress space as the plastic strain is generated. As the active surface moves and touches the next yield surface, the next yield surface is made the active surface, and the stress reduction is continued. This way the isotropic hardening, kinematic hardening, and the bias towards the past stress path (stress induced anisotropy) is modelled. The process that starts from the strain increment and leads to the stress increment is called the return mapping or the material integration. The volumetric, deviatoric parts of the stress tensor as well as the deviatoric stress tensor are computed as follows. In 2D plane strain formulation, the stress tensor is 2-by-2; however, unlike the volumetric strain, the average pressure is halved.

$$\sigma^{vol} = \frac{I_1}{3} = \frac{\sigma_{xx} + \sigma_{yy} + \sigma_{zz}}{3} \tag{4.6}$$

$$\boldsymbol{\tau} = \boldsymbol{\sigma} - \sigma^{vol}\boldsymbol{I} = \begin{bmatrix} \sigma_{xx} - \sigma^{vol} & \sigma_{xy} & \sigma_{xz} \\ \sigma_{yx} & \sigma_{yy} - \sigma^{vol} & \sigma_{yz} \\ \sigma_{zx} & \sigma_{zy} & \sigma_{zz} - \sigma^{vol} \end{bmatrix} \tag{4.7}$$

$$\boldsymbol{\zeta} = \boldsymbol{\tau} - \sigma^{vol}\boldsymbol{\alpha} = \begin{bmatrix} \tau_{xx} - \sigma^{vol}\alpha_{xx} & \tau_{xy} - \sigma^{vol}\alpha_{xy} & \tau_{xz} - \sigma^{vol}\alpha_{xz} \\ \tau_{yx} - \sigma^{vol}\alpha_{yx} & \tau_{yy} - \sigma^{vol}\alpha_{yy} & \tau_{yz} - \sigma^{vol}\alpha_{yz} \\ \tau_{zx} - \sigma^{vol}\alpha_{zx} & \tau_{zy} - \sigma^{vol}\alpha_{zy} & \tau_{zz} - \sigma^{vol}\alpha_{zz} \end{bmatrix} \tag{4.8}$$

The tensor quantities involved in the return-mapping and their matrix representations are given in Table 4.1. The compressed tensor notation is useful since it eliminates some of the repetitive steps during computations and leads to efficient storage taking advantage of certain symmetry features of stress and strain-like tensors. It is worth knowing that, in OpenSees, the material tangent and residual tensors should be implemented in Voigt notation to provide compatibility with the existing elements.

4.1.1 Elasticity

The incremental stress-strain relationship is as follows:

$$\dot{\boldsymbol{\sigma}} = \mathbb{E}: \dot{\boldsymbol{\varepsilon}}^{\boldsymbol{e}} = \mathbb{E}: (\dot{\boldsymbol{\varepsilon}} - \dot{\boldsymbol{\varepsilon}}^{\boldsymbol{p}}) \qquad \textbf{4.9}$$

In Equation 4.9, the $\boldsymbol{\sigma}$ and $\boldsymbol{\varepsilon}$ is the effective stress and the strain tensors. The dot above denotes the material derivative resulting in the same order tensor storing the increment of the given quantity. In continuum terms, $\boldsymbol{\varepsilon}$ is the small strain tensor, i.e., the linear approximation of the spatial solid deformation gradient (Prevost, 1989), and $\boldsymbol{\sigma}$ is the Cauchy stress tensor, being the energy conjugate of $\boldsymbol{\varepsilon}$.

$$\boldsymbol{\sigma} = \begin{bmatrix} \sigma_{xx} & \sigma_{xy} & \sigma_{xz} \\ \sigma_{xy} & \sigma_{yy} & \sigma_{yz} \\ \sigma_{zx} & \sigma_{zy} & \sigma_{zz} \end{bmatrix} \qquad \textbf{4.10}$$

$$\boldsymbol{\varepsilon} = \begin{bmatrix} \varepsilon_{xx} & \varepsilon_{xy} & \varepsilon_{xz} \\ \varepsilon_{xy} & \varepsilon_{yy} & \varepsilon_{yz} \\ \varepsilon_{zx} & \varepsilon_{zy} & \varepsilon_{zz} \end{bmatrix} \qquad \textbf{4.11}$$

$$\mathbb{E} = K\boldsymbol{I}\otimes\boldsymbol{I} + 2G\left(\mathbb{I} - \frac{1}{3}\boldsymbol{I}\otimes\boldsymbol{I}\right) \qquad \textbf{4.12}$$

$\mathbb{E}$ is the fourth order elastic coefficient tensor (modulus), scalar coefficients K and G are the small strain bulk and shear moduli. In Equation 4.12, $\mathbb{E}$ is shown to be separated into its volumetric and deviatoric components since this feature is useful while computing the consistent tangent operator. The $\mathbb{I}$, is the symmetric fourth order tensor. The elastic coefficients are assumed to be dependent on the effective mean stress as shown below:

$$G = G_{ref}\left(\frac{\sigma^{vol}}{p_{ref}}\right)^{np} \qquad K = K_{ref}\left(\frac{\sigma^{vol}}{p_{ref}}\right)^{np} \qquad \textbf{4.13}$$

$$\varsigma = \left(\frac{\sigma^{vol}}{p_{ref}}\right)^{np} \qquad \textbf{4.14}$$

The scalar ς is the pressure dependent modulus factor that is used in the update of the elastic moduli at the beginning of each Newton-Raphson solution iteration.

Remark I. Volumetric and deviatoric decomposition of the elastic coefficients tensor for executing efficient consistent tangent calculations at each iteration.

From an elasticity point of view, defining the multi-axial elastic modulus of a linear elastic material as follows can be beneficial, since the computation is reduced to multiplying two stored matrices by scalars, followed by a matrix summation.

$$\mathbb{E}^{ijkl} = \left(K - \frac{2}{3}G\right)\boldsymbol{\delta_{ij}\delta_{kl}} + G\left(\boldsymbol{\delta_{ik}\delta_{lj}} + \boldsymbol{\delta_{il}\delta_{jk}}\right) \qquad \textbf{4.15}$$

However, since a deviatoric-volumetric decomposition of the strain increment tensor is employed in this study, an alternative decomposed presentation of the modulus tensor might prove more practical, especially during consistent tangent computations. Hence, rearranging $\mathbb{E}^{ijkl}$ by gathering volumetric and deviatoric contributors together, we get:

$$\mathbb{E}^{ijkl} = K\boldsymbol{\delta_{ij}}\boldsymbol{\delta_{kl}} + 2G\left(\frac{1}{2}\left(\boldsymbol{\delta_{ik}}\boldsymbol{\delta_{lj}} + \boldsymbol{\delta_{il}}\boldsymbol{\delta_{jk}}\right) - \frac{1}{3}\boldsymbol{\delta_{ij}}\boldsymbol{\delta_{kl}}\right) \quad \textbf{4.12}$$

4.1.2 Yield function

The yield function, denoted by f is responsible for quantifying the amount of excess stress that needs to be relaxed to satisfy the active yield surface. It is a function of the current stress tensor, active surface back-stress tensor and the material constants associated with the active yield surface. It results in a scalar, specifying the closest distance between the input stress state and the yield surface. In an optimization point of view, the yield function is the quantity to be minimized to achieve solution.

Pressure-independent 2D $$f(\boldsymbol{\sigma}, \boldsymbol{\alpha}, R^m) = \sqrt{2(\boldsymbol{\tau} - \boldsymbol{\alpha}) : (\boldsymbol{\tau} - \boldsymbol{\alpha})} + R^m \quad \textbf{4.16}$$

Pressure-independent 3D $$f(\boldsymbol{\sigma}, \boldsymbol{\alpha}, R^m) = \sqrt{{}^3/_2\,(\boldsymbol{\tau} - \boldsymbol{\alpha}) : (\boldsymbol{\tau} - \boldsymbol{\alpha})} + R^m \quad \textbf{4.17}$$

Pressure-dependent 2D $$f(\boldsymbol{\sigma}, \boldsymbol{\alpha}, R^m) = \sqrt{2(\boldsymbol{\tau} - \acute{p}\boldsymbol{\alpha}) : (\boldsymbol{\tau} - \acute{p}\boldsymbol{\alpha})} + R^m \acute{p} \quad \textbf{4.18}$$

Pressure-dependent 3D $$f(\boldsymbol{\sigma}, \boldsymbol{\alpha}, R^m) = \sqrt{{}^3/_2\,(\boldsymbol{\tau} - \acute{p}\boldsymbol{\alpha}) : (\boldsymbol{\tau} - \acute{p}\boldsymbol{\alpha})} + R^m \acute{p} \quad \textbf{4.19}$$

where $\boldsymbol{\tau}$ and $\boldsymbol{\alpha}$ the stress deviator and the back-stress tensors, respectively. The scalars the yield radius, R, and the modified mean effective stress, $\acute{\boldsymbol{p}}$ are associated with the active yield surface m. The mean effective stress used in the return mapping is modified as in Equation 4.20 to prevent possible numerical issues such as the ambiguity in the derivative of the pressure dependent yield surface at its tip.

$$\acute{p} = \sigma^{vol} - p_0 \; where \; p_0 = 1.0 \; kPa \quad \textbf{4.20}$$

The outwards unit normal tensor to the yield surface is denoted by the letter $\boldsymbol{Q}$.

$$\boldsymbol{Q} = \boldsymbol{Q}' + Q"\boldsymbol{\delta} \quad \textbf{4.21}$$

where $\boldsymbol{Q} = \partial f / \partial \sigma$ is the derivative of the yield function with respect to the stress tensor, $\boldsymbol{Q}'$, and $Q"$ are the deviatoric and volumetric parts of the unit normal to the yield surface. Tensor $\boldsymbol{\delta}$ is the Kronecker delta operator in the respective three- or six-dimensional stress space.

Pressure-independent

$$\boldsymbol{Q} = \frac{(\boldsymbol{\tau} - \boldsymbol{\alpha})}{\sqrt{(\boldsymbol{\tau} - \boldsymbol{\alpha}) : (\boldsymbol{\tau} - \boldsymbol{\alpha})}} \quad \textbf{4.22}$$

Pressure-dependent

$$\boldsymbol{Q} = \frac{(\boldsymbol{\tau} - \acute{p}\boldsymbol{\alpha})}{\sqrt{(\boldsymbol{\tau} - \acute{p}\boldsymbol{\alpha}) : (\boldsymbol{\tau} - \acute{p}\boldsymbol{\alpha})}} + \frac{1}{3}\left(\mathrm{R} - \frac{(\boldsymbol{\tau} - \acute{p}\boldsymbol{\alpha}) : \boldsymbol{\alpha}}{\sqrt{(\boldsymbol{\tau} - \acute{p}\boldsymbol{\alpha}) : (\boldsymbol{\tau} - \acute{p}\boldsymbol{\alpha})}}\right)\boldsymbol{\delta} \quad \textbf{4.23}$$

In the multi-yield surface kinematic hardening formulation, the normal to the yield surface is computed at the current stress tensor (n+1st step). However, since the active yield surface is allowed to translate in the deviatoric stress space, the backstress tensor $\boldsymbol{\alpha}$ track the position of the centre of the active yield surface in the deviatoric stress space. Before computing the normal to the yield surface, the backstress is removed from the yield surface. In the pressure-dependent formulation, the backstress evolves as a function of the pressure; hence changes in the backstress translates to the rotation of the yield surface cone in the deviatoric stress-space.

Contact stress $\boldsymbol{\tau}^*$:

$$\boldsymbol{\tau}^* = \frac{K^m}{M_s}(-\acute{p}^{tr})\boldsymbol{\zeta}^{tr} + \acute{p}^{tr}\boldsymbol{\alpha}^m \quad \textbf{4.24}$$

$$\boldsymbol{\zeta}^{tr} = \boldsymbol{\tau}^{\boldsymbol{tr}} - \acute{p}^{tr}\boldsymbol{I} \quad \textbf{4.25}$$

$$M_s = \sqrt{{}^3\!/_2\,(\boldsymbol{\zeta}^{tr} : \boldsymbol{\zeta}^{tr})} \quad \textbf{4.26}$$

$$K^m = \sqrt{{}^3\!/_2\,R^m} \quad \textbf{4.27}$$

where R^m and $\boldsymbol{\zeta}^{tr}$ the radius of the active yield surface and the reduced stress deviator, respectively.

Remark II. Step-by-step derivation of the normal tensor to the pressure-dependent yield surface.

In a direct six-dimensional stress deviator notation, the Pressure-dependent yield function is (Prevost, 1989):

$$f(\boldsymbol{\sigma}, \boldsymbol{\alpha}, R) = \sqrt{{}^{3}/_{2}\,(\boldsymbol{\tau} - \acute{p}\boldsymbol{\alpha}) : (\tau - \acute{p}\boldsymbol{\alpha})} + R\acute{p} \tag{4.19}$$

where $\acute{\boldsymbol{p}} = \boldsymbol{p} + \mathbf{1.0}$. Note that the derivative of the back-stress tensor itself with respect to the stress tensor is zero and the derivative of the stress deviator with respect to the stress tensor is assumed to be the identity tensor. Then the normal to the yield surface becomes:

$$\boldsymbol{Q} = \frac{\partial \boldsymbol{f}}{\partial \boldsymbol{\sigma}} = \frac{(\boldsymbol{\tau} - \acute{\boldsymbol{p}}\boldsymbol{\alpha})}{\sqrt{(\boldsymbol{\tau} - \acute{\boldsymbol{p}}\boldsymbol{\alpha}) : (\boldsymbol{\tau} - \acute{\boldsymbol{p}}\boldsymbol{\alpha})}} \cdot \left(\frac{\partial \boldsymbol{\tau}}{\partial \boldsymbol{\sigma}} - \frac{\partial (\acute{\boldsymbol{p}}\boldsymbol{\alpha})}{\partial \boldsymbol{\sigma}} \right) + \boldsymbol{R} \cdot \frac{\partial \acute{\boldsymbol{p}}}{\partial \boldsymbol{\sigma}}$$

$$= \frac{(\boldsymbol{\tau} - \acute{\boldsymbol{p}}\boldsymbol{\alpha})}{\sqrt{(\boldsymbol{\tau} - \acute{\boldsymbol{p}}\boldsymbol{\alpha}) : (\boldsymbol{\tau} - \acute{\boldsymbol{p}}\boldsymbol{\alpha})}} \cdot \left(\boldsymbol{I} - \frac{\mathbf{1}}{\mathbf{3}} \boldsymbol{\alpha}\boldsymbol{\delta} \right) + \boldsymbol{R} \cdot \frac{\mathbf{1}}{\mathbf{3}} \boldsymbol{\delta}$$

Finally, rearranging the derivative as the following, the Equation 4.23 can be obtained:

$$\boldsymbol{Q} = \frac{(\boldsymbol{\tau} - \acute{p}\boldsymbol{\alpha})}{\sqrt{(\boldsymbol{\tau} - \acute{p}\boldsymbol{\alpha}) : (\boldsymbol{\tau} - \acute{p}\boldsymbol{\alpha})}} + \frac{1}{3}\left(R - \frac{(\boldsymbol{\tau} - \acute{p}\boldsymbol{\alpha}) : \boldsymbol{\alpha}}{\sqrt{(\boldsymbol{\tau} - \acute{p}\boldsymbol{\alpha}) : (\boldsymbol{\tau} - \acute{p}\boldsymbol{\alpha})}} \right) \boldsymbol{\delta} \tag{4.23}$$

Remark III. Computationally efficient implementation of the yield function

In older version of C++, the square root algorithm used to involve multiple division operations which took significantly more time than the multiplication operation in computing square. Hence, in the OpenSees implementation of PDMY02 (Yang et al., 2003), the yield surface, and the normal to the yield surface are computed in a slightly different way to improve computational speed. The implementation is mathematically equivalent to the formulation presented by (Prevost, 1989) and computes as follows:

$$f(\boldsymbol{\sigma}, \boldsymbol{\alpha}, R) = \frac{3}{2}(\boldsymbol{\tau} - \acute{p}\boldsymbol{\alpha}) : (\boldsymbol{\tau} - \acute{p}\boldsymbol{\alpha}) + (R\acute{p})^2 \tag{4.28}$$

For convenience let us substitute:

$$\boldsymbol{SU} = 3(\boldsymbol{\tau} - \acute{p}\boldsymbol{\alpha}) + \acute{p}\left[\left(\boldsymbol{\alpha} : \boldsymbol{\alpha} - \frac{2}{3} R^2 \right) - (\boldsymbol{\tau} : \boldsymbol{\alpha}) \right] \boldsymbol{\delta}$$

Then, alternatively, the normal to the yield surface can be computed as follows:

$$\boldsymbol{Q} = \frac{\partial f}{\partial \boldsymbol{\sigma}} = \frac{\boldsymbol{SU}}{\sqrt{\boldsymbol{SU}:\boldsymbol{SU}}} \qquad \textbf{4.29}$$

4.1.3 Volumetric behaviour

The flow rule plays a fundamental role in computing the plastic strain increment. A non-associated flow rule is necessary to represent the non-coaxial deformation characteristics of sand behaviour. Hence, the plastic potential function, Ψ is taken as different than the yield function.

Pressure-dependent

$$\Psi(\boldsymbol{\tau}, \boldsymbol{\alpha}, \beta) = \sqrt{(\boldsymbol{\tau} - \acute{p}\boldsymbol{\alpha}):(\boldsymbol{\tau} - \acute{p}\boldsymbol{\alpha})} + \beta\acute{p} + c \qquad \textbf{4.30}$$

where β is the plastic dilatancy, and it is the ratio between the magnitudes of plastic volumetric strain increment and plastic deviatoric increment (plastic multiplier, λ) as follows. The parameter c is a free constant that ensures the plastic potential surface crosses the yield surface at the input deviatoric stress state, $\boldsymbol{\tau}$ (Andrade et al., 2011; Boulanger & Ziotopoulou, 2022).

$$P" = \frac{\dot{\varepsilon}^{p}_{vol}}{|\dot{\boldsymbol{e}}^{\boldsymbol{p}}|} = 3\beta \qquad \textbf{4.31}$$

The outwards unit normal tensor to the plastic potential surface is denoted by the letter $\boldsymbol{P}$.

$$\boldsymbol{P} = \boldsymbol{P}' + P"\boldsymbol{\delta} \qquad \boldsymbol{P}' = \boldsymbol{Q}' \qquad \textbf{4.32}$$

where $\boldsymbol{P}$ is the derivative of the plastic potential function with respect to the stress tensor, $\boldsymbol{P}'$, and $P"$ are the deviatoric and volumetric parts of the derivative. Due to the shape of the selected plastic potential surface (i.e., no Lode angle dependency), after the derivation, the deviatoric part, $\boldsymbol{P}'$ is equal to the deviatoric part of the normal to the yield surface, $\boldsymbol{Q}'$ yielding an associated plastic flow but non-associated volumetric component (Boulanger & Ziotopoulou, 2022).

Pressure-dependent

$$\boldsymbol{P} = \frac{\partial \Psi}{\partial \sigma} = \frac{(\boldsymbol{\tau} - \acute{p}\boldsymbol{\alpha})}{\sqrt{(\boldsymbol{\tau} - \acute{p}\boldsymbol{\alpha}):(\boldsymbol{\tau} - \acute{p}\boldsymbol{\alpha})}} + 3\beta\boldsymbol{\delta} \qquad \textbf{4.33}$$

The fabric effects are considered with a scalar approach.

$$\beta(\boldsymbol{\sigma}) = \begin{cases} \left(1 - \Lambda\frac{\eta}{\eta_{PT}}\right)(c_1 + c_2\varepsilon_c)\left(\frac{\acute{p}}{p_{atm}}\right)^{c_3} & ,\eta < \eta_{PT} \\ \left(1 - \frac{\eta}{\eta_{PT}}\right)d_1(\gamma_d)^{d_2}\left(\frac{\acute{p}}{p_{atm}}\right)^{d_3} & ,\eta > \eta_{PT} \\ 0 & ,\eta = \eta_{PT} \end{cases} \quad \textbf{4.34}$$

$$\eta = \frac{\sqrt{3/2\,(\boldsymbol{\tau}:\boldsymbol{\tau})}}{\acute{p}} \quad \textbf{4.35}$$

where η is the scalar stress ratio.

In Yang & Elgamal (2008) $\boldsymbol{n}$ is defined as unit normal to an imaginary surface passing by the stress point $\boldsymbol{S}$ which is without backstress. The contraction term defines the angle of the stress ratio increment. Interested readers are referred to the **Error! Reference source not found.**, for more information on the definition and computation of the angle term. In the new version, the effect of confinement on the pore pressure build-up is considered with the new parameter $\boldsymbol{c_3}$.

Remark IV. On the handling of numerical issues in computing the pore-pressure build-up mechanism within the contraction phase. Details of the implementation done by the authors of PDMY02.

One of the improvements introduced in the second version (PDMY02) of the model concerns the pore-pressure build-up mechanism during the contractive response. In the first version of the constitutive law, the pore-pressure accumulation during small loading cycles was modelled by introducing a signum function that multiplies the volumetric part (Yang et al., 2003). In case of loading-unloading-reloading cycles within the phase transformation (PT) surface, the signum function ensures continuous calculation of positive contraction increments which leads to the build-up of pore-pressures. Authors discovered that the signum function was causing numerical instabilities due to its discontinuous nature. Hence, in the second version this problem was solved by introducing the dot-product, $\boldsymbol{\Lambda}$ shown in Equation 4.36 instead of the signum function (Yang & Elgamal, 2008).

$$\Lambda = \frac{\boldsymbol{n}:\boldsymbol{S}}{\|\dot{\boldsymbol{S}}\|} \cong sign(\dot{\boldsymbol{\eta}}) \quad \textbf{4.36}$$

The introduced implementation would solve the discontinuity issue that stems from the signum function. However, if the magnitude of the rate of stress ratio is small or zero, Equation 4.36 might result in significantly large or numerically infinite products which

may lead to other computational or precision issues. During analysis, the rate of stress might become smaller as the response approaches to the critical state. Hence, in the OpenSees source code of PDMY02 material, the direction was implemented differently than in Equation 4.36 to get ahead of any possible issue (Equations 4.37 - 4.39).

First a direction vector is obtained subtracting the corrected stress ratio from the trial stress. Since the trial stress directly relates to the strain increment, it is not affected from material internal response such as the critical state. After normalization, the result is a unit tensor $\boldsymbol{v}$ pointing outward or inward at the stress point $\boldsymbol{S}$ (Equation 4.38). The stress point $\boldsymbol{S}$ is the output of the closest-point projection process which involves relaxing the trial stress along the shortest path to the yield surface until it satisfies the yield function. For a surface with convex geometry, the shortest path to the surface from the trial stress point $\boldsymbol{S^{tr}}$ coincides with the normal $\boldsymbol{n}$ to the surface computed at the point $\boldsymbol{S}$ (Simo & Hughes, 1998). Hence, the definition of $\boldsymbol{v}$ leads to the condition that unit tensors $\boldsymbol{v}$ and $\boldsymbol{n}$ must be parallel. The orientation of $\boldsymbol{v}$ is along $\boldsymbol{n}$ in case the stress ratio is increasing or vice versa. To evaluate the modified direction expression $\boldsymbol{\Lambda}^*$ (Equation 4.37), the resulting tensor $\boldsymbol{v}$ is dotted with the normal $\boldsymbol{n}$ to the surface at $\boldsymbol{S}$. The result of the dot-product, $\boldsymbol{\Lambda}^*$ is limited to 1 or -1 depending on the orientation of $\boldsymbol{v}$. Hence, $\boldsymbol{\Lambda}^*$ behaves like the signum function (Z. Yang & Elgamal, 2008).

In a strain hardening material, the described procedure to track the direction of contractive increment would work fine as the orientation of $\boldsymbol{v}$ only depends on the strain increment direction. On the other hand, in a strain softening capable formulation, the tensor $\boldsymbol{v}$ would be allowed to have opposite sign also during loading case when the plastic modulus becomes negative, hence making the tracking procedure more challenging. However, strain softening is not considered in the PDMY02 formulation.

$$\Lambda^* = \frac{\boldsymbol{\tau}^{\boldsymbol{tr}(i)} : \boldsymbol{v}^*}{\sqrt{\boldsymbol{\tau}^{\boldsymbol{tr}(i)} : \boldsymbol{\tau}^{\boldsymbol{tr}(i)}}} \cong \frac{\boldsymbol{n} : \boldsymbol{S}}{\|\dot{\boldsymbol{S}}\|} \qquad \textbf{4.37}$$

$$\boldsymbol{v}^* = \frac{\dot{\boldsymbol{\eta}}^{\boldsymbol{p}}}{\sqrt{\dot{\boldsymbol{\eta}}^{\boldsymbol{p}} : \dot{\boldsymbol{\eta}}^{\boldsymbol{p}}}} \qquad \textbf{4.38}$$

$$\dot{\boldsymbol{\eta}}^{\boldsymbol{p}} = \frac{\boldsymbol{\tau}^{\boldsymbol{tr}(0)}}{\acute{p}^{tr(0)}} - \frac{\boldsymbol{\tau}^{\boldsymbol{tr}(i)}}{\acute{p}^{tr(i)}} \qquad \textbf{4.39}$$

In Equations 4.37 - 4.39, $\boldsymbol{\Lambda}^*$ and $\boldsymbol{v}^*$are the modified dot-product and direction vectors. The superscript of the trial total stress terms $\boldsymbol{\tau}^{\boldsymbol{tr}(0)}$ and $\acute{\boldsymbol{p}}^{\boldsymbol{tr}(0)}$ corresponds to the trial stress computed at the beginning of the Newton-Raphson iteration. Whereas $\boldsymbol{\tau}^{\boldsymbol{tr}(i)}$ and

$\acute{\boldsymbol{p}}^{\boldsymbol{tr}}{}_{(i)}$ are the corrected trial stress after the i-th material internal iteration such that when the material converges, these terms become the $(n+1)^{th}$ step stresses.

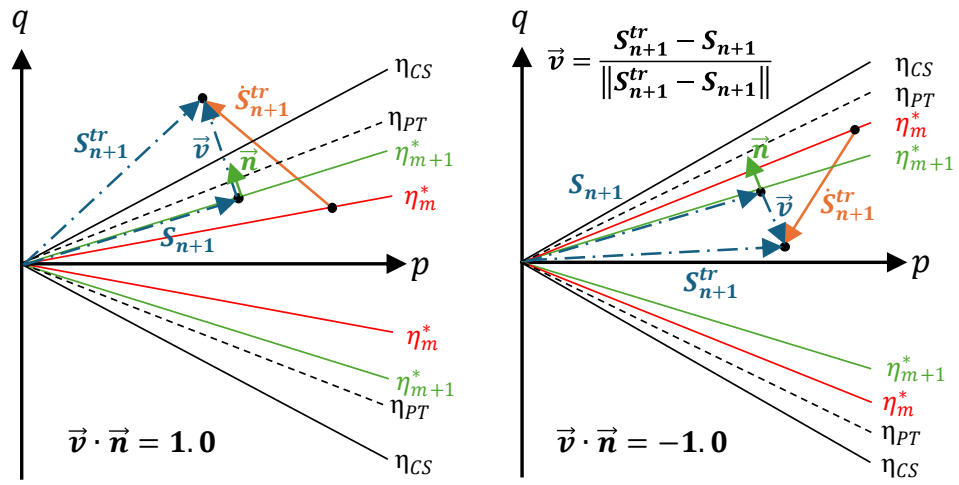

a) Loading or reloading case within the phase transformation surface. (i.e., $\eta^*_{m+1} > \eta^*_m$ or $\text{sign}(\dot{\eta}) > 0$)

b) Unloading case within the phase transformation surface. (i.e., $\eta^*_m > \eta^*_{m+1}$ or $\text{sign}(\dot{\eta}) < 0$)

Figure 4.1. Pore-pressure build-up mechanism inside the PT surface. Illustrations of the normal n to the imaginary surface satisfying the stress point S, and the negative stress correction vector v resulting from the closest-point-projection process. Axes q and p correspond to the deviatoric stress and pressure, respectively.

4.1.4 Kinematic hardening rule

The PDMY02 and PIMY models employs a kinematic hardening law to capture the hysteretic cyclic behaviour of soils under undrained shear loading. In this approach, all yield surfaces can translate in the deviatoric stress space without changing size, meaning there is no isotropic hardening involved. The translation of the current active yield surface is governed by a multi-surface plasticity framework, ensuring no overlap between consecutive yield surfaces (Elgamal et al., 2003; Mróz, 1967; Prevost, 1989).

PDMY02 model differs from the multi-yield-surface (MYS) plasticity proposed by Prevost (1989). The PDMY02 relies on an implicit scheme to compute the direction and the magnitude of translation. The surface update procedure of the model is described by Gu et al. (2009). Similar to traditional MYS plasticity, the translation direction is determined

based on Mroz's conjugate-points concept, ensuring the yield surfaces move towards the current stress point without overlapping. However, the movements of the active surface are defined in terms of a set of quadratic equations. Once the active yield surface is updated, the inner yield surfaces are also adjusted accordingly. The implicit solution implemented by Elgamal et al. (2003) significantly reduces the computational cost associated with the previously explicit update scheme used by Prevost (1989).

4.1.5 Critical state line

The critical state of a solid is defined as a state of continuous deformation under shear with no volume change. It is often associated with the failure of sands characterizing the final stress-strain and volumetric response following the contractive-hardening (loose sand) or dilative-softening (dense-sand) behaviour. Over the years, CSSM has been shown to be a powerful tool model sand behaviour by many authors (Borja & Andrade, 2006; Boulanger & Ziotopoulou, 2022; Cubrinovski & Ishihara, 1998a; Manzari & Dafalias, 1997; Nie et al., 2021; Potts & Zdravkovic, 1999; Wood & Belkheir, 1994), and many studies reported critical-state conforming observation in their experimental campaigns (Roscoe, 1970; Schofield & Wroth, 1968). The critical state is defined as the state of which the deviatoric shear q, effective mean pressure p', and void ratio, e states of the material reach the critical state values, q_c, p_c, and e_c simultaneously (Wood, 1991). In the $q - p' - e$ space, the locus of critical state values is defined by a three-dimensional line termed the critical state line (CSL). The CSL projects as a straight line on the $q - p'$ plane, and defined quantitatively by the critical state stress ratio $\eta_{cs} = q_c/p_c$ (Dafalias & Manzari, 2004).

4.1.6 Elastoplastic tangent stiffness

Elastoplastic tangent formulation to the pressure-dependent multi-yield surface model was proposed by various authors including (W.-F. Chen & Mizuno, 1990; Prevost, 1989; Simo & Hughes, 1998). Often the elastoplastic tangent is described over the Lamé parameters. In the present formulation a description using the shear, G, bulk, K and plastic H', moduli would be more relevant. Even though the analytical relationship between elastic coefficients is well-established, the definition of the elastoplastic tangent that is compatible with the specific formulation of PDMY02 may not be straightforward.

It is worth mentioning that, in FE, a consistent tangent definition is shown to be superior to elastoplastic tangent since it wiled a quadratic rate of convergence in the global Newton-Raphson solution (Simo & Taylor, 1985). Hence, Gu et al., (2011) formulates a consistent tangent for the pressure-independent case by differentiation of all material equations relating the stress increment to the strain increment. The consistent tangent for the pressure-independent case is lacking in the literature. However, the derivative of the flow rule required for the definition of a consistent tangent is worked out in Section 4.2.2.2 of this thesis. The full definition of a pressure-dependent consistent tangent is left out of

scope since it is not utilized by the PDMY02 material, perhaps since it is computationally costly to compute at each step considering the simplicity of the material compared to other available liquefaction models in the literature (Boulanger & Ziotopoulou, 2022; Cubrinovski & Ishihara, 1998a; Dafalias & Manzari, 2004).

The elastoplastic tangent associated with the pressure-independent multi-yield-surface (PIMY) material is discussed in detail in Gu et al., (2011). However, the tangent for the pressure-dependent case is considerably different than that of the pressure-dependent case, since it involves dependence on two invariants, and should be asymmetric due to non-associated flow. Furthermore, the elastic coefficients are updated based on the current mean effective pressure, resulting in hyper elasticity. The elastic coefficients are updated depending on the current pressure as shown in Equations 4.40 to 4.42.

$$G = \varsigma \cdot G_{ref} \qquad \textbf{4.40}$$

$$K = \varsigma \cdot K_{ref} \qquad \textbf{4.41}$$

$$H' = \varsigma \cdot H'^{(m)} \qquad \textbf{4.42}$$

ς is the modulus factor in Equation 4.14. H' denoted with the superscript m is the plastic modulus associated with the current yield surface. By interpretating the OpenSees code of PDMY02 from the perspective of Chen & Mizuno, (1990), as in page 245 of their textbook, the elastoplastic tangent, $\mathbb{H}$ for the pressure-dependent model writes as follows.

$$\mathbb{H} = \mathbb{E} - C_2(\boldsymbol{Q}'\otimes\boldsymbol{Q}') - C_1(\boldsymbol{I}\otimes\boldsymbol{I}) - C_3(\boldsymbol{Q}'\otimes\boldsymbol{I}) - C_4(\boldsymbol{I}\otimes\boldsymbol{Q}') \qquad \textbf{4.43}$$

The term starting with C_2 contributes to the deviatoric response, whereas the term with C_1 contributes to the volumetric stiffness. $\boldsymbol{Q}'$ is the deviatoric part of the outwards unit normal tensor to the yield surface in Equation 4.23. The terms with coefficients C_3 and C_4 lead to asymmetricity in the tensor, due to the non-associative feature of the flow. It is worth remembering that, in two invariant multi-yield-surface formulation $\boldsymbol{Q}' = \boldsymbol{P}'$. Hence, $\boldsymbol{P}'$ terms already appear in the latter (asymmetric) part of the Equation 4.43 and the contraction operation within H_0, shown in Equation 4.48.

$$C_1 = \frac{9KQ^{"}P^{"}}{(H_0 + H')} \qquad \textbf{4.44} \qquad C_2 = \frac{4G^2}{(H_0 + H')} \qquad \textbf{4.45}$$

$$C_3 = \frac{6GQ^{"}}{(H_0 + H')} \qquad \textbf{4.46} \qquad C_4 = \frac{6GP^{"}}{(H_0 + H')} \qquad \textbf{4.47}$$

$$H_0 = 9KQ^{"}P^{"} + 2G(\boldsymbol{Q}':\boldsymbol{Q}') \qquad \textbf{4.48}$$

Terms $Q^{"}$ and $P^{"}$ are the volumetric part of the normal to the yield surface (Equation 4.23) and the plastic potential (Equation 4.34), respectively.

4.2 LINEARIZATION OF THE FLOW RULE

During the explicit extrapolation stage the strain increment linearly depends on the stress increment. This is achieved by linearizing the flow rule and computing the step stress increment based on the linearized material equations. Moreover, the linearization of the material equations leads to the material tangent being constant over a given step. The most fundamental consequence of using a step-constant consistent tangent is achieving global convergence in a single step which, in highly nonlinear problems, reduces the computational cost. It is worth noting that the pressure-independent material formulation is often used as a relatively simple model of undrained fine-grained soil behaviour and omit highly nonlinear components such as the dilatative response and others. Hence, this material family is not expected to suffer from convergence issues whereas the pressure-dependent model may lead to more challenging numerical solutions especially when the pore-pressure d.o.f. is considered in the analysis. However, the impl-ex formulation may still be beneficial since pressure-independent materials are often used in conjunction with other highly nonlinear models such as pressure-dependent or damage models in soil-structure interaction models to model the undrained behaviour of fine-grained layers. In such cases, in which multiple material models are being employed in a large finite element model, having implicit-explicit mode of integration for all materials would lead to the global convergence in a single iteration. Otherwise, multiple global iterations are expected to satisfy the convergence criteria for the implicit models with no additional gain to impl-ex models since they are step constant.

The linearization of the flow rule can be achieved by following either rephrasing the flow equations to achieve linear dependence on the strain increment or replacing the nonlinear flow rule with its first order Taylor series approximation (Oliver et al., 2008). The Taylor series approximation leads to accurate but mathematically complex and costly operations following similar steps to computing a consistent tangent operator. On the other hand, the rephrased-flow approach is more simplified but consists of significantly cheaper expressions to evaluate at each gauss point. In this section, both formulations are given, however the rephrased-flow formulation is favoured over the full Taylor series expansion since the PIMY and PDMY02 (Yang et al., 2003) models in OpenSees are relatively simplified models compared to other models such as PM4Sand (Boulanger & Ziotopoulou, 2022), Manzari-Dafalias (Dafalias & Manzari, 2004) or Stress-Density (Cubrinovski & Ishihara, 1998a) models. PIMY and PDMY02 models does not include complex tensor calculations or a consistent tangent but rely on simple arithmetic calculations in multi-axial stress and strain space. Hence, the impl-ex solution achieved by Taylor series

approximation of all material equations leads to longer solution times than the implicit solution.

4.2.1 Rephrased-flow formulation

The linearization of the flow rule is obtained by rephrasing the original flow rule following the related guidelines of Oliver et al., (2008) with the aim of obtaining a constant derivative of the flow rule. The rephrased formulation is presented for the pressure-independent and pressure-dependent flavours of the multi-yield surface soil material family that is implemented in OpenSees by the research group at UC San Diego (Elgamal et al., 2003; Gu et al., 2011; Yang et al., 2003). To achieve linearization of the flow-rule several new state-variables are introduced. In an implicit-explicit integration context these variables will be explicitly extrapolated during the explicit stage and employed in the computation of a stepwise constant material tangent matrix. After convergence, the introduced state variables are corrected during the implicit stage. Further details regarding the integration are given in Section 4.3 below. In this section the derivation of the rephrased flow rule and the definition of new state variables are given.

4.2.1.1 *Pressure-independent formulation*

Let $\boldsymbol{m}(\boldsymbol{\sigma}_{n+1})$ be the derivative of the yield function $f(\boldsymbol{\sigma}_{n+1})$, such that:

$$\boldsymbol{Q}(\boldsymbol{\sigma}) = \frac{\partial f(\boldsymbol{\sigma})}{\partial \boldsymbol{\sigma}} = \frac{\boldsymbol{\tau}^* - \boldsymbol{\alpha}}{\|\boldsymbol{\tau}^* - \boldsymbol{\alpha}\|} = \frac{\boldsymbol{\tau}^* - \boldsymbol{\alpha}}{\sqrt{(\boldsymbol{\tau}^* - \boldsymbol{\alpha}) : (\boldsymbol{\tau}^* - \boldsymbol{\alpha})}} \qquad \textbf{4.49}$$

Let $\bar{\boldsymbol{\sigma}}_{n+1}$, and $\bar{\boldsymbol{Q}}$ be the rephrased stress tensor, and normal tensor to the yield surface, respectively. Then, we express the associated flow rule in the following rephrased form:

$$\bar{\boldsymbol{Q}}(\bar{\boldsymbol{\sigma}}) = \frac{1}{\chi}(\bar{\boldsymbol{\tau}}^* - \boldsymbol{\alpha}) \qquad \textbf{4.50}$$

χ is a scalar state variable introduced for the impl-ex integration, which is defined as:

$$\chi = \sqrt{(\boldsymbol{\tau}^* - \boldsymbol{\alpha}) : (\boldsymbol{\tau}^* - \boldsymbol{\alpha})} \qquad \textbf{4.51}$$

During material integration, χ is cumulated over the step. In the explicit stage, it is extrapolated whereas during the implicit stage it is computed through material equations. Then, the second derivative of the flow rule, $\bar{\mathbb{A}}$ becomes constant:

$$\bar{\mathbb{A}} = \frac{1}{\chi}\mathbb{I}^{dev} \qquad \textbf{4.52}$$

$$\mathbb{I}^{dev} = \mathbb{I} - \frac{1}{3}\boldsymbol{I}\otimes\boldsymbol{I} \tag{4.53}$$

$$\mathbb{I} = \frac{1}{2}\left(\boldsymbol{\delta_{ik}\delta_{jl}} + \boldsymbol{\delta_{il}\delta_{jk}}\right) \tag{4.54}$$

Finally, the consistent tangent becomes:

$$\mathbb{C} = \mathbb{E} - \frac{\Delta\bar{\lambda}\cdot\xi\cdot 2G}{\chi}(\bar{\mathbb{A}})$$

$$\mathbb{C} = 2G\left(1 - \frac{\Delta\bar{\lambda}\cdot\xi\cdot 2G}{\chi}\right)\mathbb{I}^{dev} + (K)\mathbb{I}^{vol} \tag{4.55}$$

4.2.1.2 *Pressure-dependent formulation*

Let $\boldsymbol{Q(\sigma_{n+1})}$ be the unit normal to the yield surface $\boldsymbol{f(\sigma_{n+1})}$, in Equation 4.28 such that:

$$\boldsymbol{Q}(\boldsymbol{\sigma}^*) = \frac{\partial f(\boldsymbol{\sigma}^*)}{\partial \boldsymbol{\sigma}} = \boldsymbol{Q'} = \frac{\boldsymbol{SU}^*}{\sqrt{\boldsymbol{SU}^*:\boldsymbol{SU}^*}} \tag{4.56}$$

$$\boldsymbol{SU}^* = 3(\boldsymbol{\tau}^* - \acute{p}^*\boldsymbol{\alpha}) + \acute{p}^*\left[\left(\boldsymbol{\alpha}:\boldsymbol{\alpha} - \frac{2}{3}R^2\right) - (\boldsymbol{\tau}^*:\boldsymbol{\alpha})\right]\boldsymbol{\delta} \tag{4.57}$$

where $\boldsymbol{\sigma}^*$and $\boldsymbol{\tau}^*$ are the contact stress tensor and contact stress computed according to Equation 4.24. The contact mean pressure $\acute{p}^* = \acute{p}$ since the contact stress only exists in the deviatoric stress plane and does not affect volumetric stress. Then, $\boldsymbol{P(\sigma_{n+1})}$ is the derivative of the plastic potential $\boldsymbol{\psi(\sigma_{n+1})}$, such that:

$$\boldsymbol{P}(\boldsymbol{\sigma}^*) = \frac{\partial \psi(\boldsymbol{\sigma}^*)}{\partial \boldsymbol{\sigma}} = \boldsymbol{Q'} + P"\boldsymbol{\delta} \tag{4.58}$$

$$\boldsymbol{P}(\boldsymbol{\sigma}^*) = \underbrace{\frac{\boldsymbol{SU}^*}{\sqrt{\boldsymbol{SU}^*:\boldsymbol{SU}^*}}}_{\boldsymbol{P'=Q'}} + 3\beta\boldsymbol{\delta} \tag{4.59}$$

where $\boldsymbol{\alpha}$ is the stress, stress deviator, and the back-stress tensors, respectively. β is the plastic dilatancy. Finally, $\boldsymbol{\delta}$ is the Kronecker delta. The plastic dilatancy controls the volumetric deformation, and it is a function stress tensor as follows:

$$\beta(\boldsymbol{\sigma}^*) = \begin{cases} \left(1 - \Lambda\frac{\eta^*}{\eta_{PT}}\right)(c_1 + c_2\varepsilon_c)\left(\frac{\acute{p}^*}{p_{atm}}\right)^{c_3} & ,\eta < \eta_{PT} \\ \left(1 - \frac{\eta^*}{\eta_{PT}}\right) d_1(\gamma_d)^{d_2}\left(\frac{\acute{p}^*}{p_{atm}}\right)^{d_3} & ,\eta > \eta_{PT} \\ 0 & ,\eta = \eta_{PT} \end{cases} \quad \textbf{4.34}$$

$$\eta^* = \frac{\sqrt{3/2\,(\boldsymbol{\tau}^* : \boldsymbol{\tau}^*)}}{\acute{p}^*} \quad \textbf{4.35}$$

where η is the scalar stress ratio and Λ is the modified dot product operation defined in **Error! Reference source not found.**. Note that $\boldsymbol{P}(\boldsymbol{\sigma}^*_{\boldsymbol{n+1}})$ is a nonlinear function of $\boldsymbol{\sigma_{n+1}}$, a nd hence, of $\boldsymbol{\varepsilon_{n+1}}$. To obtain a step linear material behaviour, the consistent tangent, which relates to the second derivative of the material equations, needs to be constant throughout the step. This is possible if the flow rule depends on the strain increment tensor linearly. $\boldsymbol{P}(\boldsymbol{\sigma}^*_{\boldsymbol{n+1}})$ can be linearized by rephrasing the flow equation to depend on the trial stress (Oliver et al., 2008). In hyperelastic materials such as PDMY02, trial stress does not relate linearly to the trial strain tensor due to the pressure dependent elastic moduli. However, the linearization can be achieved by stepwise freezing the modulus update factor, ς during the explicit extrapolation stage and then correcting it during the implicit correction stage (Tu et al., 2009). Hence, ς is considered as one of the impl-ex variables, as shown in Equation 4.35.

$$\bar{\varsigma}_{n+1} = \varsigma_n \quad \textbf{4.35}$$

Let $\overline{\boldsymbol{\sigma}}_{\boldsymbol{n+1}}$, and $\overline{\boldsymbol{P}}$ be the rephrased stress tensor, and flow rule, respectively. Then, the flow rule can be expressed as a linear function of the trial stress in the following form:

$$\overline{\boldsymbol{P}}(\overline{\boldsymbol{\sigma}}) = \frac{3(\xi\bar{\boldsymbol{\tau}}^{tr} - \acute{p}^{tr}\boldsymbol{\alpha}) + (\iota \cdot \acute{p}^{tr})\boldsymbol{I}}{\chi} + 3\kappa\acute{p}^{tr}\boldsymbol{\delta} \quad \textbf{4.60}$$

In Equation 4.60, it is worth noting that the volumetric and deviatoric split of the strain increment tensor is a linear operation which is defined in Equation 4.4. The currently introduced χ, ξ, ι and κ are scalar impl-ex state variables, which are defined as below:

Chi $$\chi = \sqrt{\boldsymbol{SU}^* : \boldsymbol{SU}^*} \quad \textbf{4.61}$$

Xi $$\xi = \frac{K^m}{M_s}(-\acute{p}) \quad \textbf{4.62}$$

Iota $$\iota = \left(\boldsymbol{\alpha} : \boldsymbol{\alpha} - \frac{2}{3}R^2\right) - (\boldsymbol{\tau}^* : \boldsymbol{\alpha}) \quad \textbf{4.63}$$

Kappa $$\kappa = \frac{\beta}{\acute{p}} \quad \textbf{4.64}$$

The impl-ex variable Xi, ξ converts the trial reduced stress deviator to contact reduced stress deviator, linearizing the process shown in Equation 4.24. During the implicit correction step, the χ, ι, and κ are cumulated over the step (see Section 4.3.2). In the explicit stage, the impl-ex variables are extrapolated whereas during the implicit stage they are computed through material equations (Oliver et al., 2008).

Then, the second derivative of the flow rule, $\bar{\mathbb{A}}$ becomes stepwise constant:

$$\bar{\mathbb{A}} = \frac{\partial \bar{\boldsymbol{P}}(\bar{\boldsymbol{\sigma}})}{\partial \varepsilon} = \frac{6G\varsigma\xi}{\chi}\mathbb{I}^{dev} - \frac{K\varsigma}{\chi}(\mathbb{I}^{vol}\cdot\bar{\boldsymbol{a}}) + \frac{K\varsigma}{3}\left(\frac{\iota}{\chi} + 3\kappa\right)\left(\mathbb{I}^{vol}\cdot\boldsymbol{\delta}\right) \quad \textbf{4.65}$$

$$\mathbb{I}^{dev} = \mathbb{I} - \frac{1}{3}\mathbb{I}^{vol} \quad \textbf{4.66}$$

$$\mathbb{I}^{vol} = \boldsymbol{\delta}\otimes\boldsymbol{\delta} \quad \textbf{4.67}$$

$$\mathbb{I} = \frac{1}{2}\left(\boldsymbol{\delta_{ik}\delta_{jl}} + \boldsymbol{\delta_{il}\delta_{jk}}\right) \quad \textbf{4.68}$$

Finally, the step-linear consistent tangent becomes:

$$\frac{\partial \boldsymbol{\sigma}}{\partial \boldsymbol{\varepsilon}} = \frac{\partial \boldsymbol{\tau}}{\partial \boldsymbol{\varepsilon}} + \frac{\partial(\acute{p}\boldsymbol{\delta})}{\partial \boldsymbol{\varepsilon}} \quad \textbf{4.69}$$

Following the chain rule the derivatives consisting of the volumetric component is expanded as follows:

1st step $$\frac{\partial\left(\sigma^{vol}\boldsymbol{\delta}\right)}{\partial \boldsymbol{\varepsilon}} = \frac{\partial \sigma^{vol}}{\partial \boldsymbol{\varepsilon}}\otimes\boldsymbol{\delta} + \sigma^{vol}\frac{\partial \boldsymbol{\delta}}{\partial \boldsymbol{\varepsilon}}\ where\ \frac{\partial \sigma^{vol}}{\partial \boldsymbol{\varepsilon}} = \frac{\partial {\sigma^{vol}}^{tr}}{\partial \boldsymbol{\varepsilon}} - \frac{\partial \dot{\sigma}^{{vol}^{p}}}{\partial \boldsymbol{\varepsilon}}$$

2nd step $$\frac{\partial {\sigma^{vol}}^{tr}}{\partial \boldsymbol{\varepsilon}} = \frac{1}{3}K\varsigma\boldsymbol{\delta}\ and\ \frac{\partial \boldsymbol{\delta}}{\partial \boldsymbol{\varepsilon}} = \mathbb{O}$$

3rd step $$\frac{\partial \dot{\sigma}^{{vol}^{p}}}{\partial \boldsymbol{\varepsilon}} = K\varsigma\frac{\partial \dot{\varepsilon}^{{vol}^{p}}}{\partial \boldsymbol{\varepsilon}} \rightarrow \frac{\partial \dot{\varepsilon}^{{vol}^{p}}}{\partial \boldsymbol{\varepsilon}} = 3\Delta\lambda\kappa\frac{\partial {\sigma^{vol}}^{tr}}{\partial \boldsymbol{\varepsilon}}$$

Finally, $$\mathbb{C}^{vol} = \frac{1}{3}K\varsigma(1 - 3\Delta\lambda\kappa K\varsigma)(\boldsymbol{\delta}\otimes\boldsymbol{\delta}) \quad \textbf{4.70}$$

$$where\ (\boldsymbol{\delta}\otimes\boldsymbol{\delta}) = \mathbb{I}^{vol}$$

Similarly, the deviatoric component is expanded using the chain rule as follows:

1st step $\dfrac{\partial \boldsymbol{\tau}}{\partial \boldsymbol{\varepsilon}} = \dfrac{\partial \boldsymbol{\tau}}{\partial \boldsymbol{e}} : \dfrac{\partial \boldsymbol{e}}{\partial \boldsymbol{\varepsilon}} = \dfrac{\partial \boldsymbol{\tau}}{\partial \boldsymbol{e}} : \mathbb{I}^{dev} \; where \; \dfrac{\partial \boldsymbol{e}}{\partial \boldsymbol{\varepsilon}} = \mathbb{I}^{dev}$

2nd step $\dfrac{\partial \boldsymbol{\tau}}{\partial \boldsymbol{e}} = \dfrac{\partial \boldsymbol{\tau}^{tr}}{\partial \boldsymbol{e}} - \dfrac{\partial \dot{\boldsymbol{\tau}}^{p}}{\partial \boldsymbol{e}} \; where \; \dfrac{\partial \boldsymbol{\tau}^{tr}}{\partial \boldsymbol{e}} = 2G\varsigma\mathbb{I}$

3rd step $\dfrac{\partial \dot{\boldsymbol{\tau}}^{p}}{\partial \boldsymbol{e}} = 2G\varsigma \dfrac{\partial \dot{\boldsymbol{e}}^{p}}{\partial \boldsymbol{e}} \rightarrow \dfrac{\partial \dot{\boldsymbol{e}}^{p}}{\partial \boldsymbol{e}} = \dfrac{\Delta\bar{\lambda}}{\chi}\left(3\dfrac{\partial(\boldsymbol{\tau}^{*} - \acute{p}^{tr}\overline{\boldsymbol{a}})}{\partial \boldsymbol{e}} + \iota \cdot \dfrac{\partial(\acute{p}^{tr}\boldsymbol{\delta})}{\partial \boldsymbol{e}}\right)$

4th step $\dfrac{\partial(\acute{p}^{tr}\boldsymbol{\delta})}{\partial \boldsymbol{e}} = \dfrac{\partial \acute{p}^{tr}}{\partial \boldsymbol{e}} \otimes \boldsymbol{\delta} + \acute{p}^{tr}\dfrac{\partial \boldsymbol{\delta}}{\partial \boldsymbol{e}} \; where \; \dfrac{\partial \boldsymbol{\delta}}{\partial \boldsymbol{e}} = \mathbb{O}$

5th step $\dfrac{\partial \acute{p}^{tr}}{\partial \boldsymbol{e}} = \dfrac{\partial \acute{p}^{tr}}{\partial \boldsymbol{\varepsilon}} : \dfrac{\partial \boldsymbol{\varepsilon}}{\partial \boldsymbol{e}} = \left(\dfrac{1}{3}K\varsigma\boldsymbol{\delta}\right) : \mathbb{I} \; where \; \dfrac{\partial \boldsymbol{\varepsilon}}{\partial \boldsymbol{e}} = \mathbb{I}$

6th step $\dfrac{\partial(\acute{p}^{tr}\overline{\boldsymbol{a}})}{\partial \boldsymbol{e}} = \dfrac{\partial \acute{p}^{tr}}{\partial \boldsymbol{e}} \otimes \boldsymbol{\alpha} + \acute{p}^{tr}\dfrac{\partial \overline{\boldsymbol{a}}}{\partial \boldsymbol{e}} \; where \; \dfrac{\partial \overline{\boldsymbol{a}}}{\partial \boldsymbol{e}} = \mathbb{O}$

7th step $\dfrac{\partial \boldsymbol{\tau}^{*}}{\partial \boldsymbol{e}} = \xi\dfrac{\partial \boldsymbol{\zeta}^{tr}}{\partial \boldsymbol{e}} + \dfrac{\partial(\acute{p}^{tr}\overline{\boldsymbol{a}}^{m})}{\partial \boldsymbol{e}}$

8th step $\dfrac{\partial \boldsymbol{\zeta}^{tr}}{\partial \boldsymbol{e}} = \dfrac{\partial \boldsymbol{\tau}^{tr}}{\partial \boldsymbol{e}} - \dfrac{\partial(\acute{p}^{tr}\overline{\boldsymbol{a}}^{m})}{\partial \boldsymbol{e}}$

9th step $\mathbb{C}^{dev} = \left(2G\varsigma\mathbb{I} - 2G\varsigma\dfrac{\Delta\bar{\lambda}}{\chi}\left(3\left(\xi\left(2G\varsigma\mathbb{I} - \left(\dfrac{K\varsigma}{3}\boldsymbol{\delta}\right) : \mathbb{I}\otimes\overline{\boldsymbol{a}}\right)\right.\right.\right.$

$\left.\left.\left. + \left(\dfrac{K\varsigma}{3}\boldsymbol{\delta}\right) : \mathbb{I}\otimes\overline{\boldsymbol{a}}\right) + \left(\dfrac{\iota \cdot K\varsigma}{3}\boldsymbol{\delta}\right) : \mathbb{I}\otimes\boldsymbol{\delta}\right)\right) : \mathbb{I}^{dev}$

10th step $\mathbb{C}^{dev} = 2G\varsigma\left(\mathbb{I} - \dfrac{6\Delta\bar{\lambda}\xi G\varsigma}{\chi}\mathbb{I} - \dfrac{\Delta\bar{\lambda}\xi K\varsigma}{\chi}(\boldsymbol{\delta} : \mathbb{I}\otimes\overline{\boldsymbol{a}}) + \dfrac{\Delta\bar{\lambda}K\varsigma}{\chi}(\boldsymbol{\delta} : \mathbb{I}\otimes\overline{\boldsymbol{a}})\right.$

$\left. + \dfrac{\iota \cdot \Delta\bar{\lambda}K\varsigma}{3\chi}(\boldsymbol{\delta} : \mathbb{I}\otimes\boldsymbol{\delta})\right) : \mathbb{I}^{dev}$

$where \; the \; terms \; including \; (\boldsymbol{\delta} : \mathbb{I}\otimes\boldsymbol{\delta}) : \mathbb{I}^{dev} = \mathbb{I}^{vol} : \mathbb{I}^{dev} = \mathbb{O}$

Finally, $\mathbb{C}^{dev} = 2G\varsigma\left(\mathbb{I} - \dfrac{6\Delta\bar{\lambda}\xi G\varsigma}{\chi}\mathbb{I} + (1-\xi)\dfrac{\Delta\bar{\lambda}K\varsigma}{\chi}(\boldsymbol{\delta} : \mathbb{I}\otimes\overline{\boldsymbol{a}})\right) : \mathbb{I}^{dev}$ ***4.71***

$$\mathbb{C} = \overline{\mathbb{E}} - \Delta\bar{\lambda}(\overline{\mathbb{E}}:\overline{\mathbb{A}}) \tag{4.72}$$

$$\mathbb{C} = 2G\varsigma\left(1 - \frac{6\Delta\bar{\lambda}\xi G\varsigma}{\chi}\right)\mathbb{I}^{dev} + \frac{2G\varsigma(1-\xi)\Delta\bar{\lambda}K\varsigma}{\chi}(\boldsymbol{\delta}\otimes\overline{\boldsymbol{a}}):\mathbb{I}^{dev} + \frac{K\varsigma}{3}\left(1 - 3\Delta\bar{\lambda}\kappa K\varsigma\right)\mathbb{I}^{vol} \tag{4.73}$$

Here, ξ, ς, $\Delta\bar{\lambda}$, χ, κ, and $\overline{\boldsymbol{a}}$ are impl-ex state variables and they need to be extrapolated at the beginning of the step. $\overline{\mathbb{E}}$ is the step constant elastic coefficient tensor. As a mathematical verification, Equation 4.73 can be obtained through two alternative methods which are the direct method given in Equations 4.65 and 4.72, or by step-by-step derivation of the linearized material equations using the chain rule outlined through Equations 4.69 to 4.71. It is worth noting that, unlike the pressure-independent case, the pressure-dependent $\mathbb{C}$ becomes asymmetric (with minor symmetries) because of the term $\boldsymbol{\delta}\otimes\overline{\boldsymbol{a}}$. Hence, the Voigt representation of tensor $\mathbb{C}$ is asymmetric when $\overline{\boldsymbol{a}}$ is different than $\mathbf{0}$.

4.2.2 Linearized-flow formulation

As an alternative to the rephrased flow formulation, in this section, the linearization of the flow rule is obtained by writing the Taylor series expansion of the original flow rule and truncating the higher-order terms. As shown in Oliver et al., (2008), a step-constant derivative of the flow rule is evaluated by taking the derivative of the linearized flow equation. As was done in the previous section, the linearized flow formulation is derived for the pressure-independent and pressure-dependent flavours of the multi-yield surface soil material family that is implemented in OpenSees by the research group at UC San Diego (Elgamal et al., 2003; Gu et al., 2011; Yang et al., 2003). Like the rephrased flow case introduction of new state-variables is necessary. In an implicit-explicit integration context these variables will be explicitly extrapolated during the explicit stage and employed in the computation of a stepwise constant material tangent matrix. After convergence, the introduced state variables are corrected during the implicit stage. Further details regarding the integration are given in Section 4.3 below. In this, section the derivation of the linearized flow rule and the definition of newly introduced state variables are given.

4.2.2.1 *Pressure-independent formulation*

In classical pressure independent plasticity, the flow rule is associated with the yield function and computes as the partial derivative of the von Mises yield function with respect to the stress tensor. In addition, kinematic hardening requires inclusion of the backstress tensor to describe the translation of each yield surface in the pi-plane, hence leads to the following flow rule. Let $\boldsymbol{Q}(\boldsymbol{\sigma})$ be the derivative of the yield function $f(\boldsymbol{\sigma})$, such that:

$$\boldsymbol{Q}(\boldsymbol{\sigma}) = \frac{\partial f(\boldsymbol{\sigma})}{\partial \boldsymbol{\sigma}} = \frac{\boldsymbol{\tau} - \boldsymbol{\alpha}}{\|\boldsymbol{\tau} - \boldsymbol{\alpha}\|} = \frac{\boldsymbol{\tau} - \boldsymbol{\alpha}}{\sqrt{(\boldsymbol{\tau} - \boldsymbol{\alpha}) : (\boldsymbol{\tau} - \boldsymbol{\alpha})}} \qquad \textbf{4.74}$$

where $\boldsymbol{\sigma}$, $\boldsymbol{\tau}$, and $\boldsymbol{\alpha}$ are the stress, stress deviator, and the back-stress tensors, respectively. Note that $\boldsymbol{Q}(\boldsymbol{\sigma})$ is a nonlinear function of $\boldsymbol{\sigma}$, and hence, of $\boldsymbol{\varepsilon}$. To obtain a step linear material behaviour, the consistent tangent, which relates to the second derivative of the material equations, needs to be constant throughout the step. This is possible if the flow is rule depends on the stress tensor linearly. $\boldsymbol{Q}(\boldsymbol{\sigma_{n+1}})$ can be written linearly by rephrasing the flow equation as follows. Let $\widetilde{\boldsymbol{\sigma}}_{\boldsymbol{n+1}}$, and $\widetilde{\boldsymbol{Q}}$ be the linearised stress tensor, and flow rule, respectively. Alternatively, the flow can be linearized by Taylor series expansion:

$$\widetilde{\boldsymbol{Q}}(\widetilde{\boldsymbol{\sigma}}_{\boldsymbol{n+1}}) = \boldsymbol{Q}(\boldsymbol{\sigma_n}) + \mathbb{A}(\boldsymbol{\sigma_n}) : \Delta\widetilde{\boldsymbol{\sigma}}_{\boldsymbol{n+1}} + \mathfrak{O}(\Delta\boldsymbol{\sigma}_{\boldsymbol{n+1}})^{\boldsymbol{2}} \qquad \textbf{4.75}$$

Truncation of the second order terms denoted by $\mathfrak{O}(\Delta\boldsymbol{\sigma}_{\boldsymbol{n+1}})^{\boldsymbol{2}}$, yields the linearized flow equation. The linearized flow depends on the evaluation of the flow equation at the committed stress step, and a linearized extrapolation to the new stress state using the derivative of the flow equation at the committed step. During computation of the term $\Delta\widetilde{\boldsymbol{\sigma}}_{\boldsymbol{n+1}}$ in the explicit stage, extrapolated state variables are used. Then, the second derivative of the flow rule, $\mathbb{A}$ becomes constant as follows.

Following the quotient rule and the chain rule:

$$\mathbb{A}(\boldsymbol{\sigma}) = \frac{\partial \boldsymbol{Q}(\boldsymbol{\sigma})}{\partial \boldsymbol{\sigma}}$$

$$= \frac{\frac{\partial(\boldsymbol{\tau} - \boldsymbol{\alpha})}{\partial \boldsymbol{\sigma}} \cdot \sqrt{(\boldsymbol{\tau} - \boldsymbol{\alpha}) : (\boldsymbol{\tau} - \boldsymbol{\alpha})} - (\boldsymbol{\tau} - \boldsymbol{\alpha}) \cdot \frac{\partial\left(\sqrt{(\boldsymbol{\tau} - \boldsymbol{\alpha}) : (\boldsymbol{\tau} - \boldsymbol{\alpha})}\right)}{\partial \boldsymbol{\sigma}}}{\left(\sqrt{(\boldsymbol{\tau} - \boldsymbol{\alpha}) : (\boldsymbol{\tau} - \boldsymbol{\alpha})}\right)^2}$$

$$= \frac{\left(\mathbb{I}^{dev}\right) \cdot \sqrt{(\boldsymbol{\tau} - \boldsymbol{\alpha}) : (\boldsymbol{\tau} - \boldsymbol{\alpha})} - \frac{(\boldsymbol{\tau} - \boldsymbol{\alpha}) \otimes (\boldsymbol{\tau} - \boldsymbol{\alpha})}{\sqrt{[(\boldsymbol{\tau} - \boldsymbol{\alpha}) : (\boldsymbol{\tau} - \boldsymbol{\alpha})]}} : \left(\mathbb{I}^{dev}\right)}{(\boldsymbol{\tau} - \boldsymbol{\alpha}) : (\boldsymbol{\tau} - \boldsymbol{\alpha})}$$

$$\mathbb{A}(\boldsymbol{\sigma}) = \frac{\mathbb{I}^{dev}}{\sqrt{(\boldsymbol{\tau} - \boldsymbol{\alpha}) : (\boldsymbol{\tau_n} - \boldsymbol{\alpha})}} - \frac{(\boldsymbol{\tau} - \boldsymbol{\alpha}) \otimes (\boldsymbol{\tau} - \boldsymbol{\alpha})}{\sqrt{[(\boldsymbol{\tau} - \boldsymbol{\alpha}) : (\boldsymbol{\tau} - \boldsymbol{\alpha})]^3}} : \left(\mathbb{I}^{dev}\right) \qquad \textbf{4.76}$$

As a result of the chain rule, the double dot operation involving $(\mathbb{I}^{dev})$ defines a contraction over two indices between two 4th order tensors (as in $D_{ijkl} = E_{ijmn}F_{mnkl}$). In compressed tensor notation the operation becomes a contraction over a common index between two second order tensors such as, $D^{ij} = E^{ik}F_k{}^j$. It is worth noting that to obtain the outcome tensor, the latter part of $\mathbb{A}(\boldsymbol{\sigma})$, as a stress-like tensor, a suitable mixed

definition of $\mathbb{I}^{dev}$ is necessary, since the tensor $(\boldsymbol{\tau}-\boldsymbol{\alpha})\otimes(\boldsymbol{\tau}-\boldsymbol{\alpha})$ is also a stress-like tensor (Helnwein, 2001).

4.2.2.2 *Pressure-dependent formulation*

Let $\boldsymbol{P}(\boldsymbol{\sigma_n})$ be the derivative of the plastic potential $\psi(\boldsymbol{\sigma_n})$, such that

$$\boldsymbol{P}(\boldsymbol{\sigma})=\frac{\partial\psi(\boldsymbol{\sigma})}{\partial\boldsymbol{\sigma}}=\frac{\boldsymbol{SU}^*}{\underbrace{\sqrt{\boldsymbol{SU}^*:\boldsymbol{SU}^*}}_{\boldsymbol{P'=Q'}}}+3\beta\boldsymbol{\delta} \qquad \textbf{4.77}$$

where $\boldsymbol{\sigma}$, $\boldsymbol{\tau}$, and $\boldsymbol{\alpha}$ are the stress, stress deviator, and the back-stress tensors, respectively.$\acute{p}$, and β are the mean pressure, and plastic dilatancy. Finally, $\boldsymbol{\delta}$ is the Kronecker delta. The plastic dilatancy controls volumetric deformation, and it is a function stress tensor as follows:

$$\beta(\boldsymbol{\sigma})=\begin{cases}\left(1-\Lambda\dfrac{\eta}{\eta_{PT}}\right)(c_1+c_2\varepsilon_c)\left(\dfrac{\acute{p}}{p_{atm}}\right)^{c_3} & ,\eta<\eta_{PT}\\ \left(1-\dfrac{\eta}{\eta_{PT}}\right)d_1(\gamma_d)^{d_2}\left(\dfrac{\acute{p}}{p_{atm}}\right)^{d_3} & ,\eta>\eta_{PT}\\ 0 & ,\eta=\eta_{PT}\end{cases} \qquad \textbf{4.34}$$

$$\eta=\frac{\sqrt{{}^3\!/_2\,(\boldsymbol{\tau}:\boldsymbol{\tau})}}{\acute{p}} \qquad \textbf{4.35}$$

where η is the scalar stress ratio and Λ is the modified dot product operation defined in **Error! Reference source not found.**. Note that $\boldsymbol{P}(\boldsymbol{\sigma})$ is a nonlinear function of $\boldsymbol{\sigma}$, and h ence, of $\boldsymbol{\varepsilon}$. To obtain a step linear material behaviour, the consistent tangent, which relates to the second derivative of the material equations, needs to be constant throughout the step. This is possible if the flow is rule depends on the stress tensor linearly. $\boldsymbol{P}(\boldsymbol{\sigma_{n+1}})$ can be written linearly by rephrasing the flow equation as follows. Let $\widetilde{\boldsymbol{\sigma}}_{\boldsymbol{n+1}}$, and $\widetilde{\boldsymbol{P}}$ be the linearised stress tensor, and flow rule, respectively. Alternatively, the flow can be linearized by Taylor series expansion:

$$\widetilde{\boldsymbol{P}}(\widetilde{\boldsymbol{\sigma}}_{\boldsymbol{n+1}})=\mathbf{P}(\boldsymbol{\sigma_n})+\mathbb{A}(\boldsymbol{\sigma_n}):\Delta\widetilde{\boldsymbol{\sigma}}_{\boldsymbol{n+1}}+\mathfrak{O}(\Delta\boldsymbol{\sigma_{n+1}})^{\mathbf{2}} \qquad \textbf{4.75}$$

Truncation of the second order terms denoted by $\mathfrak{O}(\Delta\boldsymbol{\sigma_{n+1}})^{\mathbf{2}}$, yields the linearized flow equation. The linearized flow depends on the evaluation of the flow equation at the committed stress step, and a linearized extrapolation to the new stress state using the derivative of the flow equation at the committed step. During computation of the term

$\Delta\tilde{\boldsymbol{\sigma}}_{\boldsymbol{n+1}}$ during the explicit stage, extrapolated state variables are used. Then, the second derivative of the flow rule, $\mathbb{A}$ becomes constant:

$$\mathbb{A}(\boldsymbol{\sigma_n}) = \frac{\partial \boldsymbol{P}(\boldsymbol{\sigma_n})}{\partial \boldsymbol{\sigma_n}} = \frac{\partial \boldsymbol{P'}(\boldsymbol{\sigma_n})}{\partial \boldsymbol{\sigma_n}} + \frac{\partial\left(3P^{"}(\boldsymbol{\sigma_n})\boldsymbol{\delta}\right)}{\partial \boldsymbol{\sigma_n}} \qquad \textbf{4.78}$$

The derivative of the deviatoric part computes as follows:

$$\frac{\partial \boldsymbol{P'}(\boldsymbol{\sigma})}{\partial \boldsymbol{\sigma}} = \frac{\frac{\partial(\boldsymbol{\tau}-\acute{p}\boldsymbol{\alpha})}{\partial \boldsymbol{\sigma}} \cdot \sqrt{(\boldsymbol{\tau}-\acute{p}\boldsymbol{\alpha}):(\boldsymbol{\tau}-\acute{p}\boldsymbol{\alpha})} - (\boldsymbol{\tau}-\acute{p}\boldsymbol{\alpha}) \cdot \frac{\partial\left(\sqrt{(\boldsymbol{\tau}-\acute{p}\boldsymbol{\alpha}):(\boldsymbol{\tau}-\acute{p}\boldsymbol{\alpha})}\right)}{\partial \boldsymbol{\sigma}}}{\left(\sqrt{(\boldsymbol{\tau}-\acute{p}\boldsymbol{\alpha}):(\boldsymbol{\tau}-\acute{p}\boldsymbol{\alpha})}\right)^2}$$

$$= \frac{\left(\mathbb{I}^{dev} - \frac{1}{3}\boldsymbol{I}\otimes\boldsymbol{\alpha}\right) \cdot \sqrt{(\boldsymbol{\tau}-\acute{p}\boldsymbol{\alpha}):(\boldsymbol{\tau}-\acute{p}\boldsymbol{\alpha})} - \frac{(\boldsymbol{\tau}-\acute{p}\boldsymbol{\alpha})\otimes(\boldsymbol{\tau}-\acute{p}\boldsymbol{\alpha})}{\sqrt{(\boldsymbol{\tau}-\acute{p}\boldsymbol{\alpha}):(\boldsymbol{\tau}-\acute{p}\boldsymbol{\alpha})}} : \left(\mathbb{I}^{dev} - \frac{1}{3}\boldsymbol{I}\otimes\boldsymbol{\alpha}\right)}{\left(\sqrt{(\boldsymbol{\tau}-\acute{p}\boldsymbol{\alpha}):(\boldsymbol{\tau}-\acute{p}\boldsymbol{\alpha})}\right)^2}$$

$$= \frac{\left(\mathbb{I}^{dev} - \frac{1}{3}\boldsymbol{I}\otimes\boldsymbol{\alpha}\right)}{\sqrt{(\boldsymbol{\tau}-\acute{p}\boldsymbol{\alpha}):(\boldsymbol{\tau}-\acute{p}\boldsymbol{\alpha})}} - \frac{(\boldsymbol{\tau}-\acute{p}\boldsymbol{\alpha})\otimes(\boldsymbol{\tau}-\acute{p}\boldsymbol{\alpha})}{\sqrt{[(\boldsymbol{\tau}-\acute{p}\boldsymbol{\alpha}):(\boldsymbol{\tau}-\acute{p}\boldsymbol{\alpha})]^3}} : \left(\mathbb{I}^{dev} - \frac{1}{3}\boldsymbol{I}\otimes\boldsymbol{\alpha}\right) \qquad \textbf{4.79}$$

As a result of the chain rule, the double dot operation in the latter term defines a contraction over two indices between two 4th order tensors (as in $C_{ijkl} = A_{ijmn}B_{mnkl}$). In compressed tensor notation the operation becomes a contraction over a common index between two second order tensors such as, $D^{ij} = E^{ik}F_k{}^j$. It is worth noting that to obtain the outcome tensor, the latter part of $\mathbb{A}(\boldsymbol{\sigma})$, as a stress-like tensor, a suitable mixed definitions of $\mathbb{I}^{dev}$ and $\boldsymbol{I}\otimes\boldsymbol{\alpha}$ are necessary, since the tensor $(\boldsymbol{\tau}-\acute{p}\boldsymbol{\alpha})\otimes(\boldsymbol{\tau}-\acute{p}\boldsymbol{\alpha})$ is also a stress-like tensor (Helnwein, 2001). Knowing that Kronecker delta evaluates to 2nd order identity tensor which acts as a constant multiplier over $P^{"}$, the derivative of the volumetric part computes as follows:

$$\frac{\partial\left(3P^{"}(\boldsymbol{\sigma_n})\boldsymbol{\delta}\right)}{\partial \boldsymbol{\sigma_n}} = 3 \cdot \left(\frac{\partial P^{"}(\boldsymbol{\sigma_n})}{\partial \boldsymbol{\sigma_n}} \otimes \boldsymbol{I}\right) \qquad \textbf{4.80}$$

In the derivative operator, variables η_{PT}, p_{atm}, c_1, c_2, c_3, d_1, d_2, d_3, ε_c, and γ_d are constants. Hence, the derivative of $P^{"}$ results in a 2nd order tensor and is a piece-wise function which reads as follows.

When $\boldsymbol{\eta < \eta_{PT}}$ **(contraction)**:

$$\frac{\partial P^{"}(\boldsymbol{\sigma})}{\partial \boldsymbol{\sigma}} = \left(\frac{c_1 + c_2\varepsilon_c}{\eta_{PT}(p_{atm})^{c_3}}\right)[(\eta_{PT} - \Lambda\eta\,)\acute{p}^{c_3}]. \textit{As per the multiplication rule:}$$

$$= \left(\frac{c_1 + c_2\varepsilon_c}{\eta_{PT}(p_{atm})^{c_3}}\right)\left[\frac{\partial(\eta_{PT} - \Lambda\eta\,)}{\partial \boldsymbol{\sigma}}\acute{p}^{c_3} + \left((\eta_{PT} - \Lambda\eta\,)\frac{c_3}{3}\acute{p}^{(c_3-1)}\right)\boldsymbol{\delta}\right]. \textit{Consider}$$

$$\frac{\partial(\eta_{PT} - \Lambda\eta\,)}{\partial \boldsymbol{\sigma}} = -\frac{\partial \Lambda}{\partial \boldsymbol{\sigma}}\eta - \Lambda\frac{\partial \eta}{\partial \boldsymbol{\sigma}}. \textit{Since } \Lambda \textit{ behaves like the sign function,}$$

$$\textit{the derivative of } \Lambda \rightarrow \frac{\partial \Lambda}{\partial \boldsymbol{\sigma}}$$

$$= 0\ (\textit{see}\ \text{Error! Reference source not found.}).\ \textit{Then,}\ \frac{\partial(\eta_{PT} - \Lambda\eta\,)}{\partial \boldsymbol{\sigma}} = -\Lambda\frac{\partial \eta}{\partial \boldsymbol{\sigma}}.$$

$$\therefore \frac{\partial P^{"}(\boldsymbol{\sigma})}{\partial \boldsymbol{\sigma}} = \left(\frac{c_1 + c_2\varepsilon_c}{\eta_{PT}(p_{atm})^{c_3}}\right)\left[\left((\eta_{PT} - \Lambda\eta\,)\frac{c_3}{3}\acute{p}^{(c_3-1)}\right)\boldsymbol{\delta} - (\acute{p}^{c_3}\Lambda)\frac{\partial \eta}{\partial \boldsymbol{\sigma}}\right] \qquad \textbf{4.81}$$

When $\boldsymbol{\eta > \eta_{PT}}$ (dilation):

$$\frac{\partial P^{"}(\boldsymbol{\sigma})}{\partial \boldsymbol{\sigma}} = \left(\frac{d_1(\gamma_d)^{d_2}}{\eta_{PT}(p_{atm})^{d_3}}\right)\frac{\partial[(\eta_{PT} - \eta\,)\acute{p}^{d_3}]}{\partial \boldsymbol{\sigma}}.\ \textit{As per the multiplication rule:}$$

$$\therefore \frac{\partial P^{"}(\boldsymbol{\sigma})}{\partial \boldsymbol{\sigma}} = \left(\frac{d_1(\gamma_d)^{d_2}}{\eta_{PT}(p_{atm})^{d_3}}\right)\left[\left((\eta_{PT} - \eta\,)\frac{d_3}{3}\acute{p}^{(d_3-1)}\right)\boldsymbol{\delta} - (\acute{p}^{d_3})\frac{\partial \eta}{\partial \boldsymbol{\sigma}}\right] \qquad \textbf{4.82}$$

The derivative of the stress ratio with respect to the stress tensor, $\partial\eta/\partial\boldsymbol{\sigma}$ is computed as follows. Then, the resulting 2nd order tensor can be used directly in the computation of the derivative of the volumetric behaviour in previous equations.

$$\textit{The quotient rule} \rightarrow \frac{\partial \eta}{\partial \boldsymbol{\sigma}} = \frac{\partial\left(\frac{\sqrt{3/2\,(\boldsymbol{\tau}:\boldsymbol{\tau})}}{\acute{p}}\right)}{\partial \boldsymbol{\sigma}} = \sqrt{\frac{3}{2}}\left(\frac{\acute{p}\cdot\frac{\partial\left(\sqrt{\boldsymbol{\tau}:\boldsymbol{\tau}}\right)}{\partial \boldsymbol{\sigma}} - \sqrt{\boldsymbol{\tau}:\boldsymbol{\tau}}\cdot\frac{\partial \acute{p}}{\partial \boldsymbol{\sigma}}}{\acute{p}^2}\right)$$

$$\therefore \frac{\partial \eta}{\partial \boldsymbol{\sigma}} = \sqrt{\frac{3}{2}}\left(\frac{\boldsymbol{\tau}}{\acute{p}\cdot\sqrt{\boldsymbol{\tau}:\boldsymbol{\tau}}}:\mathbb{I}^{dev} - \frac{\sqrt{\boldsymbol{\tau}:\boldsymbol{\tau}}}{3\acute{p}^2}\boldsymbol{\delta}\right) \qquad \textbf{4.83}$$

With Equation 4.83, the complete definition of the Equation 4.80, and hence the fourth order $\mathbb{A}(\boldsymbol{\sigma_n})$ tensor is available.

4.3 MIXED IMPLICIT-EXPLICIT RETURN MAPPING

Impl-ex integration technique can be used in the integration of a multi-axial elastoplastic material as initially proposed by Oliver et al., (2008).

In the explicit extrapolation stage, the impl-ex variables defined in Section 4.2 are extrapolated using the corrected values of these variables following an implicit iteration. During the implementation and testing of the material, several algorithms were trialled using different variables and extrapolation rules.

The first observation is that the linearized flow approach discussed in Section 4.2.2 leads to an increase in the computational cost that is required to evaluate an iteration compared to the implicit solution. This is expected since the implicit implementation of PDMY02 in OpenSees (Yang et al., 2003) is optimized for achieving fast solution and does not involve a consistent tangent computation or the computation of second derivatives. The model is implemented in a mathematically simpler manner than some of the more complex models such as Dafalias & Manzari, (2004). Therefore, the computation of the matrix equations that leads to the 4th order $\overline{\mathbb{A}}$ tensor required for the linearized flow formulation does not yield a significant reduction in the computational cost.

On the other hand, the rephrased flow formulation discussed in Section 4.2.1 is mathematically much simpler and more suitable for the existing implementation of PDMY02 material in OpenSees. Furthermore, the desired reduction of computational cost in the solution of a step (i.e., explicit extrapolation followed by an implicit correction) is observed to be significantly reduced (see Section 4.4).

4.3.1 Explicit extrapolation stage

In the explicit extrapolation stage, the impl-ex variables defined in Section 4.2 are extrapolated.

Step 1. Extrapolation of state variables

Considering the deviatoric response, it is observed that extrapolation of the elements in the backstress tensor, in addition to the impl-ex variable, χ, does not bring additional benefits and sometimes lead to unfavourable outcomes such as the yield surface drift effect discussed by Tu et al., (2009). Hence, in the current step, the elements of the backstress tensor are kept as the converged values.

Active surface $$\bar{m}_{n+1} = m_n \quad \textbf{4.84}$$

Modulus factor $$\bar{\varsigma}_{n+1} = \varsigma_n \quad \textbf{4.85}$$

Backstress $$\bar{\boldsymbol{\alpha}}_{n+1} = \boldsymbol{\alpha}_n \quad \textbf{4.86}$$

Lambda $$\Delta\bar{\lambda}_{n+1} = \Delta\lambda_n + \frac{\Delta t_{n+1}}{\Delta t_n}(\Delta\lambda_n - \Delta\lambda_{n-1}) \quad \textbf{4.87}$$

Chi $$\bar{\chi}_{n+1} = \chi_n + \frac{\Delta t_{n+1}}{\Delta t_n}(\chi_n - \chi_{n-1}) \quad \textbf{4.88}$$

Xi $$\bar{\xi}_{n+1} = \xi_n + \frac{\Delta t_{n+1}}{\Delta t_n}(\xi_n - \xi_{n-1}) \quad \textbf{4.89}$$

Iota $$\bar{\iota}_{n+1} = \iota_n + \frac{\Delta t_{n+1}}{\Delta t_n}(\iota_n - \iota_{n-1}) \quad \textbf{4.90}$$

Kappa $$\bar{\kappa}_{n+1} = \kappa_n + \frac{\Delta t_{n+1}}{\Delta t_n}(\kappa_n - \kappa_{n-1}) \quad \textbf{4.91}$$

The bar above a variable indicates that the variable is explicitly extrapolated whereas the bar sign is dropped after the variable is corrected by an implicit iteration. It is worth noting that the extrapolated modulus factor leads to $\bar{\mathbb{C}}^e_{n+1} = \mathbb{C}^e_n$, which is not a trivial step since the implicit elastic stiffness coefficients are a nonlinear function of mean pressure, $\acute{p}$.

Step 2. Trial stress

$$\boldsymbol{\sigma}^{tr}_{n+1} = \boldsymbol{\sigma}_n + \mathbb{E}:\dot{\boldsymbol{\varepsilon}}_{n+1} \quad \textbf{4.92}$$

$$\boldsymbol{\tau}^{tr}_{n+1} = \mathbb{I}^{dev}:\boldsymbol{\sigma}^{tr}_{n+1} \quad \textbf{4.93}$$

$$\sigma^{vol}{}^{tr}_{n+1} = \mathbb{I}^{vol}:\boldsymbol{\sigma}^{tr}_{n+1}:\boldsymbol{\delta} \quad \textbf{4.94}$$

$$\acute{p}^{tr}_{n+1} = \sigma^{vol}{}^{tr}_{n+1} - p_0 \quad \textbf{4.95}$$

$$\boldsymbol{\zeta}^{tr}_{n+1} = \boldsymbol{\tau}^{tr}_{n+1} - \acute{p}^{tr}_{n+1}\boldsymbol{\alpha}^m \quad \textbf{4.96}$$

p_0 is the residual pressure (1.0 kPa by default) for numerical stability purposes.

Step 3. Do stress correction

The volumetric component

Plastic strain increment $$\dot{\varepsilon}^{vol}{}^{p}_{n+1} = 3\Delta\bar{\lambda}_{n+1}\bar{\kappa}_{n+1}\sigma^{vol}{}^{tr}_{n+1} \quad \textbf{4.97}$$

Plastic stress increment $$\dot{\sigma}^{vol}{}^{p}_{n+1} = K\bar{\varsigma}_{n+1}\dot{\varepsilon}^{vol}{}^{p}_{n+1} \quad \textbf{4.98}$$

Current volumetric stress $$\sigma_{n+1}^{vol} = \sigma^{vol}{}_{n+1}^{tr} - \dot{\sigma}^{vol}{}_{n+1}^{p} \quad \textbf{4.99}$$

The deviatoric component

Contact stress $$\boldsymbol{\tau}_{n+1}^{*} = \langle \bar{\xi}_{n+1} \rangle \boldsymbol{\zeta}_{n+1}^{tr} + \acute{p}_{n+1}^{tr} \boldsymbol{\alpha}^{m} \quad \textbf{4.100}$$

Plastic strain increment $$\dot{\boldsymbol{e}}_{n+1}^{p} = \langle \frac{\Delta \bar{\lambda}_{n+1}}{\bar{\chi}_{n+1}} \rangle [3(\boldsymbol{\tau}_{n+1}^{*} - \acute{p}_{n+1}^{tr} \boldsymbol{\alpha}^{m}) + \acute{p}_{n+1}^{tr} \bar{\iota}_{n+1} \boldsymbol{\delta}] \quad \textbf{4.101}$$

Plastic stress increment $$\dot{\boldsymbol{\tau}}_{n+1}^{p} = 2G\bar{\varsigma}_{n+1} \dot{\boldsymbol{e}}_{n+1}^{p} \quad \textbf{4.102}$$

Current deviatoric stress $$\boldsymbol{\tau}_{n+1} = \boldsymbol{\tau}_{n+1}^{tr} - \dot{\boldsymbol{\tau}}_{n+1}^{p} \quad \textbf{4.103}$$

The combined stress tensor

$$\boldsymbol{\sigma}_{n+1} = \boldsymbol{\tau}_{n+1} + \sigma_{n+1}^{vol} \boldsymbol{\delta} \quad \textbf{4.104}$$

In Equation 4.101, the contact mean pressure $p_{n+1}^{*} = \acute{p}_{n+1}^{tr}$ since contact stress only operates in the deviatoric stress space. Moreover, the term $\langle \Delta \bar{\lambda}_{n+1} / \bar{\chi}_{n+1} \rangle$ in Equation 4.101 should be manually set to be zero if the denominator $\bar{\chi}_{n+1}$is zero, since Xi is related to the length of the normal to the yield surface and a zero length indicates zero stress which leads to no plasticity. Additionally, due to the Macaulay brackets the whole expression is always greater than or equal to 0. This condition gains importance as the explicit extrapolation might lead to negative impl-ex variables which are not physically viable which essentially indicates no plasticity.

It is worth noting that, through Equations 4.92 to 4.96, the trial stress linearly depends on the trial strain increment as usual. As a part of impl-ex explicit stage, the linear dependence on the trial strain increment is preserved during the volumetric stress computation through Equations 4.97 to 4.99 and deviatoric stress computation through Equations 4.100 to 4.103. The linear dependence is computationally advantageous since the global Newton or Newmark solution converges in a single iteration reducing the computational cost. Furthermore, the derivative of the stress increment with respect to strain increment ($\partial \boldsymbol{\sigma} / \partial \boldsymbol{\varepsilon} = \mathbb{C}$) becomes constant and positive definite throughout the analysis. However, the current stress still nonlinearly depends on the trial strain increment as in the classical material formulation, and it is computed nonlinearly during the implicit correction stage with a single iteration. Nevertheless, with increasing time step, the amount of error cannot be removed after a single iteration of implicit correction might build-up over many steps

and lead do deviations from the implicit solution. Hence, a time-step sensitivity analysis is advised for problems with strong material nonlinearities.

4.3.2 Implicit correction stage

The implicit correction stage initiates after the global convergence criteria are achieved using the extrapolated stress and consistent tangent. In OpenSees this can be implemented by, before committing the internal variables, calling an implicit calculation of internal variables from the last committed variables and committing the implicit versions. As a result, the extrapolated variables are disregarded after a single iteration of implicit integration.

Trial stress:

$$\boldsymbol{\sigma}_{\boldsymbol{n+1}}^{\boldsymbol{tr}\ (0)} = \boldsymbol{\sigma}_{\boldsymbol{n}} + \mathbb{E}\colon \dot{\boldsymbol{\varepsilon}}_{\boldsymbol{n+1}} \qquad \textbf{4.105}$$

$$\mathbb{E} = K\boldsymbol{I}\otimes\boldsymbol{I} + 2G\mathbb{I}^{dev} \qquad \textbf{4.106}$$

$$\mathbb{I}^{dev} = \mathbb{I} - \frac{1}{3}\boldsymbol{I}\otimes\boldsymbol{I} \qquad \textbf{4.107}$$

where $\mathbb{I}^{dev}$ and $\mathbb{I}$ are the fourth order stress-like deviatoric and symmetric operators, respectively.

Volumetric trial stress:

$$\boldsymbol{\sigma}_{\boldsymbol{n+1}}^{\boldsymbol{vol}\ \boldsymbol{tr}(i-1)} = \frac{1}{3}(\boldsymbol{I}\otimes\boldsymbol{I})\colon \boldsymbol{\sigma}_{\boldsymbol{n+1}}^{\boldsymbol{tr}\ (i-1)} \qquad \textbf{4.108}$$

Deviatoric trial stress:

$$\boldsymbol{\tau}_{\boldsymbol{n+1}}^{\boldsymbol{tr}\ (i-1)} = \mathbb{I}_{dev}\colon \boldsymbol{\sigma}_{\boldsymbol{n+1}}^{\boldsymbol{tr}\ (i-1)} \qquad \textbf{4.109}$$

$$\boldsymbol{\zeta}_{\boldsymbol{n+1}}^{\boldsymbol{tr}\ (m+i-1)} = \boldsymbol{\tau}_{\boldsymbol{n+1}}^{\boldsymbol{tr}\ (i-1)} - \bar{p}\boldsymbol{\alpha}^{(m+i-1)} \qquad \textbf{4.110}$$

where $\mathbb{I}_{dev}(\neq \mathbb{I}^{dev})$ is the fourth order mixed variant (operates on stress-like and leads to stress-like) deviatoric operator, and $\bar{p} = p - a$ takes mean pressure p into account after shifting attraction a where $a = c/\tan(\phi)$.

Contact stress in terms of shifted deviatoric stress:

$$\boldsymbol{\zeta}_{\boldsymbol{n+1}}^{*}{}^{(m+i)} = \frac{K^{(m+i-1)}}{K^{(i)}}\left(\boldsymbol{\zeta}_{\boldsymbol{n+1}}^{\boldsymbol{tr}}{}^{(m+i-1)}\right) \quad \textbf{4.111}$$

$$K^{(i)} = \sqrt{\frac{3}{2}\left(\boldsymbol{\zeta}_{\boldsymbol{n+1}}^{\boldsymbol{tr}}{}^{(m+i-1)}\right):\left(\boldsymbol{\zeta}_{\boldsymbol{n+1}}^{\boldsymbol{tr}}{}^{(m+i-1)}\right)} \quad \textbf{4.112}$$

where K^{m+i} represents the $\sqrt{3/2}$ times the radius of the yield surface m, and K^{i} is the length of the stress vector normal to the yield surface.

The normal to the plastic potential:

$$\boldsymbol{P}^{(m+i-1)} = \boldsymbol{P'}^{(m+i-1)} + P"^{(i-1)}\boldsymbol{\delta} \text{ and } \boldsymbol{P'} = \boldsymbol{Q'} \quad \textbf{4.113}$$

$$\boldsymbol{P'}^{(m+i-1)} = \frac{\boldsymbol{\zeta}_{\boldsymbol{n+1}}^{*}{}^{(m+i-1)}}{\sqrt{\left(\boldsymbol{\zeta}_{\boldsymbol{n+1}}^{*}{}^{(m+i-1)}\right):\left(\boldsymbol{\zeta}_{\boldsymbol{n+1}}^{*}{}^{(m+i-1)}\right)}} \quad \textbf{4.114}$$

$$P"^{(i-1)} = \frac{1}{3}\beta^{(i-1)} \quad \textbf{4.115}$$

Increment plastic multiplier (loading function), $\dot{\lambda}^{(i)}$ to the step plastic multiplier $\Delta\lambda_{n+1}$:

$$\dot{\lambda}^{(1)} = \frac{\boldsymbol{Q'}^{(m)}:\left(\boldsymbol{\tau}_{\boldsymbol{n+1}}^{\boldsymbol{tr}}{}^{(0)} - \boldsymbol{\tau}_{\boldsymbol{n+1}}^{*}{}^{(1)}\right)}{H'^{(m)} + 2G} \quad \textbf{4.116}$$

$$\dot{\lambda}^{(i)} = \frac{\boldsymbol{Q'}^{(m+i-1)}:\left(\boldsymbol{\tau}_{\boldsymbol{n+1}}^{\boldsymbol{tr}}{}^{(i-1)} - \boldsymbol{\tau}_{\boldsymbol{n+1}}^{*}{}^{(i)}\right)}{H'^{(m+i-1)} + 2G}\frac{\left(H'^{(m+i-2)} - H'^{(m+i-1)}\right)}{H'^{(m+i-2)}} \quad \textbf{4.117}$$

Update plastic strain:

$$\dot{\boldsymbol{e}}_{\boldsymbol{n+1}}^{\boldsymbol{p}}{}^{(i)} = \langle\dot{\lambda}^{(i)}\rangle\boldsymbol{P'}^{(m+i-1)} \quad \textbf{4.118}$$

$$\boldsymbol{e}_{\boldsymbol{n+1}}^{\boldsymbol{p}}{}^{(i)} = \boldsymbol{e}_{\boldsymbol{n+1}}^{\boldsymbol{p}}{}^{(i-1)} + \dot{\boldsymbol{e}}_{\boldsymbol{n+1}}^{\boldsymbol{p}}{}^{(i)} \; where \; \boldsymbol{e}_{\boldsymbol{n+1}}^{\boldsymbol{p}}{}^{(0)} = \boldsymbol{e}_{\boldsymbol{n}}^{\boldsymbol{p}} \quad \textbf{4.119}$$

$$\dot{\boldsymbol{\varepsilon}}_{\boldsymbol{n+1}}^{\boldsymbol{vol}\ \boldsymbol{p}(i)} = \langle\dot{\lambda}^{(i)}\rangle 3P"^{(i-1)}\boldsymbol{\delta} \quad \textbf{4.120}$$

$$\boldsymbol{\varepsilon}_{\boldsymbol{n+1}}^{\boldsymbol{vol}\ \boldsymbol{p}(i)} = \boldsymbol{\varepsilon}_{\boldsymbol{n+1}}^{\boldsymbol{vol}\ \boldsymbol{p}(i-1)} + \dot{\boldsymbol{\varepsilon}}_{\boldsymbol{n+1}}^{\boldsymbol{vol}\ \boldsymbol{p}(i)} \; where \; \boldsymbol{\varepsilon}_{\boldsymbol{n+1}}^{\boldsymbol{vol}\ \boldsymbol{p}(0)} = \boldsymbol{\varepsilon}_{\boldsymbol{n}}^{\boldsymbol{vol}\boldsymbol{p}} \quad \textbf{4.121}$$

$\langle\odot\rangle$ is the Macaulay bracket operator.

Update impl-ex internal variables:

$$\dot{\tilde{\lambda}}^{(i)} = \frac{\dot{\lambda}^{(i)}}{\sqrt{\left(\boldsymbol{\zeta}^{*}_{\boldsymbol{n+1}}{}^{(m+i-1)}\right):\left(\boldsymbol{\zeta}^{*}_{\boldsymbol{n+1}}{}^{(m+i-1)}\right)}} \qquad \textbf{4.122}$$

$$\tilde{\lambda}^{(i)}_{n+1} = \tilde{\lambda}^{(i-1)}_{n+1} + \langle \dot{\tilde{\lambda}}^{(i)} \rangle \; where \; \tilde{\lambda}^{(0)}_{n+1} = 0 \qquad \textbf{4.123}$$

$$\Delta\lambda^{(i)}_{n+1} = \Delta\lambda^{(i-1)}_{n+1} + \langle \dot{\lambda}^{(i)} \rangle \; where \; \Delta\lambda^{(0)}_{n+1} = 0 \qquad \textbf{4.124}$$

$$\beta^{(i)}_{n+1} = \beta^{(i-1)} \qquad \textbf{4.125}$$

Stress correction step:

$$\dot{\boldsymbol{\tau}}^{\boldsymbol{p}}_{\boldsymbol{n+1}}{}^{(i)} = 2G\dot{\boldsymbol{e}}^{\boldsymbol{p}}_{\boldsymbol{n+1}}{}^{(i)} \qquad \textbf{4.126}$$

$$\dot{\boldsymbol{\sigma}}^{\boldsymbol{vol}}_{\boldsymbol{n+1}}{}^{\boldsymbol{p}(i)} = K\dot{\boldsymbol{\varepsilon}}^{\boldsymbol{vol}}_{\boldsymbol{n+1}}{}^{\boldsymbol{p}(i)} \qquad \textbf{4.127}$$

$$\boldsymbol{\tau}^{\boldsymbol{tr}}_{\boldsymbol{n+1}}{}^{(i)} = \boldsymbol{\tau}^{\boldsymbol{tr}}_{\boldsymbol{n+1}}{}^{(i-1)} - \dot{\boldsymbol{\tau}}^{\boldsymbol{p}}_{\boldsymbol{n+1}}{}^{(i)} \qquad \textbf{4.128}$$

$$\boldsymbol{\sigma}^{\boldsymbol{vol}}_{\boldsymbol{n+1}}{}^{\boldsymbol{tr}(i)} = \boldsymbol{\sigma}^{\boldsymbol{vol}}_{\boldsymbol{n+1}}{}^{\boldsymbol{tr}(i-1)} - \dot{\boldsymbol{\sigma}}^{\boldsymbol{vol}}_{\boldsymbol{n+1}}{}^{\boldsymbol{p}(i)} \qquad \textbf{4.129}$$

Finally, the translation of the current and inner yield surfaces is handled. The magnitude and the direction of translation of the current surface are computed by solving the quadratic problem discussed in Gu et al. (2009).

4.4 SINGLE-ELEMENT CYCLIC TRIAXIAL TEST MODELLING

The implementation of the implicit-explicit solution of the PDMY02 model is validated here by comparing its performance with

1) The cyclic triaxial test results of a Ticino Sand specimen carried out by Fioravante & Giretti (2016), and
2) The traditional implicit solution obtained by using the existing PDMY02 model in OpenSees.

The PDMY02 model was previously calibrated by Özcebe et al. (2021) to match the experimental findings presented by Fioravante & Giretti (2016). Özcebe et al. (2021) was focused on modelling a centrifuge problem which the SSI interactions of a shallow founded frame structure on liquefying soil was studied within the European H2020 LIQUEFACT project. The model was prepared in OpenSees using 2D quad-up elements.

In this study, the calibration proposed by Özcebe et al. (2021) is employed to match the experimental response of the Ticino sand specimen using the novel impl-ex formulation of the PDMY02 model.

Özcebe et al. (2021) proposed a calibration based on the material properties obtained by employing the empirical expressions presented by Fioravante & Giretti (2016) to represent the cyclic triaxial response of a large database of Ticino sand specimens. Özcebe et al. (2021) performed their calibration for reference pressure value of 100 kPa. The initial void ratio ($e0$) of the sand was set to 0.740, which corresponds to a relative density of approximately 49%, representing a medium-dense state. This value was based on specimen preparation technique through dry pluviation presented by Fioravante & Giretti (2016).

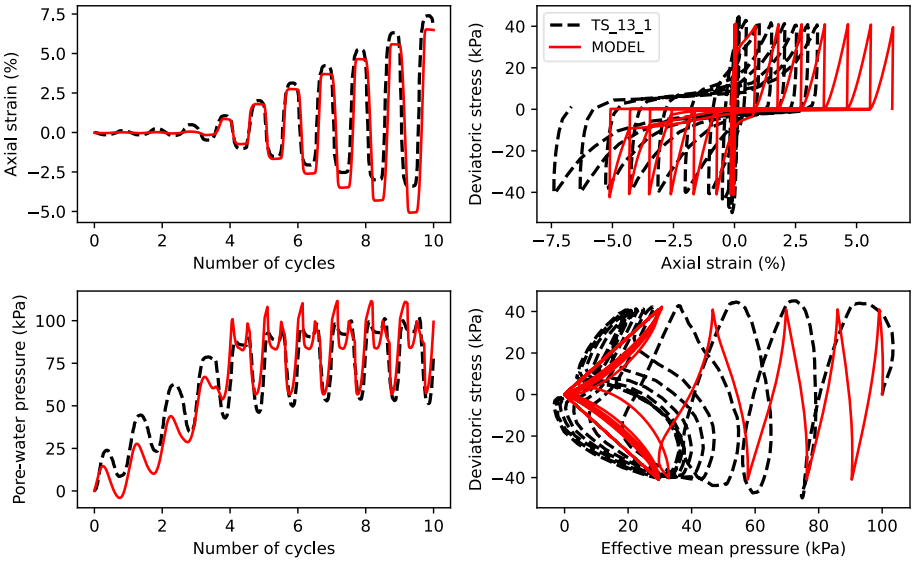

Figure 4.2. Comparison of the PDMY02 impl-ex solution to the cyclic triaxial test data of the specimen TS 13-1. A calibration result similar to the one shown by Özcebe et al. (2021) is obtained.

The small strain shear modulus (Gref) was calculated by employing the empirical formulae presented by Fioravante & Giretti (2016), which considers both the void ratio and the effective confining stress. For a reference confining stress of 100 kPa, a Gref value of 100,000 kPa was estimated. The small strain bulk modulus (Kref) was similarly determined. The shear modulus reduction response is calibrated to match the reduction curve proposed by Darendeli (2001) in the small to medium strain ranges, whereas the response in the large strain ranges, the yield surfaces were modified to achieve compatible hardening response with the internal friction angle of the material. For further details about the calibration, the

reader is referred to the original publication by Özcebe et al. (2021). The single element model presented here is prepared using the 3D *brickUP* element in OpenSees.

Figure 4.2 shows the performance of the impl-ex solution (MODEL) in comparison to the cyclic triaxial test results (TS_13_1) by Fioravante & Giretti (2016). The analysis is done with displacement control for a dU step of 0.001 meters. For the given displacement step, the impl-ex solution is successfully capable of modelling the experimental results without instabilities due to error accumulation. The computed solution is nearly identical to the one obtained by Özcebe et al. (2021).

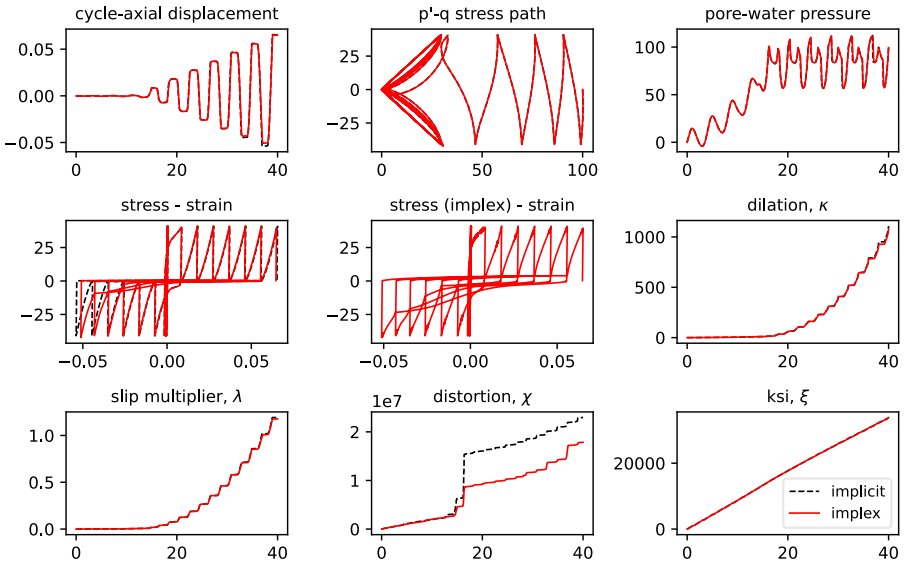

Figure 4.3. Implicit versus impl-ex single element test in OpenSees. The impl-ex solution is validated by comparison with the traditional implicit PDMY02 solution.

Figure 4.3 illustrates the difference between the traditional implicit solution and the impl-ex solution for the discussed dU step. The black dashed curve is the implicit solution, whereas the impl-ex solution is represented by the solid red line. The evolution of the newly introduced impl-ex state variables kappa, lambda, ksi and zeta in implicit and impl-ex solutions are shown for comparison. Notably, the impl-ex and the implicit solution matches for a large portion of the analysis. In the central plot of Figure 4.3, the evolution of the extrapolated (impl-ex) stress during the analysis is shown. By inspection, one can note that there is a residual error computed each time the stress returns to zero value following a stress reversal. This error is successfully corrected through implicit correction; hence the resulting stress-strain curve matches the implicit-only curve.

On the other hand, the accumulation of some error in the deviatoric response represented by the internal variable ksi can be seen in the plot located in the lower centre. This error leads to the deviation of the corrected stress-strain response after several intense dilation cycles as shown in the plot located in the left centre.

In terms of computational cost, a reduction in the solution time around 10-15% is achieved by using the impl-ex solution compared to the traditional implicit solution with a Newton-Raphson tolerance value of 1e-5. It is worth noting that the magnitude of the observed reduction in the computational cost is inversely related to the tolerance value used for the implicit solution.

To summarize, a single element model of cyclic triaxial test of a Ticino sand specimen is presented here. The implemented impl-ex solution of the PDMY02 is validated by comparison to the laboratory test and the implicit solution of the same calibration. The implicit-explicit solution is capable of modelling the pressure dependent behaviour of the soil specimen accurately with a reduced computational cost. However, depending on the step size of the solution and the number of dilation cycles, an amount of error might accumulate leading to the deviation of the element response from the implicit solution after a number of cycles.

4.5 SUMMARY AND DISCUSSION

In this chapter, the PIMY (Gu et al., 2011) and PDMY02 (Yang et al., 2003) models which are available in OpenSees are extended to offer an efficient implicit-explicit (impl-ex) solution at the material level.. A novel impl-ex algorithm is introduced, which involves explicit extrapolation of the material internal parameters followed by an implicit correction of them to increase the stability of the solution. This method is aimed to address the computational challenges of nonlinear cyclic, especially for soils prone to liquefaction. This approach offers a significant reduction in computational time while maintaining accuracy and numerical stability, making it suitable for large-scale, three-dimensional soil-structure interaction simulations.

A key element of the work is the development of a rephrased formulation to linearise the flow rule, essential for the impl-ex integration. Two different approaches are explored: rephrased-flow and linearised-flow methods. The rephrased-flow approach simplifies the governing equations, reducing computational costs and aligning well with the existing implementation of the PIMY andPDMY02 materials in OpenSees.

The performance of the novel solution in modelling cyclic triaxial response is evaluated through single-element tests. The results indicate that the impl-ex scheme provides a close match to the traditional implicit method but with a reduction in computational time.

5 THE FINITE ELEMENT MODELLING OF THE VIRTUAL LABORATORY IN OPENSEES

This chapter presents the development of a finite element virtual laboratory using OpenSees and STKO for the seismic analysis of shallow founded masonry. The chapter focuses on the direct SSI model of a historical masonry bell tower, incorporating 8-node brick elements for both structural and geotechnical domains. The masonry behaviour is modelled using a state-of-the art damage-plasticity model, while the soil behaviour is represented by kinematic hardening pressure-independent and pressure-dependent material models in OpenSees. The finite element model incorporates advanced numerical techniques such as implicit-explicit (impl-ex) methods, tied mesh coupling, and contact mechanics. The chapter also explores the efficient methodology to provide a continuous mesh connection between the tower and the soil, the optimal dissipative boundary conditions as well as the parallelisation of the large SSI domain for achieving a faster solution.

Keywords: Finite Element Method, Direct SSI, Mesh coupling, Parallel solution

5.1 THE VIRTUAL LABORATORY

The bell tower of the Santa Maria Maggiore Cathedral in Guardiagrele, Italy, is a notable medieval stone masonry structure (Figure 5.1). Today, the tower structure serves as the entrance to the cathedral and a museum. It is one of the few surviving structures in Guardiagrele after the Mw 6.8 Maiella earthquake in 1706, which destroyed much of the town. The tower's construction adheres to medieval architectural principles, with thick stone masonry walls that provide substantial stiffness and mass, enabling the tower to withstand both vertical loads and lateral forces, including seismic actions. The relatively low height-to-wall-thickness ratio of the tower leads to a relatively stable geometric configuration in which both shear and flexural controlled modes contributes to resisting the lateral forces. The walls of the tower are composed of external layers of solid stone and internal layers of rubble infill. Overall, the bell tower is a heavy, rigid structure that responds to seismic forces in a brittle manner.

Site investigations done by Biondi et al. (2009), such as endoscopy studies, have highlighted the high-quality masonry employed in the tower's construction. The investigation results were extensively discussed by Rosell (2010) in the characterisation of the material properties for detailed FE modelling. Furthermore, the tower is reinforced with steel chains in both

directions which provide some tensile reinforcement and enhance the overall stability under lateral loading which are neglected in this thesis for the sake of simplicity.

Figure 5.1. The town of Guardiagrele in the Chieti province and the St. Maria Maggiore church bell tower

The bell tower is attached to the Santa Maria Maggiore Cathedral through walls that encloses the tower from both north-south sides and the east side. The cathedral structure was built some years later than the bell tower and complements the towers functionality by providing a large mass hall for the town. The church and tower were constructed using rubble stone masonry from nearby Maiella quarries. The complex consists of four distinct segments, including the central tower and two side walls that connect to the cathedral hall. In the early 18th century, to accommodate the town's growing population, the current plan of the cathedral was obtained by linking two churches via a masonry bridge, further influencing the structural dynamics. Together, the structures exemplify the resilience of medieval architecture, having survived centuries of seismic activity. Since its construction around 1200 CE, the bell tower has undergone several renovations, some necessitated by seismic damage or damage due to bombing during the World War II (Rosell, 2010).

The tower houses a collection of nine bells on its roof which are arranged in an octagonal configuration. These bells are expected to exert significant dynamic loads on the tower during seismic shaking. The combined weight of the bells is around 6,375 kg (Rosell, 2010).

The town of Guardiagrele is located in the northwestern part of the Chieti province, on the slopes of the Maiella massif, which forms part of the central Apennines. The region is seismically active, with the 1706 Mw 6.8 Maiella earthquake causing significant damage to the town and the cathedral complex.

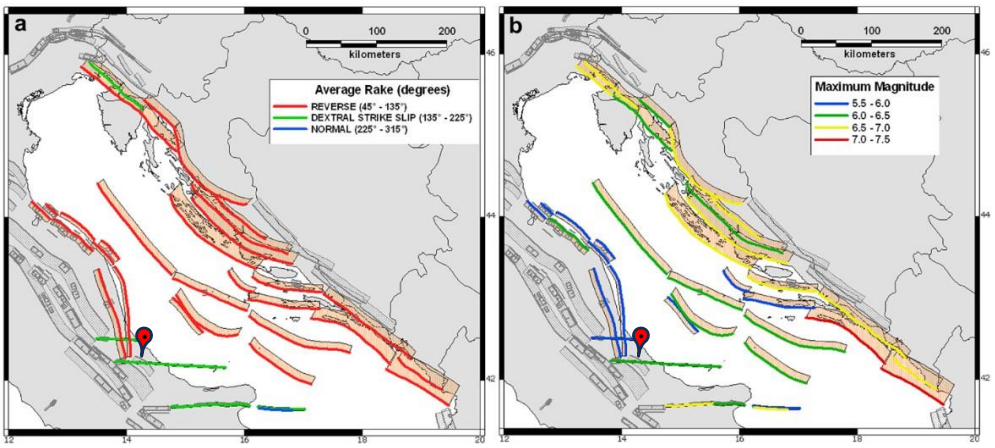

Figure 5.2. The faulting and the maximum possible event magnitude distribution in the Adriatic domain identified by Kastelic et al. (2013). Figure taken from Kastelic et al. (2013). The added teardrop marker points at the approximate location of Guardiagrele.

From a seismotectonic point of view, the town is positioned in the central west part of the Adriatic domain. Kastelic et al. (2013) study the domain's tectonic boundary conditions. The Adriatic Sea plate is compressed by the surrounding south-verging Alps from the south and the opposite verging Apennines and External Dinarides from the west and northeast. On the central west extremity, the tectonic evolution is controlled by submerging the Adria plate below the Apennines and the extension zones stretching along the Italian peninsula. This behaviour leads to thrust fronts and shear zones along the western coastline passing through the Abruzzo region, ultimately leading to normal and strike-slip faulting in the larger Chieti provincial area, capable of generating events greater than Mw 5.5 on average. Local site conditions further amplify the seismic response of the tower. Guardiagrele is situated atop a hill, and hills are known to amplify incident ground motion (Kramer, 1996).

The historical seismicity in the vicinity of Guardiagrele has been marked by numerous significant earthquakes. Some of the known significant events after the construction of the

tower in 1400 CE, are shown in Table 5.1. As listed by Guidoboni et al. (2019), several events with intensities of 10 or higher on the Mercalli-Cancani-Sieberg (MCS) scale are known, with notable occurrences in 1456, 1461, 1703, and 1706, all of which had magnitudes (Meq) exceeding 6. These events primarily affected central and southern Italy, with the 1706 Maiella earthquake being particularly destructive. The region also experienced high-intensity earthquakes in the 20th century, such as the Marsica earthquake in 1915, which reached an intensity of 11 and a magnitude of 7.

The bell tower of Guardiagrele was studied by other authors previously with the aim of seismic assessment and retrofitting. The conference paper by Camata et al. (2008) and the master's thesis by Rosell (2010) were two notable contributions in this area, both using the Abaqus finite element software to simulate the soil-structure interaction physics present in the bell tower system. These studies have utilised three-dimensional direct modelling approaches to account for the nonlinear structural behaviour of the masonry tower and the elastic behaviour of the soil.

However, in Section 8.3 of this thesis, it is demonstrated that considering linear soil behaviour and nonlinear masonry behaviour tends to overestimate the plastic response of the tower, particularly along its weak axis. This finding highlights the limitations of using a linear soil model when assessing the seismic performance of the bell tower, as it does not fully capture the soil's ability to dissipate energy, leading to an exaggerated prediction of damage in the masonry structure.

Table 5.1. Significant historical events (after 1400 CE) in the vicinity of Guardiagrele. (Guidoboni et al., 2019). Inferred Epicentral and Maximum Intensities.

Date	I_{Epi} (MCS)	I_{Max} (MCS)	M_{eq}	Lat.	Lon.	Epicentral Area	Review Level
1456.12.05	10	10.5	6.3	42.194	13.91	Italia centro-meridionale	High
1461.11.27	10	10	6.4	42.314	13.543	Aquilano	High
1703.02.02	10	10	6.7	42.435	13.292	Aquilano	High
1706.11.03	10.5	10.5	6.8	42.077	14.079	Maiella	High
1762.10.06	9	9.5	6	42.308	13.585	Aquilano	High
1786.07.31	7.5	8	5.4	42.323	13.373	Aquilano	Low

1841.06.10	7	7.5	5	42.083	14.08	Valle dell'Aventino	Low
1881.09.10	8	8.5	5.6	42.232	14.284	Abruzzo meridionale	Medium
1904.02.24	8.5	9	5.6	42.097	13.316	Marsica	High
1915.01.13	11	11	7	41.982	13.648	Marsica	High
1933.09.26	9	9	6	42.08	14.093	Maiella	High
1958.06.24	7.5	7.5	5.2	42.34	13.478	L'Aquila	Low

Camata et al. (2008) modelled the bell tower following experimental material properties, geometry, and soil stratigraphy surrounding the tower. They emphasised the influence of soil-structure interaction and the lateral constraints provided by the cathedral walls, which restrain the tower's lateral displacements. The findings revealed that the tower's response is significantly affected by the frequency content of the seismic input and the flexibility of the supporting soil, highlighting the need for careful selection of ground motion records in seismic analyses.

Rosell (2010) employed explicit nonlinear dynamic analyses to capture the soil-structure interaction between the bell tower and its soil. A detailed 3D finite element model of the tower and the surrounding soil was developed using the ABAQUS software. The model included the hilltop topography of Guardiagrele, which played a significant role in modifying seismic signals due to topographic focusing effects.

Rosell (2010) modelled the masonry of the bell tower using a concrete damage plasticity model available in ABAQUS, which accounted for the simulation of tensile cracking and compressive crushing in masonry. However, a single damage parameter determined the amount of stiffness loss both in tension and compression. This led to unrealistic scenarios in which damage due to tensile actions caused compressive failures in the tower. Hence, the damage component in the tensile strains was removed due to computational issues, and the analyses were performed in full plasticity in some cases.

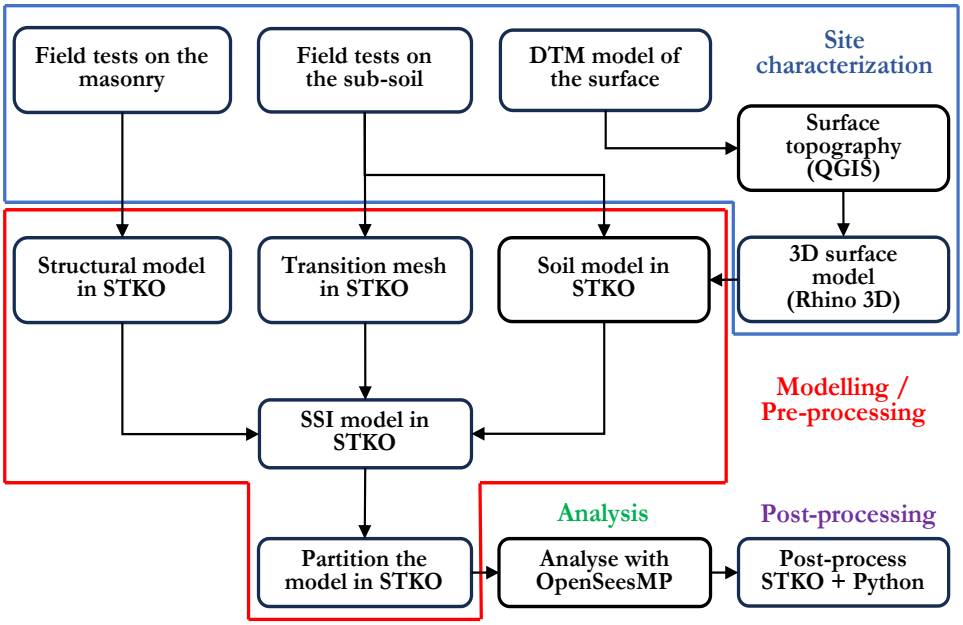

Figure 5.3. Methodology for creating the soil-structure interaction model in STKO and OpenSees

The seismic excitation was introduced at the model bottom as vertically propagating waves. These excitations were carefully selected to match the site's hazard characteristics, conditioned on an inelastic spectral acceleration definition obtained through pushover analysis. This approach ensured pointwise consistency of hazard at the selected inelastic stiffness instead of a range of periods equally crucial for the bell tower. Additionally, while a 3D model was presented, the wave propagation in the soil domain was effectively limited to 2D using periodic soil boundary conditions along the model's long axis instead of dissipative boundaries.

Rosell (2010) provided several critical insights into the seismic behaviour of the bell tower. The analysis revealed that the tower exhibits a brittle response under seismic loading, primarily due to the formation of a significant crack in the middle section. Furthermore, sensitivity analyses showed that the tensile strength of the masonry is a highly influential parameter. Variations in this property significantly affected the extent of damage, indicating the need for precise characterization of material properties in seismic assessments.

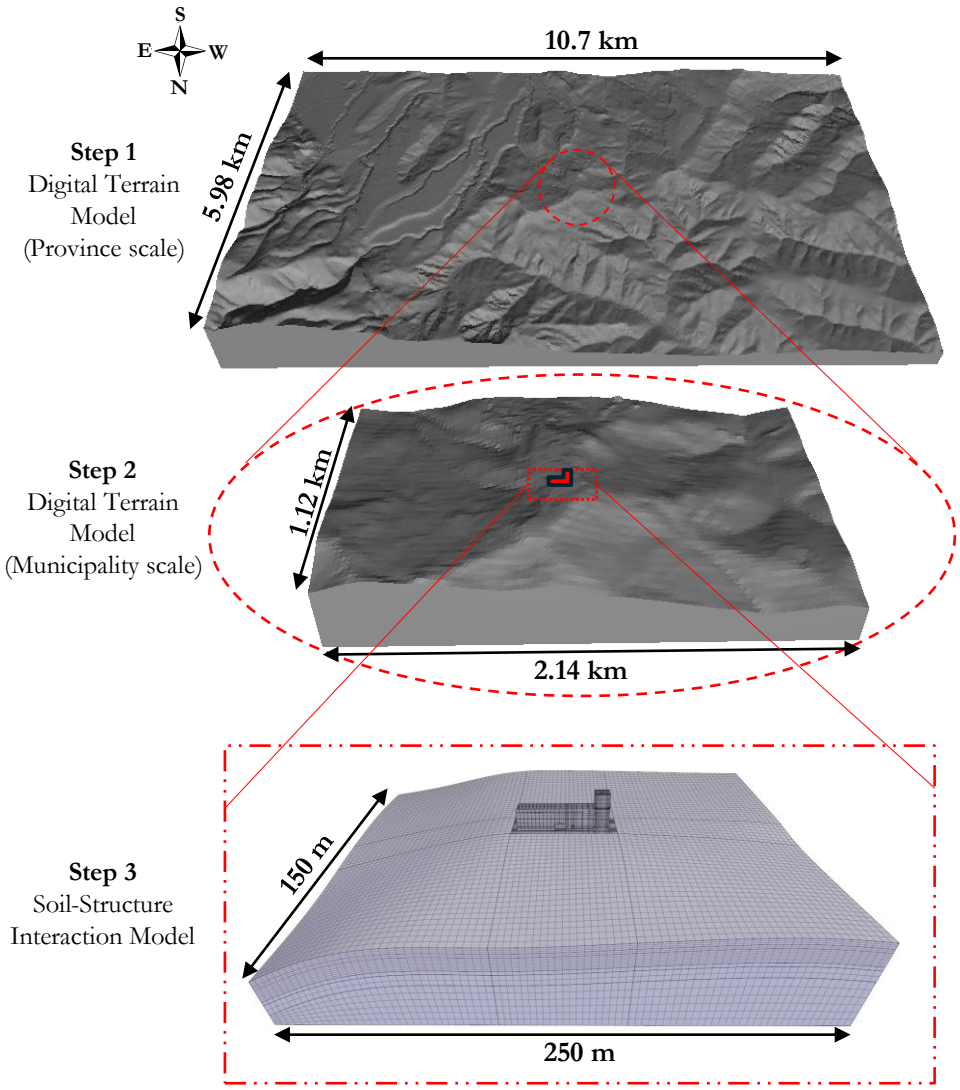

Figure 5.4. Step-by-step model generation process from the digital terrain model (plotted in QGIS) to the numerical model (plotted in STKO). DTM data (10x10m resolution) obtained from Regione Abruzzo (2015)

By comparing the SSI results with the fixed-base model, Rosell (2010) demonstrated that neglecting SSI effects fails to capture the amplification effects and realistic deformation patterns observed in the more detailed SSI model. However, the significant impact of considering SSI on the roof acceleration response was overlooked. This oversight occurred

because the characteristics of the bell tower were masked by the relative proximity of the inelastic fixed-base period to the elastic SSI period, which led to a reduced distinction in the dynamic response due to soil-structure interaction effects, as shown in this thesis.

This study aims to develop a detailed numerical model of the masonry tower, its interaction with the surrounding hill structure, and the effects of propagating seismic waves, using OpenSees. An innovative digital twin approach was taken in modelling the bell tower SSI system. The detailed model of the SSI system is achieved by following the flowchart shown in Figure 5.3 and Figure 5.4. The analysis focuses on the nonlinear material characteristics of the system's behaviour under seismic loads. Advanced numerical tools, including STKO and impl-ex integration schemes, are employed to simulate computationally demanding SSI system. Recent developments in FE modelling tools enable making of high fidelity models with accurate nonlinear behaviour, allowing for the seismic assessment of masonry tower structures.

5.2 CONTINUUM ELEMENTS AND MESH COUPLING

A combination of solid and structural elements (as in Bathe, 2016) might be necessary to model a soil-structure interaction system. Traditionally, solid domains are modelled as a Cauchy continuum in which a stress element is assumed to be in rotational equilibrium under shear forces, and shear couples are absent. The exclusion of shear couples in the solution of the rotational momentum balance equations leads to the symmetry in the strain and stress tensors. In FE formulation, such a stress element can be represented using standard brick elements having only translational degrees of freedom at each node. The translational d.o.f.s (displacements) of a node are denoted with the small letter u in this thesis. *Brick* element theory offers an accurate approximation of a continuum successfully capturing the volumetric and deviatoric stress states of a soil or structural element during elastic or inelastic wave propagation (Watanabe et al., 2017). In most applications, the Cauchy continuum is a valid approximation for modelling soil domains and some masonry micro or macro modelling approaches.

On the other hand, the simplifications made in the Cauchy continuum may result in a suboptimal performance. In structural problems controlled by bending modes, multiple brick elements might be required along the structural members bending axis to approximate the stress distribution accurately, increasing the computational cost significantly. Dedicated structural elements with bending formulations and additional rotational d.o.f.s, such as shell or beam-column elements, are widely used in the FE modelling of complex structures (Bathe, 2016).

Furthermore, in problems including strain softening response in which Drucker's stability postulate cannot be satisfied, the standard brick element theory yields mesh-dependent

results due to the localization of the strain increment following the appearance of an inelastic mechanism (Bažant et al., 1984; Chandler, 1985; Han & Chen, 1986; Jirásek, 2007; Regueiro & Borja, 1999). The problems of a Cauchy continuum might be addressed by employing nonlocal hardening laws that consider scale effects in the material response (Bažant et al., 1984) or a micro-polar medium such as the Cosserats' (Cosserat & Cosserat, 1909). Cosserat media is out of the scope of this thesis; however, its powerful application in modelling granular media and strain softening is acknowledged (Vardoulakis, 2019). Instead, the mesh dependency issues encountered in this study are handled using an alternative first-order computational homogenization approach based on keeping the fracture energy of the material constant, namely, independent from the element size (Petracca et al., 2016).

Furthermore, the soils are porous and often partially or fully saturated with water. Except for special loading conditions such as the undrained case, soil response depends on the effective stresses requiring hydromechanically coupled calculations (Biot, 1962). Effective stresses are computed in FE through dedicated coupled elements with additional pore pressure freedom. The solid and fluid phases are assumed to deform parallel with an equivalent bulk modulus. Then, the stress and stiffness contribution of the soil skeleton is computed iteratively within the solid element (Potts & Zdravkovic, 1999).

In this thesis, the rotational d.o.f.s are depicted with a small letter, r. Hence, a node with three d.o.f. is a u node, whereas a node with six d.o.f. is a $u-r$ node. Finally, the four d.o.f. node of a hydromechanically coupled element is a $u-p$ node since the pressure d.o.f. is shown with a letter p. Moreover, at the time of the conception of this thesis, finite strain *brick* or *brickUP* elements are unavailable in OpenSees. Hence, all the mentioned elements and materials follow the infinitesimal kinematics (small-strain) theory apart from the *ASDShellQ4* element, which uses the corotational formulation to handle large deformations (Felippa, 2000; Felippa & Haugen, 2005).

The variety of continuum elements required to successfully model a soil-structure interaction study gives rise to the issue of effectively connecting multiple patches of mesh with incompatible formulations and boundary conditions. Several element coupling strategies are available in OpenSees for various purposes, such as *equalDOF,* and rigid link coupling, to name a few. Recently, a new constraint element called the *ASDEmbeddedNode* was implemented in OpenSees to provide tie coupling like the one offered in Abaqus. Among others, tie coupling is used extensively in the presented study. More information about the formulation of *ASDEmbeddedNode* is available on the OpenSees GitHub pages (Petracca, 2022). Other custom strategies used in this thesis include *Shell2Solid*, *zeroLength*, and *ZeroLengthContactASDimpl-ex* coupling.

ASDEmbeddedNode coupling uses tetrahedral elements in 3D and triangular elements in 2D to tie one constrained node to 2 or 3 restrained nodes. The tie constraint is enforced using the penalty method. A suggested penalty value in shear is the shear modulus of the medium multiplied by $10e2 - 10e4$ to provide a stiff connection within the displacement range of interest. The element is compatible with a combination of nodes such as u, $u-p$, or $u-r$. The constrained nodes d.o.f.s are the weighted average of the d.o.f.s of the surrounding nodes. Hence, the constrained node must be inside the area enclosed by the restrained nodes.

Shell2Solid or *Beam2Solid* coupling aims to tie the incompatible nodes of structural and solid elements together. Structural elements often have six d.o.f.s at their nodes, and they are incompatible with solid element nodes with three d.o.f.s in direct connection. However, a fixed or pinned connection can be provided cleverly using *equalDOF* and rigid link constraints. The schematics of a fixed type of connection where the flexural forces are transmitted to solid elements on average are given in Figure 5.5.

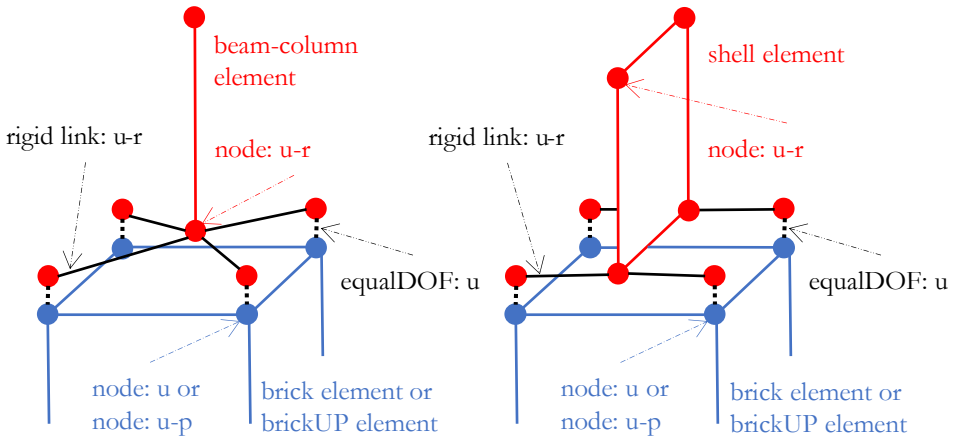

Figure 5.5. Structural element-to-solid element coupling in OpenSees using additional nodes and constraints (Beam2Solid coupling in STKO). Rigid link works in modelling the thickness of structural elements.

ZeroLength coupling involves using two node *zeroLength* elements to tie two separate meshes. A linear or nonlinear material can be attached to the *zeroLength* element to provide viscous damping, friction, fixed conditions, or combinations between the boundaries of two domains.

ZeroLengthContactASDimpl-ex coupling relies on two node contact elements to provide nonlinear contact-friction mechanics between independent meshes. In SSI, this contact is helpful in modelling pounding between structures or the slip between soil and foundation. The formulation of a contact element implemented is provided in Section 3.2. The practical details and proper use of the element command can be found in the OpenSees manual entry of the contact element (Akan & Petracca, 2022).

5.3 STRUCTURAL MODEL

The objective of the structural model is to capture the inelastic response of the stone masonry tower under dynamic loading. This involves understanding the failure mechanism of the tower and the energy dissipation leading to failure, such as the crack propagation and pattern. The body of the tower is modelled using 8-node *brick* elements (Love, 2018), whereas the out-of-plane bending controlled elements (i.e., vaults and slabs) are modelled with 4-node *ASDShellQ4* elements (Petracca, 2021). The shell section is created via the *LayeredShell* (Zhu, 2014) property in OpenSees using 5-8 material fibres depending on the criticality of the dynamic out-of-plane forces acting on the element. The structure's geometry and openings are provided in the STKO pre-processor based on the architectural drawings of the church presented by Rosell (2010), shown in Figure 11.1.

Additional care is taken to achieve a structured meshing to accommodate three-dimensional brick and rectangular shell element geometries. A structured hexagonal mesh enhances the structure's computed strain and stress fields, allowing for a coarser discretization that satisfactorily achieves the compatibility condition. Furthermore, the number of brick elements required to cover a volume is significantly less than the number of triangular elements (Figure 5.8).

Architectural drawings indicate that the wall thickness is reduced in the church's main hall (back gallery). Additionally, the behaviour of these walls in horizontal loading is expected to differ from the side walls built around the tower since the tower acts as a stiff core wall structure and attracts large horizontal forces in the front part of the church. The external and internal walls in the central hall part of the church are expected to work as out-of-plane bending and shear critical members. Hence, these members are modelled as *ASDShellQ4* elements.

Shell elements in the gallery are connected to the solid elements of the tower through *Shell2Solid* coupling (Section 5.2). It is crucial to note that special care is required to prevent stress concentration points when connecting shell or similar contact element nodes to solid element nodes. Since shell or frame elements also include rotational d.o.f.s, the stress must be transferred proportionally to the members' section thickness. Directly terminating a shell element at the node of a solid element may lead to increased artificial stresses within the

solid element. In a nonlinear setting, this may cause premature failure (softening or loss of stiffness) of materials around the connection points and prevent analysis from progressing further.

Contact elements (*ZeroLengthContactASDimpl-ex*) were added between the tower and the wall cross-sections in contact with the tower. These bodies are expected to oscillate independently during seismic excitation since, in in-situ conditions, they were built at different times and are only bonded through mortar connections. The interface between the walls and the tower is expected to fail in the early stages of shaking. Following separation, the dynamics are controlled by contact-friction mechanics. During seismic shaking, this separation leads to a pounding interaction between the tower and the rest of the structure. The effect of pounding interaction on the tower response is studied further in detail in the following chapters.

The nonlinear behaviour of the masonry is modelled with the *DamageTC3D* or *ASDConcrete3D* (Petracca et al., 2022) materials implemented in OpenSees. The *DamageTC3D* is a multiaxial damage-plasticity model for the cyclic analysis of masonry structures. It has fundamental features to model masonry behaviour, such as tension-compression damage accumulation and anisotropy in tension and compression stress paths. As a damage-plasticity material, *DamageTC3D* conveniently decomposes plastic strain into a damage and plasticity part. It offers two parameters to calibrate the percentage of plasticity associated with the damage and the elastoplastic processes, differently in tension and compression. Additionally, *ASDConcrete3D* material is the latest version of this generation of materials, and it also includes a crack plane assumption to guide the damage and plastic strain increment directions along a user-defined smoothing angle. More details regarding these materials are provided in Section 2.5.1.

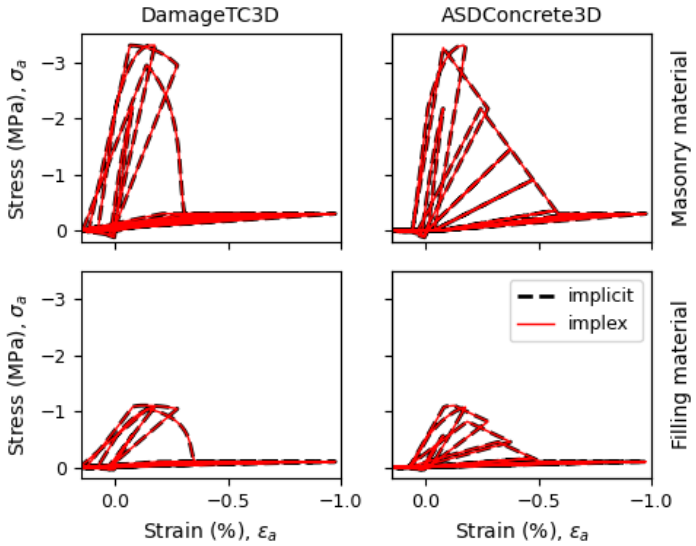

Figure 5.6. Masonry (top) and filling (bottom) material cyclic stress-strain response using implicit and implicit-explicit integration.

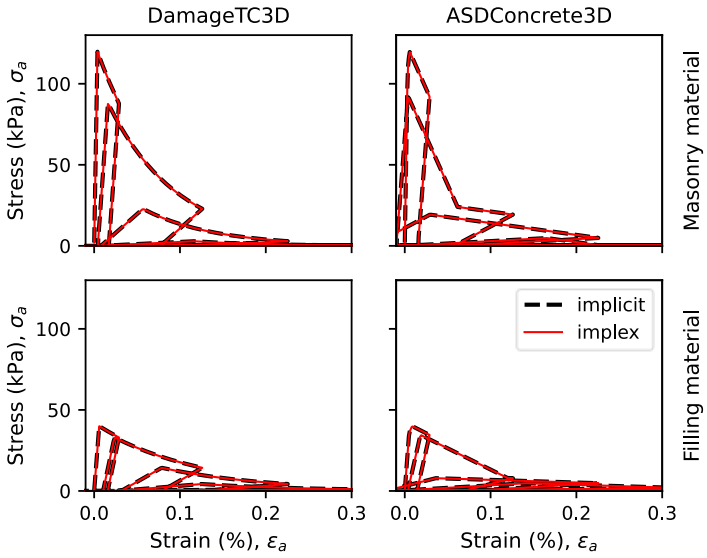

Figure 5.7. Masonry (top) and filling (bottom) material cyclic tensile response using implicit and implicit-explicit integration.

The field test data made available by Rosell (2010) and the references therein indicate that the mechanical property of the masonry is not isotropic but spatially variable within the cross-section. The cross-section of the tower is a meter-thick hollow rectangle that consists of three distinctive layers: the relatively higher strength outer and inner layers and a softer inner filling layer. Drilling core specimens indicate that the high-quality stones were employed at the inner and outer shells with compressive strengths up to 6-7 MPa. Furthermore, flat jack tests showed a significant stiffness contrast between the inner and outer layers of masonry (in the order of 5-6 times). However, no more information is available on the inelastic mechanical properties of the materials, such as the tensile strength or tensile/compressive fracture energies, which are crucial for this study. Rosell (2010) copes with the lack of data using the stone masonry parameters suggested by the Italian Seismic Codes (NTC 2008). In the same year, Magenes et al. (2010) conducted a comparative analysis of the parameters outlined in NTC 2008 and Eurocode 6 against experimental tests on stone masonry specimens. Their findings indicate that the values specified in the codes are slightly underestimated. Subsequently, shake table tests were conducted on representative historical stone masonry structures (Guerrini et al., 2017; Penna et al., 2016; Senaldi et al., 2018; Tomić et al., 2023). *DamageTC3D* and *ASDConcrete3D* materials models are calibrated to model these experiments in Section 3.5.

The mechanical properties of the masonry materials calibrated by interpreting the observations of Magenes et al. (2010), Rosell (2010) and Senaldi et al. (2018) are provided in Table 5.2. The internal masonry layer was assumed to be around five times softer and three times weaker than the external masonry layer. The ductility of the material is controlled through the shape of the stress-strain curve by increasing or decreasing the tensile or compressive fracture energy within reasonable limits.

Table 5.2. Parameters of the DamageTC3D material employed for the outer stone masonry and inner filling (units in kPa)

Parameter	Masonry	Filling	Definition
$\boldsymbol{rho}$	2.24	1.94	Density in tons per cubic meter
$\boldsymbol{E}$	3,250,000	700,000	Young's modulus
$\boldsymbol{v}$	0.15	0.15	Poisson's ratio
$\boldsymbol{ft}$	120	40	Tensile strength
$\boldsymbol{Gt}$	0.1	0.03	Tensile fracture energy
$\boldsymbol{fc0}$	100	100	Compressive elastic limit
$\boldsymbol{fcp}$	3300	1100	Compressive peak strength

fcr	300	100	Compressive residual strength
ep	0.0025	0.003	Compressive strain at peak strength
Gc	15	5	Compressive fracture energy
c1	0.30	0.65	Compressive response shape parameter (initial response)
c2	0.90	0.9	Compressive response shape parameter (peak region)
c3	1.01	1.01	Compressive response shape parameter (residual region)
surf_t	Rankine	Rankine	Type of tensile surfaces: Rankine or Lubliner
bm	1.16	1.16	Compressive bi-axial strength factor (effects dilatancy)
m1	0.16	0.16	Shear-Compression reduction factor
Kc	0.6667	0.06667	Triaxial compression shape factor
eta	0.00	0.00	Viscosity parameter
pdf_t	0.40	0.40	Plastic-Damage factor for tensile response [0: full damage ... mixed ... 1: full plasticity]
pdf_c	0.50	0.50	Plastic-Damage factor for comp. response [0: full damage ... mixed ... 1: full plasticity]
autoReg.	active	active	Option to scale Gt and Gc by the element characteristic length

Table 5.3. Parameters of the ASDConcrete3D material employed for the outer stone masonry, and inner filling (units in kPa)

Parameter	Masonry	Filling	Definition
rho	2.24	1.94	Density in tons per cubic meter
E	3,250,000	700,000	Young's modulus
v	0.15	0.15	Poisson's ratio
ft	120	40	Tensile strength
Gt	0.1	0.05	Tensile fracture energy

fc0	100	400	Compressive elastic limit
fcp	3300	600	Compressive peak strength
fcr	300	100	Compressive residual strength
ep	0.0025	0.002	Compressive strain at peak strength
Gc	12	4	Compressive fracture energy
PSc_T	0.40	0.40	Plastic-Damage factor for tensile response [0: full damage ... mixed ... 1: full plasticity]
PSc_C	0.50	0.50	Plastic-Damage factor for comp. response [0: full damage ... mixed ... 1: full plasticity]
autoReg.	active	active	Option to scale Gt and Gc by the element characteristic length

It is worth noting that the lack of tension-compression anisotropy was one of the limitations identified by (Rosell, 2010). This is fundamental for masonry structures since a unified damage variable could lead to a premature compression degradation of the structure during stress reversals at the locations where some minor tensile cracking is expected due to gravity loading. Figure 5.6 shows the hybrid damage-plasticity behaviour in cycles. As the damage accumulates, the reloading stiffness reduces, in addition to some amount of permanent strain accumulation.

Furthermore, the model offers automatic fracture energy regularization based on the characteristic element length. The input tensile and compressive fracture energy is scaled with the element characteristic length to provide an element size-independent material response. Size effects become essential in the softening portion of the material response. Since the stiffness becomes negative, Drucker's stability postulate does not hold, and the response becomes subjective to the element's size. A fracture energy-based regularization aims to correct such size effects by scaling the material response accordingly. However, it should be noted that a regularization based on the characteristic length is a first-order approach and becomes more effective as mesh distortion is controlled.

Finally, an implicit-explicit strategy is employed to integrate the material state variables. Details regarding the implicit-explicit formulation of *DamageTC3D* are provided in Section 2.5.1.3. Like the *DamageTC3D* and *ASDConcrete3D* materials, the *ZeroLengthContactASDimpl-ex* contact element operates with an implicit-explicit internal algorithm for increased stability, and the plastic slip evolves as a function of damage (Section 3.2). Therefore, the loss of convergence due to highly nonlinear contact conditions

during pushover and time history analysis is not an issue in the presented model (Oliver et al., 2008).

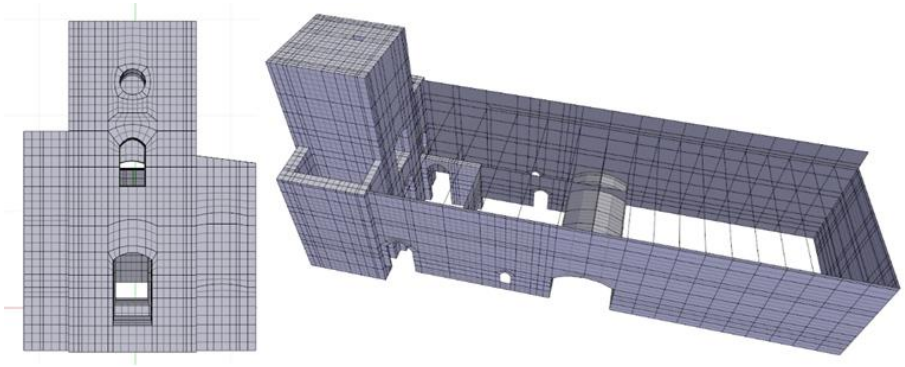

Figure 5.8. The geometry and spatial discretization of the model are displayed in the STKO pre-processor.

During dynamic analysis, ill-conditioned elements with material nonlinearity could generate infinite accelerations, which could lead to a loss of solution stability in the case of an impl-ex material. In an initial model, the side walls attached to the tower were modelled as shells instead of solids. The impact between shell and brick element nodes caused the dynamic analysis to lose stability.

The self-weight of the structure is assigned as volume forces for brick elements and face forces as shell elements. Volume and face forces are STKO automation that converts an assigned force density to nodal forces at the connecting nodes of an element. In addition, staircases spiralling within the tower towards the roof and the bells at the roof are modelled as dead loads. Furthermore, two kilonewtons per square meter of live load is applied to the slabs to model the service loads. Masses equivalent to the structure's weight are also assigned as volume and face masses. STKO converts the assigned mass densities to nodal masses accordingly. Finally, in addition to the shell2solid coupling constraints, a rigid diaphragm is added in the back gallery to model the slab of the main church hall. The rigid diaphragm does exclude the tower nodes at the same level but only includes the walls below the grand hall. Since the grand hall consists of a large slab, this area of the structure is expected to displace monolithically in the horizontal d.o.f.s.

Finally, elastic slender struts were added to model the roof of the tower. As an exception, beam elements were directly pinned to shell element nodes. A maximum element size of 0.5 meters is chosen to properly model the mechanism or possible structural crack formation on the façade of the tower. The mesh size of the shell elements in the back gallery was gradually increased. Figure 5.8 shows the model geometry and the obtained mesh for the structural model.

5.4 GEOTECHNICAL MODEL FOR TOTAL STRESS ANALYSIS

A realistic soil profile was prepared using the limited field test data available. The shear wave velocity profile of the underlying subsoil, obtained through a down-hole test, along with qualitative observations regarding the type of material present in Guardiagrele, are provided by Camata et al. (2008), Rosell (2010) and the references therein (Table 5.4).

Table 5.4. Shear wave velocity profile and the small strain shear moduli inferred from shear wave velocities.

Layer No.	Thickness (m)	Vp (m/s)	Vs (m/s)	G (MPa)	ν (assumed)	PI (assumed)
1	5	714	220	99	0.49	30
2	7	1820	125	32	0.49	30
3	2	1820	350	250	0.49	30
4	6	1340	350	250	0.49	30
Bedrock	Inf.	2100	800	1,566	0.49	-

Unfortunately, the available data on the subsoil is limited to Vp and Vs velocities obtained from a single borehole. As shown in Table 5.4, unreasonably high Vp values are observed in layers 2 and 3. Typically, Vp values exceeding 1500 m/s suggest the presence of a water table; however, the down-hole test report indicates that no water table was encountered. The report does, however, note the presence of fine-graded clay and silt materials throughout all layers, with occasional sand lenses in the second layer. In their efforts to develop an elastic isotropic soil model, Biondi et al. (2009) and Camata et al. (2008) interpreted the soil profile as consisting of gravel, sand, and clay layers from the surface to the bottom. In contrast, Rosell (2010) assumed the presence of clayey lime, sand, and sandstone layers.

Given the lack of comprehensive data, this study proposes an alternative nonlinear soil profile. The provided shear wave velocities, combined with material type observations, strongly suggest the presence of fine-grained material throughout the soil profile. Although the field test report indicates the absence of a water table, the observed Vp velocities—exceeding 1500 m/s, which is higher than the velocity of water—imply the possible presence of pore water. This observation reinforces the likelihood of fine-grained material at the site. It is plausible that during the relatively short duration of the down-hole test, the

operator did not observe water accumulation in the borehole due to the low permeability of the fine-grained material.

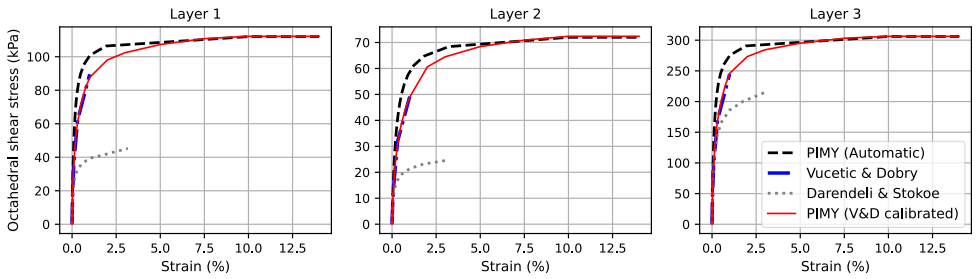

Figure 5.9. Stress-strain curves [Equivalent linear G/G$_{max}$ curves are taken from Strata (Kottke & Rathje, 2008)]

Based on these considerations, a reasonable soil profile is determined as follows: a bottom layer of medium-stiff clay with a Vs velocity of approximately 350 m/s, a softer intermediate clay layer with a Vs velocity around 125 m/s, and a medium-to-soft fine top layer with a Vs velocity of about 220 m/s (Table 5.5). Under rapid dynamic loading, this soil profile is best modelled under undrained conditions, where deformation occurs primarily in shear with minimal volumetric response due to high pore water saturation. The ultimate behaviour is captured using a pressure-independent material model, with an incompressible Poisson's ratio set at 0.49 to prevent numerical issues(Potts & Zdravkovic, 1999).

Table 5.5. Pressure-Independent multi-yield surface material parameters

Parameter	Layer 1	Layer 2	Layer 3	Definition
rho	2.05	2.05	2.05	Density in tons per cubic meter
Gref	98,674	31,855	249,745	Shear modulus at Pref
Kref	953,856	307,934	2,414,203	Bulk modulus at Pref
cohesion	160	65	410	Shear strength at Pref (S_u)
ep	0.1	0.1	0.1	Strain at peak strength
Phi	0.0	0.0	0.0	Friction angle
Pref	50	170	320	Reference pressure
m	0.0	0.0	0.0	Pressure dependency power
TNYS	20	20	20	Total number of yield surfaces

In this case, the nonlinear material behaviour becomes a function of the shear stiffness, and the undrained shear strength, S_u. Due to the absence of direct data on the undrained shear strength of the soil profile, stiffness-to-strength ratios from the literature were employed, as demonstrated by Kanellopoulos et al. (2023) and the references therein. Kanellopoulos et al. (2023) proposes estimating undrained shear strength (Su) using G_{max}/S_u or E_u/S_u ratios for different types of clay in which the former ranging between 150 to 1,000 as mentioned by Anastasopoulos et al. (2011) and Das (2011).

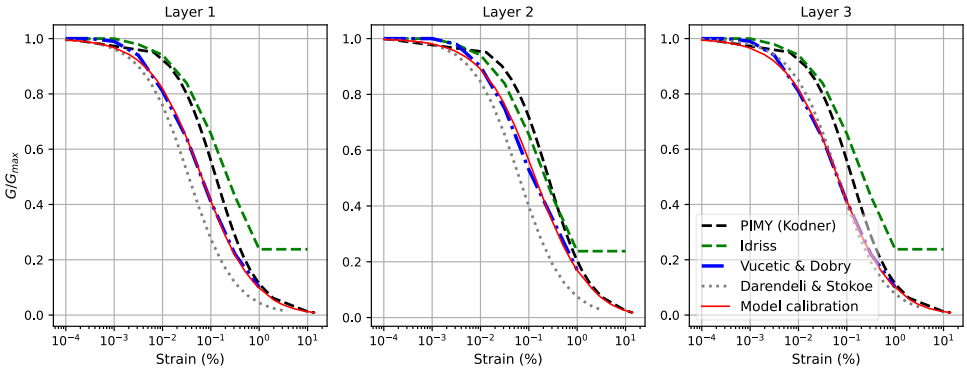

Figure 5.10. Comparison of shear stiffness reduction response obtained with the pressure-independent multi-yield material and other methods [Equivalent linear G/G$_{max}$ curves are taken from Strata (Kottke & Rathje, 2008)]

Following the approach by Kanellopoulos et al. (2023), the clay soil constitutive model for each layer was calibrated to match well-known shear degradation models used in site response analysis of clayey strata. The target S_u for each layer is computed assuming a G_{max}/S_u ratio of 600, except for the topmost layer which is taken as 550 due to some expected over-consolidation. Two separate calibrations were performed in this thesis: the first matched the G/Gmax response as proposed by Vucetic & Dobry (1991) for clayey soils, and the second aligned with the Hyperbolic hardening model introduced by Kondner (1963) (Figure 5.11). A comparison of the employed G/G_{max} curve with the other approaches (Darendeli, 2001; Vucetic & Dobry, 1991) in the literature is given is Figure 5.10. By comparing the sharpness of the G/G_{max} curves, larger hysteretic circles may be expected for the PIMY material, indicating relatively increased damping in larger strains.

The Vucetic & Dobry model defines distinct stiffness degradation rules based on the plasticity index (PI) of each layer which are shown in Table 5.4. The PI value is a proxy of plasticity in fine-grained material and influenced by factors such as mineral composition, clay particle content, and structure. High-PI clays, typically associated with high undrained shear strength, were assumed around the foundation of the bell tower, with a PI value of

30 assigned for all layers. The sensitivity of the SSI systems response to the chosen G/G_{max} response is further discussed in Section 8.4.

The pressure-independent multi-yield surface model employed for clay behaviour is a simplified model featuring kinematic hardening. The unloading-reloading rule is a function of the G/G_{max} curve and follows a modified Masing type hysteretic behaviour. The model is designed to reach the Critical State at the peak shear strain value. Key parameters required for the model include G_0, K_0, peak shear strain, the undrained shear strength, and the G/G_{max} versus octahedral shear strain curve.

The surface topography of the Guardiagrele was obtained from the Digital Terrain Models (DTM) in the 10x10 meters resolution made available by the Abruzzo Regional Administration (Regione Abruzzo, 2015). The DTM models are offered in .tif format and can be read by the open-source GIS software QGIS. In QGIS, the area of interest was isolated and exported in the .stl file format using the DEMto3D plug-in. Later, the raw surface in. stl format was manipulated in the Rhino3D software to obtain a high-definition surface using quads using the STKO structured meshing algorithm. In STKO, after the surface shape is imported, the surface is copied, and the resulting surfaces are stacked on top of each other to create layers, if the submerged topography of the soil layers follows the surface topography. In a limited zone, assuming an internal structure akin to or relating to the surface topography might be reasonable, considering the depositional layering or the sedimentary process. Finally, the bottom face of the model was truncated in a flat face by appending the bedrock layer (Figure 5.12).

The size of the soil domain was determined to capture the sloping of the ground in the East-West direction (model global X axis) and provide a medium that is large enough to enable the propagation wavefront generated by the structural vibrations within the domain. Rosell (2010) conducts a sensitivity analysis and establishes the significance of the soil-to-structure mass ratio, reporting that beyond a mass ratio of about 50 times, the wavefront generated within the model is unaffected by the presence of dissipating boundaries around the model. Hence, the chosen soil dimensions yield at least a 50 times heavier domain (Figure 5.12).

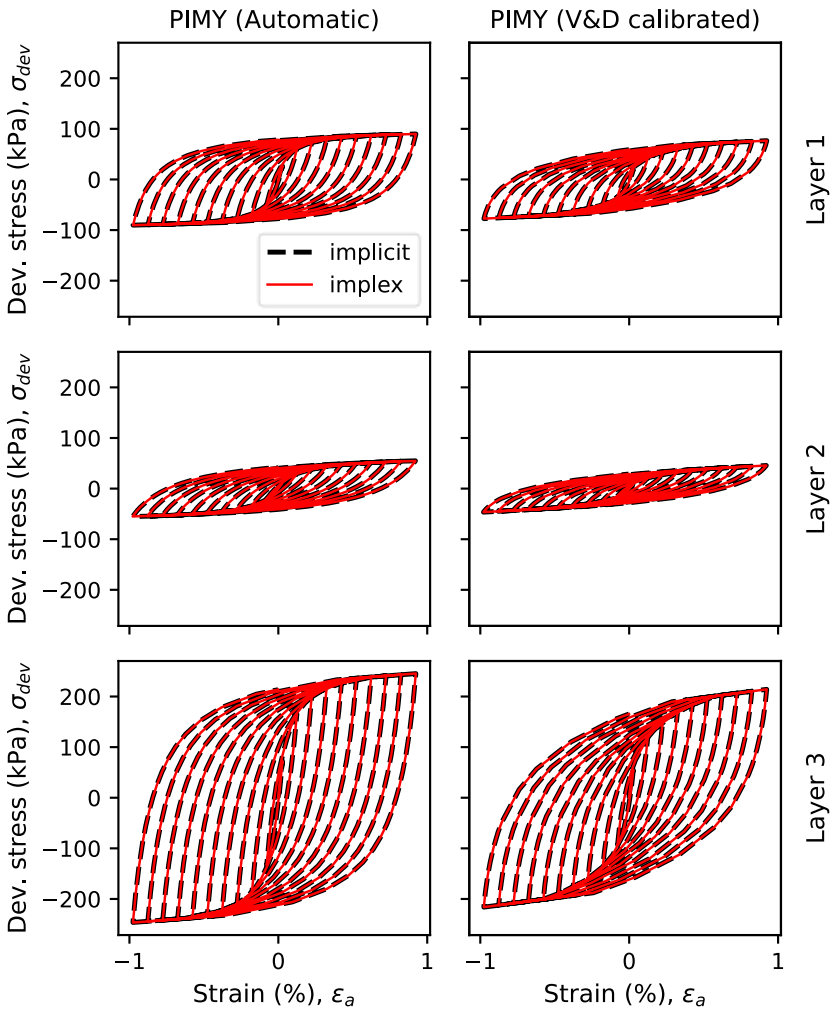

Figure 5.11. Pressure-independent multi-yield (PIMY) surface material cyclic shear stress-strain response computed at the layer centre.

To conclude, the element size accommodates wave propagation with a maximum frequency of 18 Hz in the vertical direction. The target wavelength is computed based on the shear wave velocity of each layer. Since the bedrock layer thickness is variable, the thickest part of the bedrock was considered with a height of 39 meters. Then, the target wavelength is divided into ten elements to compute the target vertical mesh size for the layer. The smallest element size was obtained for the second layer, 0.7 meters. To ensure a minimum 18 Hz frequency elastic wave propagation resolution, convenient element sizes less than or equal to the maximum element size were chosen.

Table 5.6. Vertical mesh design for a target 18 Hz frequency

Layer No.	Thick. (m)	Vs (m/s)	Max λ	Max ele. size (m)	No ele.	Ele. size (m)	fmax (Hz)
1	5	220	12.22	1.22	5	1.00	22.0
2	7	125	6.94	0.69	10	0.70	17.9
3	8	350	19.44	1.94	8	1.00	35.0
Bedrock	39	800	44.44	4.44	10	3.90	20.5

On the other hand, the maximum horizontal wave propagation frequency is related to the size of the soil elements in horizontal axes. Unlike advanced meshing software such as CUBIT (Sandia, 2023), varying the density of horizontal elements with the depth of the model is not possible in STKO. Hence, a single density of elements was propagated throughout the depth of the model. To limit the computational cost, a maximum of 4 Hz horizontal wave propagation frequency at the layer with the lowest Vs (i.e., layer 2) was targeted, leading to a horizontal element size of about 3.6 meters. It is worth noting that while the low-frequency resolution in the second layer might lead to filtering of the topographic effects travelling horizontally from deeper layers, the most significant amount of horizontally travelling waves, i.e., the surface waves, are expected to propagate within the topmost layer which is a stiffer medium than the second layer.

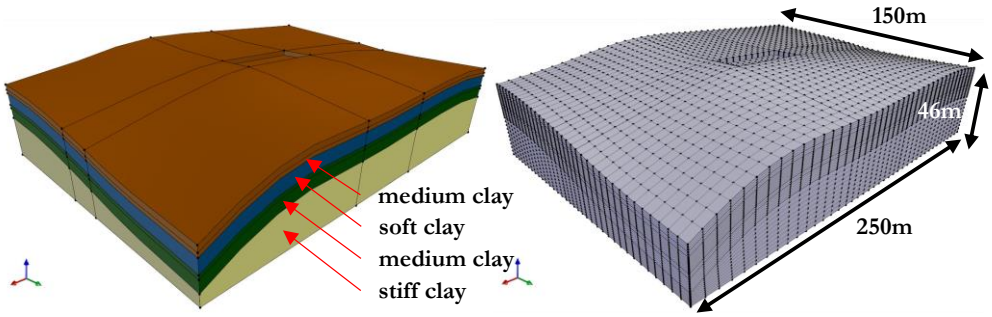

Figure 5.12. The 3D soil model and the mesh design aim for a maximum of 18 Hz vertical and 4 Hz horizontal wave propagation resolution

The final soil model has a total volume of 2,248,900 cubic meters, a footprint of 43,759 square meters, and an average depth of 51.4 m, excluding the boundary elements.

5.5 GEOTECHNICAL MODEL FOR EFFECTIVE STRESS ANALYSIS

A second soil profile is prepared to study the behaviour of the bell tower when liquefaction occurs at a deep layer. To achieve the soil profile, the second layer of the soil profile presented in the total stress model is replaced with a clean sand layer. Therefore, a profile in which a sand layer that is sandwiched between two medium stiff clay layers is obtained.

The sand layer is modelled using the pressure-dependent multi-yield surface model (PDMY02) first implemented by Yang et al. (2003) in OpenSees and then implemented in this thesis following the impl-ex formulation discussed in Section 4.3. The PDMY02 model is calibrated to model the cyclic triaxial test response of Ticino sand specimens tested by Fioravante & Giretti (2016). The model calibration results and steps are discussed in Section 4.4, as a part of the validation study of the implemented impl-ex formulation of the PDMY02 material.

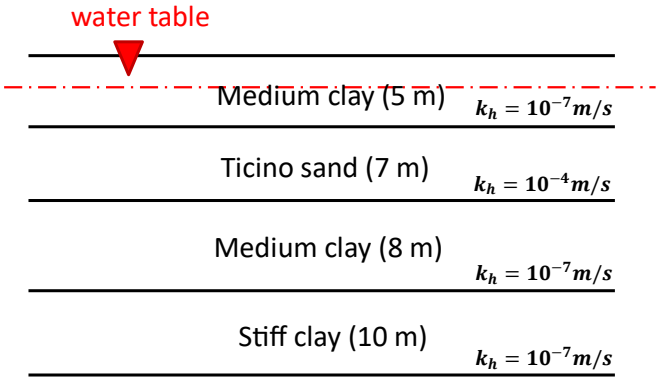

Figure 5.13. The soil profile chosen for the effective stress analyses

The water table is assumed to be at 2 meters deep, in about the centre of the first clay layer, which is consistent with the Vp values shown in, Table 5.4. To include the hydromechanical coupling between the sand layer and the water, an effective stress analysis is done using the Biot (u-p) element formulation. The hydraulic conductivities are taken as 1E-4 m/s for the sand layer, and 1E-7 m/s for the clay layers following the centrifuge test model presented by Özcebe et al. (2021). The vertical and horizontal permeability coefficients required by the u-p elements are computed as shown in Equation 5.1 below:

$$k = \frac{k_h}{\rho_f \cdot g} \qquad \textbf{5.1}$$

where k is the permeability coefficient used in the analysis, k_h is the hydraulic conductivity in meter per seconds, ρ_f is the pore-fluid density, and g is the acceleration of gravity. Unlike the total stress model, the effective stress soil model is only assumed to have a flat surface, as shown in Figure 5.22.

5.6 TOWER-TO-SOIL CONNECTION

As discussed in Sections 5.2 and 5.4, the structural and the geotechnical models were prepared as separate domains with no connection. Having separate models is beneficial since each model has specific geometry and mesh design requirements. For example, the mesh size in the structural model is dictated by the crack propagation (Section 7.3) and the distribution of forces. In contrast, the mesh size is related to the minimum wavelength of interest (Section 6.2). However, connecting two different domains requires additional computational cost due to additional nodes and tie elements compared to a monolithic domain where soil and structure elements share the nodes at intersecting planes. In addition, in geotechnical analysis, replicating the history of the stress conditions that the subsoil has been through might be relevant to the current analysis. Such an initial state analysis might bring additional analysis steps in which the soil domain is brought step-by-step from the application of the gravity loads to the point of structure construction. In the scope of this thesis, an initial state analysis is necessary (covered in Section 8.2) to prepare the soil domain for tower-to-soil connection and then for the dynamic analysis, which includes excavating a portion of the soil domain to place the foundation of the tower.

When all the specific requirements of mesh compatibility, initial state analysis, and available tools in OpenSees are considered, three distinct connection methods are proposed. Each software, such as Plaxis, FLAC or Abaqus offers different techniques to structure and soil mesh, allowing users to create models with varying complexity. A discussion of the proposed techniques, together with methods available in other software, is given below. Among these trialled methods, only the final technique was efficient enough to yield an acceptable solution with a reasonable computational cost.

The first method is a brute-force approach where the structural mesh is propagated into the soil domain, which is available in all software due to its simplicity. This approach repeats the mesh geometry at the foundation faces at the corresponding soil domain faces to provide node-to-match between soil and structure mesh. Then, depending on the meshing capabilities of the software, the fine mesh is gradually transitioned within the large soil domain until it is matched with the geometry of the soil mesh size enforcement and the boundary conditions, resulting in a complex internal geometry. It is worth noting that, in Plaxis and FLAC, continuous mesh strategy is the primary method of providing compatibility. Often, the domain is meshed using nonstructured tetrahedral elements to accommodate the intricate internal mesh. Since tetrahedral elements are relatively inefficient in approximating forces, higher-order elements might be necessary, increasing the computational cost exponentially in large models. Finally, excavation, mesh activation, and deactivation methods are used to satisfy the initial state analysis requirements.

On the other hand, due to mesh continuity, there is no need for additional nodes and elements, somewhat reducing the computational cost. Similarly, a continuous mesh is provided using hexahedral elements in OpenSees (Figure 5.14). The resulting model is enormous, consisting of 585,824 nodes and about a million elements. Considering the size of the model, a static analysis was run, dividing the model into 64 parallel partitions. However, the solution failed since the memory of the available computer (128 gigabytes) was not enough to accommodate the whole model. Once all the elements were activated, the analysis failed during the global matrix factorization stage. Considering that the model consumes high computational resources during static analysis, it was apparent that solving dynamic problems would be even more demanding. Since generating a more advanced meshing using hexahedral elements is not possible in STKO yet, or the cost of using any gradual transition is extreme, the continuous transition strategy is abandoned.

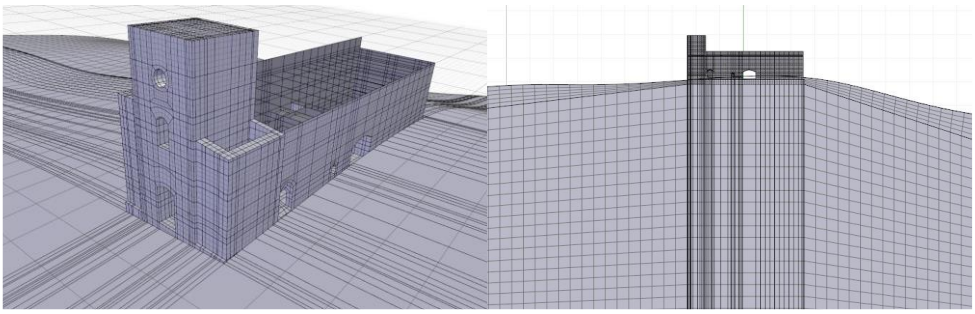

Figure 5.14. Continuous transition. Structural mesh is propagated into the soil mesh. The model size is > 128 GB during matrix factorization with 585,824 nodes and about a million elements. (Abandoned)

The second strategy involves limiting the transition into a controlled volume by enforcing a transition mesh zone where the internal mesh geometry is unconstrained. The transition zone is provided in the soil domain by cutting a 3-meter-thick portion of the first layer and modelling it as a separate soil box. The upward face of the box fits node-to-node to the structure model, whereas the bottom and side faces of the box fit node-to-node to the soil mesh geometry. Within the box, a Delaunay mesh is left free to evolve if the boundary conditions on the faces are met. A solution to this geometric boundary value problem is available only if tetrahedral elements are used and each face has more than a certain number of nodes. The resulting transition zone and the model are shown in Figure 5.15 and Figure 5.16. The three separate domains are connected using *equalDOF* constraints at the intersecting nodes. As the unstructured portion of the transition mesh is localized in a zone, the computational cost is significantly reduced. Now, the model consists of 149,365 nodes and 307,231 elements, a size nearly one-fifth of the previous model, making the analysis much easier and faster. However, the gravity analysis reveals that the strain and stress fields computed in the transition zone are largely incorrect (Figure 5.20). Furthermore,

unacceptably large stress jumps are present between domains, yielding an untrustworthy model. Hence, the transition approach was abandoned as well.

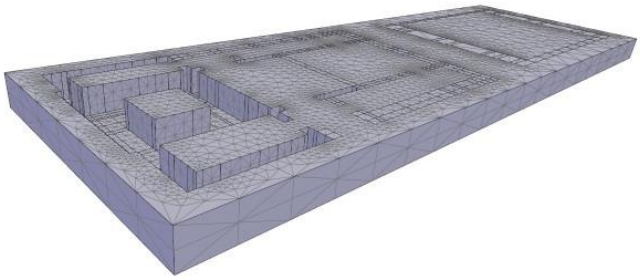

Figure 5.15. The transition zone. A Delaunay mesh that is compatible with the node boundary conditions on the soil and the structure model faces is generated.

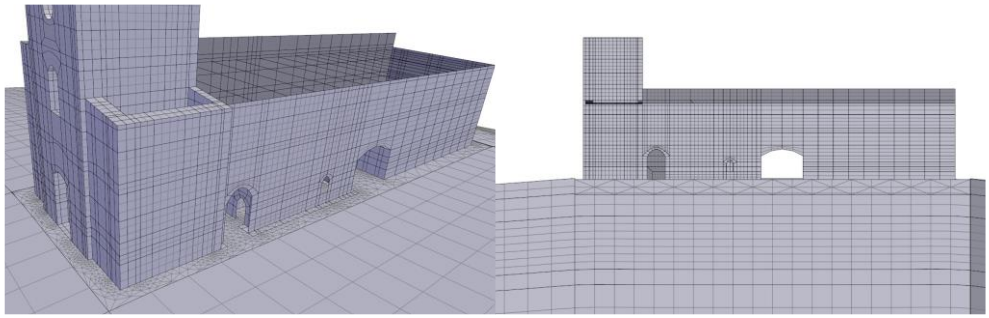

Figure 5.16. SSI model following the transition zone approach. A mesh-compatible transition between the soil and structure is provided by tetrahedral elements. (Abandoned)

Finally, a third approach is applied to connect the structure and soil models, in which the new mesh tie capabilities introduced in OpenSees by the research group in Pescara were employed (Figure 5.18). Following the mesh capabilities offered by the FE software Abaqus and the results obtained by other studies of the bell tower using Abaqus tie elements (Camata et al., 2008; Rosell, 2010), a new mesh tie element called the *ASDEmbeddedNode* Element was implemented in OpenSees by Dr Massimo Petracca to be used in this study. The displacements of the constrained node in the *ASDEmbeddedNode* are restricted to represent the weighted average of displacements from neighbouring retained nodes. Similarly, if the constrained node possesses rotational degrees of freedom, the infinitesimal rotation undergoes a similar weighted averaging process. The element is also capable of

tying two domains with different degrees of freedom, e.g. one domain has a pore-pressure degree of freedom, and the other domain does not, which is helpful in effective stress analysis.

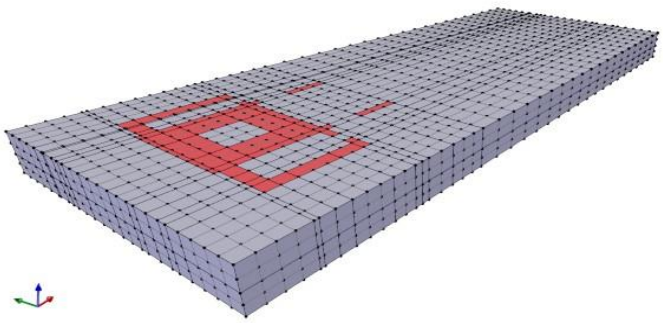

Figure 5.17. ASDEmbeddedNode node transition. A structured transition mesh with hexahedral elements connects the subsequent structure and soil domains using tie elements. (Red hatched zone is removed (excavated) before attaching the tower)

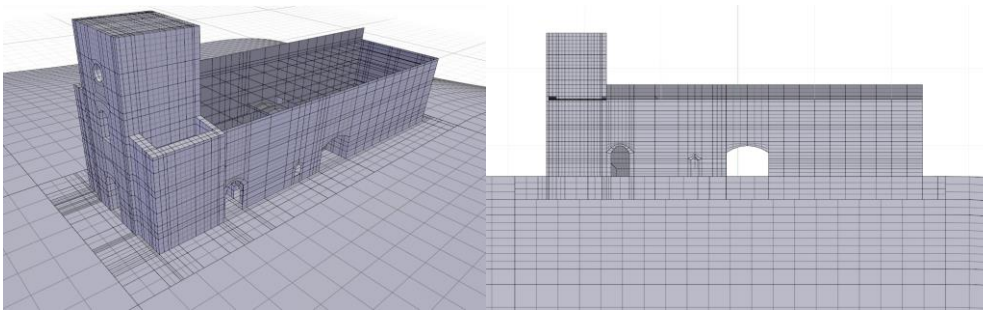

Figure 5.18. SSI model following the embedded node transition approach. An incompatible transition between the soil and structure is provided with hexahedral elements. (Abandoned)

In the next version of the transition soil model, hexahedral elements are used, as shown in Figure 5.17. As a result of employing the embedded node elements, the computed displacement field becomes continuous without a jump, and the number of elements required to mesh the transition soil is reduced considerably. The transition soil model generated following this approach is far more efficient than the previous options. However, dynamic sensitivity analyses reveal that the force-displacement response of the bell tower is mesh size dependent. Figure 5.19 shows the change in the force-displacement response due to the Lazio-Abruzzo 1984 event (Section 6.1) as a function of the mesh size. Notably, as the element size gets smaller, the element displacements and structural displacements, such as vertical settlements, become higher. The settlement amount begins to increase at an increasing rate as the element size becomes smaller than 1.0 meters.

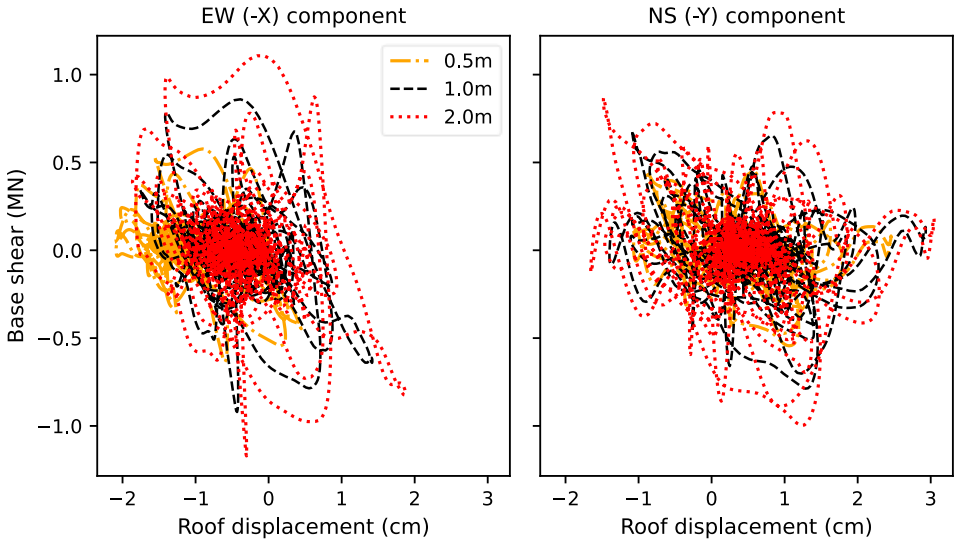

Figure 5.19. The dependency of the recorded force-displacement response of the bell tower on the soil mesh size.

In light of this observation, a kinematic hardening pressure-independent model equipped with a nonlocal hardening law would help overcome the mesh dependency issues around the foundation. Furthermore, considering the potentially complex geometry and mesh of the soil-to-structure connection zone, having a nonlocal hardening capable soil model would also considerably reduce the modelling efforts required to have an unbiased model.

Unfortunately, nonlocal hardening laws have not yet been implemented in OpenSees, leaving most of the models solved in the existing framework prone to localization and mesh bias issues. To offer a case-specific practical solution to this problem, a regular mesh consisting of 1x1x1 meter size elements is used in the transition model. Such a setup does not fix localization issues; however, at the very least, it ensures the calibrated stress-strain response in the soil elements. Achieving a regular mesh within the transition soil box is challenging due to the complex geometry of the bell tower's foundation. The dimensions of the bell tower in contact with the soil elements are rounded to the nearest integer to prevent the need for any fractional-size elements to fill the box volume. The difference between the irregular and regular mesh is illustrated in Figure 5.20.

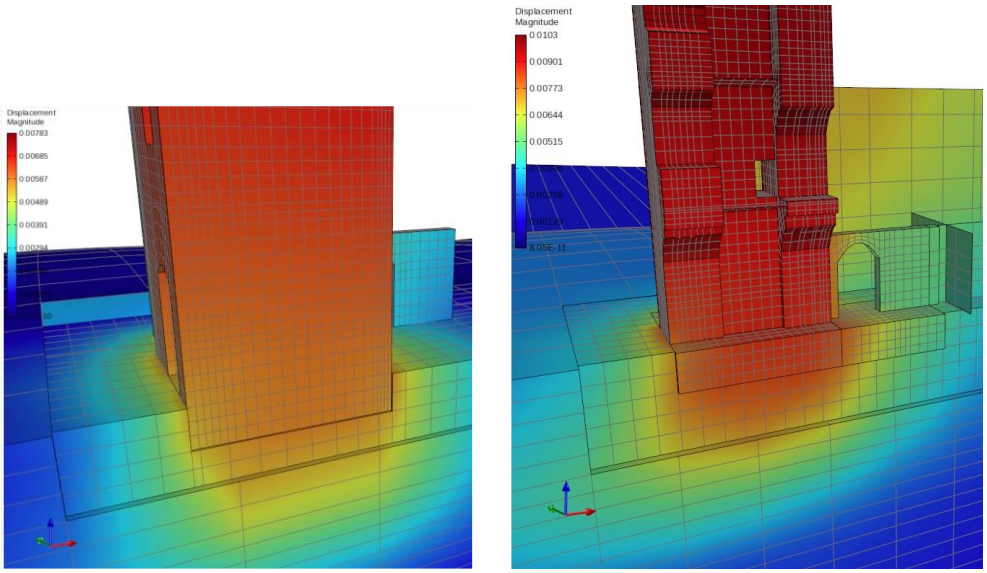

a) Irregular transition soil mesh (Abandoned) **b) Regular transition soil mesh (1x1x1m elements)**

Figure 5.20. Computed displacement field due to the gravity load with a) irregular mesh and b) regular (1x1x1m) mesh with hexahedral elements

To conclude, a series of tower-to-soil connection strategies available in OpenSees are tested. Each connection strategy has advantages and disadvantages. However, an optimal solution is possible using the recently implemented *ASDEmbeddedNode* elements in OpenSees. A transition from the soil layer elements on the meter scale to the structure elements on the centimetre scale by preparing a transition soil box. Meanwhile, the mesh bias issue induced by the foundation displacements within the transition box must be handled. A nonlocal hardening kinematic soil model is suggested. However, a practical workaround is provided in this study, which employs uniform 1x1x1m soil elements within the transition box. This way, at least, the calibrated soil behaviour is ensured in every element.

5.7 DISSIPATIVE BOUNDARY CONDITIONS

It is imperative that the boundaries of the model can dissipate incoming waves reflected from various sources, such as the free surface, topography, soil layering, and structure. Due to structural oscillations and kinematic effects, the foundation is expected to behave like a source in the model and introduce waves propagating towards the boundaries of the model. If the free-field dissipation conditions at the boundaries are not adequately addressed, reflections can occur, leading to significant numerical errors in the model response. Several

approaches available in the literature to address this issue, including the use of viscous dashpot elements (LK elements) (Lysmer & Kuhlemeyer, 1969), free-field column elements (Nielsen, 2006), bulky boundary column models (Su et al., 2019), and the domain reduction method (Bielak et al., 2003; Yoshimura et al., 2003).

At the time of the conception of this work, the available dissipative boundary options in OpenSees were limited to viscous dashpot elements and other custom methods, such as bulky column elements. The most brute-force approach to control boundary reflections is to leave enough space between the boundaries and the structure so that the reflected waves are damped out as they travel to the structure. This method is straightforward and compatible with most models. However, in computationally demanding models like those presented in this work, increasing the model size to accommodate such an effect might unnecessarily increase the computational cost.

Another approach is to use *zeroLength* viscous dashpot (Lysmer & Kuhlemeyer, 1969) elements at the boundaries. However, wave propagation and dissipation characteristics obtained using dashpot elements may be suboptimal since they perform poorly in propagating waves approaching with a skewed angle incidence to their principal axes (Rosell, 2010). Preceding authors tried alternative approaches to overcome this issue. The dashpot elements were added to free-field column-like elements at the boundaries to dissipate the remaining reflections within the model (Petracca et al., 2019; Rosell, 2010).

The Lysmer & Kuhlemeyer, Free-Field (LK-FF) model by (Nielsen, 2006) leverages FF columns to neutralize a significant portion of the upward-traveling waves along the boundaries through destructive interference, while the residual waves are managed by LK dashpots. This approach has been adapted into the OpenSees framework as the ASDboundary element. Within this element, reactions computed at the shear column are applied as forces onto the connecting nodes of the soil model, accompanied by the utilization of a viscous dashpot element. As postulated by theory, these reactions are contingent upon the properties of the boundary material (Nielsen, 2006). Notably, the boundary element faithfully captures the wave propagation solution for an elastic multi-layer model with horizontal layers. However, challenges manifest in nonlinear soil behaviour, particularly at the model edges. Since the ASDboundary element is limited to elastic materials, a stiffness mismatch occurs between the boundary elements and the soil model following the shear modulus degradation of the material. This leads to the dissipation of higher frequencies within the soil body, while elastic wave propagation occurs in the boundaries. As a result of the pronounced amplitude disparity between incident waves within the boundary and the soil model, the boundaries introduce additional waves propagating inward, akin to a secondary source. This phenomenon escalates notably in thicker and narrower models, necessitating careful consideration.

The domain reduction method (DRM) has recently been implemented in OpenSees (Abell et al., 2022). DRM has proven effective for modelling complex soil-structure interaction (SSI) scenarios and was recently applied to model a nuclear energy complex and its reactor (Kanellopoulos et al., 2023). However, when this work was conceived, the implementation of DRM elements was still in progress. Additionally, using DRM boundaries incurs extra computational costs, as a portion of the soil domain outside the boundaries must be modelled, albeit to a limited extent (Abell et al., 2022).

Finally, the bulky column approach was demonstrated by Su et al. (2019) in modelling a wharf structure as an efficient strategy to model dissipating boundaries for a model with nonlinear soil. As per this approach, 2D shear columns with a relatively sizeable second dimension (~50 times larger) were attached to the extremities of the soil model. The column faces in the second dimension were tied by constraining the far node to the opposite retained node via an equal d.o.f. constraint. The wave propagation approaching the boundaries is transferred to the bulky columns and eliminated by taking advantage of the poor displacement field approximation characteristics of a quad element with significantly high aspect ratio distortion. Hence, the boundary columns replicate the infinite free field conditions.

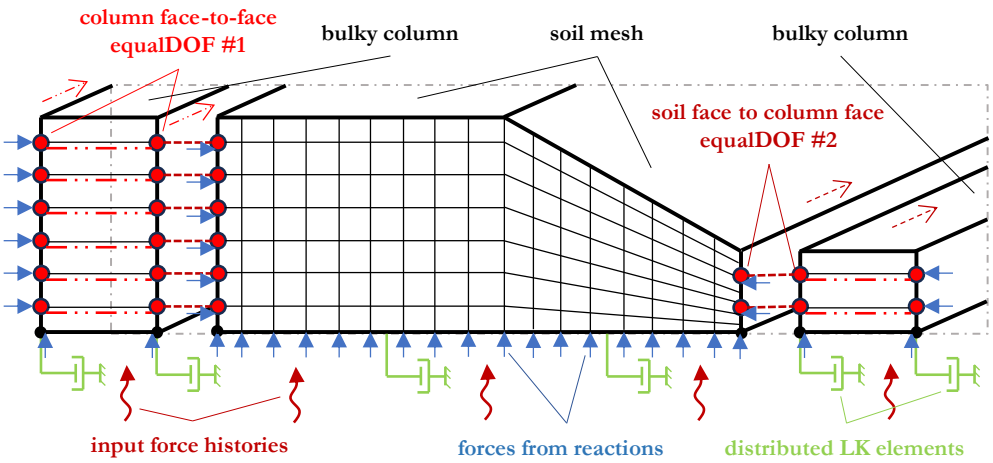

Figure 5.21 Proposed 3D dissipating boundary conditions (BCs). Extension of the bulky column approach used by Su et al. (2019) by adding force boundary conditions to eliminate initial boundary deformations. BCs depicted on the plane view repeat in the third dimension.

A 3D extension of the bulky column approach was employed at the sides of the presented model. All displacement boundary conditions are released after attaching the boundaries via *equalDOF* constraints to provide wave propagation within the boundary columns. As an extension of the approach employed by Su et al. (2019), the dynamic equilibrium is

satisfied by taking the reactions computed at the gravity analysis step and applying these as forces at each node (Figure 5.21). This strategy allows no or insignificant artificial deformations at the boundaries due to the release of static BCs, and the dynamic boundary conditions can be attached to the model without further considerations. In fact, at the beginning of the subsequent analysis stage after the release of fixities, no wave propagation due to the deformation of the model is observed around the model and at the boundaries.

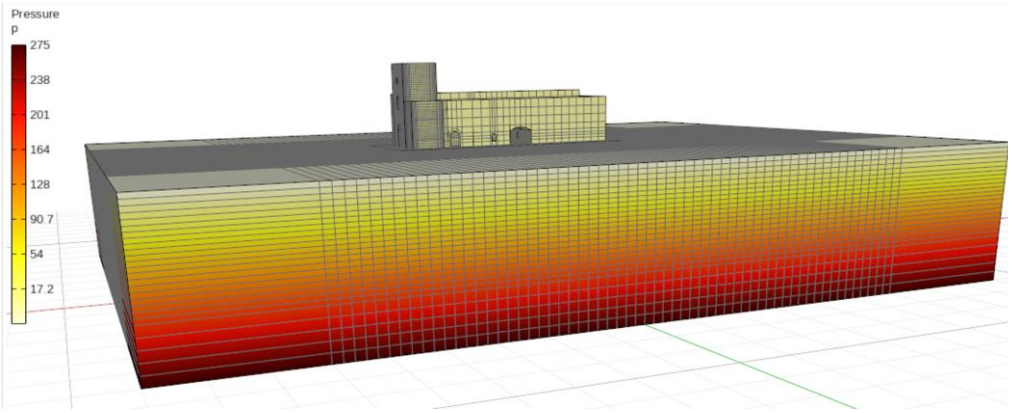

Figure 5.22. The computed pressure field in the bell tower with church model as the result of initial state and gravity analyses

At the bottom of the model, the returning waves reflected from layer interfaces, surface, and topography, as well as waves generated due to the oscillation of the structural masses within the model, are dissipated with viscous dashpots. The viscous damping coefficient is computed according to the elastic bedrock medium that the elements are attached to and then scaled with the element area as in Equation 5.2. In STKO, the scaling operation can be done automatically and with ease, since the software offers automation to scale the material constants of a *zeroLength* element (LK element in this case) with the area of the attached solid element, A_{ele} as shown in Equations 5.2 and 5.3.

$$C_{normal} = A_{ele} \cdot \rho \cdot V_p \qquad \textbf{5.2}$$

$$C_{transverse} = A_{ele} \cdot \rho \cdot V_s \qquad \textbf{5.3}$$

The input motion is applied as a force history on the bottom face of the soil model to prevent any modification by the acceleration-sensitive LK elements present at the nodes. The conversion to force is done by integrating the acceleration history with the velocity history. Then, the resulting signal is multiplied by the medium's damping coefficient, C, to obtain force. The force history applied at each global axis can be found by multiplying the corresponding velocity history by the axis damping coefficient. The details of the boundary elements can be seen in Figure 5.21.

Finally, the pore pressure d.o.f. can be added to the soil elements to model the hydromechanical coupling between the water and the soil skeleton (Figure 5.22). One challenge that still needs to be solved is the application of the vertical motion at the bottom of the model when the dissipating boundaries are modelled with the free-field column and viscous dashpot elements. In OpenSees, the direction of gravity is essential in the u-p element formulation in computing the hydrostatic pressure. The u-p elements need the vertical fixes to achieve a solution. Therefore, the force boundary conditions are not enough to achieve dynamic equilibrium in this case. This means that the vertical motion cannot be applied with the boundary conditions that are described in this section. This problem can be solved by switching to other types of boundaries such as the DRM method in which all the extreme boundary nodes can be fixed. However, using the pressure d.o.f. and a soft material inside the DRM box must be studied further to understand how to deal with possible numerical instabilities in such a setup.

In horizontal boundaries, the dynamic equilibrium can be provided using the force boundary conditions and heavy free-field elements to prevent initial horizontal displacements at the boundaries. However, the horizontal displacements cannot be eliminated unlike the case without pressure d.o.f.s. Hence, a small amount of displacement that does not cause significant consequences in the dynamic analysis is expected at the boundaries. In case the model is large enough, the slip at the boundaries can be further improved by employing periodic boundary conditions by tying each d.o.f. at the boundary to the corresponding node at the opposite side of the model.

5.8 PARALLEL MODELLING AND SOLUTION

The computational framework employed for solving the model is OpenSeesMP, the parallel counterpart of the OpenSees code, designed to harness the capabilities of the MPI (Message Passing Interface) multithreading API (Mckenna & Fenves, 2007; McKenna, 1997). The exploration of parallel computing applications in civil engineering problems was previously investigated by numerous authors (Bahçecioğlu, 2011; Ben, 2013; Bui & Meschke, 2020; Frohne et al., 2016; Guo & Zhao, 2016; Lu et al., 2012; McKenna, 1997; Simpson et al., 2023; Tian et al., 2015). In OpenSees, parallelization options are offered through OpenSeesSP and OpenSeesMP versions. Each software uses the MPI toolkit as a core but differs in solution objectives. OpenSeesMP is designed to run concurrent solutions of the same model, whereas OpenSeesSP has the capability to decompose a large model into small partitions and solve in parallel (Mckenna & Fenves, 2007).

However, STKO uses an alternative parallelization approach. First, a substantial problem is decomposed into independent sub-domains or threads. Each thread is uniquely identified by a process ID ranging from 0 to the number of threads minus one, with process ID 0 designating the primary thread. STKO mesh builder decomposes the model into the

designated number of partitions. Each domain composes of elements and nodes of the large model that fall into the corresponding sub domain. In OpenSeesMP, concurrently running models share the same domain even if they do not share any degree of freedom. Continuity between adjacent domains is provided by duplicated nodes (providing shared d.o.f.s) at the intersecting boundaries. Hence, the nodes at the extremity (surface) of a sub-domain make the boundary conditions for the intersecting domains. During the solution, partition stiffness matrices are individually assembled in parallel, and the solution of the global matrix is provided by the parallel system of equations handler. The factorization cycle is triggered following the completion of assembly in each partition through a barrier condition.

Following an iteration of the nonlinear solution algorithm, such as the Newton-Raphson method, the nodal deformations of the entire model are computed. Subsequently, based on the partitioning, these nodal deformations are applied as boundary conditions to each sub-model. Simultaneously, the elements and materials within each partition are updated in parallel. Ultimately, the residual and stiffness matrices generated in each partition are consolidated in the main thread, returning to the global matrix factorization step to complete the iteration. The MUMPS (Multifrontal Massively Parallel Sparse Direct Solver) system in OpenSeesMP is chosen for its compatibility with such a solution algorithm (Amestoy et al., 2001, 2019). Notably, the MUMPS system can also conduct the solution of the global matrix equation in parallel, leveraging suitable matrix decomposition algorithms.

The adopted solution scheme in STKO allows users to achieve parallelization for any material and element implemented in OpenSees, even in cases where the source code was not implemented with the parallelization of the element or material in mind. Therefore, any model that works in the sequential version of OpenSees can be parallelized using the adopted approach.

5.8.1 System of equations and the global integration algorithm

In this section, a parallel reverse Cuthill-McKee algorithm is employed to assign unique degrees of freedom (d.o.f.) to nodes within the created partitions (Cuthill & McKee, 1969). Notably, certain nodes, particularly those associated with dissipating boundary elements, are subject to multiple constraints. To address this, a penalty constraint handler is selected to enforce fixities and ties between nodes. Determining an appropriate penalty value is crucial, considering the values within the stiffness matrix, as an inadequate value may result in suboptimal mesh compatibility, a singular matrix, or a precision issue. Experience shows that a penalty value around eight orders of magnitude larger than the most significant number in the stiffness matrix is enough to enforce boundary conditions and provide a smooth displacement field.

The convergence condition is pursued by evaluating the norm of the displacement increment vector in the global system of equations akin to a sequential solution. It is worth noting that checking the norm of the unbalanced force vector may result in convergence issues due to the presence of large forces in the vector due to the penalty method. The strategic selection of components constituting the solution procedure significantly impacts the final computational cost. In problems involving implicit-explicit (impl-ex) methods, the step order of accuracy (i.e., first-order accuracy) is demonstrated to be equivalent to that of the implicit solution (Oliver et al., 2008). However, the committed error is larger in the impl-ex solution. Hence, unlike the implicit approach, the stability of the solution is not inherently guaranteed. As acknowledged, a marginal error may accrue at the conclusion of each step, accumulating over subsequent steps.

To mitigate error accumulation, it is imperative to employ a sufficiently short time step, aligning with the Courant-Friedrichs-Lewy (CFL) condition (Courant et al., 1928). This condition necessitates a small enough error step to ensure a stable and accurate solution. For impl-ex materials, the optimal time step lies between the explicit (micro-seconds) and implicit (hundredths of a second) solutions. In seismic assessment scenarios, the analysis step is typically chosen as the record sampling frequency or as an interval that preserves the maximum frequency the mesh is designed to capture or corresponds to the significant frequency content of the event (often 0.1 - 20 Hz). In the context of this study, a stable solution is achieved using a time step not larger than the sampling interval of the input motion.

The TRBDF2 composite integrator (Bathe, 2007) in OpenSees is employed to enhance stability. This integrator employs a two-sub-step approach, where the first half-step is integrated using the trapezoidal rule and the second via a three-point backward Euler step. While possessing second-order accuracy akin to the trapezoidal method, TRBDF2 requires fewer iterations for convergence on average (Bathe, 2007). Furthermore, the introduction of numerical damping in the solution, resulting from the application of a three-point backward Euler scheme, serves to enhance stability by damping higher frequency oscillations, such as point-wise instabilities. It is noteworthy that the numerical damping of higher frequencies is not anticipated to impact the response of the structure significantly.

5.8.2 Domain decomposition considering analysis staging

Decomposing the domain into many partitions can become a challenging task in a staged analysis, as shown in Figure 5.23. The staging of the analysis might become necessary in computing the initial stress state of the soil model before the dynamic analysis, especially during effective stress analysis. During th initial stages, some elements in the model might need to be turned on and off depending on the evolution of the model. For example, an

excavation of the topsoil would need removal of some of the elements whereas the construction of the tower would be done by adding new elements.

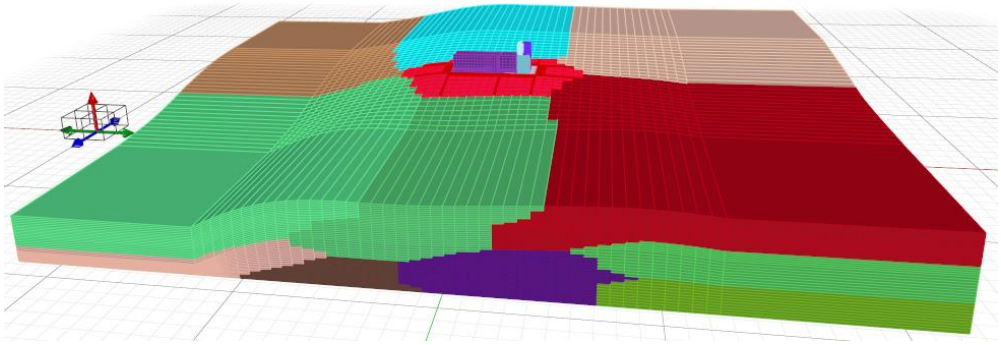

Figure 5.23. The illustration of domain decomposition in STKO achieved for 24 parallel proceses.

In Plaxis, the staged analysis can be done by turning on and off the elements in the model. The software allows multiple elements to exist at the same location and if an element is turned off, that elements is not included in the FE assembly process. This approach is convenient since the whole model is written in the domain at the beginning of the analysis, leading to no empty partitions. However, at the time of conception of this work, a technique to switch elements on and off in a systematic manner have not been implemented in OpenSees yet. Therefore, a staged analysis can only be achieved by systematically removing and adding new elements and nodes in the domain. If a large portion of the model is omitted at the beginning of the model such as the bell tower, the domain might start with empty partitions which would lead to the global failure of the analysis.

In this study, the whole model is added to the domain at the beginning of the analysis to prevent empty partitions. However, the connection between the bell tower and the soil model is not provided until the construction stage. Instead, the structure is modelled as independently in the domain without any loads and fixed boundaries to prevent numerical instabilities. Before the construction stage, the fixes were removed, and tie connections are provided between the tower and the soil elements. To prevent issues at the tie connections, the soil deformations are reset keeping the stress state computed up to that stage of the analysis. This way no partitions begin the analysis empty making parallel analysis possible.

5.8.3 Other practical observations

In the context of a sequential solution in OpenSees, memory management is a relatively straightforward process. The system either possesses sufficient memory space to accommodate the entire model or it does not. In cases where memory limits are exceeded, data is paged from the slower long-term memory into the RAM, and in severe instances,

the operating system may freeze or shut down. Contrastingly, in a parallel solution using OpenSeesMP and the MUMPS, the amount of memory required to solve the model is unknown a priori. The memory occupied by the model depends on the number of partitions and the size of each partition. Since, as each partition may exhibit distinct number of elements and nodes, a unique amount of space in the memory is required to be allocated to each partition. However, estimating the exact size of each partition before analysis can be challenging. Consequently, the MUMPS solver initiates by establishing a static space in memory for the entire model, assuming a fixed size for each partition as a function of the number of entries of the largest matrix (Amestoy et al., 2019). Typically, this estimated size is anticipated to accommodate only the matrix factorization, and additional memory must be allocated for other processes, such as recorders for example. The user can exert control over the percentage increase in estimated memory through the memory relaxation parameter, ICNTL14, which amplifies the allocated memory for each partition. It is imperative that the requested memory space aligns with the available memory for the solution cycle to start. Given the diversity in partition properties, the memory relaxation parameter is set to the lowest value preventing a system crash, typically corresponding to the largest partition. Hence, in complex models, finding the optimal ICNTL14 parameter can become an optimization problem that should be solved by trial and error. Depending on the recording requirements and model complexities, the ICNTL14 parameter can increase up to around 80% for static cases and more than 100% for dynamic scenarios (Figure 5.24).

The amount of required memory for each model is contingent on various modelling choices, including the number and properties of model features, the number of recorded outputs between steps, and, for parallel problems, the number of processors. Notably, the size of recorded outputs, the number of nodes, d.o.f.s, and the type of analysis (dynamic or static) significantly impact the maximum memory occupancy. This is because, after each step, all results must be stored in memory until they are written for long-term storage. The total number of d.o.f.s directly influences the size of the global matrix equation obtained after the factorization process, while dynamic analysis demands more space due to the inclusion of mass and damping matrices.

Conversely, as the model is subdivided, the time allocated to solve each partition approaches the time required for integration at the parallel barrier condition. Beyond a certain point, increasing the partition size may result in a bottleneck rather than optimizing solution time. Based on the author's experience, in the case of the CPU, AMD Ryzen Threadripper 3990X with 64 physical cores, utilized in this study, significant improvement in solution time is not observed beyond having less than around 8,000 elements or 12,000 nodes in a partition on average.

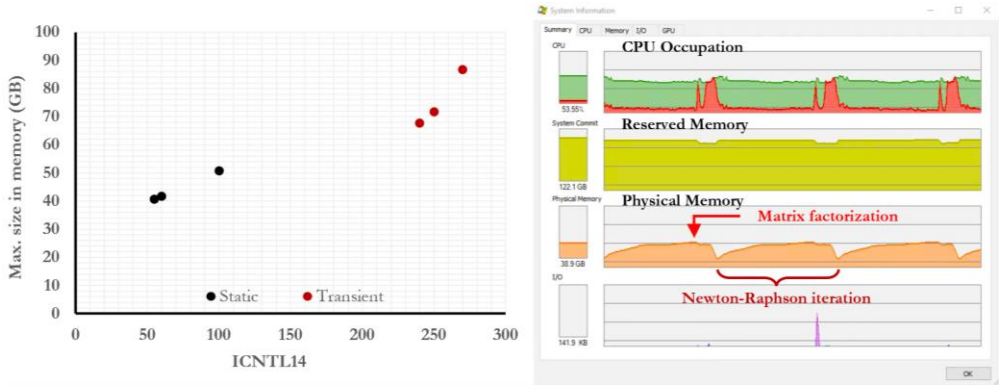

Figure 5.24. Amount of memory occupied by the nonlinear SSI model during matrix factorization versus the MUMPS solver ICNTL14 parameter. The tested model consists of 435,000 elements and 64 partitions.

Finally, considering the thermal aspects of parallel computing, monitoring the processor temperature is vital to prevent potential damage and interruption. Excessive temperatures exceeding 100 degrees Celsius or prolonged exposure to temperatures above 90 degrees Celsius may jeopardize the CPU. Operating systems or CPU drivers often intervene by throttling down system performance or, as a last resort, restarting the system to flush active processes while maintaining the cooling system active. Such interventions may lead to extended analysis times or abrupt interruptions without notice, rendering incomplete results. Therefore, efficient cooling strategies and careful consideration of CPU loads, particularly in relation to the number of partitions, are paramount. The number of partitions chosen directly controls the maximum CPU wattage observed, which in return controls the heat generated by the CPU during the most intensive solution period. Determining the optimal number of partitions involves iterative evaluation of available cooling potential while monitoring CPU temperature and load through dedicated software.

To conclude, it is essential to recognize that, for large models, shared memory (RAM) consumption can be as limiting as processing power. Effectively managing memory is a fundamental challenge in the presented numerical model. Adequate memory allocation between partitions is crucial to ensure a healthy solution at each step. Improper memory settings may lead to bottlenecks, slowdowns in solution time, malfunctioning output recorders, or even complete solution failure.

5.9 SUMMARY AND DISCUSSION

In this chapter, the finite element modelling of the virtual laboratory was presented. The virtual laboratory consists of the bell tower of Guardiagrele, and the St. Maria Maggiore cathedral SSI system. The model combines advanced numerical techniques implemented

in OpenSees, including the impl-ex contact elements, as well as advanced mesh coupling methods to control the computational cost of one analysis. Mesh coupling techniques, including *ASDEmbeddedNode* elements, were critical in bridging the structural and geotechnical domains.

The bell tower and the soil profile are modelled with brick elements. The masonry is modelled with a suitable damage-plasticity material, while the soil profile was defined using two different assumptions. First the profile is assumed to consists of fine-grained layers that are modelled with the pressure-independent material model consistent with the total stress analysis approach. Then, the soft clay in the second layer is replaced with a clean sand layer to model a liquefaction scenario. In the second case, effective stresses were considered by employing u-p elements that follows the coupled Biot formulation.

Practical modelling information regarding the mesh transition, boundary conditions, and the challenges of parallel solution are discussed.

In conclusion, this chapter highlighted the capability and challenges of modern FE techniques and numerical tools in modelling complex SSI problems. While achieving robust SSI models is possible, further refinement is needed to mitigate mesh dependency issues at the foundation soil. Future work could explore the use of nonlocal hardening laws to address mesh bias in the soil domain and enhance the model's performance in simulating geometrically complex soil-structure interaction systems.

6 GROUND MOTION DEFINITION AND FREE FIELD SITE RESPONSE ANALYSES

This chapter focuses on ground motion definition and free-field site response analyses for evaluating the seismic behaviour of the bell tower. Eleven ground motions are selected to match the conditional spectrum conditioned on average spectral acceleration (AvgSA) expected at the site with a 475-year return period. In this study, the AvgSA is defined as the range of predominant frequencies that are important in the vibration characteristics of the bell tower SSI system. The strong motions are selected for outcropping bedrock conditions. Then, proper deconvolution and careful processing of the signals are carried out to prepare the record set for time history analysis. Nonlinear 1D free field response analyses are carried out to obtain the free surface motion set for the fixed base analyses. Additionally, the chapter investigates two- and three-dimensional topographic amplification effects and the influence of liquefaction on the observed free surface accelerations.

KEYWORDS: Ground Motion Selection, Site Response Analysis, Soil Amplification

6.1 1D GROUND RESPONSE ANALYSIS PROBLEM

The amplification or de-amplification of ground motion due to the local soil conditions is critical to defining the shaking characteristics expected at the structure's foundation. Site response analysis is often used to characterize the seismic shaking at the location of interest, given an acceleration recorded at a seismic station. One way to compute the acceleration history at the free-surface due to a recorded strong motion is by solving the 1D ground motion problem following the steps outlined below.

Steps of a 1D ground motion problem:

1. Define a suitable intensity measure (IM) for the problem.
2. Select a set of ground motions recorded at the outcropping bedrock.
3. Deconvolution techniques are employed to obtain the incoming (within) motion corresponding to the soil profile's bottom.
4. Solve the free field 1D linear, equivalent linear, or nonlinear soil column to obtain the acceleration history at the surface.

It is worth noting that information such as the bedrock depth and soil profile are required, including the bedrock properties. Additional challenges might occur in finding enough

ground motions recorded at outcropping bedrock that suit the search criteria. However, as a result, the mean spectral shape of the record set computed at the free surface strongly reflects the site's characteristics, which may not be achieved by using scalar proxies, such as Vs30, to guide the record selection process. From a structural perspective, the acceleration history obtained from the 1D ground motion problem is suitable for running fixed-base analyses since the fixed-base boundaries are fully reflective, and the accelerations at the fixed nodes are imposed. However, kinematic effects such as foundation filtering are disregarded in this process, which might alter the high-frequency content of the records, as well as SSI effects such as foundation rotations.

On the other hand, the direct SSI model explicitly incorporates the 1D ground motion problem mentioned above, including the kinematic and inertial SSI effects. Hence, the deconvolved motions corresponding to the model base depth must be applied. This way, the results obtained from the SSI model can be compared with the fixed base model.

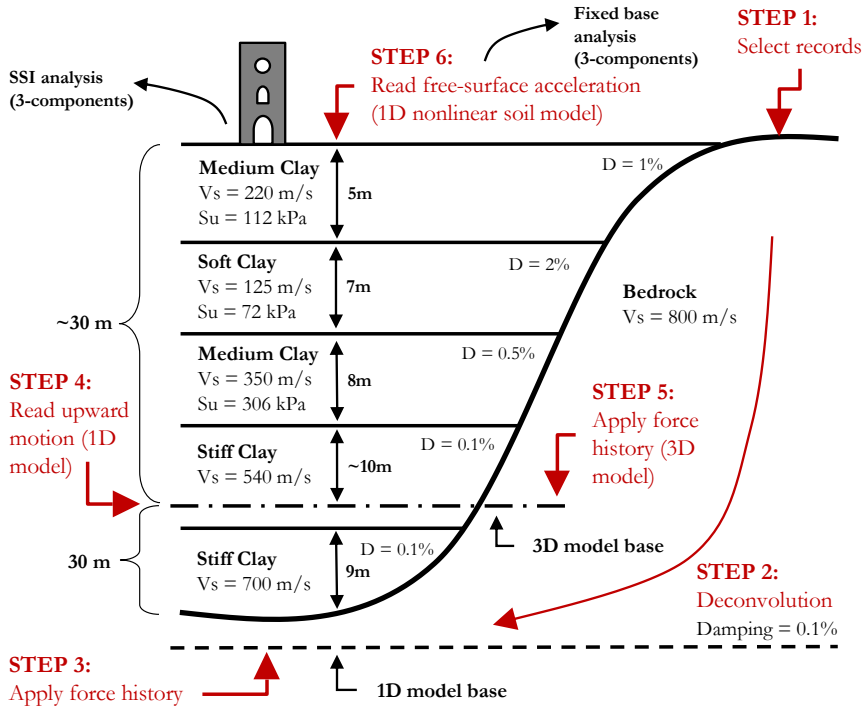

Figure 6.1. Illustration of the 1D ground response problem considered in the thesis. The aim is to ensure that the accelerations acting on the tower during the SSI and fixed-base analyses are compatible.

Furthermore, as the incident motion travels upwards, its amplitude and frequency content are expected to be modified due to topographic effects. As mentioned in Section 5.1, the bell tower is located at the top of a sloping ground, mainly in the east-west direction (coinciding with the global X direction of the model). Concave features in the topography are known to focus the incoming waves at a focal point aligned with their apex. Hence, some amount of amplification is expected. However, due to possible hysteretic damping of higher frequencies, the frequency range of the amplification and the propagation path of the wave front until it reaches the foundation of the bell tower might play a significant role in the observed amplifications. Hence, the size of the topographic features required to be included in the model in order to capture the topographic and basin effects accurately is an open question studied by many authors (Dawadi et al., 2024; Hallal & Cox, 2023; Mohammadi et al., 2024).

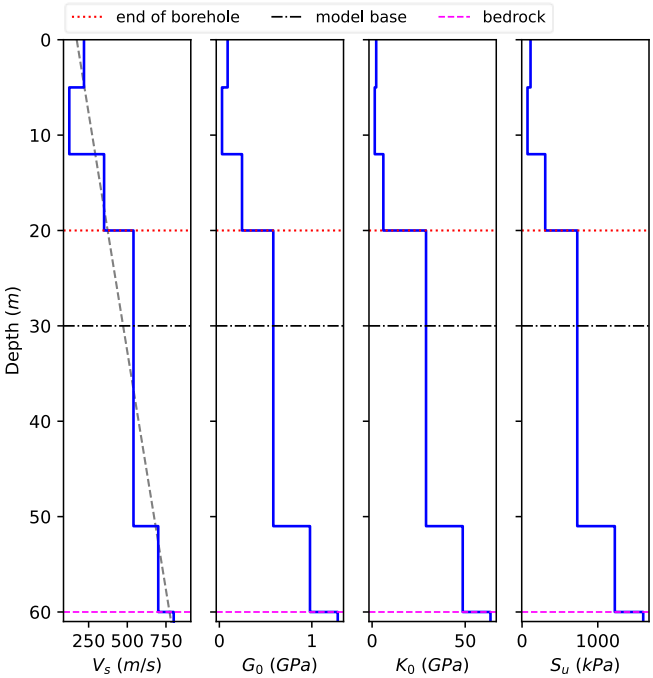

Figure 6.2 Assumed bedrock depth and the shear wave velocity profile.

The 1D ground response problem shown in Figure 6.1 ensures a compatible shaking intensity across the bell tower models proposed in Chapter 5, given a set of ground motions. First, the record set is selected for the outcropping bedrock properties (Section 6.4). Then, the selected motions are deconvolved to obtain the motion at the bedrock depth (Section 6.2). Since the bedrock depth is unknown, a depth of 60m is assumed by linearly extrapolating the shear wave velocity (Vs) profile until the shear wave velocity of 800 m/s

is achieved (Figure 6.2a). Along with the parabolic gradient, generic gradient, and the Gibson model, the linear gradient approach is widely used to assume a bedrock depth when the site investigation data is incomplete (Andreotti et al., 2018; Cascone et al., 2022). The elastic properties of the profile are computed as a function of the shear wave velocity, as shown in Figure 6.2. Finally, the undrained shear strength is computed as a linear function of the shear wave moduli or the undrained Young's modulus, as suggested by other studies (Anastasopoulos et al., 2011; Das, 2011).

The 1D column and SSI models are 30m deep to reduce the computational cost. In Figure 6.1, the location of the model base depth within the assumed 1D soil profile can be seen. Since the motion at the bedrock is used, the acceleration caused by the bedrock motion at the model bottom is computed by solving an additional step of 1D site response analysis between the bedrock and the model bottom. The deconvolution process is done using the software STRATA (Kottke & Rathje, 2008). Then, the obtained motion is used in solving the nonlinear 1D, 2D, or 3D total, and effective stress models discussed in the following chapters of this thesis.

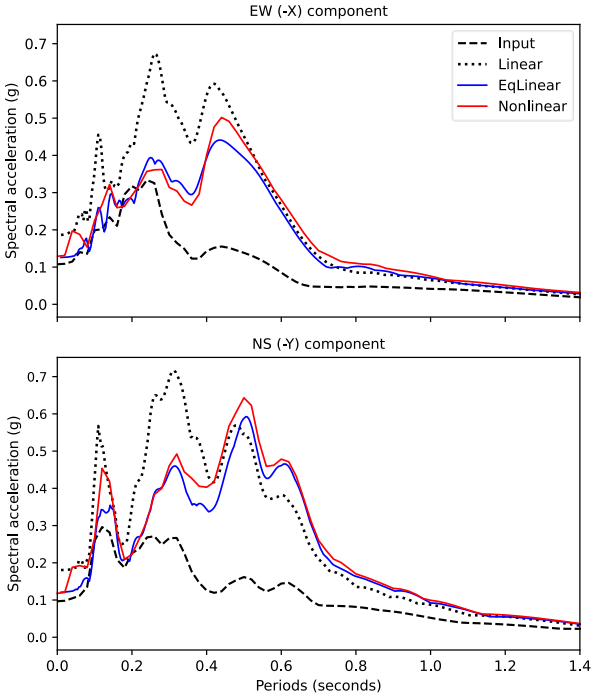

Figure 6.3. (Lazio-Abruzzo 1984) 1D site response comparison of linear, equivalent linear, and nonlinear amplifications. The input spectrum is plotted at outcropping bedrock.

Figure 6.3 shows the results of the 1D site response analyses for linear, equivalent, and nonlinear soil profile assumptions. The nonlinear and equivalent linear soil properties are calibrated to match the stiffness reduction curves suggested by Vucetic & Dobry (1991) and discussed in Section 5.4. The input motion is the Mw 5.9 Lazio-Abruzzo event in 1984 recorded at the "ATINA" station. This motion was selected for the bell tower of Guardiagrele by Rosell (2010) using inelastic SaT (spectral acceleration at the elongated period as a result of pushover analysis) and employing the REXEL record selection platform.

6.2 RECORD PROCESSING AND DECONVOLUTION

In this section, deconvolution and signal processing procedures are described. The ground motions selected at the outcropping bedrock are deconvolved to obtain the bedrock motions at 60m depth. Furthermore, the downloaded ground motions, either downloaded from the NGA West2 (Ancheta et al., 2014) or the ESM (Luzi et al., 2020) databases, are further processed to reduce the record time as much as possible without significantly altering the frequency content and the properties of the records.

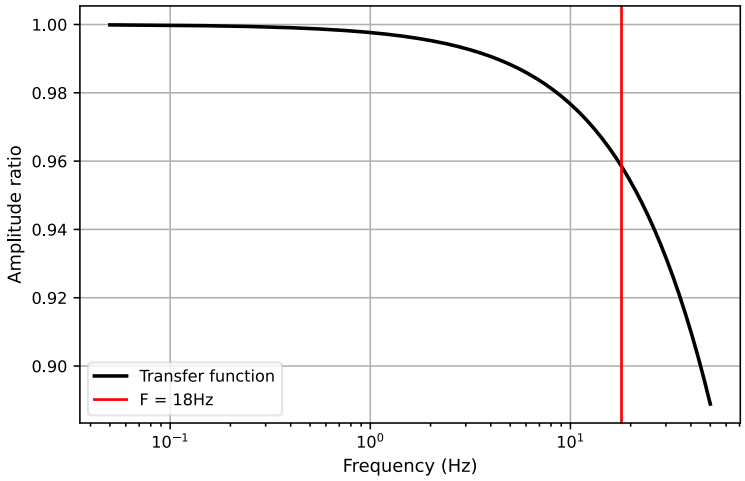

Figure 6.4. Outcropping bedrock to 60m deep bedrock transfer function. Linear model with vs = 800 m/s and 0.1% damping. It is computed in Strata.

The deconvolution of horizontal components is done for a homogenous layer of 60m thick bedrock with a Vs of 800 m/s. Some 0.1% damping is included to model the energy dissipation in the bedrock due to elastic oscillations. A similar approach is followed for the deconvolution of the vertical components using the P-wave modulus of the medium. During deconvolution, the within motion at the bottom of the soil column is computed

mainly using frequency domain methods, given the acceleration history of the surface motion. Figure 6.4 shows the transfer function of the deconvolution profile. Alternatively, for shallow profiles, the bedrock within motion is obtained by multiplying the outcropping motion to strip the input motion from the surface effects. This method is used as a practical method to obtain the input motion when a direct deconvolution is not done. In the case of the scaling approach, a limited loss of 4% at 18 Hz would be expected, which is the design frequency of the 1D, 2D, and 3D models in OpenSees, which might be acceptable considering the scope of this study.

On the other hand, the selected ground motions are processed before analysis to achieve the following goals:

1. Reduce overall analysis time to the minimum duration possible.
2. Filter frequencies higher than 18Hz to prevent noise in post-process.
3. Remove any artificial permanent displacement due to the applied time and frequency windows.
4. Integrate the acceleration histories to obtain velocity histories.

The signal processing is done in Python using the SciPy library. The ground motion is multiplied with a time window in the time domain to reduce the analysis time. A smooth Tukey window is chosen to prevent undesired distortion effects of employing a sharp window in the frequency domain. The corner times of the time window are chosen to provide natural characteristics of the ground motion. The start time is taken as the time when the vertical component reaches 5% Arias intensity, whereas the end time is taken as the maximum of the times when the horizontal components reach 95% Arias intensity. Table 6.1 summarizes the chosen corner times for the time window.

Table 6.1. Time window corner values and corresponding Arias intensity values.

Component	T_{Start} (seconds)	max (T_{End}) (seconds)
UD	5% Arias intensity	-
EW	-	95% Arias intensity
NS	-	95% Arias intensity

After the ground motions are cropped, a fourth-order bandpass filter is applied to allow frequencies between 0.1 Hz to 18 Hz. Next, any permanent displacement at the end of the record is removed with a second-order baseline correction. Finally, the processed records are integrated to obtain the velocity histories to be converted to force histories.

6.3 SUITABLE INTENSITY MEASURE DEFINITION

The intensity measure (IM) selection for the analysis could substantially influence the results. Intensity measures are quantitative parameters that characterize the severity of anticipated ground motion at a specific location for a given return period. The intensity measure best suited to each problem is strongly related to the engineering demand parameters (EDP) under investigation and may vary depending on the specific nature of each problem. Effective IMs are sufficient, i.e., for a given value of the IM, the distribution of the EDPs does not depend on other earthquake characteristics; efficient, minimizing the variability in EDPs given the IM; and practical, being computable with relative ease using existing hazard frameworks (Kohrangi et al., 2016; Luco & Cornell, 2007). Possible IMs include:

1. Peak ground acceleration, PGA,
2. Spectral acceleration, SA,
3. Average spectral acceleration, AvgSA,
4. Pseudo-spectral velocity, PSV,
5. Cumulative absolute velocity, CAV, and
6. Arias intensity, IA.

In this study, the ground motion selection is done by scaling motions to match the conditional spectrum (CS) (Baker, 2011; Kohrangi, Bazzurro, et al., 2017; Lin et al., 2013) using an efficient, sufficient, and practical intensity measure (Luco & Cornell, 2007). SA is a well-established, efficient, and sufficient IM for assessing structural response, especially for assessing structural EDPs such as roof displacement, RD, or inter-storey drift ratio, IDR. Numerous ground motion models (GMMs), hazard models, and record selection algorithms are available in the literature for SA; hence, SA is also practical. However, using only peak transient IMs such as SA yields suboptimal results in computing vertical settlements compared to evolutionary IMs that accumulate throughout shaking, such as cumulative absolute velocity (CAV). Regarding foundation rotations, PSV was identified as the most efficient IM (Bullock et al., 2018; Dashti & Karimi, 2017; Karimi & Dashti, 2017). There is a wide range of literature and practice on the predictability of CAV and CAV-based record selection; however, this topic is still maturing. PSV is a more practical IM compared to CAV; however, accessible hazard models such as SHARE (Woessner et al., 2015) do not support producing hazard curves and disaggregation in PSV due to the employed GMMs in some of the logic trees. To address this issue, empirical correlations between spectrum-based intensity measures and PGV and CAV have been proposed by Bradley (2012b) and Wang & Du (2012), respectively.

Another issue in using CAV and PSV is the relatively strenuous selection procedure compared to SA using generalized conditional intensity measure methods (Bradley, 2012a; Kwong & Chopra, 2016). As an alternative, AvgSA is a highly practical IM since the existing

framework for SA can be directly used in the computation of AvgSA. Furthermore, AvgSA is shown to be efficient and sufficient for a variety of structural EDPs. Due to its definition, as the geometric mean of a range of SA values, AvgSA directly correlates with SA; hence, most of the advantages of using SA are carried over. (Kohrangi, Bazzurro, et al., 2017; Kohrangi, Vamvatsikos, et al., 2017; Zuccolo et al., 2021).

$$AvgSA = \left[\prod_{i=1}^{n} SA(t)_i\right]^{1/n} \qquad \textbf{6.1}$$

Recently, the AvgSA has been shown to have an acceptable, second to best, correlation with the foundation settlements (Macedo & Bray, 2018). Finally, unlike other IMs, Equation 6.1 suggests a structure-specific IM. Therefore, AvgSA requires computing a structure-specific hazard and disaggregation. The record selection procedure for the CS conditioned on the AvgSA is demonstrated by (Kohrangi, Bazzurro, et al., 2017). Hence, from numerous perspectives, the AvgSA is a good candidate as the suitable IM for this study.

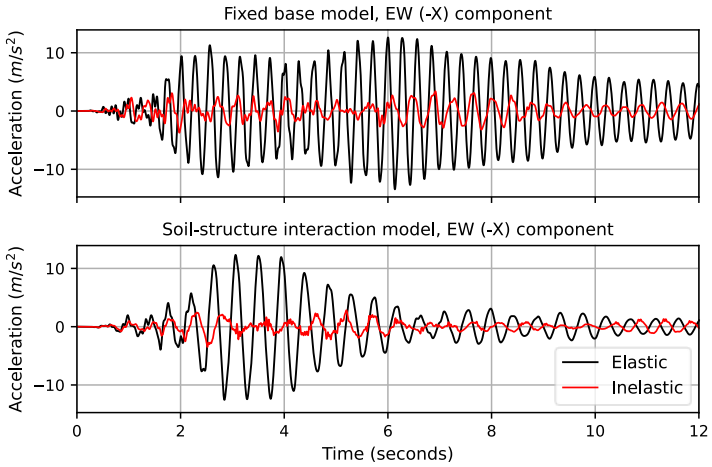

Figure 6.5. EW component of the acceleration history recorded at the roof of the fixed-base (top row) and the SSI (bottom row) models.

In their study, Kohrangi, Bazzurro, et al. (2017) adopt an AvgSA definition using SA values ranging from $0.2T_1$ to $1.5T_1$. This definition results from attempting to cover the contribution of higher and inelastic structural modes in the hazard computation. However, such a definition might not include all the significant modes for the SSI problem described in this study. Therefore, an alternative range definition is necessary to include the SSI mechanics in the AvgSA computation.

The spectrum of significant frequencies contributing to the overall fixed-base and SSI models can be identified through Fourier analysis of the acceleration history recorded at the roof of the structure. The roof motion consists of the response of all components in the model, including the applied base motion, soil response, and structural response. Hence, the frequencies of the predominant mechanics in the system are expected to generate spikes in the frequency domain. This information can identify a window of relevant frequencies, which can then be used to define a range to compute the AvgSA suited for the problem.

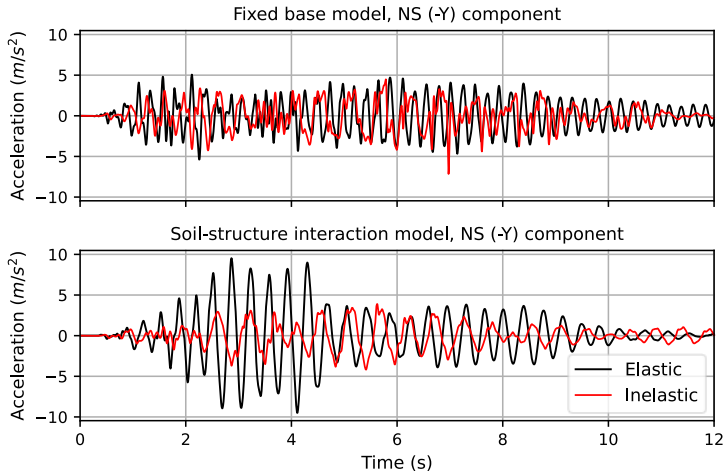

Figure 6.6. NS component of the acceleration history recorded at the roof of the fixed-base (top row) and the SSI (bottom row) models.

The acceleration history at the roof can be computed by analysing the models for an input motion with a relevant frequency content, which can take the structure into the nonlinear response. However, notably, the intensity of the motion might determine the amount of period elongation experienced by the structure. The shaking intensity could affect the AvgSA definition and the ground motion selection procedure. Therefore, the selection procedure might require several iterations to converge to an AvgSA and a ground motion set pair compatible with each other regarding the nonlinearity induced in the structure given a return period level. For a 475-year return period, the record of the Lazio-Abruzzo 1984 event discussed in Section 6.1 is used. This record is advantageous since it belongs to a set of records selected for the bell tower of Guardiagrele conditioned on the inelastic fundamental period by a previous author, Rosell (2010).

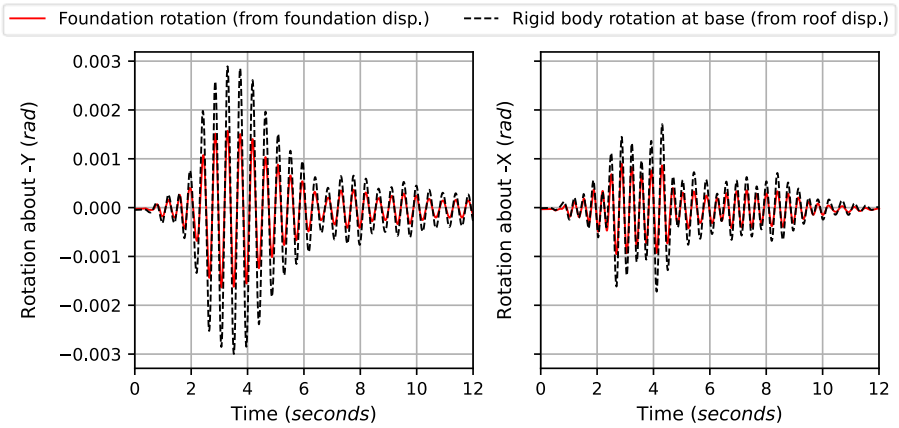

Figure 6.7. Foundation rotations are computed through two independent approaches: 1) angle of rotation at the geometric centre of the foundation obtained from differential foundation corner displacements and 2) Rotation at the base level due to relative roof displacement divided by the tower height (≈ roof drift ratio, RDR)

Figure 6.5 and Figure 6.6 compare the tower response under fixed-base (no soil) versus the compliant base (soil-structure interaction) assumptions. The seismic record at the bedrock level is assumed to be the same for both models. For the nonlinear model, the free surface motion recorded at the top of the nonlinear 1D soil column is applied to the fixed-base model. In contrast, the upward propagating wave at the model base depth (30 m) in the 1D soil column is applied as force history at the base of the SSI model (three-component motion in both models). The linear analyses are done following the same approach but using 1D linear column accelerations.

Figure 6.5 and Figure 6.6 show the discrepancy in the recorded acceleration history at the model roof due to the Lazio-Abruzzo ground motion. Two cases are displayed: the linear solution plotted on top of the nonlinear solution. Focusing on the linear elastic solution, one can see in Figure 6.5 that the acceleration patterns recorded in fixed-base and SSI cases are significantly different. In the SSI case, the foundation rotation governs the oscillation behaviour, whereas the structure's first mode plays a critical role in the fixed-based model.

In Figure 6.7, the foundation rotation angle, θ, is calculated and compared using two approaches. The red curve shows the amount of rotation at the geometric centre of the foundation computed through the vertical displacements recorded at the edges of the foundation. This rotation matches reasonably well with the black curve, which is the base rotation computed by scaling the horizontal displacement recorded at the roof by the tower height. The horizontal roof displacement divided by the height is the roof drift ratio, RDR, and it relates to the rotation at the tower's base. For a rigid building, $RDR \approx tan(\theta)$, and

as per the small angle approximation $RDR \approx \theta$. If the flexibility of the tower is considered, $RDR \approx \theta + \varphi$ where φ is the contribution from the structural deformations. Hence, the linear elastic tower displacements can explain the increased response in the black curve. However, the structural deformations notably follow the foundation rotation pattern, and there is an initial portion in which strong motion is not intense enough to induce significant structural deformations (Figure 6.7).

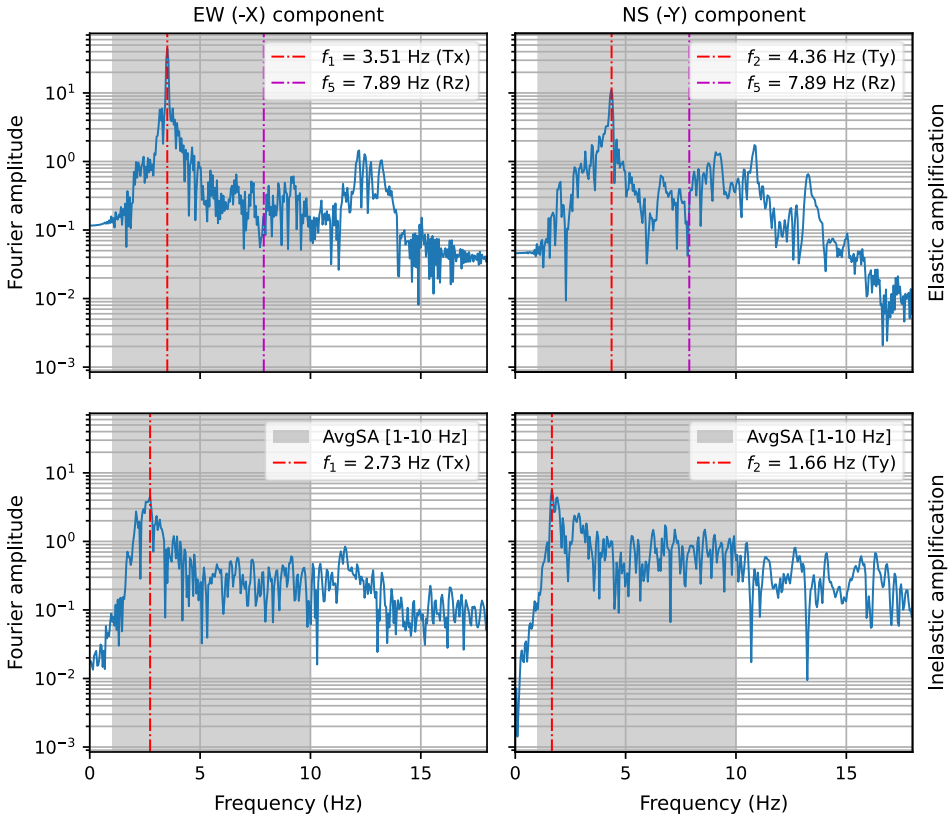

Figure 6.8. (Fixed-base) Amplified frequencies computed at the roof of the bell tower. The vertical line is the fundamental frequency of the bell tower computed through the modal analysis. The shaded area marks the period range [0.1 - 1 sec] included in the AvgSA definition.

Fourier analyses of the acceleration history recorded at the roof node, shown in Figure 6.8 and Figure 6.9, confirm the behaviour observed in Figure 6.7. Figure 6.8 plots the Fourier spectra of the roof acceleration for the fixed-base model. The first row concerns the linear behaviour in both NS and EW components. The peaks observed in the frequency domain

match the fundamental frequency computed through modal analysis. This trend also extends to the inelastic response shown in the second row. The fundamental frequency can be observed to shift as the shaking induces nonlinearity in the masonry. The amount of inelastic response is higher in the NS direction due to the existing openings, and a significant crack mechanism appears during shaking.

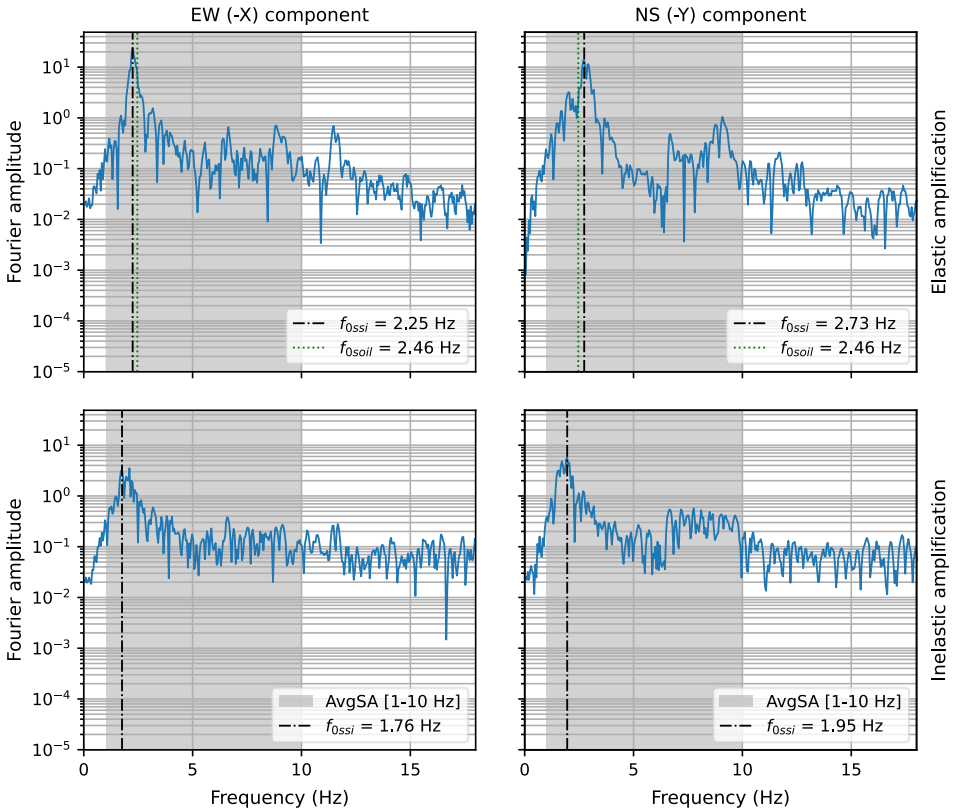

Figure 6.9. (SSI) Amplified frequencies are computed at the bell tower roof when the soil is present. The vertical line is the fundamental frequency, $f_{0,}$ of the soil layer. The shaded area marks the period range [0.1 - 1 sec] included in the AvgSA definition.

Similarly, Figure 6.9 displays the Fourier analyses of the roof accelerations recorded in the SSI model. It is worth noting that the peak in the linear elastic response is far from the structural fundamental period, i.e. 0.45 seconds compared to 0.28 seconds in the fixed model. The SSI system period nearly matches the soil column fundamental period of 0.41 seconds. Similarly, the proximity of the SSI period (at the second structural mode) to the soil column fundamental period was observed by di Lernia et al. (2024) in their study of a slender bell tower, which had a much longer fundamental period than the bell tower of

Guardiagrele. This phenomenon causes a resonance in system oscillations and results in high accelerations observed in the bottom rows of Figure 6.5 and Figure 6.6. Romero-Sánchez et al. (2024), who studied the nonlinear SSI effects in a slender masonry tower, also reported increased shaking intensity when SSI is considered. However, the authors did not comment on the proximity between the SSI and soil column periods.

Moreover, in the SSI model, the structural fundamental frequency is not highlighted in the frequency domain as intuitively expected. This observation is supported by the inelastic analysis depicted in the second row. Compared to linear analysis, nonlinear analysis leads to lower acceleration peaks at specific frequencies, thus reducing the masking of other predominant frequencies. However, no significant peak around the period corresponding to the first mode of the structure (i.e., 0.28s) can be identified by observing the second row of Figure 6.9. Nevertheless, this does not indicate that the structural modes are not excited. On the contrary, the damage pattern recorded at the end of the shaking shows the initiation of the significant crack related to the fundamental structural period along the NS axis of the tower (Figure 7.12). The structural nonlinearities are discussed in further detail in Section 7.4.

Figure 6.8 and Figure 6.9 summarise the significant effect of considering system response in the behaviour of rigid and brittle structures such as the masonry tower structure considered here. The foundation rotation phenomena may control the structural response and the observed damage. Hence, not considering the system response through fixed-base-only analysis may lead to inaccurate estimations of structural EDPs. In light of the observed mechanics, intensity measures tailored for foundation rotation assessment, such as PGV (Karimi & Dashti, 2017; Macedo & Bray, 2018), and structural response, such as SA, or their vectorial combinations, may prove efficient and sufficient IMs in the SSI analyses of shallow-founded masonry towers. In the case of SA, more than five distinct periods are identified in this study, which are:

1. Structural fundamental periods (T_x, T_y and R_z)
2. Elongated structural periods ($T_{x\_shifted}$ and $T_{y\_shifted}$)
3. SSI fundamental periods in both directions (T_{SSI_x} and T_{SSI_y})
4. Elongated SSI periods ($T_{SSI\_x\_shifted}$ and $T_{SSI\_y\_shifted}$)
5. Soil column fundamental period (T_{soil})

Since these periods are relatively close, using AvgSA may be considered an integral and innovative approach to the SSI problem described here. Finally, based on the range of frequencies identified in the Fourier analyses in Figure 6.8 and Figure 6.9, an AvgSA definition covering the periods from 0.1s to 1.0 with 0.1s intervals is chosen as the suitable IM for the record selection procedure.

6.4 HAZARD CONSISTENT RECORD SET SELECTION

The input ground motion should accurately model the site's seismic hazard and seismotectonic characteristics. Since the finite element (FE) model is designed to simulate the dynamic response from the bedrock to the structure, a hazard-consistent definition of the incident wave at the model's base is essential. Following the approach in Section 6.1, all ground motions are assumed to be recorded at an outcropping bedrock site at the model's location. A deconvolution process is then conducted to compute the within motion at the depth corresponding to the base of the FE model (Kramer, 1996). Consequently, hazard consistency must be sought for the outcropping bedrock conditions. A set of eleven ground motions that, on average, capture the expected seismicity at the site are selected. Various international assessment codes and guidelines, such as EC8 and NIST reports (Whittaker et al., 2011), regulate the hazard modelling approach and the corresponding required number of records.

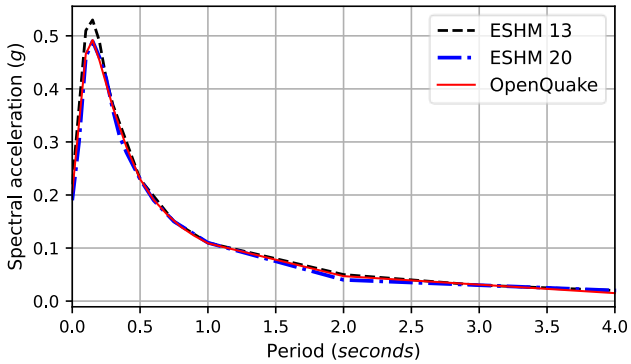

Figure 6.10. The 475yrs uniform hazard spectrum (UHS), computed at the bell tower coordinates using the OpenQuake engine, is compared with the European seismic hazard model.

The record selection is performed using the conditional spectrum (CS) tools available in the EzGM library (Ozsarac et al., 2023). The EzGM library provides CS-based ground motion selection from online databases and integrates with OpenQuake (Pagani et al., 2014) for probabilistic hazard assessment and disaggregation. The AvgSA chosen as the geometric mean of SA from 0.1s to 1.0s with 0.1s intervals (Section 6.3). The hazard disaggregation at the site is computed for AvgSA using the OpenQuake engine, employing the SHARE (Woessner et al., 2015) hazard model for continental Europe. The hazard is calculated at bedrock conditions, considering seismic events within a 200 km radius around the bell tower. It should be emphasized that the computational cost of running the SHARE model is significant due to the project's size and detail. Hence, some simplifications are made by considering the hazard at a single point and employing only one of the GMM

logic tree branches. Consequently, the uniform hazard spectrum (UHS) for a 475 years return period computed at the site using the OpenQuake model is compared to the publicly available UHS provided for the site by the 2013 and 2022 editions of the European seismic hazard model to ensure the computed hazard is acceptable (Figure 6.10).

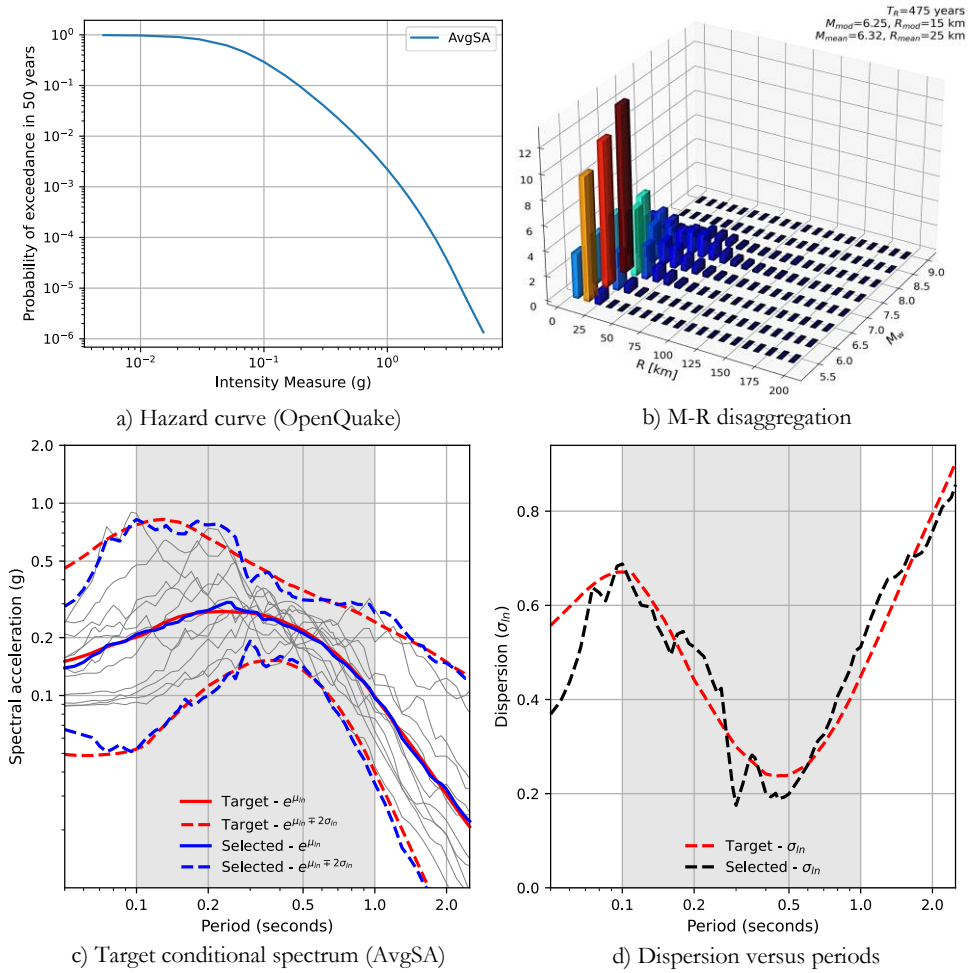

a) Hazard curve (OpenQuake) b) M-R disaggregation

c) Target conditional spectrum (AvgSA) d) Dispersion versus periods

Figure 6.11 a) Hazard curve for AvgSA evaluated at Lat: 42.1907 Lon: 14.2216 b) Magnitude and distance disaggregation for 475 years return period c) Target (475 yr.) versus selected motion spectra d) Target versus selected dispersion

A disaggregation analysis is done to identify the significant magnitude (M), distance (R), and epsilon values. Then, the conditional spectrum for AvgSA is determined for a 475-year return period. The GMM by (Boore et al., 2014) is utilized to generate the conditional

spectrum. Subsequently, eleven ground motion records are selected based on relevant magnitudes, distances, faulting mechanisms, and Vs30 values (> 800 m/s) from the NGA West 2 database (Ancheta et al., 2014). Reverse and strike-slip faulting mechanisms are expected based on the seismotectonics reviewed in Section 5.1. Finally, the strong motions are scaled (Maximum scaling factor = 3) at the AvgSA to match, on average, the conditional spectrum and the target dispersion. The results obtained at the end of each step of the record selection process are summarised in Figure 6.11.

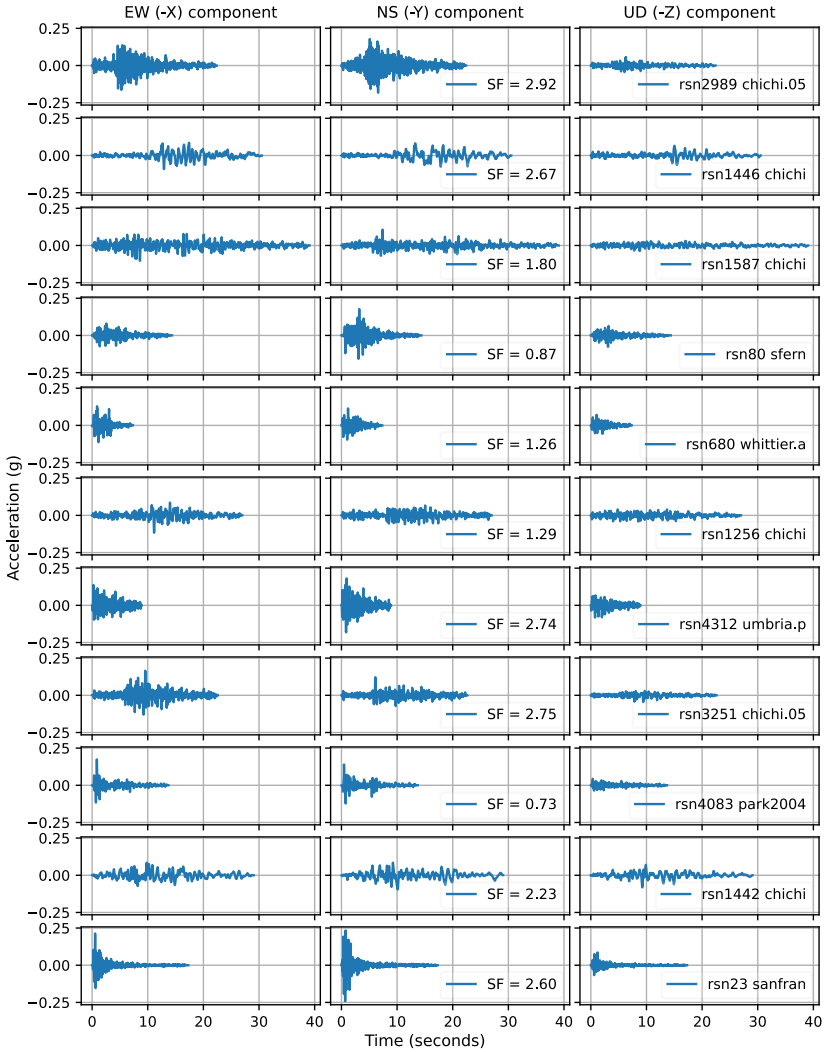

Figure 6.12. Processed strong motion set at the bedrock (in g unit). Motions are scaled, cut (I_{Arias} 5-95%), and baseline corrected (232.4 s.).

The component-wise directionality of the hazard is handled by using the fifty percentiles of the rotated IM (RotD50) during the selection process (Boore, 2010; Boore et al., 2006). There is ongoing discussion in the literature about possible underestimation of the hazard due to using RotD50 and overestimation due to using RotD100, as well as proposals of more suitable definitions of non-directionality for seismic assessment (Poulos & Miranda, 2022).

An additional constraint for the record set is the computational cost of the total number of analysis steps after cutting the records following the procedure described in Section 6.2. As a proxy of the total number of steps, a limit of two hundred forty seconds on the total signal duration is imposed, corresponding to an expected total solution time of twenty days on the allocated workstation. The waveforms, the code names and the scaling factors of the resulting record set are shown in Figure 6.12.

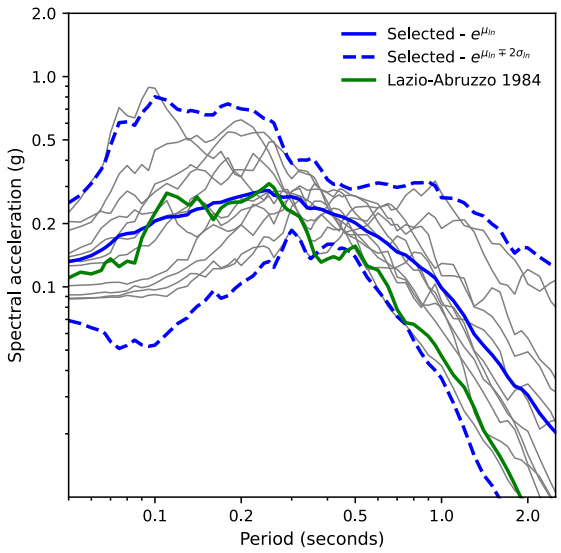

Figure 6.13. Comparison of the Lazio-Abruzzo strong motion used in the dynamic analyses led to the chosen AvgSA definition, with the selected ground motion set conditioned on the AvgSA.

Figure 6.13 compares the Lazio-Abruzzo motion used in Section 6.3 to define the range of SA values included in the AvgSA to the selected ground motion set. Notably, the Lazio-Abruzzo motion falls within the mean and the dispersion of the selected ground motions. The amount of nonlinearity induced by the motion in the structure is comparable to the mean of the selected set for a 475-year return period. Therefore, using the Lazio-Abruzzo motion to obtain the expected inelastic periods yields relevant results for selecting a ground motion set for a 475-year return period.

6.5 TOTAL STRESS BASED NONLINEAR DYNAMIC FREE-FIELD ANALYSES

In this section, the site response characteristics are studied step-by-step. The soil profile discussed in Section 5.4 is modelled as a 1D shear column to study the soil amplification properties for an upward propagating wavefront. The 1D nonlinear response obtained in OpenSees is compared to the 1D equivalent linear response obtained through independent software for validation.

Then, a 2D topographic model is presented to study the effects of introducing the sloping topography present at the site, on the free-surface motion recorded at the tower's location. Furthermore, a 2D mesh sensitivity analysis is conducted to determine the largest horizontal mesh size that does not lead to a significant frequency content loss in the solution, given the topographic properties and material nonlinearity. Finally, the 3D topographic model is discussed in studying the differences in the topographic amplifications and the stability of the slope when the entire topography is considered.

6.5.1 1D soil column amplification response

A one-dimensional site amplification response study was undertaken to

1) Study the soil profile amplification,
2) Represent the resonance characteristics of the soil profile,
3) Include nonlinear soil affects, and
4) Obtain the free-surface acceleration history for fixed-base analyses.

Site response analysis yields crucial information regarding the intensity and the characteristics of the shaking that might be expected at the surface and below the foundation of the structure. Even in cases where a direct SSI problem is solved concerning the structure of interest, results obtained from site response analyses might give important insight regarding the contribution of the soil profile behaviour in the results. In this thesis, site response analyses are crucial in obtaining a framework to compare fixed base versus direct SSI seismic response and isolating the effects of foundation deformations on the behaviour of the structure.

A 1D soil column model was prepared in OpenSees, following the total stress site response example presented in the OpenSees geotechnical examples manual (McGann & Arduino, 2011). Following the example, a 1D shear column behaviour was modelled by making a slender vertical column using 2D quad elements. The thickness of the column is covered by a single element, whereas multiple elements were used in the vertical direction enough to provide an upwards wave propagation resolution of around 20 Hz. The horizontal d.o.f.s are tied at each level to model shear column displacements. The column is free to move in the horizontal direction to accommodate incident seismic wave propagation at the bottom.

Viscous dashpots are placed at the bottom nodes of the column to dissipate returning waves. The wave field in applied as a force history at the bottom. The soil profile and the nonlinear behaviour were described in Section 5.4.

The Lazio-Abruzzo 1984 motion, discussed in Section 6.1, is used for studying the 1D soil amplification characteristics. Each record presented here is treated following the deconvolution procedure defined in Section 6.2 before application. According to the 1D ground motion problem defined in Figure 6.1 and the soil profile shown in Figure 6.2, the model base is located at 30 meters, whereas the deconvolved motions are considered to be at the bedrock which is at 60 meters deep. Hence, another 1D ground response analysis is solved in Strata software, a priori, to move the records from 60 meters depth to model base. Then the upwards travelling (A only) motion at 30 m (model base) is applied to the 1D soil column.

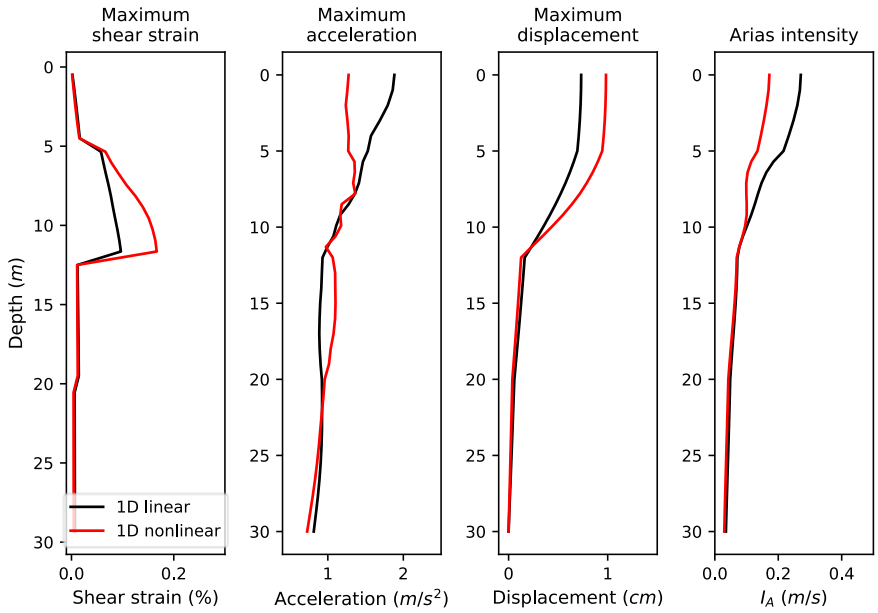

Figure 6.14. Linear versus nonlinear 1D site response analyses. Lazio-Abruzzo 1984 motion.

Figure 6.14 depicts the 1D soil column response to the Lazio-Abruzzo 1984 motion. The model response is as expected. During strong shaking the soft clay layer between 5 to 12 m behaves as a partial isolator. Comparing the linear and nonlinear curves, one can observe the trade-off between the reduced accelerations in return of increased displacements. The increased amount of shear straining in the soft clay layer leads to larger displacements and reduced accelerations at the surface. This overall cause a decrease in the intensity of shaking

at the surface starting from the interface of the soft clay and the medium clay layer below, which can be seen through the Arias intensity profile shown in Figure 6.14, above.

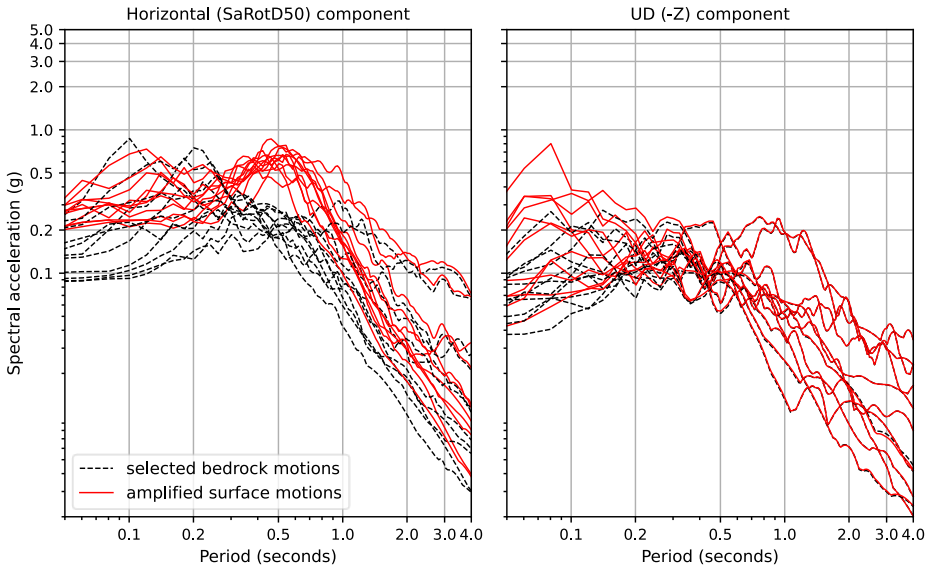

Figure 6.15. Nonlinear soil amplification computed in OpenSees. SaRotD50 component is plotted. Input motions for fixed base analyses.

In the next step, the set of amplified surface motions is computed by solving the 1D soil column for each of the ground motions in the selected set shown in Figure 6.11. The directionless horizontal (SaRotD50) component spectra of the surface motions are plotted in Figure 6.15. The effect of the soil profile is notable as a peak occurring around 0.5 seconds in the response spectra of the motions. This is sensible since the fundamental frequency of the profile is 0.41 seconds, and this elongates to around 0.5 seconds when the soil nonlinearity is considered.

Furthermore, it is worth noting that the uncertainty in the acceleration observed at low periods is decreases following the site response analysis. This is due to the damping effect of the soil plastic response in the high frequency accelerations. A reduction in the accelerations observed at the long periods cannot be observed since a smaller number of large strain cycles are induced by the input motions; hence the effect of hysteretic damping is much lower.

Finally, the amplification in the vertical motion is plotted in Figure 6.15. The 1D vertical amplification is computed by solving the linear 1D soil column profile using the elastic p-wave modulus instead of the shear wave modulus. The p-wave modulus is computed from

the p-wave velocity profile, or if not available, the shear wave modulus and the Poisson ratio of the soil layer or using the combinations of elastic coefficients. In Figure 6.15, amplification in the high frequency vertical acceleration as a result of solving the linear site response problem. However, the difference between the outcropping bedrock motion and the surface motion is not significant in the longer periods since the considered surface to bedrock depth of 60 meters is relatively shallow when the p-wave moduli are concerned.

6.5.1.1 *Equivalent linear site response*

Equivalent linear response provides a middle step between the linear and the nonlinear site response analyses. Furthermore, the results of equivalent linear analyses might be more accessible in seismic engineering practice since many site response analysis packages offer equivalent linear analysis, and it requires significantly less amount of material parameters than the nonlinear site response analysis. In this study, equivalent linear analysis provides a reliable benchmark and validation for the nonlinear site response analysis results presented in Section 6.5.1.

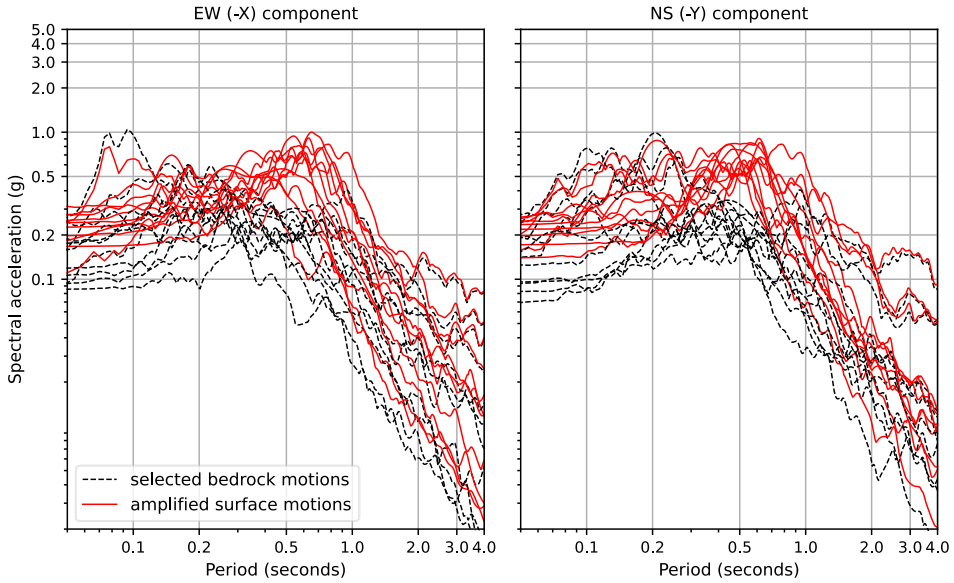

Figure 6.16. Equivalent linear amplifications using Strata (Kottke & Rathje, 2008). Individual horizontal components are plotted.

Equivalent linear analysis considers the shear modulus reduction, G/Gmax, and equivalent damping characteristics of the soil profile to compute a representative nonlinear response. Equivalent linear analysis results are widely used for studying response to moderate shaking, and it gives valuable insight into where more complex, nonlinear behaviour begins.

The equivalent linear solution for the soil profile considered in Figure 6.2 is computed in the Strata software (Kottke & Rathje, 2008). The G/Gmax and damping response proposed by Vucetic & Dobry (1991) is used to define layer response which is the approach used in calibrating the nonlinear soil model in Section 5.4. The whole soil profile from the surface up to the bedrock depths of 60 meters is modelled. The input motions are treated following the deconvolution procedure defined in Section 6.1.

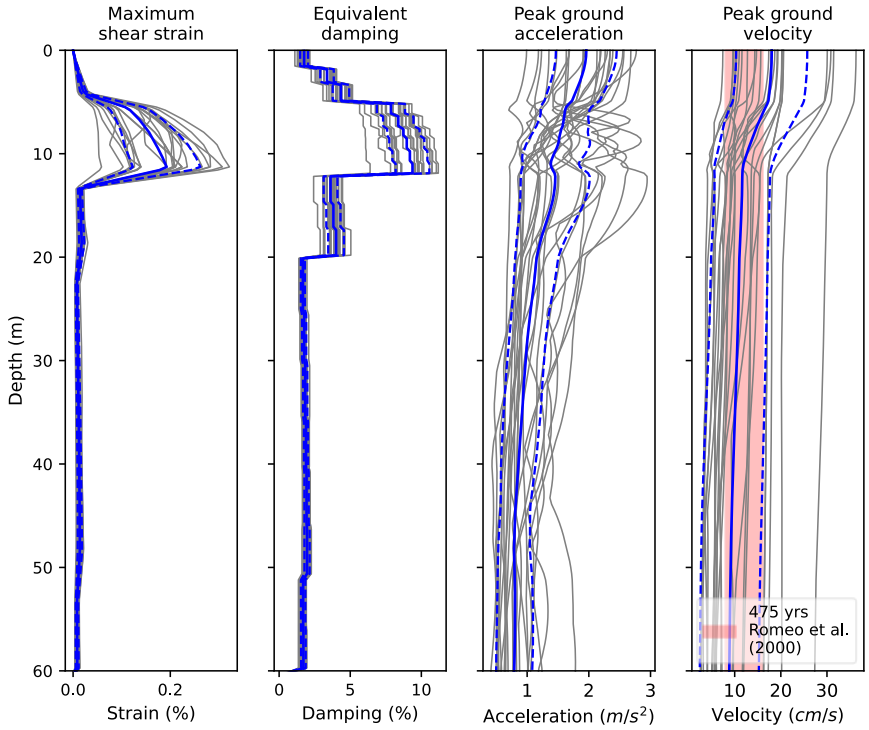

Figure 6.17. Equivalent linear maximum shear strain, damping and peak ground velocity profiles.

Figure 6.3 shows the comparison between the linear, equivalent linear and nonlinear solutions for the Lazio-Abruzzo 1984 ground motion. Notably, the equivalent linear and nonlinear solutions are similar. This is because the stiffness reduction characteristics of both models are tuned to match each other within the range of shear strains that are induced by the Lazio-Abruzzo 1984 ground motion. However, the equivalent linear solution predicts consistently lower accelerations. Even though the difference is insignificant, this result gives insight regarding the damping characteristics of the chosen models. The difference in Figure 6.3 might indicate that the damping versus strain curve used in the equivalent linear analysis estimates larger hysteresis loops than the nonlinear model used in this study. This is sensible since the PIMY is based on a modified Masing

type hysteresis with smaller cycles (Figure 5.11) which is more suitable to model clay like behaviour compared to a traditional Masing unloading-reloading response.

Finally, the maximum shear strain and equivalent damping profiles are shown in Figure 6.17. The average maximum shear strain profile obtained from the equivalent linear analyses matches that of nonlinear analysis shown in Figure 6.14. As expected, the equivalent damping computed follows the amount of shear strain computed in each layer. High amounts of damping are obtained in layers 2, 3 and 1 in descending order.

6.5.2 2D and 3D topographic amplification response

This section concerns the two and three-dimensional response of the hill structure, focusing on comprehending the influence of hill geometry on wave propagation and the displacements at the surface. First, the quality of the chosen mesh in capturing the desired range of frequencies is tested.

Then the convergence of the wavefront towards the apex of the hill namely the wave-focusing phenomena is studied. The damping effect of soil nonlinearity is shown. Finally, the topographic effects in 3D are shown in comparison to the 2D results.

6.5.2.1 *The captured frequency range and the mesh quality*

The adequacy of the frequency range that is captured by the proposed mesh in Section 5.4 is discussed here. The material inelastic response together with the element size along the second dimension are expected to reduce the frequency definition of the model. Therefore, the response of the proposed mesh is compared to a refined version for validation.

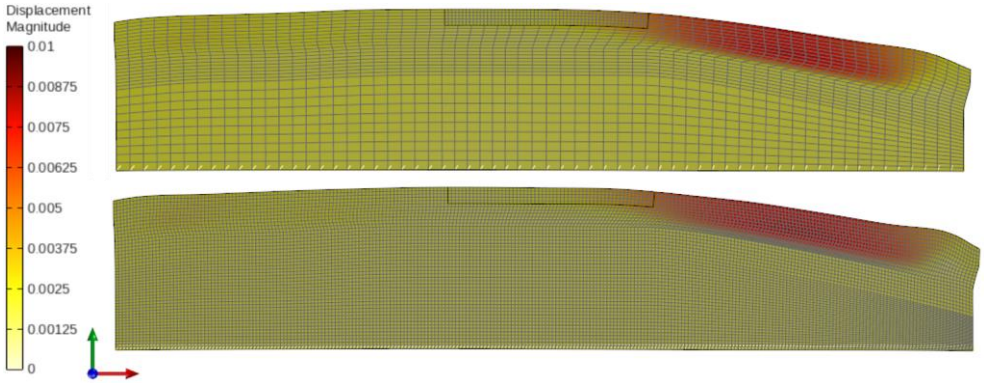

Figure 6.18. The proposed versus refined mesh (1x1m). Slope displacement (m) at the end of the analysis (1000 times exaggerated).

The 2D model is prepared by taking a cross-section of the 3D topography at the location of the bell tower along the sloping EW (-X) axis (Figure 6.18). Then, the model is built following the techniques described in Chapter 5. The mesh is refined by using 1x1 meter quad elements throughout the model. The ground motion is applied at the bottom of the model in two-components. The EW component of the motion is applied along the -X axis whereas the UD component is applied along the vertical -Y axis.

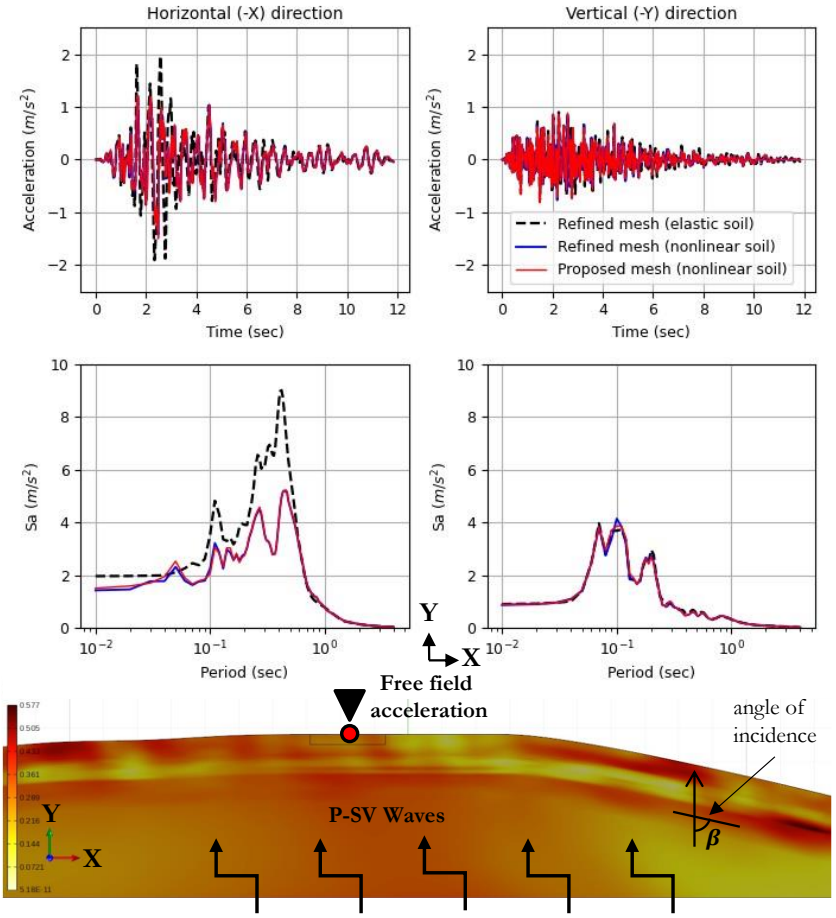

Figure 6.19. Two-component acceleration spectra computed at the free field (no foundation). The discrepancy between the plotted spectra is attributed to mesh size and soil nonlinearity assumptions for a component. The proposed mesh is discussed in Section 5.4.

Figure 6.19 displays the comparison of the acceleration response spectra obtained through analysing the refined and proposed model. The proposed model appears to match the refined mesh acceleration response when a nonlinear soil is considered. Hence, a horizontal

element size of 4 meters and the proposed vertical element configuration in Section 5.4 can be safely used in multi-dimensional wave propagation analysis in terms of accelerations.

However, there is a slight difference in the computed slope displacements between the refined and proposed models. The final displacement contours of both models are shown in Figure 6.18. The amount of slip occurred in the slope within the soft clay layer around 12 meters depth after shaking can be seen. Careful studying of the permanent displacement field reveals that the slip is localized in the elements located at the interface between the 3rd and 2nd layers. As a natural result of the localization, the amount of slip is a function of the element size. Hence, the amount of slope displacement computed by the proposed mesh is slightly lower than the amount computed by the refined mesh. It is worth noting that, in case of localization, mesh refinement may not lead to more accurate results in traditional FE solutions (Jirásek, 2007). From a practical perspective, the discrepancy between the final displacements in Figure 6.18 are not significantly far apart, leading to a satisfactory mesh configuration for large SSI analysis, in the overall.

6.5.2.2 *2D and 3D topographic amplifications*

In this section the topographic response of the 2D and 3D models is discussed. The vertical component is included in all 2D, and 3D analyses presented here. The 2D model is analysed using the EW (-X) component of the selected station and event, whereas the second horizontal component (NS) is also included in the 3D model. All analyses are done in OpenSees using the STKO pre- and post-processor. The free surface accelerations and result profiles are shown at the location of the tower in the figures below.

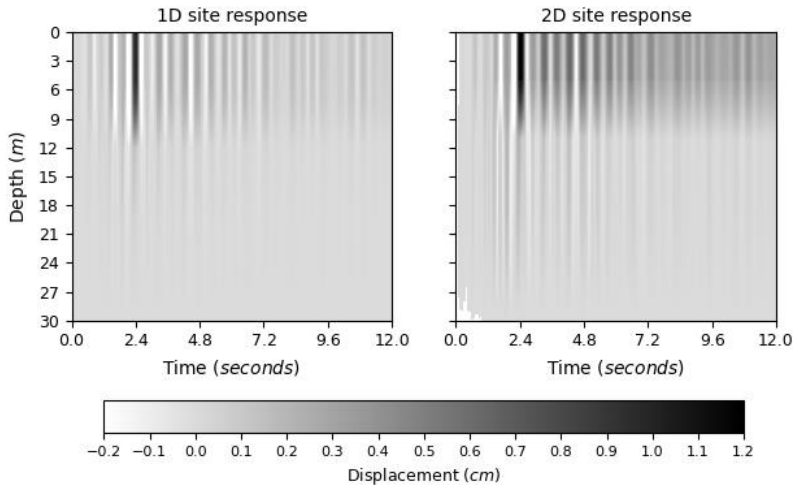

Figure 6.20. 1D versus 2D inelastic site displacement contour plots. (Lazio-Abruzzo 1984 ground motion)

Figure 6.20, shows the evolution of the displacement profile along the 1D and 2D site response model. The soft clay material in the second layer can be easily identified by studying the plots. In 1D response, the amplitude of displacements drastically increases between 0 to 12 m. However, a limited amount of residual displacements computed in the first and the second layers. In contrast, the displacement of the first two layers is much larger in the 2D case following the strong cycle occurring around the 2.4th second of the earthquake. By studying the final displaced shape of the slope, shown in Figure 6.18, the displacement observed in the first two layers can be attributed to the cascading effect of the soil mass that slipped downslope on the location of the tower. This observation is further supported by studying the 1D and 2D soil profile behaviours.

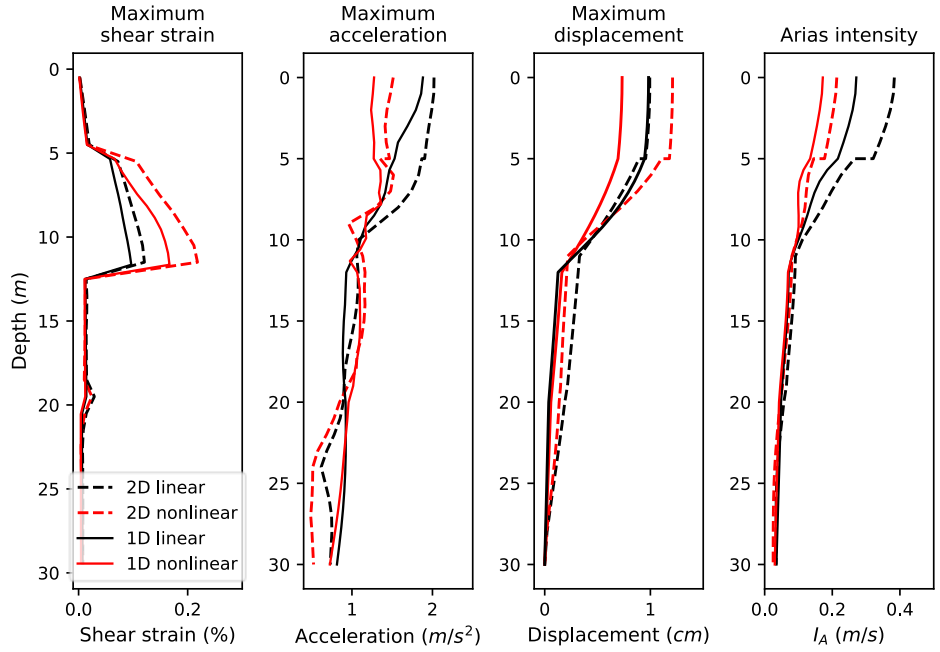

Figure 6.21. 2D topographic amplifications. 2D versus 1D site response analyses. (Lazio-Abruzzo 1984 ground motion)

The 1D and 2D soil profile behaviours at the location of the tower are shown in Figure 6.21. Interestingly, the maximum displacements computed at the surface in elastic analyses match, indicating the displacement demand of the event is similar in 1D and 2D linear elastic conditions. The maximum displacement reduces in the 1D inelastic case due to hysteretic damping, confirmed by the reductions observed in the maximum acceleration and Arias intensity when soil nonlinearity is considered. The largest maximum displacement is computed when the soil nonlinearity is considered in addition to the 2D topography due to the slip of the slope during strong shaking.

The largest Arias intensity and acceleration are computed for the 2D linear case, indicating that the inclusion of the slope topography leads to the focusing of the upward propagating waves at the tower location. The focusing effects observed in the 2D linear response appears to fade away in 2D nonlinear response due to inelastic strains and hysteretic damping. However, the acceleration and Arias intensity computed for the 2D nonlinear case is still larger than the 1D nonlinear case, indicating some persistence effect in the contribution of topographic effects in the nonlinear case.

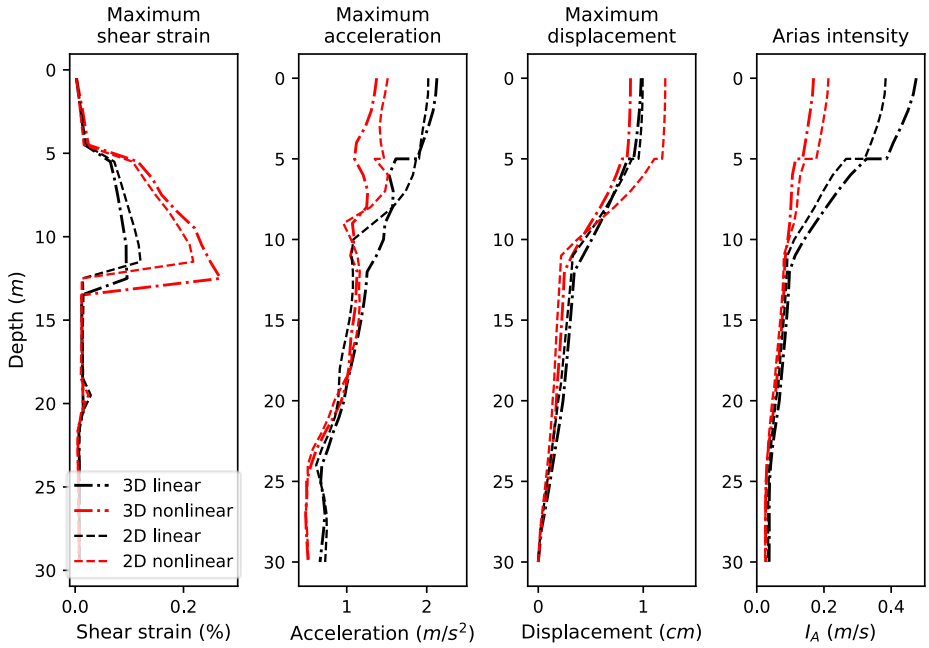

Figure 6.22. 3D topographic amplifications. 2D versus 3D site response analyses. (Lazio-Abruzzo 1984 ground motion)

Introduction of the complete topography in 3D lead to an increase in the intensity of the shaking observed at the location of the tower, when linear elastic soil response is considered (Figure 6.22). This is intuitive since the tower area is located at the apex of a bi-directional slope, as shown in Figure 6.23. However, an overall reduction is observed in the maximum displacement, acceleration and Arias intensity computed along the slope axis compared to the 2D case, when the soil plastic response is included (Figure 6.22). The soil plastic response in 3D is higher than that of 2D due to the bi-directional loading conditions achieved in the 3D model. Since the modulus reduction behaviour of the soil model is a function of the octahedral stress-strain response, the combined loading cases lead to an increased reduction in the shear modulus which leads to further reduction in the accelerations and forces observed at the free surface.

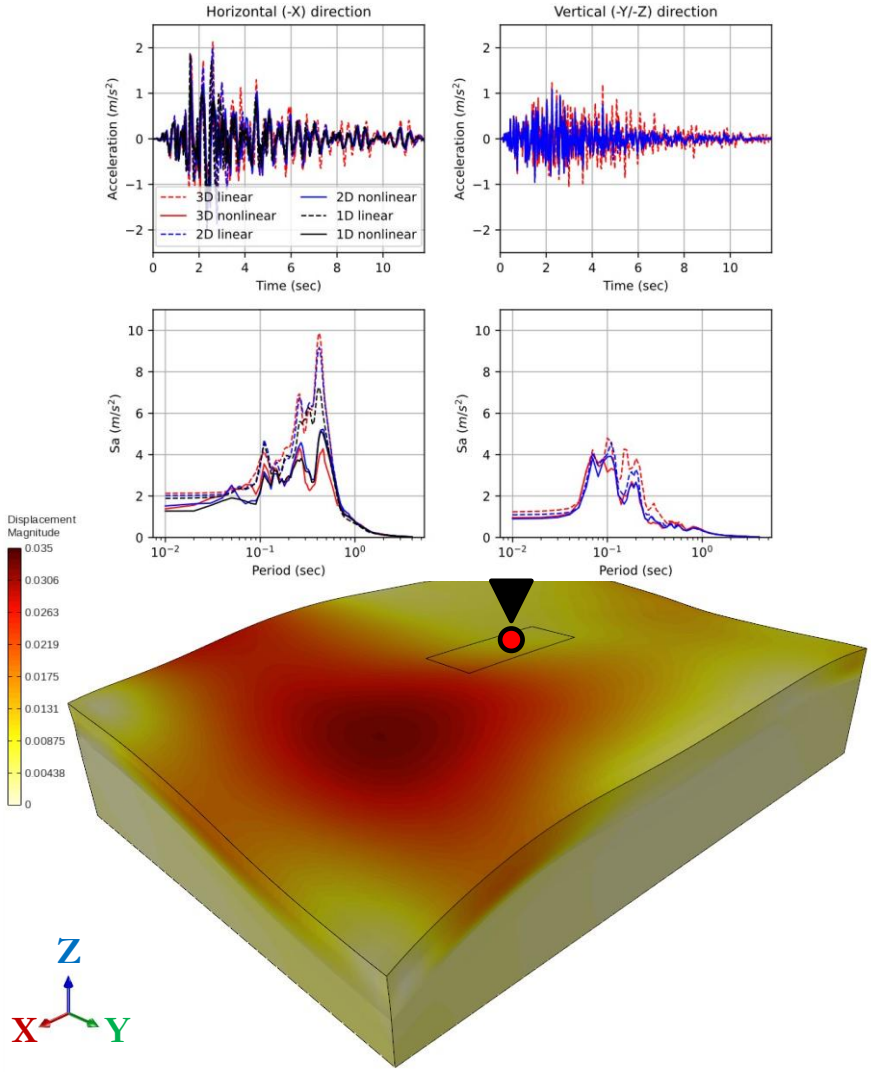

Figure 6.23. 3D slope displacements and the topographic amplifications. (Lazio-Abruzzo 1984 ground motion)

It is worth noting that, a reduction in the accelerations and shaking intensity is often poses larger displacements, which is the case in 2D analysis shown in Figure 6.21. In contrast, a decrease is observed in the displacements for the 3D case shown in Figure 6.22. However, this can be explained by studying the 3D displacement contours shown in Figure 6.23. The bulk of the displaced soil mass translates further away from the location of the bell tower in the third dimension when the 3D geometry is considered. Hence the maximum displacement is shared between the EW (-X) and NS (-Y) components. Since, only the EW

component of the displacement is shown in in Figure 6.22, it appears to be less than the 2D displacements shown in Figure 6.21.

Finally, Figure 6.23 shows comparison of the acceleration response spectra computed for the 1D, 2D and the 3D cases. The increase in the horizontal accelerations due to the focusing effects can be clearly seen in the linear spectra. The difference between the 1D and 2D spectra are significant for peaking periods whereas the difference between 2D and 3D is not much, consistent with the topography of the site. Similarly, the vertical acceleration also increases slightly due to the topographic effects. However, the plastic response of the soil leads to damping of high frequency effects, especially due to the isolating effect of the slip occurring at the slope.

6.6 EFFECTIVE STRESS BASED NONLINEAR DYNAMIC FREE-FIELD ANALYSES

In this section, the consequences of considering an alternative soil profile in which a liquefiable clean sand layer exists sandwiched between the first and third clay layers are discussed. The 1D soil column model of the soil profile described in Section 5.5 is solved to monitor the changes in the pore-pressures, accelerations and the deviatoric stress-strain response. The effect of pore pressure build-up on the free surface accelerations are discussed. The surface ground motion set for the alternative soil profile is computed by using the bedrock motion selected in Section 6.4. Finally, motions that trigger strong liquefaction response in the clean sand layer were identified.

6.6.1 1D soil column amplification response

A one-dimensional site amplification response study was undertaken to

1) Study the soil profile amplification,
2) Represent the resonance characteristics of the soil profile,
3) Include nonlinear soil affects,
4) Obtain the free-surface acceleration history for fixed-base analyses, and
5) Identify ground motions within the set that trigger liquefaction.

Site response analysis yields crucial information regarding the intensity and the characteristics of the shaking that might be expected at the surface and below the foundation of the structure. Results obtained from 1D effective stress analyses might give important insight regarding the liquefaction characteristics of the soil profile. Liquefaction may lead to significant displacements such as lateral spreading in the free field or excessive settlements in foundations of structures.

This thesis investigates the potential for significant settlements in the foundation of the bell tower due to liquefaction, as well as the associated impact on structural damage. The bell

tower is a considerably heavy structure; hence it exerts substantial overburden pressure on the soil beneath the foundation. This means that a large buildup of pore pressure might be required to induce liquefaction in the clean sand layer. While a full pore pressure buildup may occur in the free field, partial pore pressure buildup might occur beneath the foundation of the tower which could lead to large foundation settlements. These settlements may reduce the seismic forces transmitted to the tower, potentially limiting the extent of cracking observed in the superstructure. Consequently, a coupled seismic analysis of the bell tower SSI system could provide valuable insights.

However, performing a full 3D effective stress analysis of the bell tower's SSI system is computationally intensive. Therefore, 1D soil column analyses were used to identify seismic records from the selected set that have a high likelihood of triggering liquefaction at the site. By consistently using the seismic records identified in this section, a cross-comparison can be made between the structural responses observed in the fixed-base, total stress, and effective stress models.

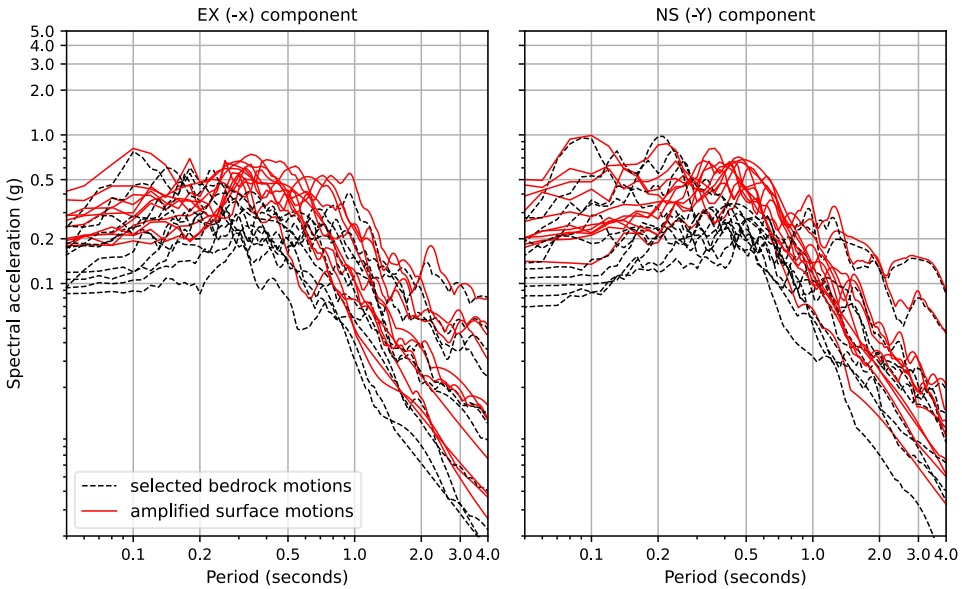

Figure 6.24. Effective stress based free surface amplification computed in OpenSees. The ground motion set selected in Section 6.4.

Figure 6.24 shows the acceleration response spectra computed at the free surface of the 1D soil column model. A peak around the 0.5 second period is noticeable in both components of the surface motion spectra. Similar to the response observed in Figure 6.15, the nonlinear soil response leads to a narrower dispersion in lower period accelerations. However, the peak acceleration response is much lower in Figure 6.24 than in Figure 6.15.

This points at a reduction in the amplifications that is obtained due to increased plastic energy dissipation in the second layer.

The increased plastic response is illustrated in the deviatoric stress-strain and pore pressure plots shown in Figure 11.9 and Figure 11.10, in the Appendix, for each ground motion. Figure 11.9 and Figure 11.10 indicates that the records reaching 200 kPa pore-pressure trigger strong plastic deviatoric stress-strain response. Some records achieved liquefaction in one of the components whereas in few records reached to a 200 kPa pore pressure buildup in both components. Among the records in the ground motion set, liquefaction is observed during the 1D soil column analyses for both components the following three records:

- RSN2989 CHICHI.05 CHY102 (23 seconds)
- RSN4312 UMBRIA.P I-GBB (9 seconds)
- RSN1256 CHICHI HWA002 (27 seconds)

Hence, due to their strong potential of creating large deformations in effective stress analysis these records are chosen for the dynamic analyses in Chapters 7 and 8. This way the changes in the seismic response of the bell tower with and without liquefaction can be studied using the same three ground motions for the fixed base, total stress and effective stress cases.

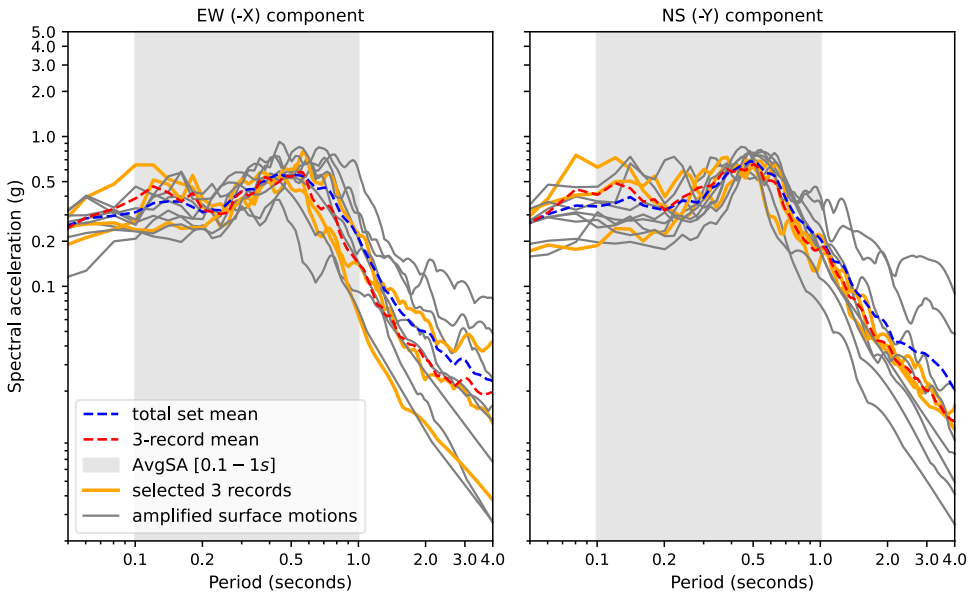

Figure 6.25. The ground motions that trigger strong liquefaction-induced deformations at the site. Three records are selected for carrying out dynamic analyses in Chapters 7 and 8.

Finally, Figure 6.25 shows the mean spectra of the selected three records in comparison to the mean of the total stress surface motion set. It is worth noting that the mean of the three records is not far off from the mean of the surface motion set, indicating a degree of loyalty to the seismic hazard at the site.

6.7 SUMMARY AND DISCUSSION

This chapter focuses on ground motion selection and site response analyses, with a focus on preparing a strong motion set for the seismic assessment of the masonry bell tower in Guardiagrele. A key contribution is the use of average spectral acceleration (AvgSA) as the intensity measure (IM) for selecting ground motions, effectively capturing a wide range of important frequencies relevant to the vibration characteristics of the soil-structure interaction (SSI) system. An AvgSA definition that spans periods from 0.1 to 1.0 seconds is found to be particularly suited to assess the dynamic response of the bell tower. By encompassing both the fundamental and elongated structural periods, along with the soil and SSI periods, the AvgSA-based IM provides a robust framework for simulating the complex interactions between the structure and site-specific seismic conditions.

The conditional spectrum (CS) method is employed for ground motion selection, ensuring hazard consistency at the bedrock level and matching the seismicity of the site for a 475-year return period. This tailored approach ensures that the selected ground motions reflect site-specific tectonic conditions, including magnitudes, distances, and faulting mechanisms, with limited scaling applied to match AvgSA.

Detailed comparisons of 1D, 2D, and 3D site response analyses are presented, highlighting the effects of soil nonlinearity and topographic amplification on the free field response. Furthermore, the motion set corresponding to the free field is calculated using a nonlinear 1D soil column model. Nonlinear soil behaviour, particularly in the soft clay layer, significantly reduces surface accelerations through hysteretic damping. The 2D and 3D analyses further reveal that wave-focusing effects due to the sloping terrain amplify seismic waves at the tower's location, with 3D models showing additional intensification due to the bi-directional topography.

These findings emphasize the importance of an integrated approach to ground motion selection and site response analysis. The results demonstrate the critical role of SSI system response in record selection process, demonstrating an innovative strategy of selecting hazard consistent ground motions for the prediction of the seismic behaviour of masonry towers on complex soil profiles.

7 FIXED-BASE SEISMIC RESPONSE OF THE BELL TOWER

An implicit-explicit damage-plasticity material is used to model the masonry to achieve a fast and stable solution. Similarly, an implicit-explicit contact element simulates the separation between the adjacent structural segments during dynamic excitation. The model is calibrated based on the fundamental period estimations based on ambient vibration and finite element studies published previously. A hazard consistent ground motion set is defined in Section 6.4. The input motion is defined as the 3-component acceleration history computed at the free surface of the 1D nonlinear soil column. The model predicts key structural characteristics, and the damage pattern observed by previous studies. Practical observations were made regarding the parallel solution, favourable time-step, and solver combinations for hybrid implicit-explicit models in OpenSees. It is shown that implicit-explicit integration offers an optimised computational cost versus controlled error balance and enables continued analysis even after failure. Key contributions include:

1. Material orthotropy is shown to be significant in the seismic behaviour of towers.
2. The pounding interaction between adjacent structures can lead to critical results.
3. The vertical component might be critical if the PVA arrives later than the PHAs.

KEYWORDS: impl-ex integration, masonry tower, damage-plasticity, stone masonry, material nonlinearity, strain localization

7.1 NUMERICAL MODELLING APPROACH

This section presents the solid FE model of the bell tower structure. The bell tower is a medium-tall structure with thick walls; hence, it is expected to deform under combined shear and bending effects during seismic shaking. Furthermore, the tower response is expected to modify due to the walls of the adjacent church structure enclosing and interacting with the tower. This leads to the inclusion of contact nonlinearities in the model during dynamic analysis. Hence, solid brick elements were chosen instead of shell elements since they offer a balanced shear and flexure formulation with finite thickness, which is vital in distributing the contact forces.

The dynamic analysis of the tower is carried out with fixed-base assumptions, which is a widely used approach by structural engineers in structural analysis. As per the fixed-base assumption, the nodes at the model's base are fixed in translation in all d.o.f.s (Dirichlet boundary conditions). Hence, the fixed-base boundaries are fully reflective. The dynamic

loading is applied as uniform acceleration history at the fixed nodes. This leads to the assumption of fully knowing the history of the acceleration at the base of the tower, which is the applied strong motion (Chopra, 2015). It is worth noting that, due to the wave propagation in the model, applied mechanical waves will reflect from the structural members and return to the foundation. The fundamental assumption of knowing the acceleration history at the model's base is only possible with fully reflective boundaries at the base (i.e., the fixed-base conditions).

Finally, since the acceleration history at the base of the model is enforced, the input acceleration history is required to be the acceleration recorded at the point of application. Hence, the input acceleration history should be chosen as the strong motion recorded at the free surface as a result of all the amplifying and modifying effects, such as soil amplification, free-surface effects, and topographic effects.

The details of the bell tower model are described in Section 5.3. First, an attempt to validate and compare the model with other models available in the literature through fundamental period estimations is presented. Then, the nonlinear static response of the tower is discussed. The following research questions are studied:

1. Considering that the impl-ex algorithm is conditionally stable and accurate, what is the permissible step to achieve an accurate solution?
2. What are the dynamic characteristics of the bell tower in the inelastic range, and how do ground motion characteristics affect the structural performance?
3. What is the effect of ignoring the pounding interaction between the tower and the church walls?
4. How does considering an isotropic material over a more realistic anisotropic masonry behaviour affect the structural behaviour?
5. How does including the vertical component alongside two horizontal components affect the structural behaviour?

In summary, the implicit-explicit (impl-ex) algorithm effectively captures the key mechanical behaviour of the bell tower. The solution remains consistent for time steps that are one-fourth or shorter than the record sampling interval. The tower's elastic oscillation periods are shorter when the adjacent walls are included in the model. However, the period shifts observed with the free-surface ground motion set defined in Section 6.4 are within a similar range for both the tower-only and tower-with-wall models. Notably, the pounding interaction results in increased roof displacements in the restrained direction due to the formation of large cracks around the pounding surfaces.

Moreover, assumptions on the material isotropy significantly affect the structural response. An isotropic material leads to a concentrated plastic response, leading to limited energy dissipation compared to the anisotropic equivalent. Finally, considering the vertical

component, increased cracking damage is observed in some cases when the peak vertical acceleration arrives later than the peak horizontal acceleration.

7.2 FUNDAMENTAL PERIOD ESTIMATIONS

The fundamental period is directly related to the initial stiffness of the structure. Hence, even though it is a scalar variable, it packs significant information about the state of the structure. If available, comparing in situ measured period values and numerical estimations is a widely used approach to calibrate or validate structural models. Here, a cross-comparison between ambient vibration tests and fundamental period estimations of other studies that previously studied the bell tower of Guardiagrele is given.

Rosell (2010) reports on ambient vibration tests conducted by Biondi et al. (2009) on the bell tower of Guardiagrele during the installation of new bells. In Table 7.1, the range of frequencies identified by *Biondi et al.,* alongside the estimations of two FE studies conducted in Abaqus, are given (Camata et al., 2008; Rosell, 2010).

Table 7.1. Modal analysis results for the bell tower, including the side walls (values smaller than 0.5% are omitted and replaced with a dash sign).

Mode	Ambient Vibration	Modal Analysis	Mass Participation			Rosell (2010)	Camata et al. (2008)
	(Hz)	(Hz)	$M_X(\%)$	$M_Y(\%)$	$R_Z(\%)$	(Hz)	(Hz)
1	3.45 - 4.07	3.52	55.14	-	-	3.33	3.78
2	6.95 – 7.44	4.35	-	65.34	-	3.65	3.93
5	7.95 – 8.45	7.88	-	-	52.75	7.37	8.53
6	10.04 – 11.56	11.01	-	12.72	-	10.11	11.85
7	13,70 – 15.16	12.40	20.422	-	-	12.25	13.32
8		13.36	2.23	-	0.79	13.05	14.86

For this study, the fundamental frequency of the bell tower model is adjusted to fit in between the frequencies identified by the previous studies. This is achieved by using a stone masonry stiffness of 3.25 GPa and a rubble infill stiffness of 0.7 GPa, which are compatible with the stiffness contrast between the masonry and the fill material through in-situ flat jack tests reported by Rosell (2010). Even though the weak direction is along the NS (-Y), the fundamental period is along the EW (-X) direction due to the church walls present in the NS (-Y) direction. The torsional period is identified as the fifth mode, whereas the

vertical oscillation period is associated with the eighth mode. The eighth mode has a period $T_8 = 0.075$ sec and $M_z = 53.55\%$. It is identified as the vertical fundamental period since it is the first mode with a mass contribution in the vertical direction higher than 5%.

7.3 THE PERMISSIBLE TIME STEP FOR IMPL-EX ANALYSIS

The sensitivity of the impl-ex solution to the chosen time step and the mathematical reasoning behind this sensitivity are discussed in Sections 3.2, 3.4, 4.2 and 4.4. It is explained that depending on the frequency of the solution function, a time step that allows the accurate sampling of the solution function is necessary. Otherwise, the error generated at each step, even if small, might accumulate over time, leading to significant mechanical deviations or, if the time step is too large, complete divergence of the solution. In the case of the harmonic oscillator with a constant vibration period discussed in Section 3.4, identifying the solution step that sufficiently approximates the solution is relatively straightforward. However, as the problem becomes more complex, a trial-and-error approach might be necessary to identify a suitable time step that accurately captures the expected mechanical behaviour.

A time step sensitivity analysis is carried out with the fixed-base bell tower model to find the highest time step that accurately captures the dynamic behaviour of the tower during seismic shaking. Notably, the frequency content of the input ground motion is a significant factor in determining the oscillation frequency of the solution. Furthermore, as observed in the case of the harmonic oscillator, the amount of material nonlinearity that the tower is expected to exhibit is another factor. Unlike the harmonic oscillator, the material discussed here can soften in addition to isotropic hardening. Hence, a poor temporal approximation during the softening phase could overestimate the structure's nonlinear response. Similarly, a higher time step would lead to an underestimation of nonlinearities during the hardening phase. This means that, depending on the size of the time step, some cracking and failure response might go unnoticed unless the time step is reduced, and the model is rerun with the same strong motion.

The "Umbria" ground motion defined in the Section 6.4 of this thesis is chosen as the input motion since it has the highest frequency content within the identified response range (Figure 6.8) of the tower. The Umbria motion is a short and strong burst of acceleration that immediately leads to significant cracking along the weak direction of the structure. When the Umbria ground motion is combined with the fixed-base boundary condition, the resulting analysis results in a structural worst-case scenario given the three strong motions shown in Figure 6.25. Therefore, the resulting time step following the sensitivity analysis is assumed to be suitable for the remaining analyses discussed in this thesis. The analyses are carried out using the three component motions recorded at the free surface (2H+1V). The free surface motion is computed following the procedure outlined in Section 6.5.1.

During the analysis, the sampling interval of the input motion, dt, is taken as a starting point. The set of suitable time steps can likely be around the sampling frequency of the input motion since it determines the motion with the highest possible frequency that might be present in the solution. Then, the time step is halved at each consecutive analysis to increase the number of interpolations to approximate the motion with the highest frequency. The resulting roof displacements are taken as a criterion of success. The roof displacement history is an integral engineering demand parameter (EDP) and contains information regarding the evolving state of the structure during shaking. Therefore, the permanent displacement, i.e., the irrecoverable roof sway at the end of shaking, represents the captured inelasticity and the accumulation of error.

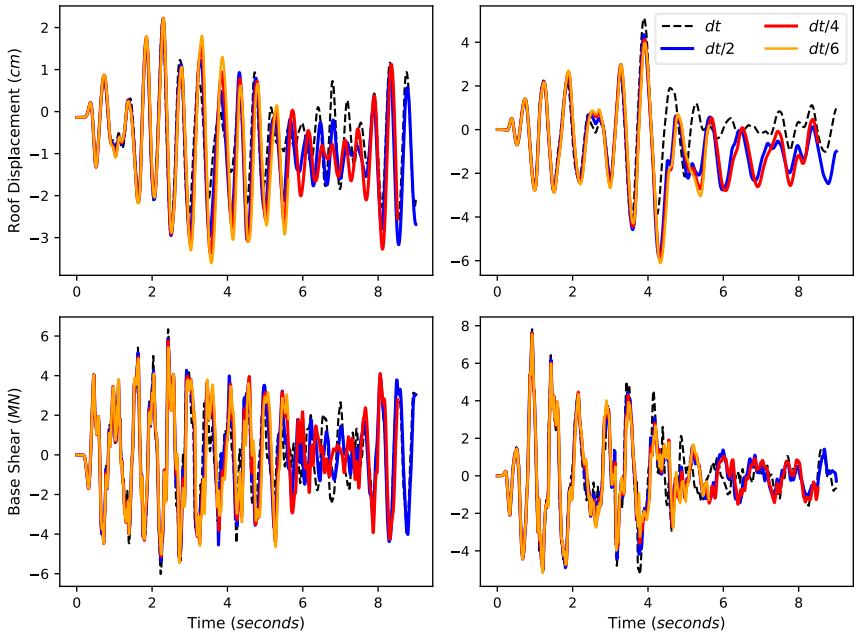

Figure 7.1. Roof displacement versus the solution time step in which dt is the sampling interval of the seismic record.

In Figure 7.1, the change in the computed roof displacement response history for the time step is shown. The permanent displacement in the weak (-Y) direction is underestimated when the analysis is run directly with the sampling time step of the record. However, halving the time step significantly improves the nonlinearities of the captured structure, as the most permanent sway is captured along the global -Y direction. Further, decreasing the time step positively affects the response along the -X axis. However, decreasing the time step beyond one-fourth of the sampling step yields insignificant changes in the observed roof displacement along the -X axis.

Similarly, the cracking damage plots shown in Figure 7.2 indicate consistent results with the displacement histories. On the west and east facades, a significant crack nucleates from the edges of the circular opening and propagates towards the roof, which is only captured if the time step is smaller than half of the sampling interval. Considering the remaining parts of the tower, further decreasing the time step improves the resolution of the estimated cracking damage.

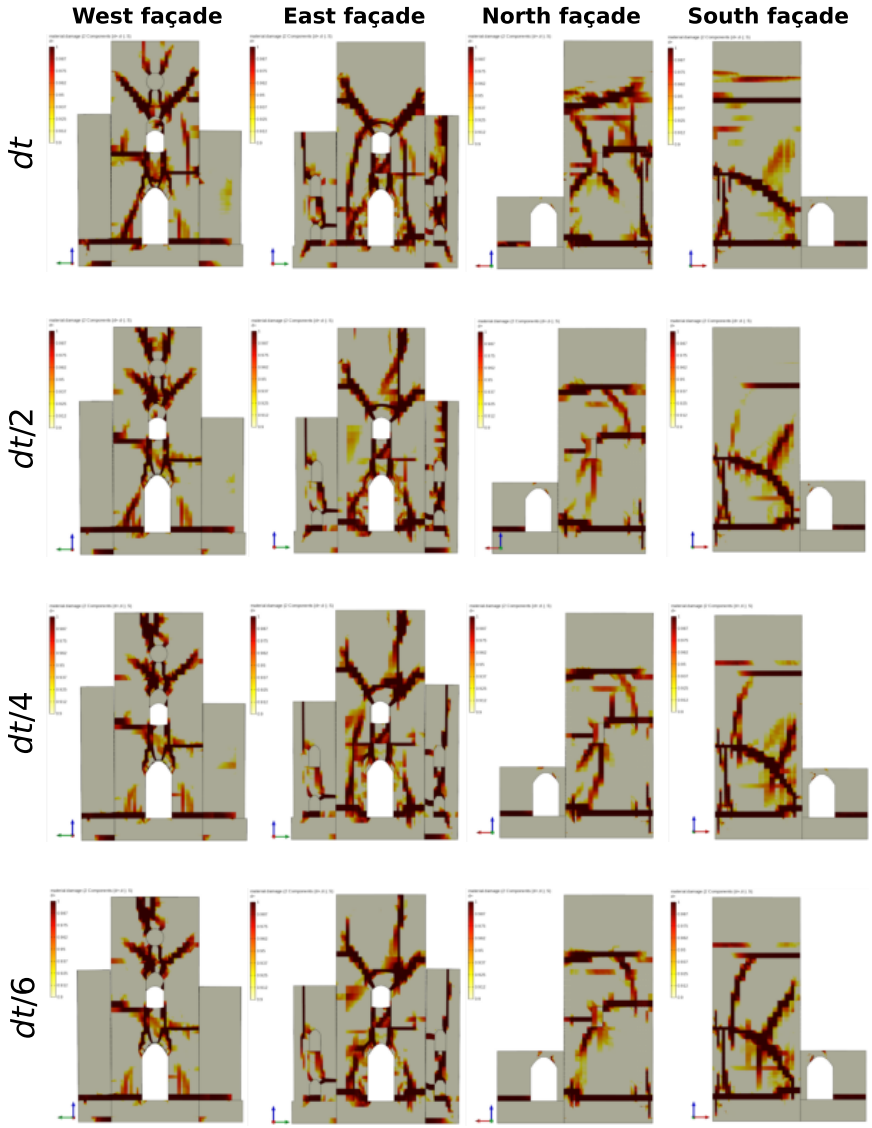

Figure 7.2. The difference in the observed cracking damage at the end of shaking by reducing the time step. dt is the ground motion sampling interval. UMBRIA ground motion (Section 6.4)

The sensitivity analysis reveals that the significant frequencies in the solution waveform are much lower than the sampling frequency. This allows these wavelengths to be accurately approximated when a time step of around dt/2 is used. Therefore, based on the model's performance and results:

- A time step of one-fourth of the sampling interval has been selected for the analyses presented in this thesis, ensuring that the dynamic behaviour of the tower during seismic shaking is captured with sufficient accuracy.

7.4 THE EFFECT OF CRACK PLANE ORIENTATION ON THE DYNAMIC BEHAVIOUR OF THE BELL TOWER

The directional isotropy in the material behaviour is a common assumption in the FE analysis of large structures. Often, the masonry behaviour is modelled through continuum damage plasticity models that are unable to capture the directionally anisotropic stiffness due to the bricklaying technique employed in the construction of the structure or the rotation of the principal tensile strain planes along the brick-mortar joints. This section evaluates the consequences of assuming an isotropic versus orthotropic response in the global response of the bell tower of Guardiagrele.

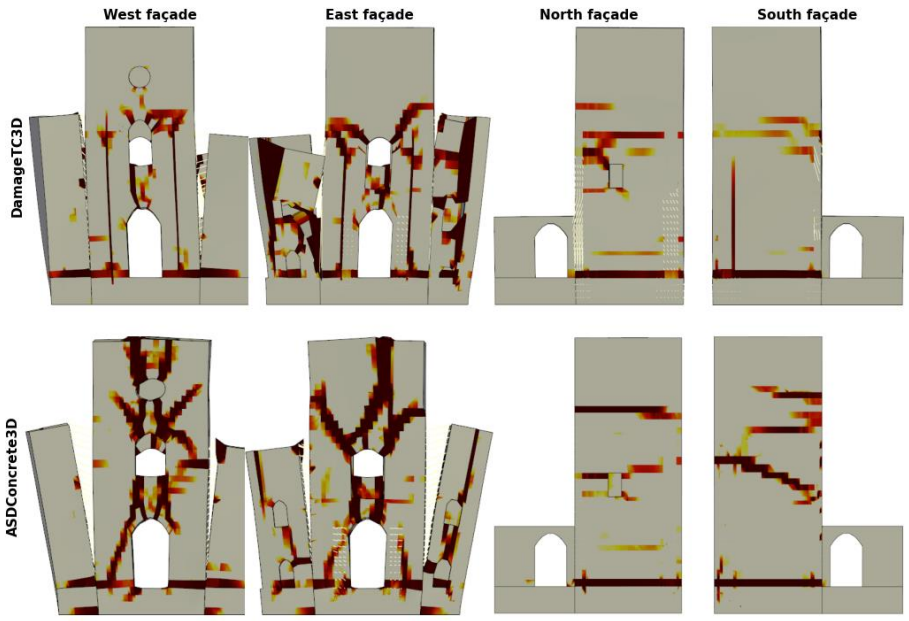

Figure 7.3. The discrepancy in the resulting cracking damage patterns between isotropic (DamageTC3D) and the orthotropic (ASDConcrete3D) models.

Two equivalent models with different constitutive models are prepared to provide a comparison. The isotropic behaviour is modelled with the DamageTC3D material, whereas the orientation of the crack planes is guided towards a 45-degree angle in the anisotropic model via the crack plane assumption option offered in the ASDConcrete3D model. DamageTC3D and ASDConcrete3D models belong to the same family of damage-plasticity models with only minor differences in their stress-strain backbone behaviour. The relevant formulation of these models is covered in Section 2.5.1. Hence, both materials are calibrated to provide an equivalent stress-strain response, as shown in Figure 5.7. The Lazio-Abruzzo 1984 record, discussed in Section 6.1, is used as the input motion.

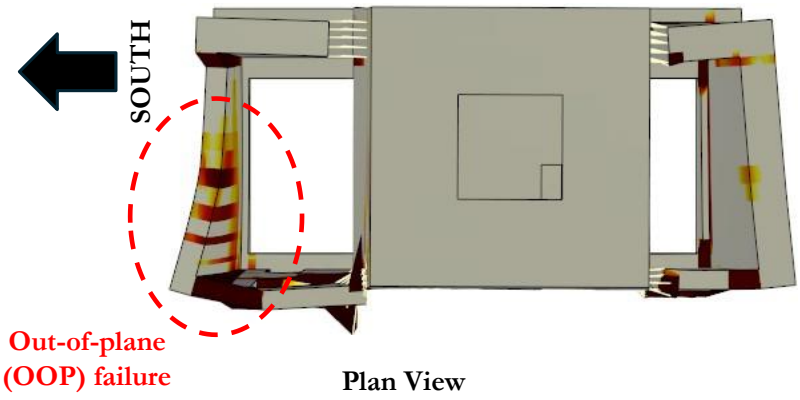

Figure 7.4. An out-of-plane (OOP) failure mechanism appears towards the south in the isotropic (DamageTC3D) model.

The cracking damage pattern computed for the two different assumptions can be seen in Figure 7.3. The most significant difference between the top row (isotropic material) and the bottom row (orthotropic material) is the wider spread of the cracks resulting from the orthotropic material assumption. In the isotropic model, the cracks appear to be relatively localized compared to the orthotropic model. In the East façade, the church wall on the left is heavily damaged, and a local collapse at the second level can be observed. A long crack spreads from top to bottom at the corner joint of the wall, creating a free boundary condition for the western and southern-facing parts of the wall. On the south façade, this leads to an out-of-plane folding mechanism shown in Figure 7.4.

On the other hand, such a localized mechanism does not appear in the orthotropic (ASDConcrete3D) model since the cracks are distributed throughout a wider area and

extend at a 45-degree angle. Furthermore, more realistic crack paths appear in the north and south facades, where no or limited openings are present. Cracks that propagate in a perfectly vertical direction can be observed in the isotropic model. Such cracking cannot be expected in a solid masonry wall under cyclic shear loading due to the masonry laying patterns and the significant difference in strength between the mortar and the stones. The cyclic shear loading test of a stone masonry pier is discussed in Section 3.5.

The effects of strongly localized damage due to the isotropy assumption can also be observed in the recorded roof acceleration history. Notably, in Figure 7.5, the acceleration history starts identically in both directions, indifferent to the material anisotropy. This is intuitive since the anisotropic behaviour considered in this study concerns the directional anisotropy of strength and ignores the directional changes in the stiffness. Hence, if properly calibrated, the small strain behaviour must be the same in DamageTC3D and ASDConcrete3D materials. On the other hand, as the cracking damage accumulates, differences in behaviour between the two different assumptions become apparent. In the top row (EW direction) of Figure 7.5, the damping response achieved with different isotropy assumptions significantly differs after high accelerations occurred in the model. The more efficient energy dissipation of the anisotropic model can be noticed as the magnitude of acceleration quickly fades out compared to the isotropic model. This is due to the larger crack surface area present in the orthotropic model. Hence, the seismic energy is dissipated over a larger area than the limited area computed in the isotropic model.

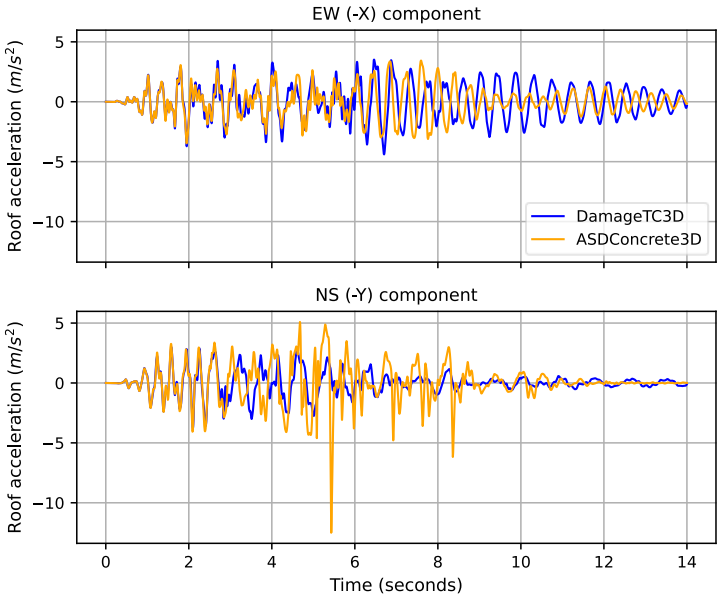

Figure 7.5. Acceleration histories recorded at the tower's roof for the isotropic and the orthotropic material assumptions.

In addition, in the bottom row (NS direction) of Figure 7.5, the anisotropic model seems to generate high-frequency acceleration spikes compared to the smoother response of the DamageTC3D model. A comparison of the acceleration spikes with the damage propagation reveals that the spikes occur when cracks propagate rapidly towards the tower's roof in a sudden, burst-like motion. These spikes result from the abrupt reduction in structural stiffness as the cracks form and extend. As the structure loses stiffness, it releases stored energy, which manifests as sharp increases in acceleration. The larger the crack, the greater the loss of stiffness and the more energy released, resulting in more pronounced acceleration spikes. This behaviour highlights the direct relationship between crack growth and dynamic response in the tower. Depending on the width of the crack, the frequency range of these cracks can be greater than 20 Hz for smaller cracks or within the range of 5-15 Hz for larger global cracks. Therefore, the roof acceleration history yields consistent results with the information obtained from the cracking damage plots.

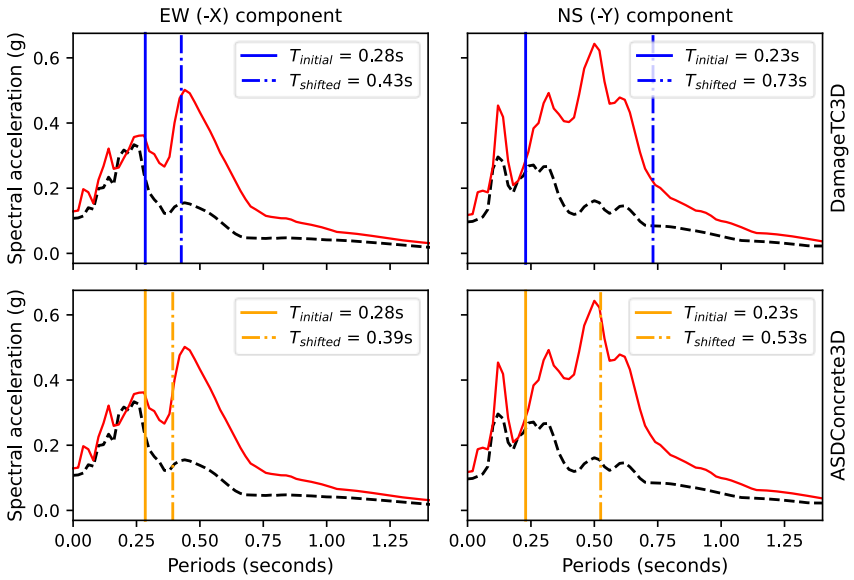

Figure 7.6. The difference in the elastic versus inelastic periods computed considering an orthotropic masonry behaviour.

Similarly, the effect of material isotropy is reflected as a considerably larger inelastic period. The roof acceleration response spectra for both models are plotted in Figure 7.6 after filtering frequencies higher than 20 Hz, which is the maximum frequency expected to be generated by a seismic event. As expected, the resulting roof spectra look similar in both

models, with slightly increased acceleration amplitudes in lower periods in the ASDConcrete3D model. Regarding inelastic performance, the limited energy dissipation in the ASDConcrete3D model leads to an increased inelastic response indicated by a larger period shift in the predominant period.

Finally, the reason for an increased inelastic response in the isotropic model can be connected to the seismic demand by studying the force-displacement plots in Figure 7.7. Since the same ground motions are used for all analyses, the seismic demand is the same for both models at the beginning of the analysis. However, in the nonlinear response range, the demand starts to differ since the tower models display different amount of softening. At the initial stage of the analysis, when the seismic demand is similar for both models, the isotropic model must reach increased softening to meet the displacement demand of the seismic motion. This is because the isotropic model has a limited number of localized cracks and relies on these cracks to achieve the impose displacements by the ground motion. On the other hand, the orthotropic model can provide a higher displacement capacity with a relatively lower inelastic material response since distributed cracks lead to increased flexibility. This can be seen in Figure 7.7, which compares the NS components of the models.

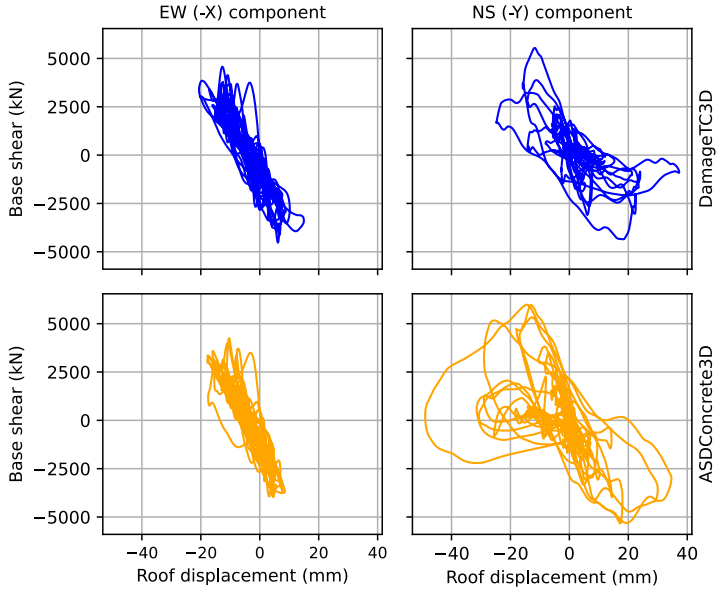

Figure 7.7. Difference in the roof displacement versus force response considering an orthotropic masonry behaviour.

To summarize, it is evident that assuming an orthotropic material response leads to a more realistic cracking damage response for large masonry structures. Furthermore, the effects of local cracking alter the global response of the structure significantly, providing the structure with an increased but accurate seismic capacity due to the distributed cracking behaviour and more representative energy dissipation characteristics.

7.5 NONLINEAR DYNAMIC RESPONSE OF THE BELL TOWER

The dynamic response of the bell tower during the Lazio-Abruzzo strong motion is introduced in Section 6.3. However, the discussion focuses on defining a structure-informed intensity measure (IM) suitable for selecting a ground motion set. This section discusses the seismic response of the fixed-base tower model, including the church walls (Tower-Wall model), emphasising the damage material response. The ground motion set selected in Sections 6.4 and 6.5.1 are used. However, due to the high computational cost of running an analysis, only the three ground motions identified within the ground motion set are studied. The reader is referred to Section 6.6.1 for further details about the record elimination process. The analyses are carried out using the three component motions recorded at the free surface (2H+1V).

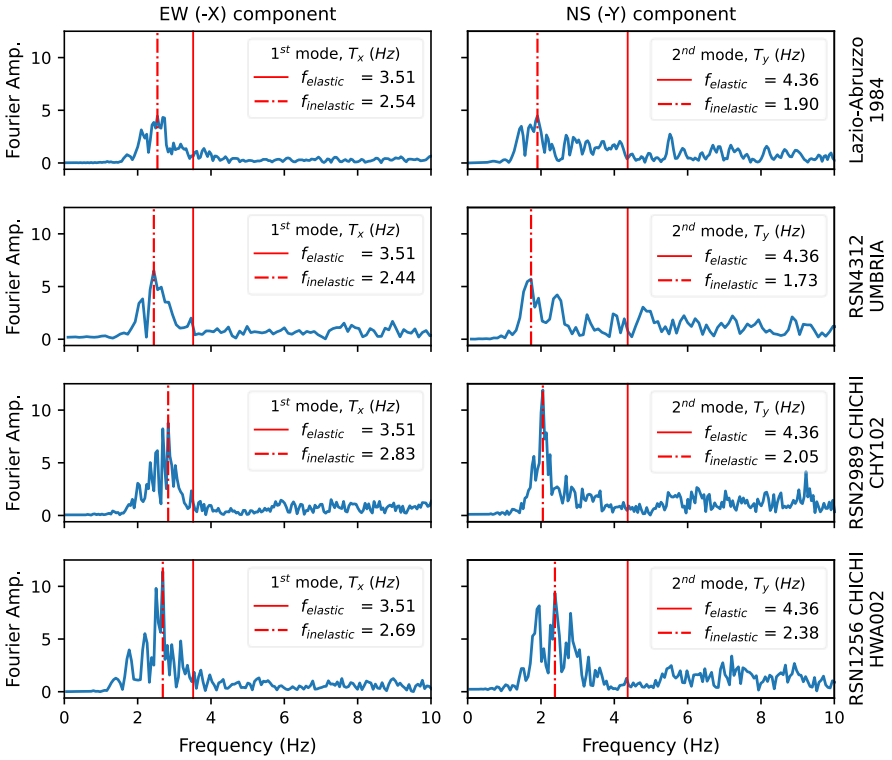

Figure 7.8. (Tower-Wall model) Fourier spectrum analysis of the roof acceleration for different strong motions.

Figure 7.8 presents the results of Fourier analysis performed on the roof acceleration histories. The elastic fundamental frequency of the tower in each direction (from linear analysis) and the peaks of each Fourier spectrum are indicated by solid and dash-dot vertical lines, respectively. These plots illustrate the shift in predominant frequencies caused by the material's nonlinear behaviour. Notably, the frequency shift in the NS (-Y) direction is significantly larger for all ground motions compared to the EW (-X) direction. This is expected, as the large openings along the NS (-Y) direction lead to extensive cracking and inelastic response. The cracking damage plots in Figure 7.12 confirm this, showing that a greater number of Gauss points with tensile damage exceeding 0.9 (on a scale of 1.0) are present in the NS (-Y) direction compared to the EW (-X) direction.

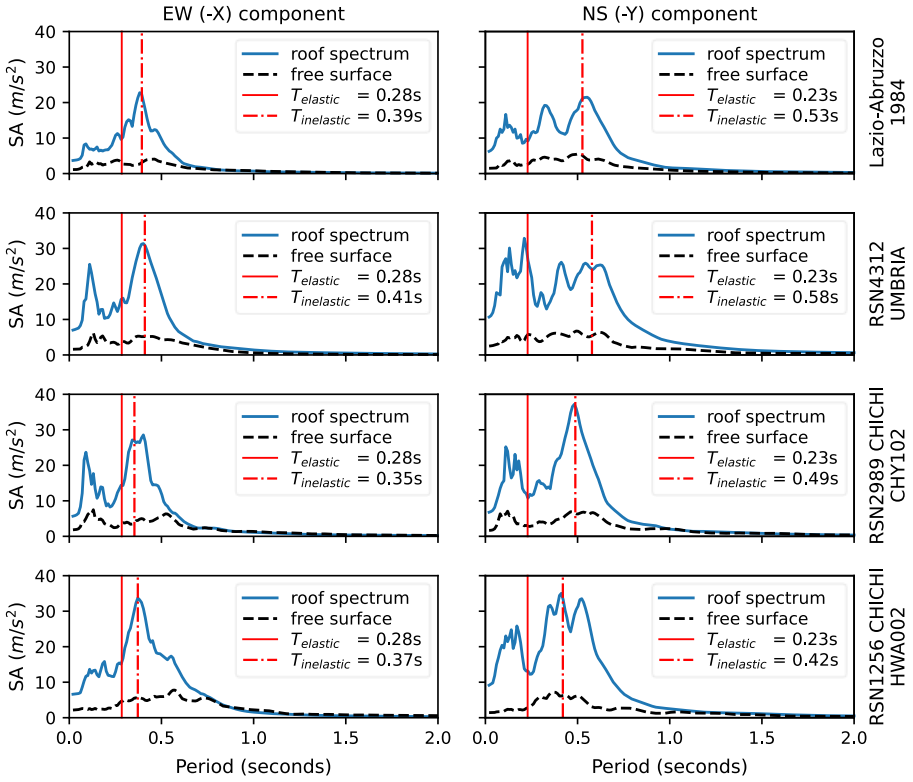

Figure 7.9. (Tower-Wall model) Roof acceleration spectra for different strong motions. Input motion is recorded at the free surface.

On the other hand, within each direction, the inelastic predominant frequencies are in close range, averaging at 2.65 Hz and 2.05 Hz with a standard deviation of 0.14 Hz and 0.23 Hz for the EW and NS components, respectively. This behaviour can be explained by studying the input and roof motion response spectra. In Figure 7.9, the dashed curves represent the input response spectra evaluated at the free surface of the 1D nonlinear soil column, whereas the solid curves are the resulting roof spectra. Each strong motion triggers a nonlinear response in the bell tower and increases the modal periods due to damage accumulation. Almost all input motions peak consistently around a period of 0.5 seconds, which is larger than the elastic response range of the bell tower. The reason for the appearance of pronounced demands around 0.5 seconds in the input spectra is the 1D soil column response discussed in Section 6.5.1. Depending on the amount of softening due to damage accumulation in the tower, the tower period shifts towards the peak of the input spectra. This shift leads to increased forces and, in return, increased damage to the tower. The amount of expected shift is also a function of the displacement response spectrum and mainly the demand on the structure, which can be best identified by comparing the force-displacement response of the tower with the acceleration-displacement response (ADRS) spectrum (Fajfar & Gašperšič, 1996).

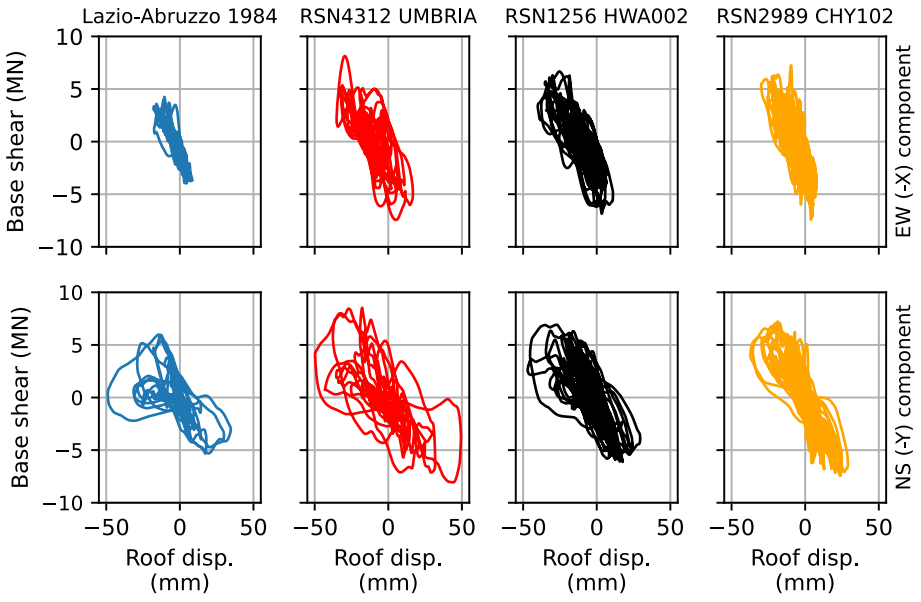

Figure 7.10. (Tower-Wall model) Roof displacement versus base shear response for different strong motions.

As intuitively expected, roof displacements during shaking are more prominent in the NS direction. Figure 7.10 shows the tower's dynamic force-displacement response, where the

Lazio-Abruzzo motion results in a notably smaller cyclic response area compared to other motions. This outcome is anticipated, given that the Lazio-Abruzzo motion is not part of the selected ground motion set. As illustrated in Figure 6.13, this motion falls within the dispersion of the set but consistently tracks the lowest bound for periods over 0.4 seconds, indicating a lower AvgSA than the set's average. Consequently, despite a matching inelastic period shift, the Lazio-Abruzzo motion generates a smaller response envelope. This suggests potential behavioural differences in brittle structures when using ground motion sets conditioned on SA and AvgSA. However, further research with a statistically significant dataset is required to confirm any consistent discrepancy in seismic demands.

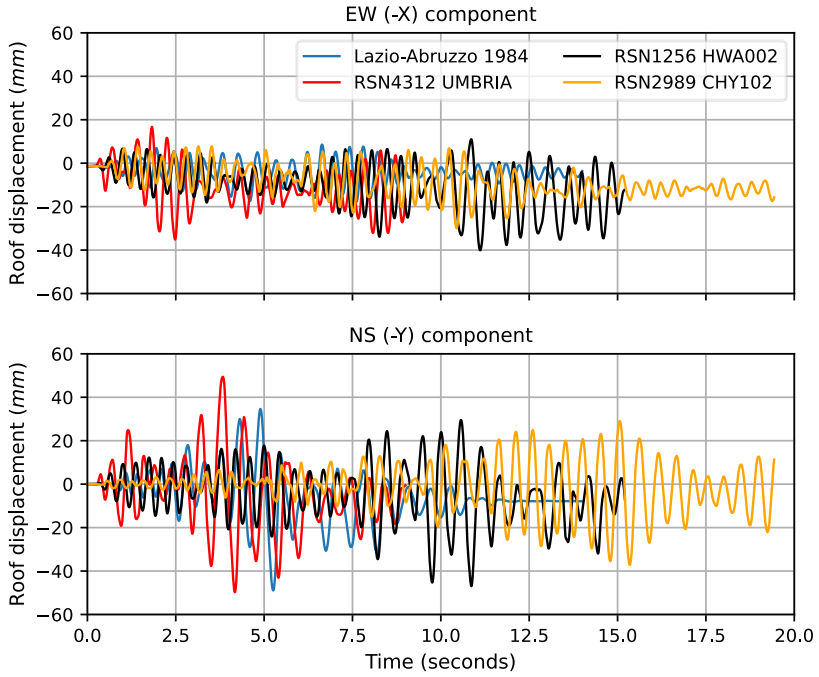

Figure 7.11. (Tower-Wall model) Permanent roof displacement for different strong motions.

Despite the more severe inelastic response along the NS direction, the average permanent roof displacement is similar in both directions. This is due to the crack closure phenomenon in the damage-plasticity material behaviour. Unlike pure plasticity theory, where energy is lost due to irrecoverable deformations, damage mechanics accounts for energy dissipation from fracturing by reducing the material's unloading-reloading stiffness. The ASDConcrete3D material, which combines damage and plasticity, is capable of modelling both irrecoverable deformations and the fracturing process typical of brittle

materials like masonry. The balance between damage and irrecoverable deformation is controlled by two scalar parameters, one for tensile and one for compressive loading. As plasticity's contribution increases, the magnitude of permanent roof displacements is expected to rise. Further discussion on the calibration of these parameters and their effects can be found in Section 3.5, with reference to a cyclic in-plane loading test on a squat masonry pier.

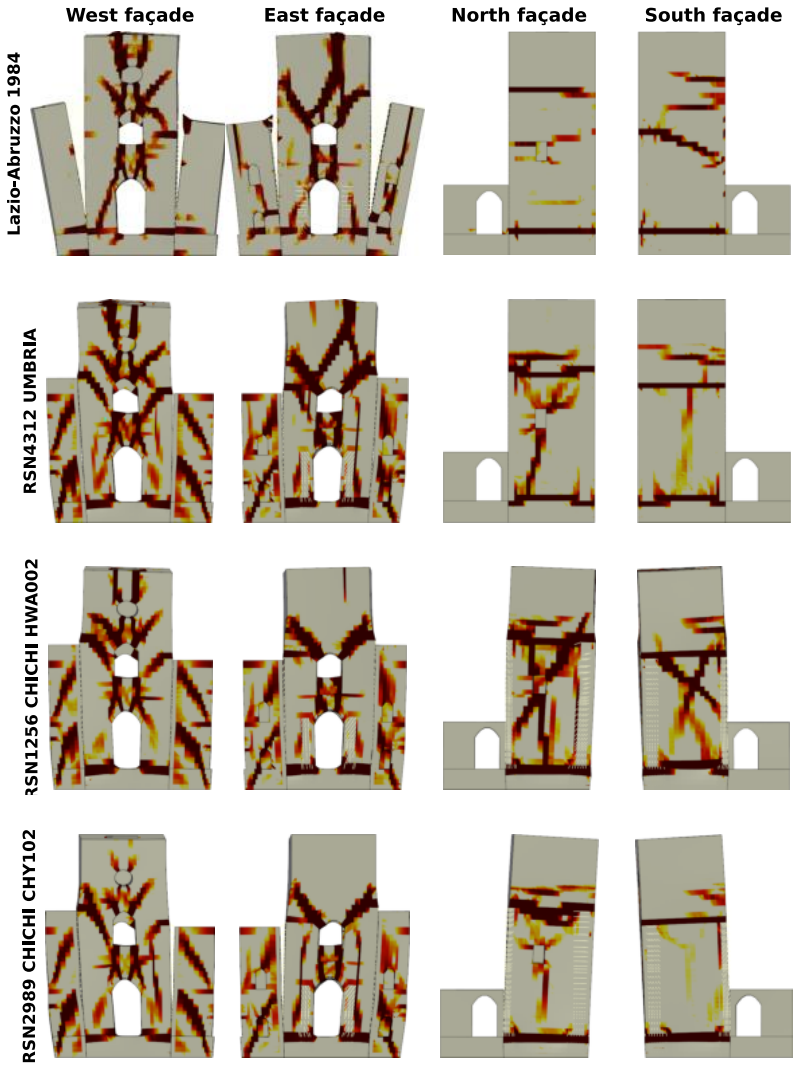

Figure 7.12. (Tower-Wall model) Tensile cracking damage patterns. The Gauss points having a damage value of less than 0.9 are not shown.

Finally, the cracking damage patterns computed for each ground motion can be seen in Figure 7.12. Notably, the East and West facades exhibit consistent cracking patterns across all ground motions. A prominent crack extends from the circular fenestra on the West façade, through the roof, and toward the arch of the opening on the second level of the East façade. This crack is most pronounced in the Lazio-Abruzzo and Umbria motions, with initial formation visible in the Chichi chy102 and hwa002 motions. The development of this crack correlates closely with the maximum roof displacement along the NS direction, as shown in the displacement history in Figure 7.11.

To conclude, the following significant observations are made based on the results obtained in this section:

1. The bell tower is observed to experience amplified shaking due to an inelastic period shift if the peak of the input response spectrum occurs at a longer period than the structure's fundamental period.
2. Damage-plasticity ratio variables in tension and compression significantly affect the dynamic response of the structure since they control the unloading-reloading stiffness and the permanent displacements during strong shaking.
3. Structural openings play a crucial role in guiding cracking damage patterns, potentially leading to results that are relatively insensitive to variations in ground motion, in contrast to continuous, solid facades.

7.6 THE EFFECT OF SEISMIC POUNDING INTERACTION ON THE DYNAMIC RESPONSE OF THE FIXED-BASE MODEL

The dynamic behaviour of the bell tower during earthquake shaking is strongly affected by the adjacent church structure, primarily due to the pounding interaction between the bell tower and the church walls that are in contact with the tower along the NS direction (Section 7.5). However, modelling the bell tower without the adjacent church walls (Tower-only model) might also be a valid modelling decision. In this case, the stiffening contribution of the adjacent walls is ignored, altering the vibrational characteristics of the tower compared to the Tower-Wall model. Furthermore, the Tower-only model would also be used to gain insight into the dynamic behaviour of the tower following the partial or total collapse of the adjacent walls. Therefore, the behaviour of the tower-only model is studied in this chapter. This section aims to quantify the contributions of the pounding response observed in the Tower-Wall model and understand if ignoring the presence of adjacent structures brings crucial outcomes in the analysis of masonry towers.

The adjacent walls along the NS direction and the buttresses connecting the east façade of the tower to the main church hall are removed to obtain the tower-only model. The same

ground motions used in the analysis of the tower-wall model are used in the tower-only model for a fair comparison.

The most immediate outcome of removing the adjacent walls can be seen in the modal analysis results. Following the removal of the walls, the fundamental period becomes the translation mode along the NS direction with T_y = 0.37 seconds. It is worth noting that the fundamental period is along the EW direction with T_x = 0.28 seconds in the tower-wall model due to the stiffening effect of the adjacent walls, even though the weak direction of the tower is along the NS direction. In addition to the alteration in the direction of the first mode, a change of around 40% occurs in the vibration period along the NS direction.

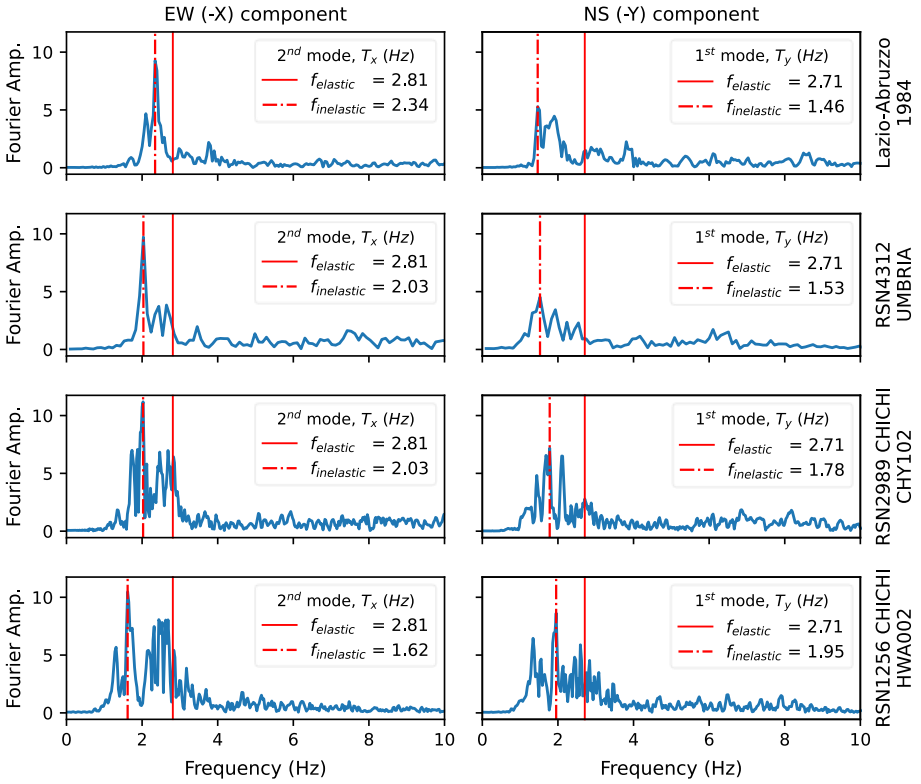

Figure 7.13. (Tower-only model) Fourier spectrum analysis of the roof acceleration for different strong motions.

Figure 7.13 shows the inelastic predominant periods of the tower-only model, computed using Fourier spectrum analysis. Similar to the tower-wall model, a more significant period shift is observed in the NS direction, primarily due to the increased inelastic response caused by the large openings. Unlike the EW direction, the period shift in the NS direction

remains consistent across all ground motions. This consistency is explained by the cracking damage pattern shown in Figure 7.17, which remains similar for all ground motions. The cracking follows a path that minimises energy, largely controlled by the openings. Overall, the removal of adjacent walls results in a reduction of most of the predominant structural frequencies.

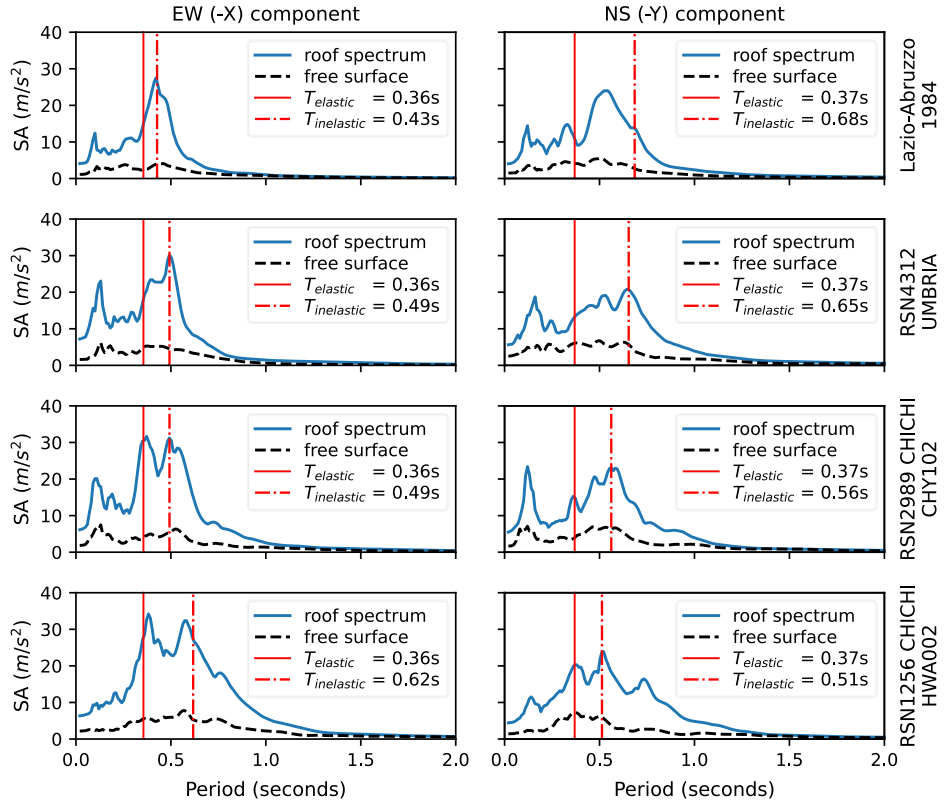

Figure 7.14. (Tower-only model) Roof acceleration spectra for different strong motions. Input motion is recorded at the free surface.

Figure 7.14 shows the roof acceleration spectra of the tower-only model. Comparing the tower-only model with Figure 7.9, one can see that the tower acceleration response is affected by the removal of the walls. Except for the "Lazio-Abruzzo" motion, a decrease is observed in the low-period accelerations, whereas an increase is obtained in the longer-period accelerations. This is intuitive since the walls act as stiffening elements and limit displacements to an extent. Hence, the high frequencies are increasingly excited as the structure becomes stiffer.

As discussed in Section 7.4 , if the floors located in the adjacent walls are not modelled, the walls may fail at their corner joints on all sides due to inadequate support. This leads to freed boundary conditions, resulting in the out-of-plane failure of the walls through diagonal folding. Since this study focuses on the bell tower, the floors in the adjacent walls are modelled as rigid. However, the finite stiffness of these floors can influence the horizontal behaviour of the walls. As the floors become more rigid, the walls increasingly behave as shear elements, since rigid floors enforce the "plane sections remain plane" assumption at slab heights. While modelling the slabs with shell elements is an option, the separation allowed between the walls and the tower, and the need for one edge of the slab to be supported by the tower façade, introduces numerical instabilities. These arise as the slab gains and loses contact with the tower, affecting the tower's damage material response. To simplify the problem and ensure numerical stability, rigid links are used at the slab levels to create stiff, stable floors.

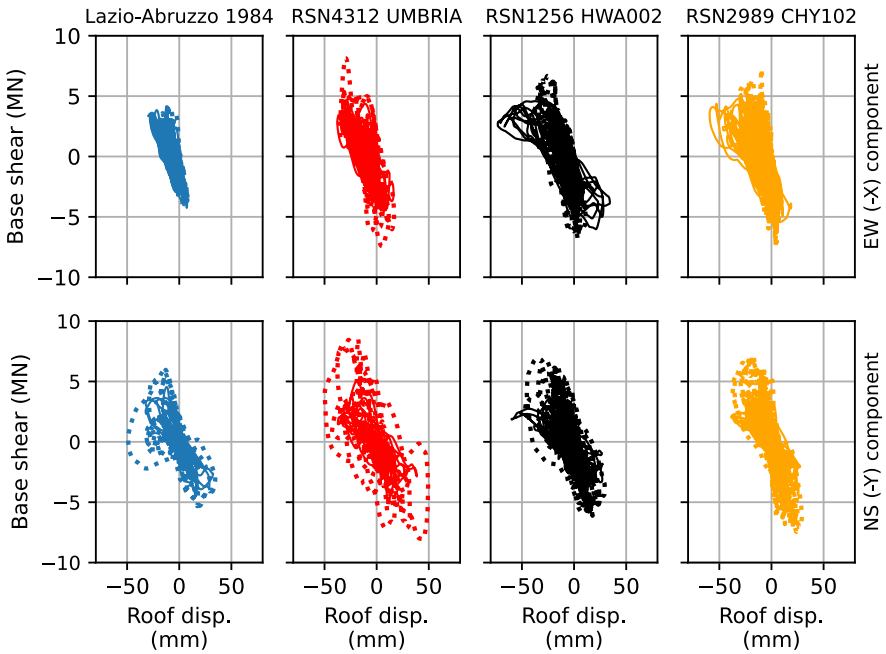

Figure 7.15. (Tower-only model) Roof displacement versus base shear response for different strong motions. The dotted curves are the tower-wall model response discussed in Section 7.5.

Figure 7.15 shows the force-displacement response of the tower-only model (solid curves) compared to the tower-wall model (dotted curves). Notably, the force-displacement response in the tower-wall model is greater than that of the tower-only model in the NS

direction, which corresponds to the tower's weak axis. In the tower-wall model, the adjacent walls provide additional support along the NS direction, leading to an expected increase in base shear compared to the tower-only model. Despite this increase in base shear, which would typically result in reduced roof displacement, the roof displacement in the tower-wall model is actually larger than in the tower-only model.

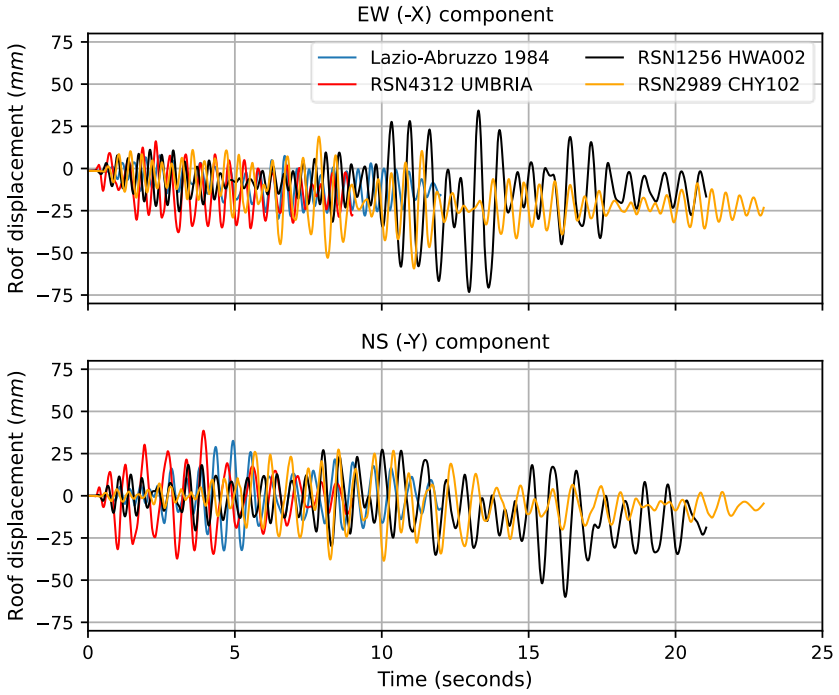

Figure 7.16. (Tower-only model) Permanent roof displacement for different strong motions.

Further investigating the cracking damage patterns in Figure 7.12 and Figure 7.17 yields that in addition to the damage obtained in the tower-only model (Figure 7.17), wide cracks that extend from the arch of the main entrance towards the edges where the adjacent walls meet the tower can be seen (Figure 7.12). These are deep and propagate through the thickness of the tower, hence dividing the tower into top and bottom parts. The bottom part is stiffer due to the continuing interaction with the adjacent walls and oscillates with a higher frequency. This leads to the observed higher forces. Meanwhile, the top part of the tower is free to move and can accommodate substantial displacements due to partial rocking behaviour. The complex inelastic rocking behaviour can be captured due to the crack closing-opening feature of the damage mechanics. Most importantly, a solution can be found at this stage of the analysis due to the remarkable stability of the IMPL-EX algorithm (discussed in Section 7.3).

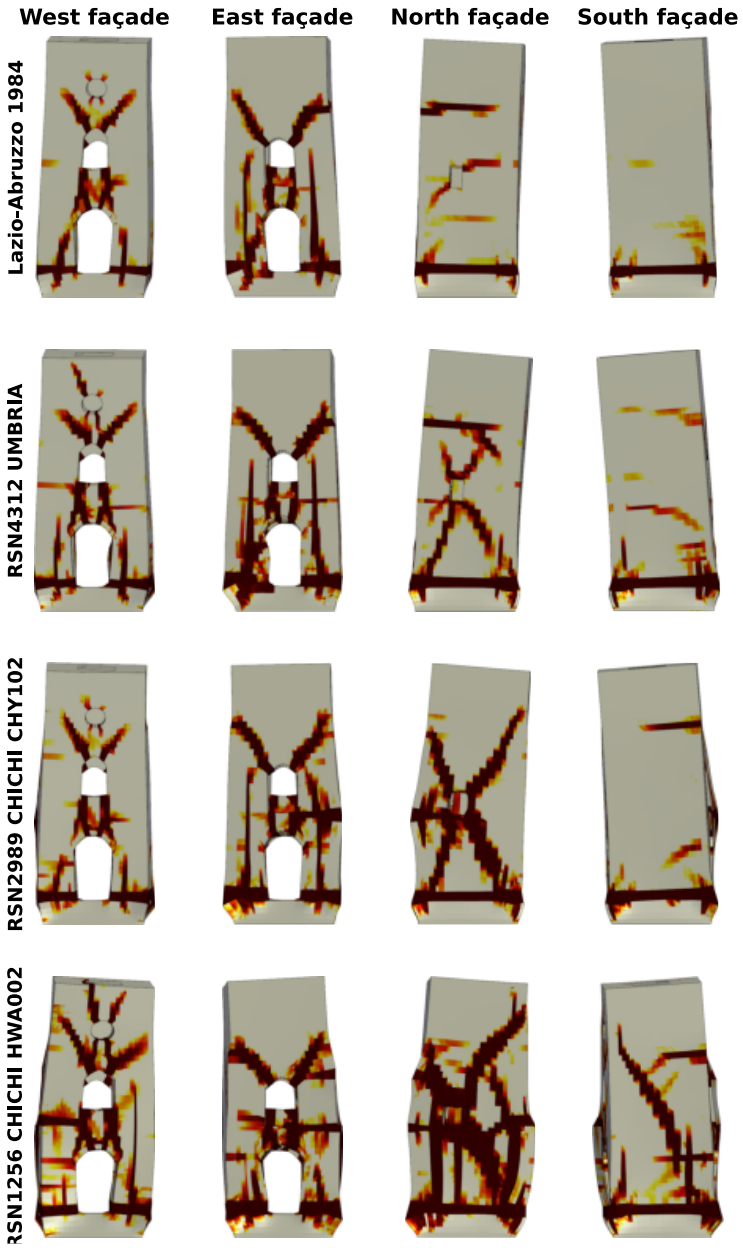

Figure 7.17. (Tower-only model) Tensile cracking damage patterns. The Gauss points having a damage value of less than 0.9 are not shown.

The tower-wall and the tower-only models exhibits an inelastic rocking mechanism during the initial phases of shaking due to extensive cracking at the foundation-to-tower connection. However, the intensity of the cracking at the tower base is much stronger in

the tower-only model (Figure 7.17). This failure is one of the main reasons for the observed permanent roof displacement, as shown in Figure 7.16. In the EW component, the tower attains permanent roof sway due to the powerful shaking of the "Chichi hwa002" motion. However, some permanent displacement is recovered later due to a consecutive, weaker push towards the other direction. This is easily possible since the plastic zone is concentrated at the bottom of the tower-only model.

To summarize, the key finding of this section is that even though the pounding interaction between adjacent structures may provide increased stiffness to tower structures, the cracking damage created by the pounding may lead to local mechanisms that may be detrimental considering the seismic behaviour of the masonry towers.

7.7 THE EFFECT OF THE VERTICAL COMPONENT IN THE MATERIAL ONLY NONLINEAR ANALYSIS OF THE BELL TOWER

The intensity of the horizontal motions and their vectorial combinations have been shown to have the most significant effect on the performance of a structure (Boore, 2010; Boore et al., 2006; Poulos & Miranda, 2022). In the traditional seismic assessment of structures, the vertical component is often ignored during analysis, if the contribution of the forces that arise due to the vertical acceleration is insignificant. However, following the seminal field observations of Papazoglou & Elnashai (1996), recent studies focused on the effects of vertical motion on the structures with increasing interest (Carydis et al., 2012; Di Michele et al., 2020; Elgamal & He, 2004; Harrington & Liel, 2016; Kallioras et al., 2022). These studies have a range of outcomes supporting the contribution of the vertical component to the structural response of masonry and reinforced concrete (RC) structures in some cases. They indicate no significant contribution of vertical motion in other cases. The ongoing dispute about the importance of considering the vertical component indicates the complex relationship between the possible actions due to the vertical component and the observed structural damage.

This section uses the bell tower model to study the potential effects of considering or not considering the vertical component. It is worth mentioning that all the analyses presented in this thesis include 3-component acceleration if otherwise stated. Hence, here, the effect of the vertical component is studied by rerunning the models by only considering the horizontal components and disregarding the vertical component. Then, the resulting behaviour is compared with the 3-component behaviour discussed in the previous sections. The tower-only model is selected since it is the simplest model to study and is isolated from the effects of pounding interaction, as discussed in Section 7.6. The input ground motions are the records discussed in Section 6.6.1, selected in Section 6.4 and processed in Section 6.2, in addition to the Lazio-Abruzzo 1984 motion discussed in Section 6.1.

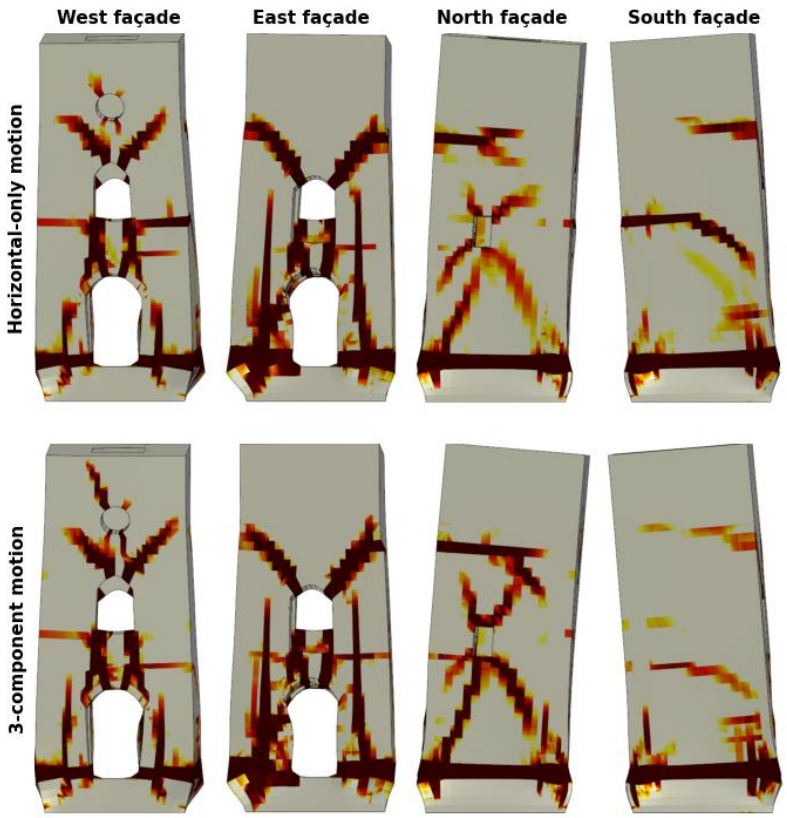

Figure 7.18. The observed cracking damage patterns due to the "Umbria" motion. Comparison of 2 versus 3 component acceleration.

Figure 7.18 and Figure 7.19 show the cracking damage patterns for the "Umbria" and the "Chichi hwa002" motions. The two-component (horizontal-only) ground motion is considered in the top row, whereas all the three-components are applied for the analysis depicted in the bottom row. Interestingly, a different cracking damage pattern is observed for the "Umbria" ground motion for the two and three-component motions, whereas no significant change is present for the "Chichi hwa002 motion". Focusing on Figure 7.18, the "Umbria" motion, one can observe that the computed cracks slightly rotate toward the vertical axis in the presence of the vertical accelerations. This indicates the rotation of the principal tensile strain axes within the model. In Figure 7.18, the rotation phenomenon is strongly noticeable at higher elevations and around the openings where compressive stresses can be lower than the bottom levels, where the behaviour is governed by the overburden pressures.

This finding is consistent with the observations of Di Michele et al. (2020) and Harrington & Liel (2016). Di Michele et al. (2020) found that the changes in the axial forces of the

vertical load-bearing members of masonry structures might alter the observed failure mechanisms expected at the higher storeys. Harrington & Liel (2016) observed a similar phenomenon in RC columns.

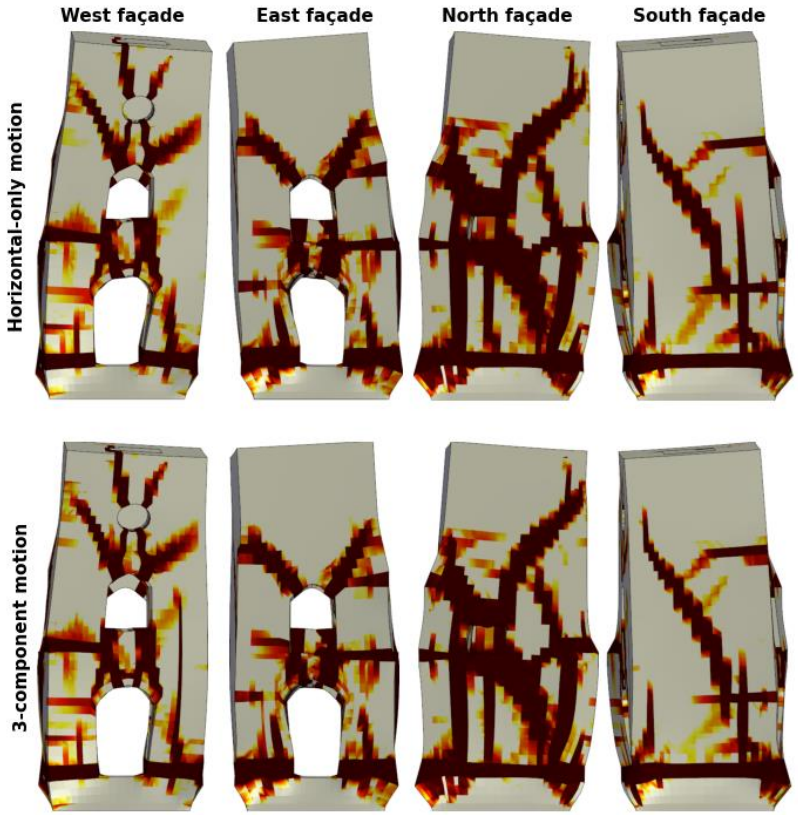

Figure 7.19. The observed cracking damage patterns due to the "Chichi hwa002" motion. Comparison of 2 versus 3 component acceleration.

To further investigate the reasons behind the change in the cracking damage patterns due to the "Umbria" motion, the principal tensile stress-strain response is plotted in Figure 7.20. Two elements are selected, shown in the b and c parts of Figure 7.20. In both "Umbria" and "Chichi hwa002" ground motions, vertical accelerations increase the strain demand. Furthermore, some rotation in the principal tensile axis can be seen in the north façade of the bell tower by studying the cracking damage patterns in Figure 7.18. Nevertheless, the effect is more noticeable in the "Umbria motion" since first, the forces caused by the vertical acceleration are stronger, and second, the tensile damage has room to develop further with the changing principal stresses due to the vertical accelerations. On

the other hand, in the case of the "Chichi hwa002" motion, since the horizontal component of the motion is powerful, the recorded tensile principal stress-strain curve reaches the residual state regardless of the presence of vertical accelerations. This indicates that the effect of the vertical component on the structural damaging response might be tied to the damage caused by the horizontal response.

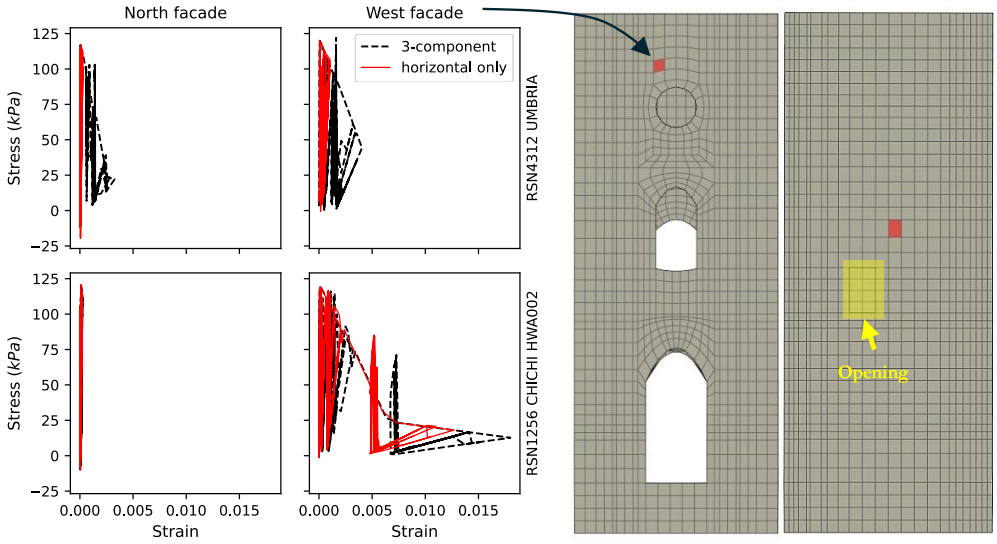

a) Principal max response **b) West façade** **c) North façade**

Figure 7.20. Discrepancy in the computed principal tensile stress-strain when the two or all motion components are considered.

The vertical acceleration response spectra computed at the roof of the bell tower for each ground motion are shown in Figure 7.21. Of note is the amplification of the vertical accelerations observed during the "Lazio-Abruzzo" and the "Umbria" motions, which are significantly higher than the other two "Chichi" motions. The roof vertical spectra computed for the "Chichi" motions are insensitive to the vertical accelerations. Furthermore, the difference between the elastic and inelastic predominant vertical periods may appear to be smaller than the order of magnitude of the period shift generally observed in the tower due to the horizontal behaviour. However, the change is significant when considered in terms of percentage values. The observed limited shift in the vertical period is consistent with the experimental findings presented by Kallioras et al. (2022), in which no or little change in the vertical periods is observed after numerous testing sequences.

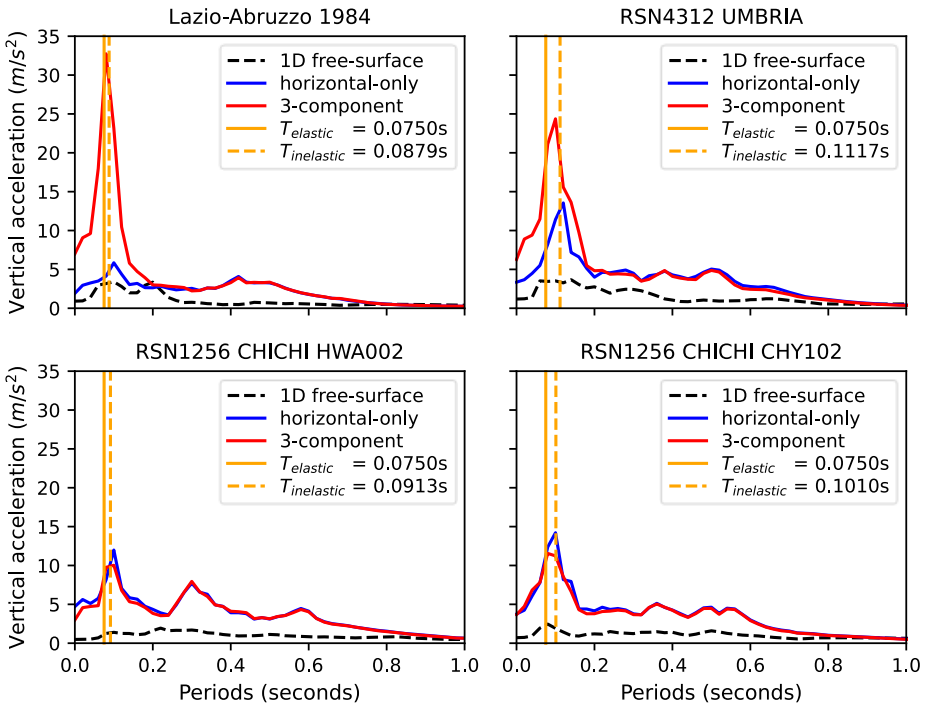

Figure 7.21. Vertical roof acceleration spectra computed at the roof for two and three-component motion assumptions. The predominant vertical periods for each motion are marked.

One possible explanation for the idiosyncratic amplification behaviour observed in Figure 7.21 can be found in Table 7.2. The peak accelerations and the time of peak accelerations are given in Table 7.2 for all four motions. The strong motion begins when the vertical component reaches 5% Arias intensity. The interested reader is referred to Section 6.2 for detailed information regarding the time windowing strategy chosen for this study.

Remarkably, the motions in which the peak vertical acceleration occurs later than one or both peak horizontal accelerations cause an amplified response in the vertical spectral accelerations recorded at the tower's roof. This might indicate that the prior damage caused by the horizontal components can lead to increased vertical amplifications in the tower. This phenomenon is supported when the relationship between the horizontal and vertical tensile principal stress-strain response (Figure 7.20) is considered which is also consistent with the experimental observations of Di Michele et al. (2023).

Unfortunately, the experimental observation of the possible effects of the later arrival of the peak vertical acceleration is not available. In their shake table experiments, Kallioras et al. (2022) observed no significant effect on structural damage when the vertical component is included. However, they only considered an input motion intentionally selected to have a slightly earlier peak vertical acceleration arrival time than the peak horizontal acceleration. Nevertheless, the observed amplification response here might be able to explain the exponential increase in the vertical amplifications as they linearly scale the input motion (10% increase) in each sequence of the shake table test. Amplification in the vertical roof acceleration, higher than 10%, might be expected at the consecutive analysis as the horizontal component of the previous sequence induces damage in the structure.

Table 7.2. List of maximum accelerations and time of maximum accelerations for each ground motion (Time since the start of the strong motion).

Ground Motion	Vertical component		NS component		EW component	
	Max Accel. (m/s^2)	Time of Max. Accel. (seconds)	Max Accel. (m/s^2)	Time of Max. Accel. (seconds)	Max Accel. (m/s^2)	Time of Max. Accel. (seconds)
LAZIO-ABRUZZO	0.91	**2.02**	1.58	**2.51**	1.24	**1.67**
RSN4312 UMBRIA	1.18	**1.98**	1.53	**0.44**	2.69	**0.92**
RSN1256 CHICHI HWA002	0.48	**8.53**	2.44	**10.24**	1.52	**9.64**
RSN2989 CHICHI CHY102	0.71	**4.68**	1.74	**4.80**	1.79	**6.83**

Nevertheless, the effect of the vertical component is not immediately apparent. Figure 7.22 displays the cracking damage pattern computed due to the "Lazio-Abruzzo" motion. Unlike the "Umbria" motion, any significant change in the crack patterns concerning the west and east facades is not notable. On the other hand, minor changes in the length of the computed cracks can be seen on the north and south facades. However, the effects of these cracks do not significantly change the tower's global response.

As a result, the tower-only model is run multiple times with the two and three-component combinations of the selected records to assess the effect of including the vertical component in the analysis of a masonry tower. The results indicate that high vertical

amplifications are observed at the roof of the tower if the arrival time of the peak vertical acceleration is later than the peak horizontal acceleration. Considering the evolution of the tensile principal stress in the model, the high accelerations are attributed to the masonry material softening due to the intense horizontal action preceding the peak vertical acceleration. Finally, it is shown that observing high vertical accelerations at the roof of the structure may not always translate into more severe cracking damage patterns.

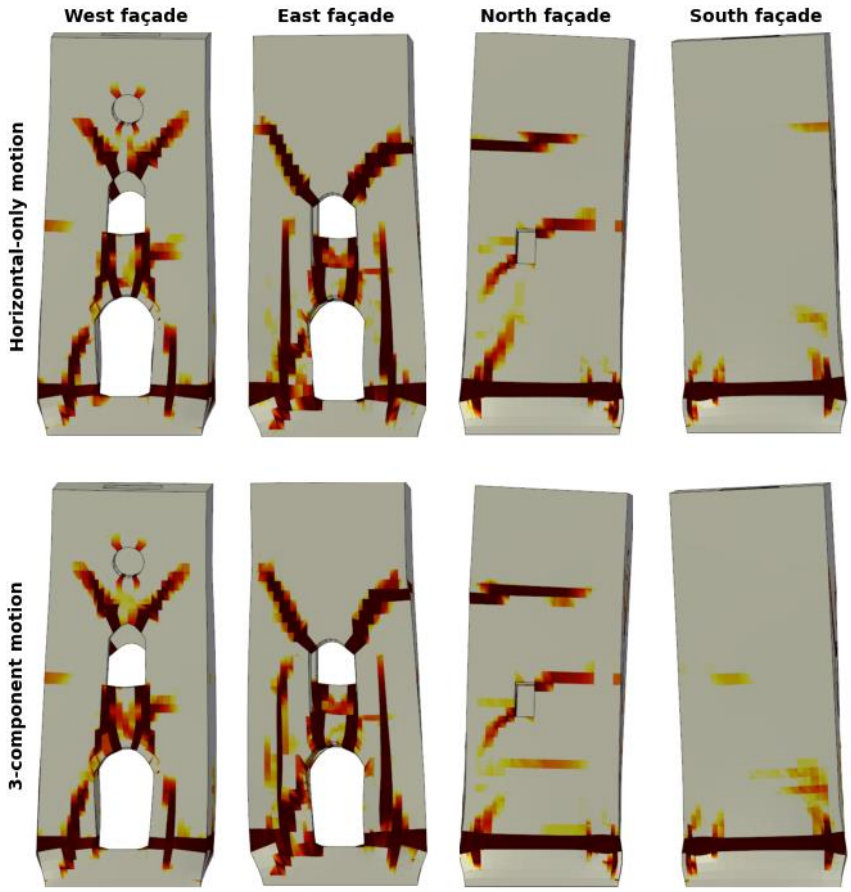

Figure 7.22. The observed cracking damage due to the "Lazio-Abruzzo" motion. Comparison of 2 versus 3 component acceleration.

7.8 SUMMARY AND DISCUSSION

In this chapter, the dynamic response of the bell tower at St. Maria Maggiore Cathedral is investigated under fixed-base conditions. The model is calibrated to match the fundamental oscillation period identified by previous studies on the tower's dynamic behaviour and

ambient vibration measurements, ensuring a realistic representation of the structural response during seismic events. The finite element model of the tower employs an implicit-explicit integration scheme to assess the effects of seismic loading on the structure. Hence, the sensitivity of the solution to the chosen time step is assessed. A time step of one-fourth of the record sampling interval is found to yield consistent results in terms of residual roof displacements and cracking patterns.

Key topics discussed in this chapter include the influence of material nonlinearity, the role of contact elements between the tower and adjacent structures, and the effect of vertical acceleration on the tower cracking damage response.

One of the key findings is that material orthotropy plays a significant role in determining the seismic performance of masonry towers. Simulating masonry as an anisotropic material produces more distributed cracking patterns and efficient energy dissipation, whereas an isotropic assumption leads to concentrated damage and unrealistic local failures. This difference affects both the structural deformation and the frequency content of the tower's seismic response. The analysis shows that the orthotropic model captures a broader range of crack formations and a more natural failure process, enhancing the accuracy of the seismic assessment of masonry towers.

Another important contribution is the quantification of seismic pounding interaction between the bell tower and adjacent structures. The contact forces between the tower and the church walls significantly stiffen the system, leading to changes in the dynamic characteristics of the tower. However, this interaction also causes localised damage at the points of impact, introducing new failure mechanisms that are not present in isolated models of the tower.

Finally, the study examines the effect of vertical seismic components on the tower's response, showing that when the peak vertical acceleration arrives later than the horizontal components, amplification in the vertical response of the bell tower can be observed. In some cases, the vertical component leads to increased tensile damage at higher elevations. This finding underscores the importance of including vertical acceleration in seismic analysis, particularly for complex masonry structures.

8 SEISMIC RESPONSE OF THE BELL TOWER SOIL-STRUCTURE INTERACTION SYSTEM

Soil-structure interaction may play a fundamental role in the seismic behaviour of masonry structures. Soil amplification and topographic reflections modify the strong motion signal acting on the foundation, whereas the base rotations might significantly alter the structures' vibration characteristics. The resulting system may control the observed cracking damage pattern and the global collapse mechanism. A finite element model is presented to study the effect of site-specific conditions and the soil-structure-interaction-induced modifications on the response of the St. Maria Maggiore Cathedral's bell tower in Guardiagrele. The soil domain is modelled with 8-node solid elements in OpenSees with the Scientific Toolkit for OpenSees (STKO) pre-processor. The topography and the details of the hill structure are reproduced using the available digital elevation measurements. The model's footprint is 43,759 square metres with an average depth of 51.4 metres. The domain comprises around 240,00 elements with a maximum vertical elastic wave propagation frequency of 18 Hz. The soil nonlinearity is modelled with a state-of-the-art multi-yield surface anisotropic hardening plasticity equation. A hazard consistent ground motion set is defined in Section 6.4. The 3-component deconvolved ground motion histories are applied at the bottom of the SSI model as force histories.

Some of the key contributions discussed in the chapter are as follows:

1. Foundation rotation and settlement may reduce the demand for short events at the bell tower.
2. The strength of the foundation soil plays a significant role in the cracking damage patterns observed in the bell tower.
3. Impacts during pounding interactions may cause severe damage to the tower structures and lead to partial collapse.
4. The effect of vertical components is much less pronounced than in the SSI analysis of masonry towers due to structural reverberation.
5. Records with powerful high-frequency content may trigger the primary failure mechanism of the bell tower, whereas low-frequency signals lead to foundation failure.

KEYWORDS: impl-ex integration, soil-structure interaction, stone masonry, total stress analysis

8.1 NUMERICAL MODELLING APPROACH

In this chapter, the boundary conditions of the bell tower model are updated to study the effects of the behaviour of the underlying sub-soil on the dynamic amplification response and the overall energy dissipation in the SSI system. The presence of a soil-structure interaction system is expected to alter the structural response significantly, as discussed thoroughly by Lai & Martinelli (2013). To account for SSI, the tower and subsoil are modelled explicitly using the direct SSI approach. The soil is surrounded by dissipative boundaries to simulate the free-field conditions. Ground motion is applied based on the compliant boundary condition assumption, where the acceleration beneath the foundation is no longer prescribed but is computed within the model due to incident waves and wave propagation. The upward-travelling ground motion is applied as a force history at the bottom of the model, while downward-travelling waves are dissipated by viscous dashpot elements located at the soil boundaries. As a result, the acceleration at the model base is the sum of both upward and downward-travelling waves.

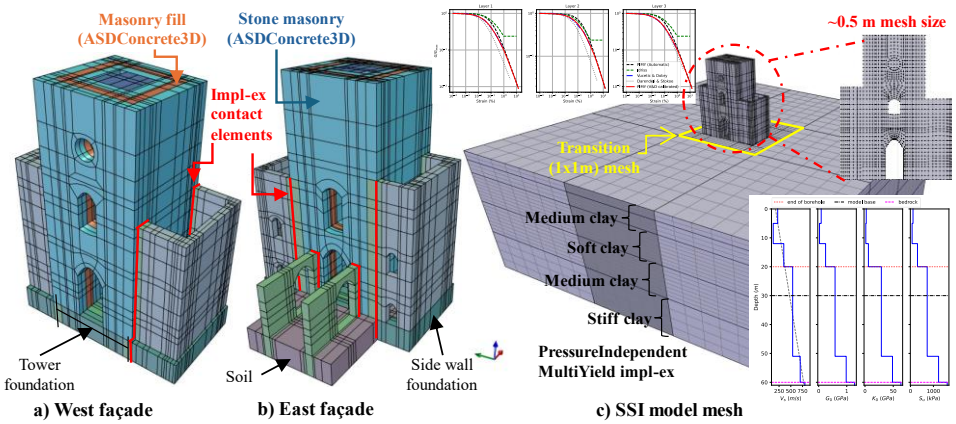

Figure 8.1. Summary of the total stress, flat surface and the tower-wall soil-structure interaction (SSI) model (Chapter 5)

Some energy dissipation is expected first as the mechanical waves propagate through the model, introducing cyclic strains, and second, due to foundation deformations during structural oscillations. In addition to the structure's modes of oscillations, foundation deformation modes are expected where the foundation of the tower rotates around its horizontal and vertical axes and the tower follows rigidly, creating a rocking motion. It is of interest to this study how the structure's global inelastic mechanism, and the energy dissipation mechanism will be affected by the flexibility of the foundation. Furthermore, it is a well-known fact that soils behave in a particular hardening behaviour in which the shear stiffness gradually reduces with increasing levels of straining and ultimately reaches a constant volume, a pure shearing state known as the critical state (Schofield & Wroth, 1968; Wood, 1991). The tower rocking response is tied to the soil stiffness immediately around

the foundation. As the soil approaches failure, the overall vibration frequency of the system is expected to decrease. The interplay between the ground motion's frequency characteristics, the nonlinear soil-structure system, and the tower's damage is studied.

8.2 INITIAL STATE ANALYSIS

The stress state of the soil-structure interaction (SSI) model, expected before nonlinear static and dynamic analyses, is established by modelling the historical evolution of the soil and the structure in stages. The final state at the end of each stage serves as the starting point for the next stage. This staging sequence prepares the model for the primary analysis (e.g., pushover or time history). Staging is a well-established feature in commercial geotechnical finite element (FE) software such as Plaxis and FLAC. For example, in Plaxis, the entire model is initially added to the domain, and parts of the mesh can be activated or deactivated in subsequent stages to simulate different conditions. Activating elements update their geometry based on the current deformed state, while deactivated elements are ignored in the global stiffness matrix computation. The model is then analysed for equilibrium with the new domain definition in each stage. However, a step-by-step staging approach may not be suitable for problems requiring consideration of temporal interactions between model components, such as deep excavation over existing tunnels.

In OpenSees, staging can be implemented by adding or removing elements from the domain. However, since no direct option exists in OpenSees to activate or deactivate elements, extra care is needed to prevent numerical instabilities, such as memory segmentation faults. These faults can be challenging to debug because they might cause an immediate crash or lead to unexpected failures later in the analysis.

In this study, the entire mesh, except for the embedding and Lysmer-Kuhlemeyer (LK) elements, is added to the domain within designated partitions. Since there are no empty partitions, the partitioned stiffness matrix remains non-singular, allowing the MUMPS solver to function without issues. If the empty partition case is avoided, elements can be added or removed from partitions in later stages without problems. Initially, the structure mesh is not connected to the soil model, and static boundary conditions are applied at the extremities of the soil model. The structure mesh is fixed at its base to prevent numerical instability, with no loading applied. At this point, three separate models (structure, soil, and dissipative boundary elements) exist in the domain, unaware of each other.

The analysis of the bell tower is divided into the following stages:

1. Soil self-weight (Elastic)

The stress state of the soil domain and the boundary elements under their self-weight are computed. At this stage, the soil model is forced to behave as an elastic material by a modelling command. Furthermore, the material initial state wrappers are activated.

Table 8.1. Initial analysis steps and stage descriptions

No.	Stage	Description
1	Soil self-weight (Elastic)	Computes the stress state of the soil domain and bulky columns under self-weight, with the soil model forced to behave as an elastic material
2	Soil self-weight (Plastic)	Updates internal parameters, allowing the soil model to exhibit hardening in response to overburden pressure, with a transient analysis for steady state.
3	Excavation	Removes brick elements and self-weight at the foundation area, allows soil heave, and applies lateral support to prevent soil hardening due to excavation.
4	Reset Deformations	Resets deformations while maintaining the stress state, enabling the structure to be attached to the excavated zone without compatibility issues.
5	Structure self-weight	Attaches the tower to the soil mesh, applies structure self-weight incrementally, and achieves the initial stress state corresponding to in-situ conditions.
6	Error stabilisation (IMPL-EX)	Before the time history analysis, a large time step dynamic analysis is performed to clear residuals from material internal parameters.
7	Time history analysis	The dynamic response of the structure under seismic loading is computed.

2. Soil self-weight (Plastic)

A stage without applying any additional load is computed to update the material internal parameters of the soil model. The soil model is activated at this stage and allowed to compute plastic strain and exhibit a hardening response based on the overburden pressure computed because of the previous stage. A transient analysis is caried out in two large steps

with a limited amount of Rayleigh damping (1% at 0.2 Hz and 20Hz) to model the steady state.

3. Excavation

The brick elements and the self-weight located at the foundation area are removed to model the excavation and the stress release.

4. Reset Deformations

After the excavation, the deformations are reset by deactivating the material's initial state wrappers. The *InitialStateAnalysisWrapper* in OpenSees is a mechanism that allows for the development of an initial stress field while maintaining the original geometry. It stores and manages the material's initial stress and strain states, ensuring that the material behaviour can be resumed or adjusted in subsequent analysis stages. During the dynamic step, while the previously computed domain stress state is preserved, the nodes' coordinates are returned to their initial positions. By resetting the domain geometry in this way, the structure can then be attached to the excavated zone in the next stage without compatibility issues. However, since resetting the displacement to zero can sometimes introduce undesirable vibrations in dynamic analysis, a static relaxation step with constant load is applied to dampen any potential numerical instabilities and stabilise the system.

5. Structure self-weight

The tower is released and tied to the soil mesh by adding the *ASDEmbeddedNode* elements to the domain. The self-weight and the loading on the structure are applied incrementally in ten dynamic steps over a long duration. Due to material nonlinearity, each step converges to a solution in multiple iterations (~6-7 on average). The immediate vertical settlement of the foundation is slightly overestimated due to the prior reset heaving deformation on the bottom of the excavation. At this stage, the initial stress state corresponding to the in-situ conditions is assumed to be achieved.

6. Error stabilisation (IMPL-EX)

Before starting the time history analysis, a dynamic analysis with a large time step and constant self-weight is performed to prepare the model. In the implicit-explicit (impl-ex) integration scheme, the material tangent stiffness and stress are computed based on the internal parameters from previous steps, as they are explicitly extrapolated from the committed values at times. As a result, the current stiffness and stress depend on the loading history. This means that residual stresses from the previous loading path may

persist for a few steps. Starting a dynamic analysis with these residual stresses can cause numerical instabilities, as the residual stress state may induce artificial accelerations in the model. Although the magnitude of these accelerations may be small, the errors can accumulate over time, potentially causing the solution to diverge. To prevent this, a five-step analysis is applied to clear the residuals from the material's internal parameters before proceeding with the time history analysis.

7. Time history analysis

The final stage involves analysing the dynamic response of the structure under seismic loading.

8.2.1 Additional considerations for pore-pressures

If the pore pressure d.o.f.s are modelled, a few alterations are necessary to prevent numerical problems. First, to ease convergence during the self-weight calculations, the soil plasticity is turned on after the self-weight calculations, moving the Step 2 to Step 5. This way the soil and structure nonlinearity are introduced in the model gradually, making the solution smoother.

Second, additional measures are required to start the time history analysis without causing artificial accelerations in the model. The artificial accelerations occur due to horizontal slip at the free-field boundaries following the removal of the displacement boundary conditions. The amount of slip can be reduced by applying force boundary conditions and increasing the size of the free-field columns however it cannot be eliminated as in the case of the total stress case, due to the formulation of the u-p elements. Hence, a small amount of slip is required to be accommodated in the model. This can be done by adding an intermediate step before Step 5 (now plastic gravity analysis) in which the boundary conditions are released. The resulting accelerations are damped due to Rayleigh damping by solving multiple steps of large time step analyses.

Third, the initial state analysis should be initiated with large initial permeabilities for each layer to relax the convergence conditions. The real layer permeabilities are forced by an update parameter condition before starting the time history analysis.

Finally, due to the need for solving multiple steps with large time steps, using the impl-ex integration option during these stages could result in instabilities in the solution. Therefore, a command to switch to impl-ex solution during the analyse is implemented. The method of integration is switched to impl-ex by the following command:

```
updateMaterialStage -material $tag -stage 11      8.1
```

where $tag is the PDMY02Implex or PIMYImplex material tag. Requesting "-stage 11" leads to impl-ex solution whereas "-stage 10" switches to implicit solution. As an alternative, the material can be switched back and forth between impl-ex and implicit solution during the solution based on a criterion that checks ease of convergence.

8.3 NONLINEAR DYNAMIC RESPONSE OF THE SSI SYSTEM

An introduction to the dynamic response of the bell tower located on the flat surface (tower-wall-flat model) under the total stress soil behaviour assumption was given in Section 6.3. The elastic response of the SSI model and the significant differences in the modal periods of the SSI model compared to the fixed model were discussed. Then, an AvgSA range for the bell tower was defined to select hazard-consistent records. This section discusses the nonlinear soil structure interaction and the effect of soil and structure material nonlinearities. The selected record set in Section 6.4 is processed and applied at the bottom of the SSI model as force history. Due to the computational cost of running multiple analyses, three records were chosen from the selected set. The interested reader is referred to Section 6.6.1 for further details on the employed record elimination process.

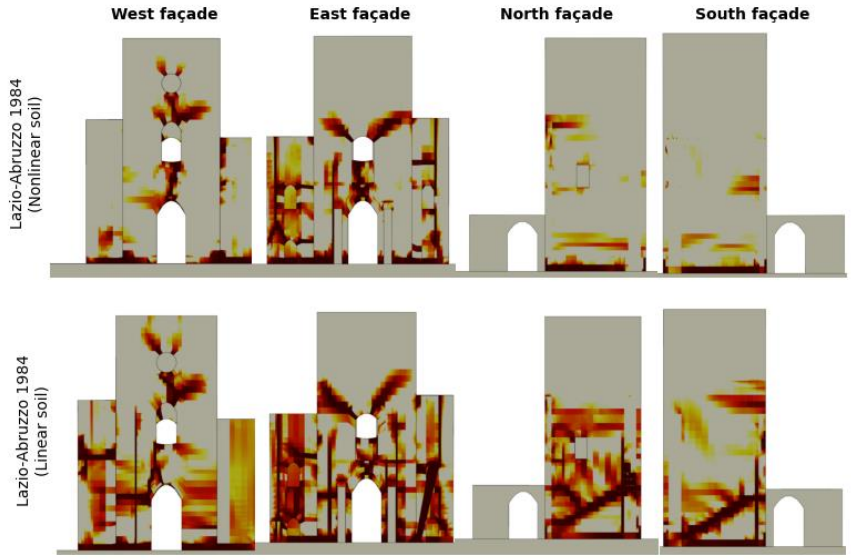

Figure 8.2. (Tower-Wall-Flat model) Tensile cracking damage patterns. Only the damage values between 0.5 and 1.0 are shown.

The discussion in Section 6.3 regarding the nonlinear behaviour of the nonlinear SSI model can be extended. In Figure 6.9, the elastic and inelastic predominant periods of the SSI model were identified through Fourier analysis. Fourier analysis is helpful for analysing the contribution coefficients and the frequencies of the harmonic waves that make an

acceleration history. Hence, the Fourier transform of the roof acceleration history yields insightful information regarding the superposition of structural and SSI behaviour that results in the recorded acceleration history. However, since the information is transferred to the frequency domain by applying the Fourier transform, the temporal characteristics of the shaking behaviour, such as the time evolution of the period shift as the structure softens, are lost. Nevertheless, such information can be recovered by the time-frequency analysis, namely the Stockwell transform, of the recorded acceleration history (Chen et al., 2013; Kramer, 1996; Watanabe et al., 2017). Recently, Ozer et al. (2022) used the Stockwell transform to analyse the evolution of the fundamental period of a dual masonry-RC structure that was tested at the large shake table at Eucentre. They used the time-frequency analysis to analyse the evolution of the fundamental period through the Stockwell transform of the empirical amplification function computed between the roof and the structure's base.

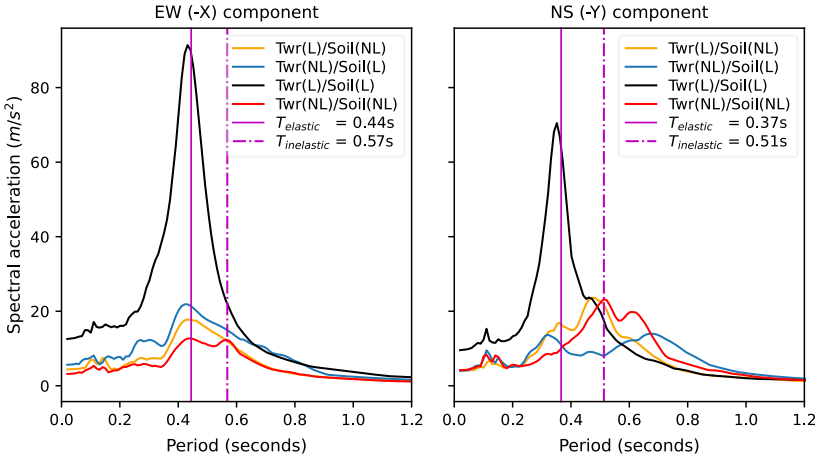

Figure 8.3. (Tower-Wall-Flat model) Effect of linear and nonlinear material response on the tower roof accelerations (Lazio-Abruzzo 1984).

Following Ozer et al. (2022), Figure 11.13, Figure 11.14, Figure 11.15 and Figure 11.16, in Appendix, show the Stockwell transforms of the tower amplification functions. In this case, the amplification function is obtained by dividing the roof acceleration history by the free-surface acceleration history. Unlike the apparent shift in the period at the time of maximum roof acceleration observed by Ozer et al. (2022), the inelastic period oscillates around the frequency identified by the Fourier analysis. This might be attributed to the kinematic hardening property of the soil material. In kinematic hardening, the soil shear stiffness is reset after stress reversals. Hence, depending on the intensity of the strains induced by the shaking, the soil softens and recovers its stiffness. This means that, unlike the fixed-base case, the identified inelastic period by the Fourier analysis might not necessarily be the

shifted period of the system. However, it indicates the maximum degree of softening the model reached during the dynamic analysis. In light of this observation, a damage-informed kinematic hardening model might perform better during this exercise.

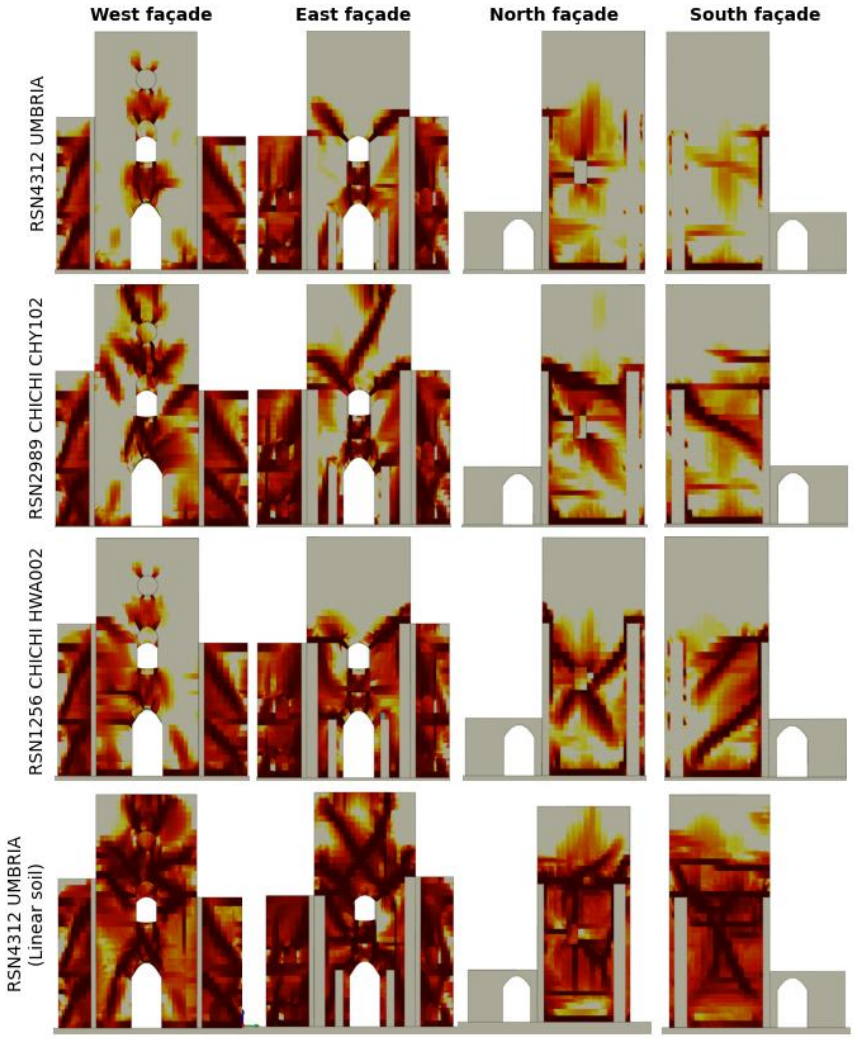

Figure 8.4. (Tower-Wall-Flat model) Tensile cracking damage patterns. Only the damage values between 0.5 and 1.0 are shown.

Figure 8.3 shows the reduction in the recorded roof acceleration spectra as nonlinearity is progressively introduced into the model. The most notable effect is the significant reduction in acceleration due to soil nonlinearity, particularly in the EW component of the response spectra. The soil dissipates more energy than the structure's cracking, as shown

by the upper bound of the linear soil, nonlinear structure curve. When structural cracking is included alongside soil plasticity, the roof response spectra decrease further. However, only the difference between the curves representing the nonlinear soil–linear structure and nonlinear soil–nonlinear structure models represent the seismic load carried by the structure. This notably reduces the cracking damage in the structure, compared to the linear soil–nonlinear structure model (Figure 8.2 and Figure 8.4).

In contrast, the NS component's behaviour is strongly affected by the choice of material nonlinearities. A markedly different response is predicted under the linear soil–nonlinear structure assumption compared to other combinations. This discrepancy between linear and nonlinear soil assumptions is striking yet logical. In the NS direction, cracking induced by openings governs the nonlinear behaviour, leading to extensive cracking and seismic energy dissipation when the foundation soil is modelled as linear. Conversely, if the soil is allowed to behave nonlinearly, a significant portion of the energy is dissipated through plastic foundation rocking deformations.

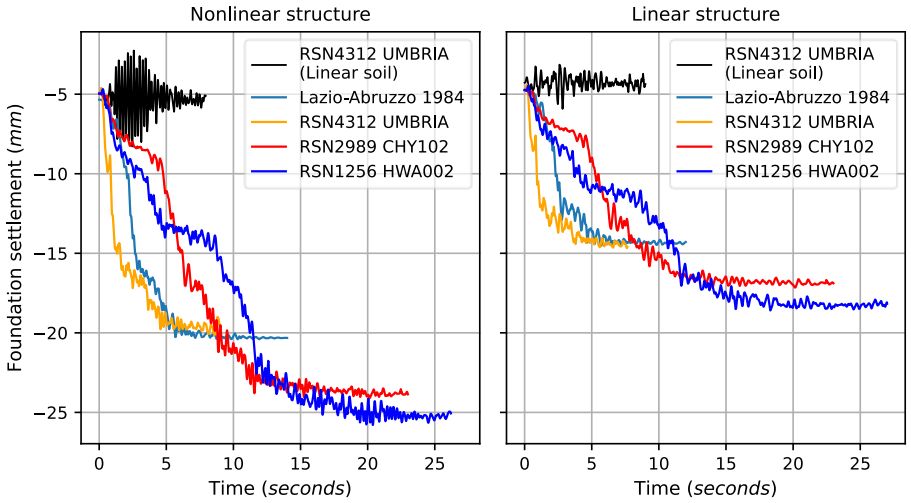

Figure 8.5. (Tower-Wall-Flat model) Foundation settlement is computed when the structure is allowed to soften versus forced to stay elastic.

Worthy of mentioning, the accelerations recorded at the roof of the nonlinear SSI response (Figure 8.3) are around 30% lower than the nonlinear fixed-base response (Figure 7.9). Furthermore, the SSI roof spectra have a wider frequency content than the fixed-base roof spectra. Hence, a greater range of frequencies is excited with less acceleration within the SSI model than the fixed-base response. This reduction has immediate effects on the observed cracking damage response. The intensity of the cracking damage in different boundary condition assumptions can be sorted as follows. The most intense cracking

appears in the fixed-base model (Figure 7.12), followed by the linear soil model. Finally, the lowest amount of cracking is observed in the nonlinear soil-structure interaction model (Figure 8.2 and Figure 8.4). In addition, unlike the fixed-base conditions, the observed cracking damage patterns are more sensitive to the input motion in the SSI model (Cracking damage patterns in Figure 7.12 versus Figure 8.4). In Figure 8.4, the cracks are asymmetric and propagate along preferred directions.

The foundation settlements computed for the nonlinear and the linear models of the tower can be seen in Figure 8.5. As observed by Dashti et al. (2010b), the settlement is highly sensitive to the characteristics of the input motion. The shorter motions with considerable high-frequency content, such as the "Umbria" and "Lazio-Abruzzo", induce settlement over a single but powerful step, whereas longer motions, such as the "Chichi" records, can induce multiple steps of settlement over a longer duration. As a function of the significant duration, the permanent settlement observed due to the "Chichi" motions are higher than the "Umbria" and "Lazio-Abruzzo" motions.

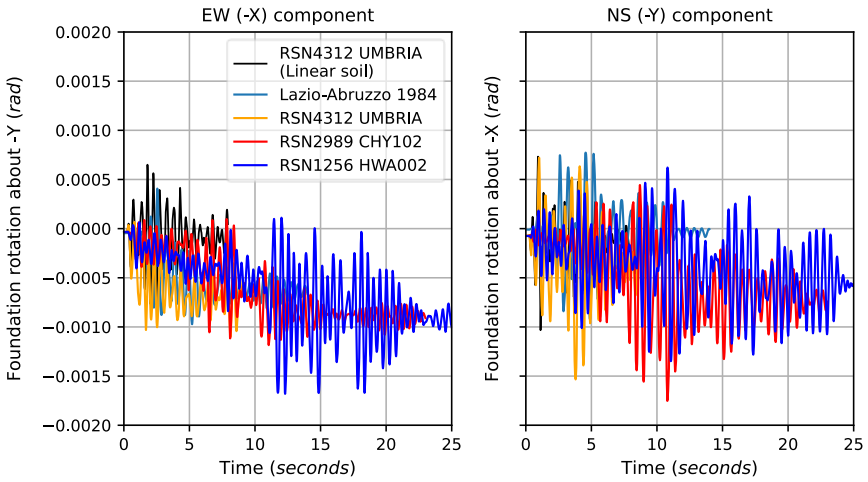

Figure 8.6. (Tower-Wall-Flat model) Foundation rotation about the X and Y axes that is computed for the nonlinear structure – nonlinear soil model.

Regarding foundation rotation (Figure 8.6), similar to the settlement, longer motions trigger rotations with larger magnitudes and leaves greater residual rotations which directly effects the cracking damage response. Since the foundation rotation controls the structural response (as discussed in Section 6.3), the cracking damage patterns intensify directly proportional to the maximum foundation rotation observed during shaking. In Figure 8.6, the residual foundation rotation about the -X direction is less than that about the -Y direction. The adjacent walls permit a limited amount of residual displacement

accumulation along the NS (-Y) axis even though the tower's foundation has approximately the same width and length. In Figure 8.7, some torsional foundation rotations can be observed. Notably, the residual rotation is higher for the short-impulse-like motions since the mismatch in the peak accelerations between the NS and EW components of these motions can potentially be stronger.

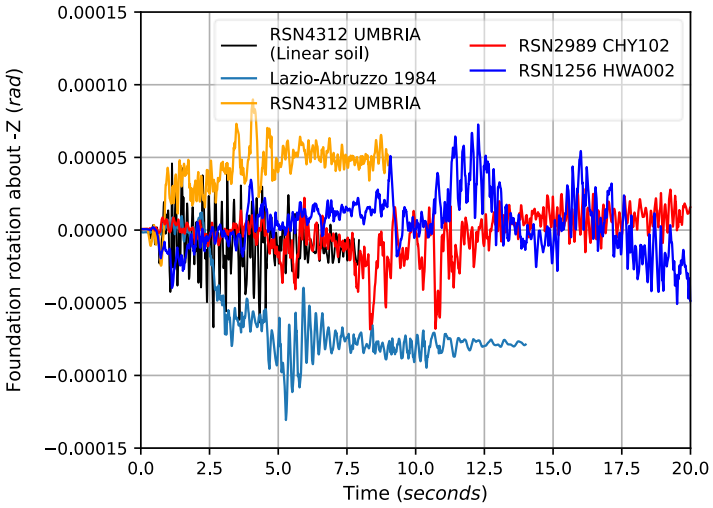

Figure 8.7. (Tower-Wall-Flat model) Foundation rotation about the Z axis computed for the nonlinear structure.

In Figure 8.5, the settlements recorded for the nonlinear structure are consistently higher than those computed for the linear structure. This discrepancy arises due to the softening of the masonry foundation due to damage accumulation. It is worth noting that the fully saturated soil profile assumption discussed in Section 5.4, leads to undrained conditions during shaking. Given undrained conditions, volumetric deformations are constrained by adopting high Poisson's ratio values, ensuring that the soil volume is conserved during the analysis. Therefore, the computed settlements in Figure 8.5 can only be attributed to the translation and rotation of soil elements around the foundation due to distortion. As the foundation softens during shaking, the soil elements in contact with the foundation are allowed to undergo larger distortion, resulting in increased foundation settlements. Hence, the accurate modelling of the softening of the masonry foundation significantly influence the amount of vertical settlements. This phenomenon is further validated by examining the stress-strain response of the soil elements in contact with the foundation.

The octahedral shear stress-strain curves of the elements below the foundation are plotted in Figure 8.8. Both in nonlinear and linear structure models, the envelope of the stress-strain curves is within the same range for each ground motion, with an exception for the

"hwa002" motion in the east element. A similar stress-strain response around the foundation indicates that the nonlinear rocking response due to each ground motion is relatively similar. This observation is supported by the Fourier analysis results shown in Figure 8.9. Like the stress-strain response, the inelastic predominant periods are approximately the same, indicating that much energy dissipation occurs in the foundation soil.

On the other hand, comparing the soil behaviour in the linear and nonlinear structure models, the affect of reduction in the masonry foundation stiffness on the vertical settlement becomes apparent. As the foundation softens and becomes increasingly flexible, the foundation soil is allowed to distort more and more. Therefore, the loss of stiffness in the foundation masonry due to damage accumulation is a significant factor in accurately capturing the vertical settlements of masonry towers.

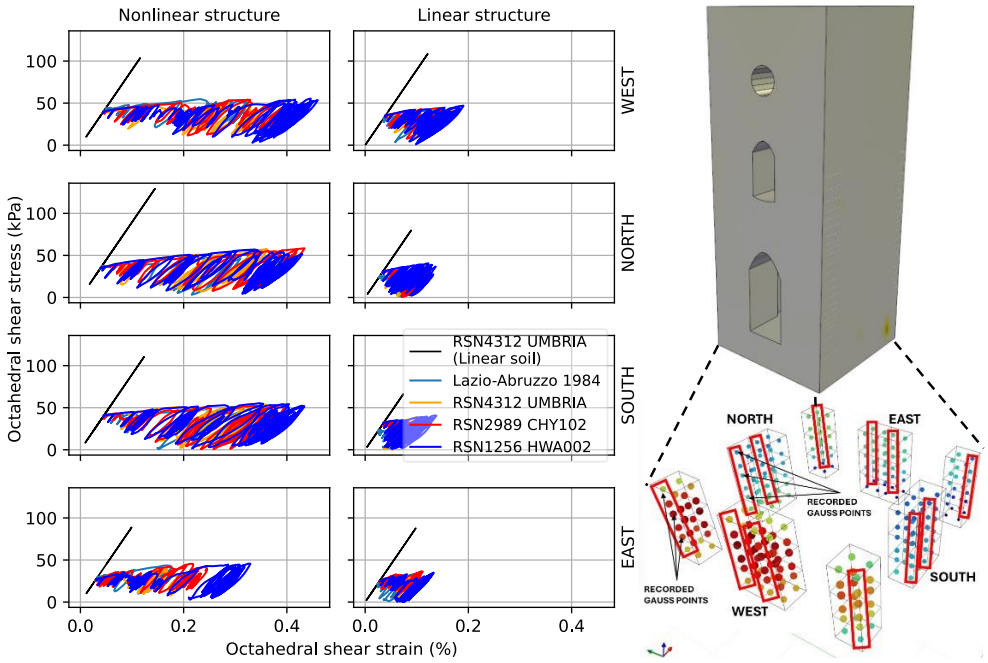

Figure 8.8. (Tower-Wall-Flat model) Octahedral shear stress-strain response of the soil below the foundation. The topmost Gauss point is plotted.

In Figure 8.9, the Fourier analysis of the recorded roof acceleration histories and the identified inelastic predominant periods in each direction of the tower is shown. A wider range of frequencies is excited in the SSI model compared to the fixed-base model (Figure 7.8). In all ground motion scenarios, trends in the amplification behaviour are obtained using the fixed-base or the SSI assumptions. The SSI model appears to cause a shift in most

predominant frequencies and reduce the overall amplification. Meanwhile, the fixed-base model leads to powerful excitation in the structural periods and higher accelerations in the structure. Therefore, the period shift or the amount of softening predicted by the fixed-base assumption is much greater than the SSI model. The resulting inelastic periods in both fixed-base and SSI analyses are very similar. This becomes advantageous in applications such as defining an AvgSA range suitable for both boundary conditions, allowing direct comparison of the resulting fragility curves in the same figure.

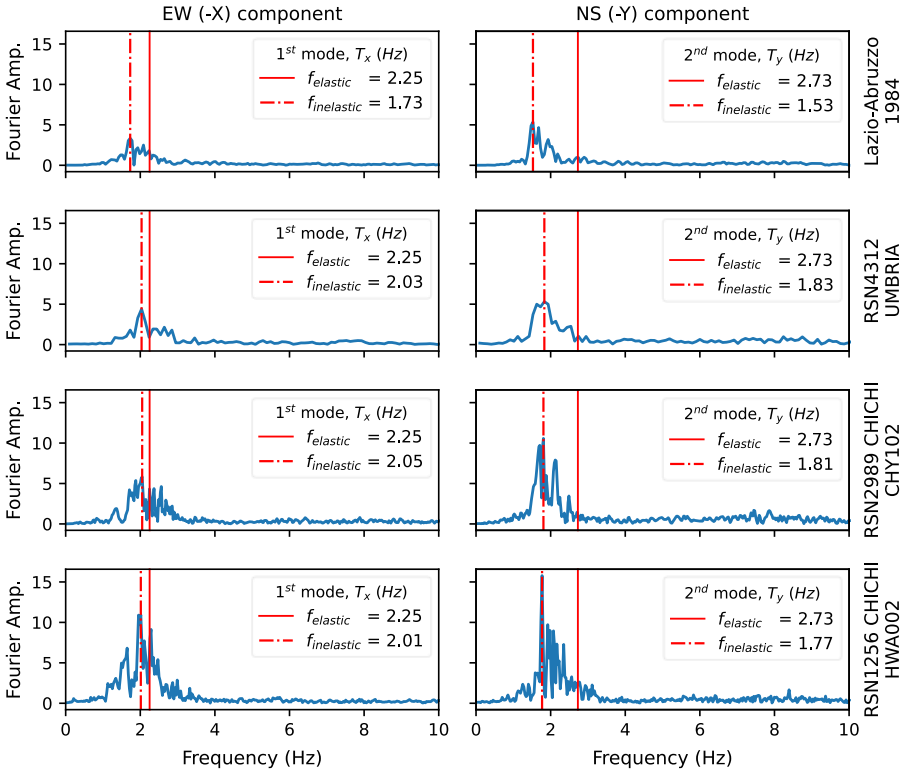

Figure 8.9. (Tower-Wall-Flat model) Fourier spectrum analysis of the roof acceleration for different strong motions.

In Figure 8.10, the roof response spectra are shown. There is a considerable decrease in the high-frequency content of each spectrum compared to the fixed-base counterparts (Figure 7.9). This creates an extremely beneficial circumstance for the bell tower. Stiff and brittle structures are sensitive to the high-frequency range of the input motion. It appears that, in Figure 7.9, the bell tower is directly exposed to high-frequency rich motions due to using fixed-base boundaries. Consequently, the nature of the problem is significantly missed as the modification of the seismic signal due to the foundation rocking mechanism is ignored.

It is as if the foundation creates a "rocking isolation" mechanism, which is a phenomenon observed by other authors, especially for RC frame structures (Gazetas, 2015; Gelagoti et al., 2012b).

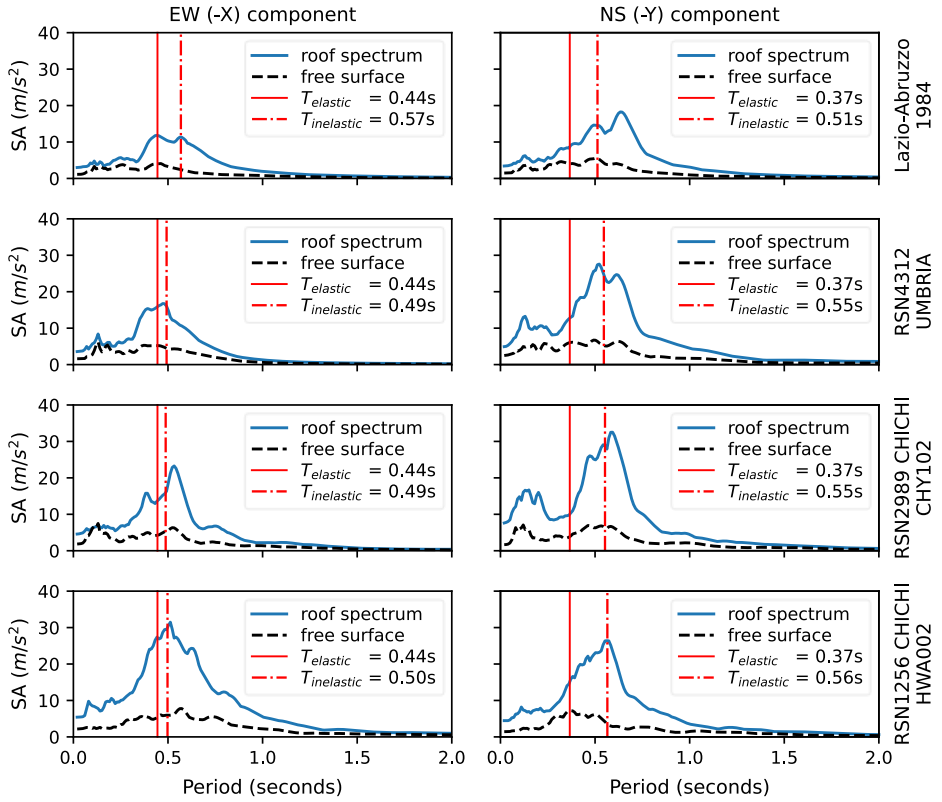

Figure 8.10. (Tower-Wall-Flat model) Roof acceleration spectra for different strong motions. The black dashed line represents the motion recorded at the free surface.

An interesting qualitative observation can be made in light of the rocking isolation system present in the bell tower As discussed in Section 5.1 (**Error! Reference source not f ound.**), the historical seismicity within a 50 km radius of the bell tower includes numerous events that fall within the magnitude and distance range associated with a 475-year return period. These events are listed in Table 5.1, while the seismic hazard at the site for this return period, along with the disaggregation of contributing events, is shown in Figure 6.11. Despite records of significant damage to the bell tower of Guardiagrele during strong events such as the Mw 6.8 Maiella earthquake in 1706, which led to multiple repairs (Rosell,

2010) , no signs of severe structural cracking, such as the patterns shown in Figure 7.12, are evident in current photographs of the tower (Figure 5.1and Figure 11.2).

This discrepancy between the actual damage state of the tower and the predicted damage state—considering 475-year return period motions in previous studies, including Section 7.5 of this thesis —might be explained by the reduction in high-frequency content due to the observed rocking isolation mechanism. The damping of high-frequency accelerations at the foundation caused by rocking isolation could result in cracking patterns similar to those in Figure 8.4, which are easier to repair than the severe cracks depicted in Figure 7.12.

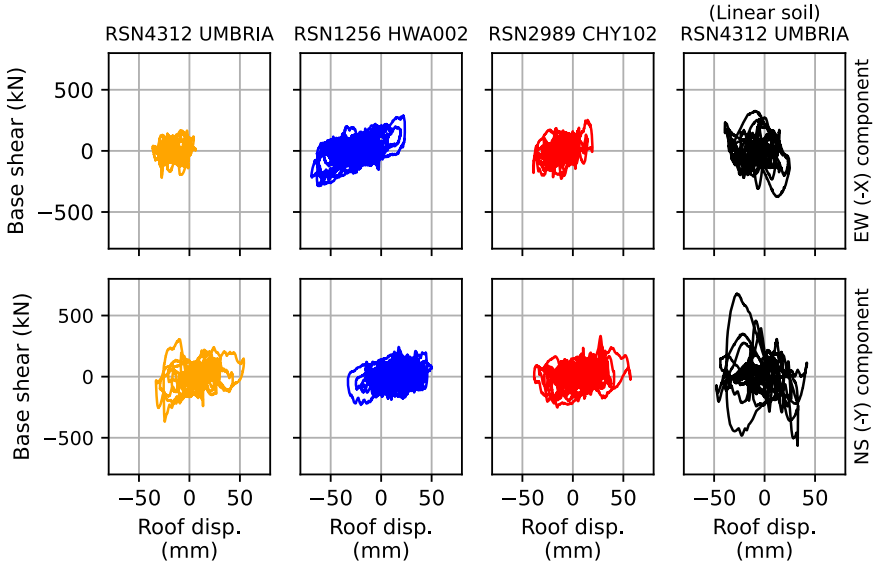

Figure 8.11. (Tower-Wall-Flat model) Roof displacement versus base shear response for different strong motions.

Figure 8.11 shows the force-displacement demand due to the applied ground motions. The nonlinear SSI model can accommodate the displacement demand with significantly reduced foundation reactions. This occurs because much of the seismic energy is absorbed by the surrounding soil before it reaches the foundation. The ductile behaviour of the soil plays a key role here. Strong ductile behaviour allows for high displacement capacities, as seen in Figure 8.11 , which is a desirable feature in seismic assessments. Perfectly plastic behaviour may occur in natural soft or medium clay deposits, as well as in restructured soils. In contrast, structured soils and stiff clays may exhibit softening behaviour, which would reduce the displacement capacity of the foundation soil. However, since the foundation soil is unlikely to be in a virgin state after the tower's construction, the kinematic hardening behaviour used in the model provides a reasonable approximation of the in-situ soil conditions.

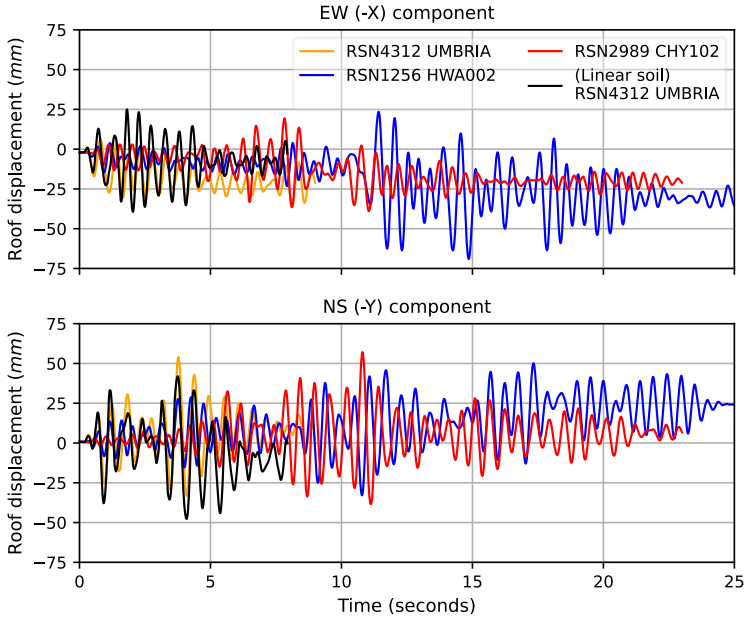

Figure 8.12. (Tower-Wall-Flat model) Permanent roof displacement for different strong motions.

Finally, in Figure 8.12, the permanent roof displacements are shown. As per Figure 6.7, the roof displacements and the residual displacement at the end of shaking are directly correlated. Depending on the tower's height, a small residual rotation in the foundation can translate into significant roof sway. In the SSI model, the roof sway is the total displacement caused by the foundation rotation plus the tower flexibility. In contrast, only the tower displacement is present in the fixed-base model. Hence, the contribution of the superstructure in the roof displacement is not the same in both models. The SSI model predicts around 30% larger residual displacements than the fixed-based model. The contribution of the residual foundation rotation in the residual roof displacement is around 70%, which is significant. However, it should be emphasized that the maximum foundation rotation and the residual in Figure 8.6 are around 0.0015 and 0.0010, respectively, which are much less than 0.0020 (1/500), i.e., the serviceability limit state specified in the Annex H of Eurocode 7, Part 1 (EN 1997-1, 2004). Gazetas (2015) also observes residual foundation rotation values for RC frames, which does not violate the serviceability limits.

This section presents the main findings of the thesis. The seismic behaviour of the bell tower's soil-structure interaction (SSI) model, including the pounding interaction between the tower and adjacent walls, is analysed under multiple ground motions. The selected motions represent seismic events with a 475-year return period at the bell tower's location.

Additionally, the SSI model's response is compared with a fixed-base model's. Some of the key findings are:

1. **Foundation rocking:** The SSI response is primarily governed by foundation rocking, with the contributions of both elastic and inelastic rocking periods being critical in predicting seismic behaviour.
2. **Rocking isolation mechanism:** A "rocking isolation" mechanism is observed, similar to the findings of Gazetas (2015) and Gelagoti et al. (2012) for RC frame structures.
3. **Inelastic period estimates:** More accurate inelastic period estimates could be achieved by employing a damage-informed kinematic hardening model.
4. **Linear soil-nonlinear structure assumption**: Assuming linear soil behaviour with a nonlinear structure may lead to erroneous results, particularly in masonry structures with many openings. This can result in unrealistically intense damage patterns, as seismic energy would be dissipated only through crack formation in the structure.
5. **Sensitivity to spectral shape**: Cracking damage patterns become more sensitive to the spectral shape of the input ground motion due to the reduced contribution of the structural first mode in the system response.
6. **Cracking damage intensity**: The intensity of cracking damage is directly proportional to the maximum foundation rotation observed during seismic shaking.
7. **Foundation damage and settlements:** Stiffness loss in the foundation material due to damage accumulation is a significant factor in accurately capturing vertical settlements.
8. **High-frequency accelerations**: The SSI assumption appears to reduce high-frequency accelerations, whereas the fixed-base model tends to amplify excitations at the structure's natural periods, leading to more detrimental conditions.
9. **PIMY model limitations**: The perfectly plastic response of the PIMY model at the critical state may result in an unrealistically ductile response, potentially overestimating the displacement capacity.

8.4 THE EFFECT OF SOIL STRENGTH ON THE TOWER CRACKING DAMAGE RESPONSE

In Sections 6.3 and 8.3, the dynamic response of the SSI system is shown to be sensitive to the foundation rocking period, which is significantly longer than the first structural mode of the bell tower. The beneficial effects of the foundation soil nonlinearity were extensively discussed by many authors (Anastasopoulos et al., 2010, 2012; Gazetas, 2015; Gelagoti et al., 2012b; Loli et al., 2016; Mylonakis & Gazetas, 2000). The undrained strength directly affects the G/Gmax hardening response of the soil surrounding the foundation. The shear stiffness reduction characteristics of the soil around the foundation may control the

accelerations transferred to the structure. As a result of nonlinear soil response, the high-frequency content accelerations can be significantly reduced. High-frequency content is one of the controlling factors of increased damage observed in the super structure (Section 7.5). In this section, the effect of changing soil strength on the tower response is studied by systematically changing the strength of the soil around the foundation while keeping the behaviour of the soil layers constant.

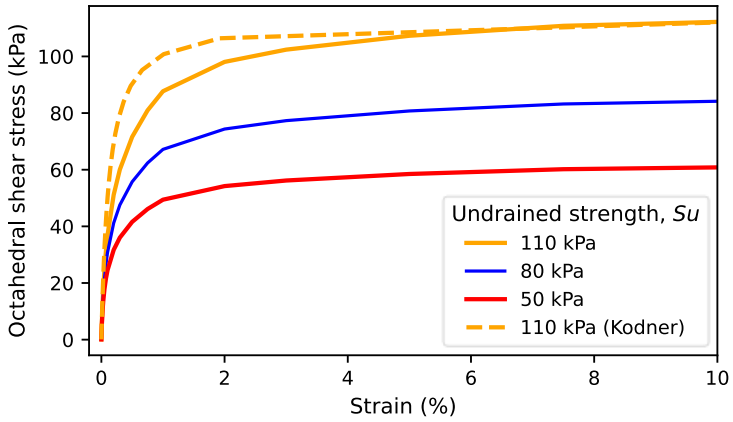

Figure 8.13. The set of octahedral shear stress-strain curves is used only for the foundation soil. The soil layers are kept unchanged.

Figure 8.13 displays the set of stress-strain curves prepared for the study. The layer 1 response is taken as a benchmark point, represented by the "110 kPa" curve. The "80 kPa" and "50 kPa" curves are obtained by keeping the parameter a constant and reducing the γ_{peak} in Equation 8.2 until the desired strength value is reached.

$$\frac{G}{G_{max}} = \frac{1}{1 + \left(\frac{\gamma}{\gamma_{peak}}\right)^{a}} \qquad \textbf{8.2}$$

Since a is the same for all curves, the reduction curve follows Vucetic and Dobry (1991). One more test is prepared in which the undrained strength is kept at 110 kPa, but the hyperbolic stiffness reduction proposed by *Kodner* in 1963 (Gu et al., 2011) (alternative a parameter) is employed. Therefore, the effect of the rate of stiffness reduction is isolated in the test. As for the seismic analysis, one combination in which the Tower-Wall-Flat model is run with the "Umbria" motion is chosen. The results are as follows.

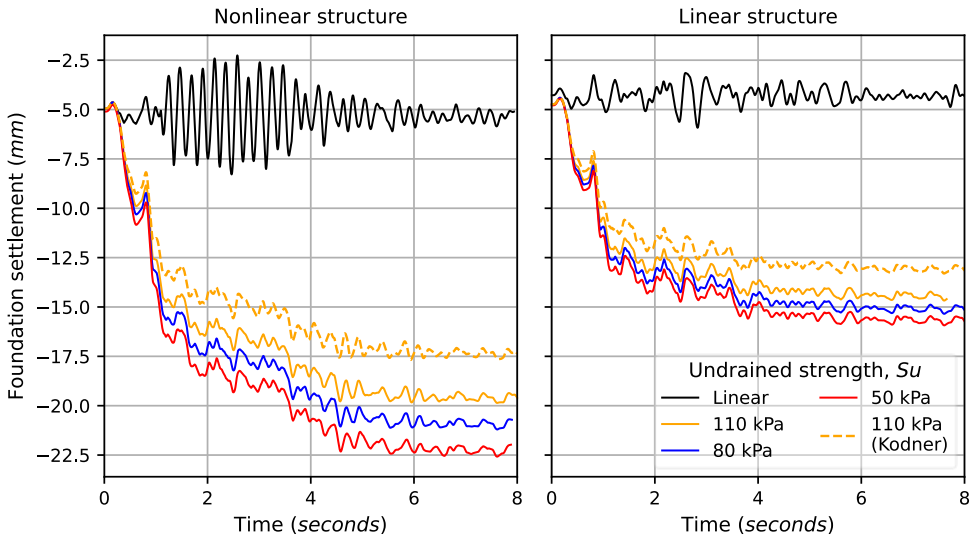

Figure 8.14. Increasing foundation settlements for the nonlinear versus linear structure models.

Figure 8.14shows the increase in settlements as soil strength decreases. As expected, a reduction in soil strength leads to greater settlements. However, comparing the effects of hyperbolic stiffness reduction (dashed curve) with changes in undrained strength (solid curves) yields interesting results. The rate of stiffness reduction during shaking has a more significant impact than changes in soil strength. The Kodner curve, with its extended "initial" portion followed by a sharp stiffness reduction (higher a value), allows more high-frequency energy to reach the tower before hardening, compared to the Vucetic and Dobry curves, which are nonlinear from the start. This suggests that the characteristics of soil stiffness reduction play a more critical role in determining foundation settlement than undrained soil strength.

It is worth noting that an undrained strength of 50 kPa represents significantly soft, low-quality soil. Considering the weight of the bell tower, very high settlements only due to the gravity loading might be expected. However, comparable settlements are computed using this variant since the analysis is volume-conserving due to the fully saturated (undrained behaviour) assumption. The soil elements are only allowed to deform in distortion; hence, observed settlements are only due to the translation and rotation of the soil elements due to distortion. This observation also explains the reason behind the consistently higher settlements computed when the structure is nonlinear compared to when the structure is linear. As the foundation accumulates damage, the masonry material becomes softer, allowing the foundation soil to deform more.

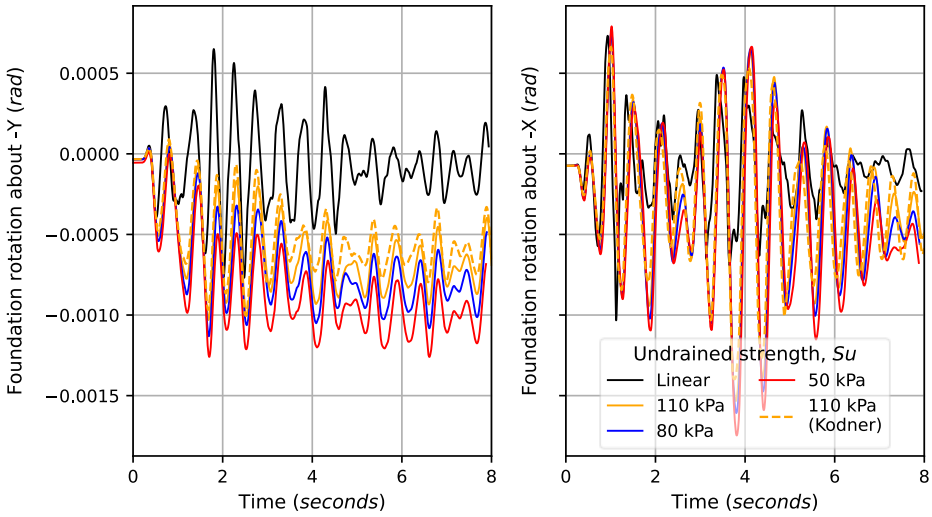

Figure 8.15. Change in the foundation rotation because of decreasing soil strength.

In contrast, the foundation rotation, shown in Figure 8.15, is more sensitive to the soil's undrained strength. More rotation about the -Y axis is observed as the undrained strength reduces. Interestingly, the rotation about the -X axis does not seem to be affected by either the rate of stiffness reduction or the soil strength. This is because the adjacent walls prevent roof sway and increase the foundation width of the tower.

Alternatively, the increased settlements when the structure is allowed to accumulate damage can be evaluated from the seismic demand perspective. Figure 7.16 shows the response spectra computed at the free surface due to the input "Umbria" motion. In the NS (-Y) component, increased accelerations are expected when nonlinearity is allowed as the inelastic predominant period shifts towards the peak of the response spectrum. This might result in increased forces acting on the tower and may lead to increased horizontal shaking. As the foundation soil only deforms due to distortion, the increased horizontal response of the tower might lead to powerful ratcheting motion at the foundation.

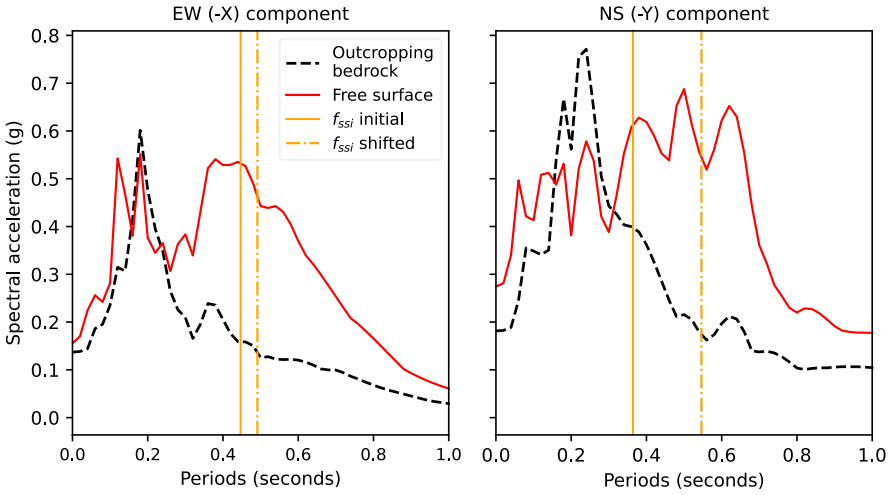

Figure 8.16. (110 kPa model) Response spectra of the free surface motion due to the Umbria signal.

Such ratcheting-induced soil nonlinearity can be confirmed by studying the stress-strain response of the soil elements around the foundation. Figure 8.17 compares soil stress-strain response for the cases when the structure is allowed to soften and forced to stay elastic. The transition of the stress-strain curves from linear to low-strength soil is captured in Figure 8.17. Similarly, the settlement, the significant factor appears to be the rate of stiffness reduction more than the undrained strength. Notably, the soil nonlinear stress and strain response are orders of magnitude higher for the nonlinear structure case. Increased nonlinearity is possible due to the softer foundation material and the increased horizontal tower oscillations due to slightly higher seismic forces.

In Figure 8.18, the change in the seismic demand as the soil strength reduces is shown. As expected, the force demand significantly reduces when the soil nonlinearity is considered. The horizontal demand increases when the structure is nonlinear, consistent with the foundation soil stress-strain response. Interestingly, the seismic demand between different soil strength curves stays approximately constant. This suggests that the effect of soil strength or the rate of stiffness reduction on the tower response might be limited. However, observing the cracking damage plots in Figure 7.19 illustrates the detrimental effect of the rate of stiffness reduction on the tower.

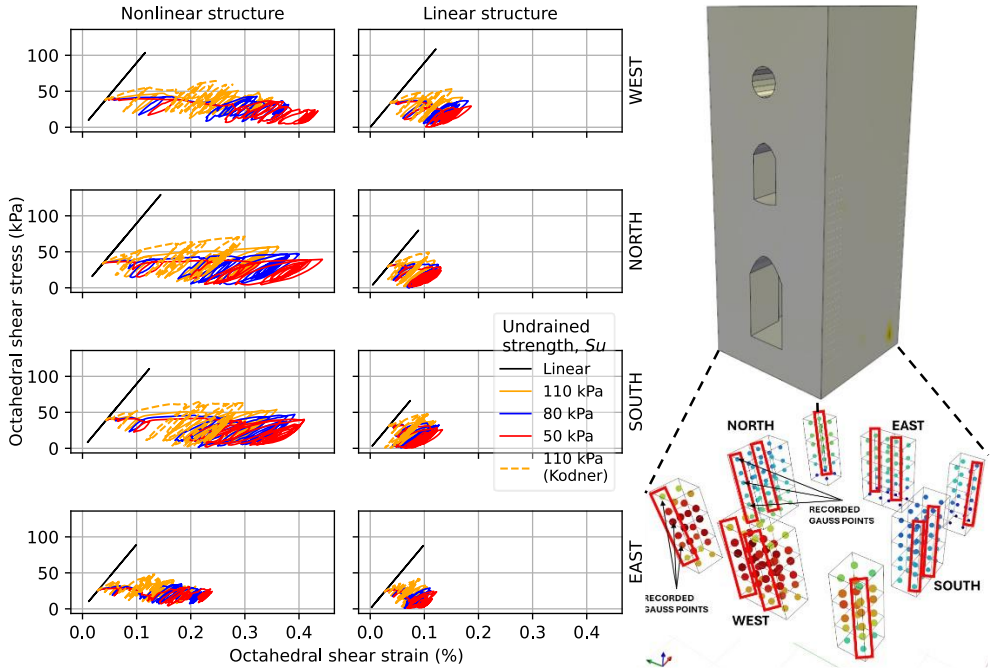

Figure 8.17. The change in the octahedral shear stress-stress response of the foundation soil is a function of the soil's undrained strength.

In Figure 7.19, there is a clear trend towards an increased cracking damage response as the soil strength increases. The most severe damage is observed when the soil is forced to stay linear during shaking. This makes sense since no energy is dissipated at the foundation soil. As the soil strength decreases, more energy is dissipated at the foundation soil, reducing the contribution of the structural response. It is worth noting that the real contributing factor is the rate of stiffness reduction determined by the selected G/Gmax curve. A more significant change is observed between the cracking responses when comparing the hyperbolic stiffness reduction curve (Kodner) versus the curves by Vucetic and Dobry rather than comparing the curves with reducing strength. This hints at the sensitivity of brittle structures such as the masonry tower discussed here to the width of the initial, linear portion in the foundation stress-strain soil response. A wider linear range in which strains relate to stresses linearly leads to a larger stress capacity at the beginning of shaking. The larger stress capacity of the foundation soil increases the high-frequency accelerations experienced by the tower. This phenomenon can also be observed in the vertical settlements in Figure 8.14. A slower stiffness reduction characteristic leads to the saturation of the settlement earlier during the shaking. In return, the higher frequency motion is transmitted towards the tower, and more damage is obtained.

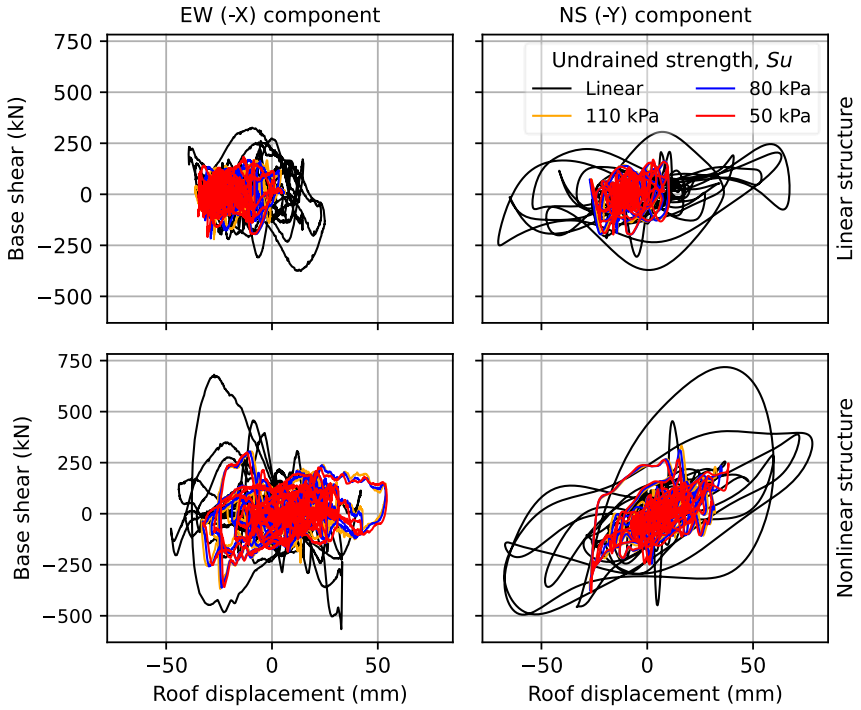

Figure 8.18. Roof displacement versus shear force demand for varying foundation soil undrained strength values.

In conclusion, the detrimental effects of having stiff soils around the foundation are discussed. In this study, soil stiffness and undrained strength are closely related to the chosen G/Gmax curve. Consequently, a reduction in strength also leads to an earlier loss of elastic stiffness. It is observed that increased nonlinearity in the soil surrounding the foundation benefits the tower by reducing seismic actions. A similar effect on shallow-founded reinforced concrete structures was discussed by Gazetas (2015) and introduced as the 'rocking isolation' effect, which might also be applied in the design of new RC frame structures (Gelagoti et al., 2012b). Gazetas (2015) demonstrates the reduction in seismic action and prevention of collapse in an RC frame structure by reducing foundation widths to trigger further nonlinear soil stress-strain response during shaking. Similar behaviour is observed for masonry towers in this study. The observed cracking damage in the masonry tower decreases significantly depending on the undrained strength and rate of stiffness reduction of the soil around the foundation, and vice versa. As a future study, the effect of soil heterogeneity beneath the foundation could be investigated. Heterogeneous soil may cause differential settlements, potentially leading to more severe conditions for the structure. Additionally, the size of the foundation could be another key factor in determining the extent of differential settlements observed in the tower.

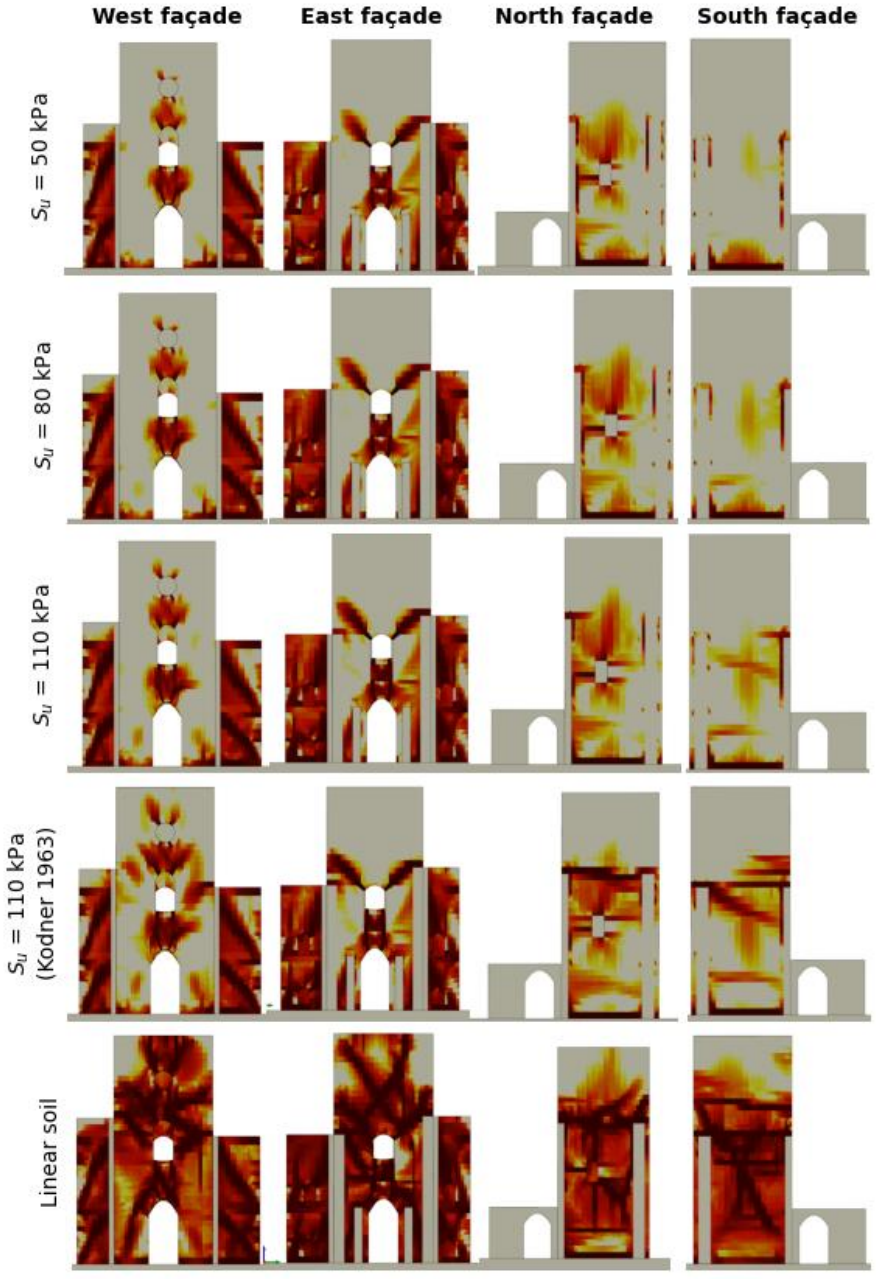

Figure 8.19. Effect of soil strength on the tensile cracking damage patterns. The Gauss points having a damage value between 0.5 and 1.0 are shown.

8.5 THE EFFECT OF SEISMIC POUNDING INTERACTION ON THE DYNAMIC SSI RESPONSE OF THE TOWER

The dynamic response of the bell tower SSI model with adjacent walls is discussed in Sections 8.3 and 8.4. As discussed in 7.6, modelling the bell tower without the adjacent walls could be an alternative modelling option. However, it was shown that the pounding interaction between the bell tower and the adjacent church walls significantly alters the dynamic response of the bell tower, often leading to more critical cases than the tower-only response. In section 8.3, it is found that considering SSI caused a reduction in the computed damage patterns and led to more realistic results. Furthermore, a more complete picture of the mechanics behind the problem is modelled by capturing the rocking isolation response.

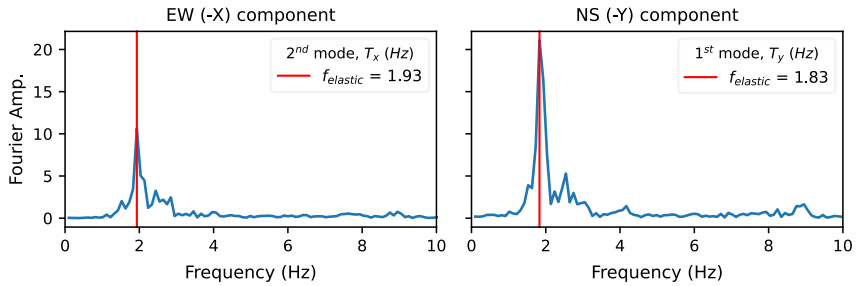

Figure 8.20. (Tower-only-Flat model) Elastic predominant frequencies computed through the Fourier analysis of the roof acceleration versus the modal analysis (vertical line).

This section focuses on assessing the significance of pounding interaction in quantifying the dynamic response of the bell tower, particularly in relation to SSI-induced mechanisms such as foundation rotation and rocking isolation. To evaluate the contribution of the adjacent walls to the response observed in Section 8.3, the walls were removed, and the analyses were rerun using the same ground motion set. The selected ground motion set remains compatible with the bell tower-only SSI model, as the elastic and inelastic periods of the model still fall within the 0.1 to 1.0-second range—corresponding to the AvgSA range conditioned upon in Section 6.4. The initial oscillation periods of the bell tower-only model are illustrated in Figure 8.20. Due to the substantial computational cost of running the entire set multiple times, three ground motions were selected for analysis. For details on the record selection process, refer to Section 6.6.1.

The changes in the oscillation frequencies of the tower are shown in Figure 8.20 and Figure 8.21. Most immediately, the switch in the direction of the first mode can be noticed in Figure 8.20. As in the case of the fixed-base model, the direction of the first mode switches to the weak (NS) direction of the bell tower when the walls are removed. Furthermore, a drop in the initial frequencies of around 30% is observed. During shaking, the predominant

frequencies reduce due to the SSI system's softening. The amount of shift observed in Figure 8.21, along the EW direction, is very similar to the tower-wall model shown in Figure 8.9. Since the west façade of the bell tower is free and there are buttresses in contact with the tower only in the east façade, the amount of inelastic behaviour in the tower-only model is not much different from that of the tower-wall model.

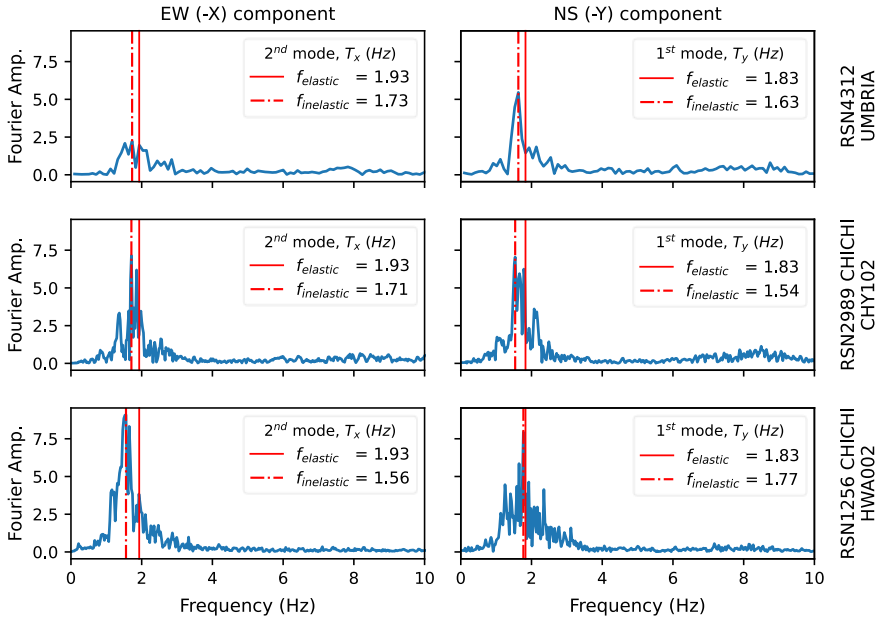

Figure 8.21. (Tower-only-Flat model) Fourier spectrum analysis of the roof acceleration for different strong motions.

However, the effect of removing the walls is much more pronounced along the NS direction. The shifts in frequencies observed in Figure 8.21 are considerably lower compared to the shifts recorded in Figure 8.9. This indicates that the bell-tower-only model experiences much less softening, which translates to less damage. The rocking isolation mechanism is more potent in the tower-only model than in the tower-wall model. Anastasopoulos et al. (2010) and Gazetas (2015) observe an increased isolation effect for RC frames by reducing the dimensions of each footing foundation. Furthermore, they discuss the possibility of deliberately under-designing the footings of new RC frame structures to activate the rocking isolation mechanism. In line with their findings, removing the adjacent walls decreases the foundation width of the bell tower along the NS direction since the foundation of the walls works together with the tower walls when the contact and stick conditions are satisfied. As a result, the rocking isolation mechanism is activated further.

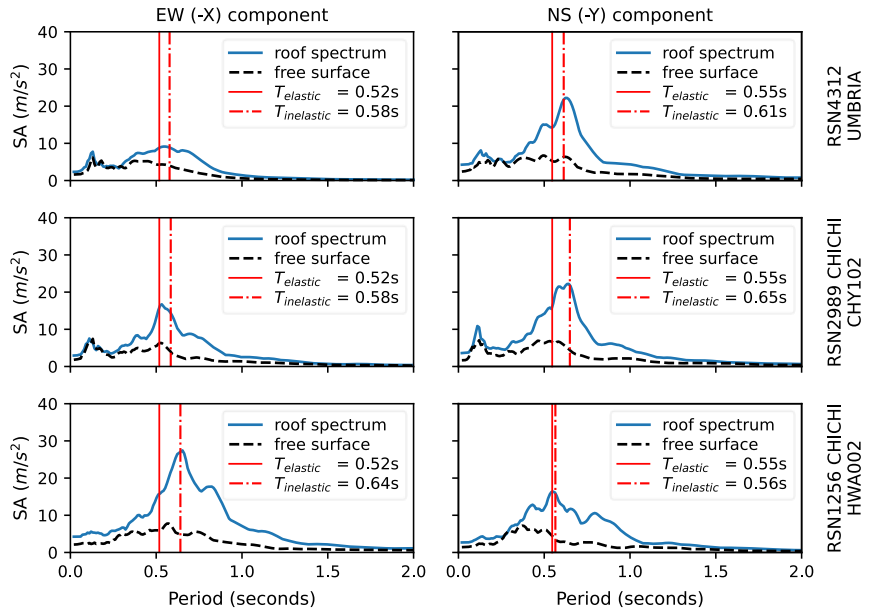

Figure 8.22. (Tower-only-Flat model) Roof acceleration spectra for different strong motions. The black dashed line represents the motion recorded at the free surface.

Regarding roof accelerations, the response spectra are slightly lower in the tower-only model (Figure 8.22) compared to the tower-wall model (Figure 8.10). Furthermore, a secondary peak in the low period range can be seen in Figure 8.10 in the response spectra of the tower-wall model that can be associated with the adjacent wall response. Overall, the tower-only response is concentrated around the fundamental oscillation periods, whereas the amplification features are broader in the tower-wall response spectra.

Significant differences in the cracking damage between the tower-only and tower-wall models are observed. The cracking in Figure 8.23 is much more localized than in Figure 8.4. The cracks initiate from the edge of the openings and propagate outwards in the tower-only model; meanwhile, in the tower-wall model, additional cracks surround the pounding interaction surfaces. Furthermore, some failure mechanisms observed in the tower-wall model, such as the cross-type fracturing around the square opening in the north façade, are not activated when the walls are removed. Notably, the contribution of pounding interaction is not as significant when fixed-base boundaries are used. Between Figure 7.17 and Figure 7.12, the cracking damage intensifies; however, the mode of cracking is not drastically affected by the removal of the walls. This is partly because of the detrimental effect of the fixed-base boundaries compared to the conditions by considering the mechanisms that appear in the direct SSI model. The terminal modes of failure overshadow

some cracking modes. Therefore, modelling the interaction between adjacent structures might be much more critical in SSI models where the rocking isolation mechanism is expected to control the behaviour.

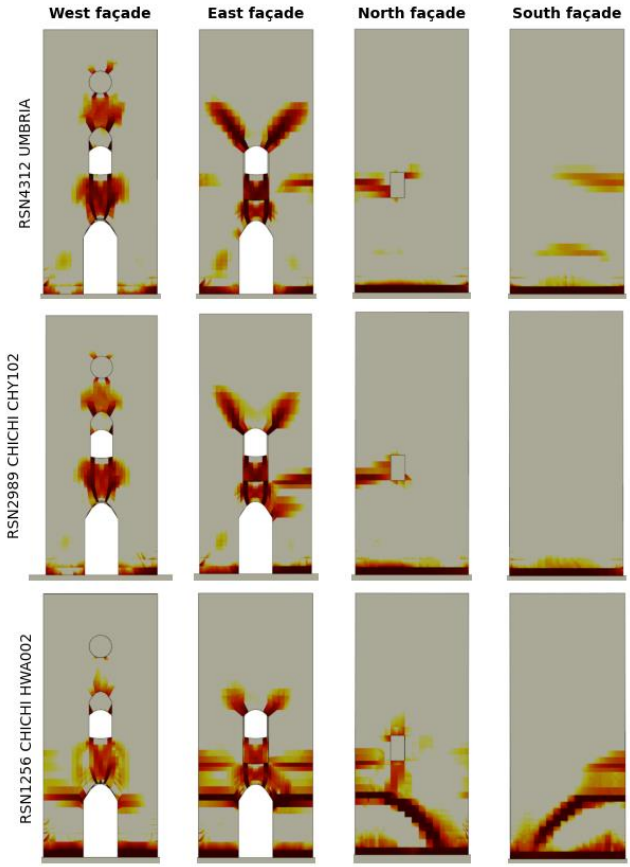

Figure 8.23. (Tower-only-Flat model) Tensile cracking damage patterns. The Gauss points with a damage value between 0.5 and 1.0 are shown.

The increase in the settlements shown in Figure 8.24 compared to Figure 8.5 is consistent with the previous observations, as the reduced foundation dimensions lead to increased deviatoric strains in the foundation soil (Figure 11.17). In return, the foundation displacement response amplifies. It is worth noting that the evolution of settlement does not change between ground motions. However, removing the walls resulted in the scaling of the settlements.

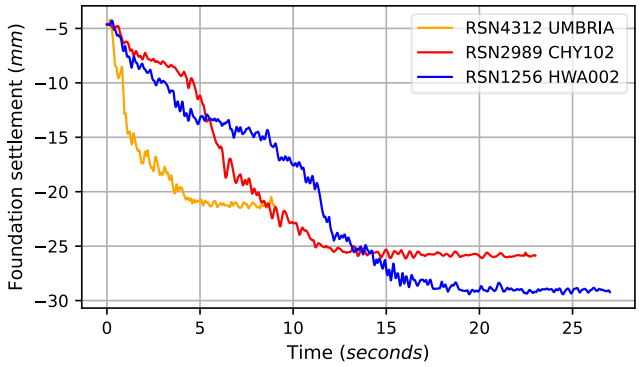

Figure 8.24. (Tower-only-Flat model) Foundation settlement computed when the structure is allowed to soften

The residual foundation rotations are reduced when the analyses are run without the adjacent walls. In Figure 8.26, higher amplitudes of foundation rotation are observed in all directions due to reducing the foundation size compared to those of Figure 8.6. Moreover, the rotations are symmetric along both axes in the tower-only model, as the presence of walls with asymmetric heights might cause asymmetric deviatoric stress evolution around the bell tower foundation during shaking. Perhaps the larger and symmetric rotation values explain the reduced residual rotations when the walls are removed. As an outcome of this exercise, it might be extrapolated that increased residual rotations might be expected in aggregate masonry buildings if the setup of adjacent structures is asymmetrical in height, weight or stiffness.

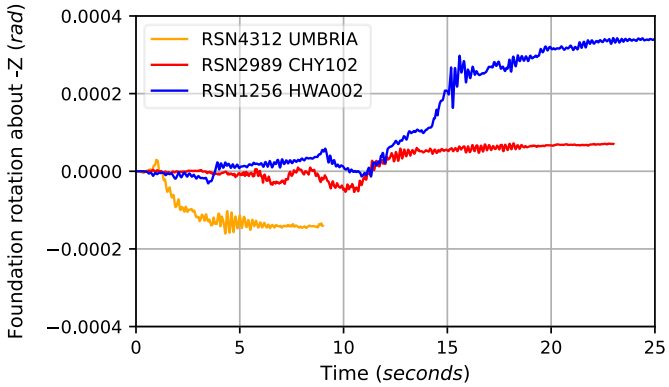

Figure 8.25. (Tower-only-Flat model) Foundation rotation about the Z axis computed at the foundation of the nonlinear structure and soil model.

On the other hand, a phase difference in the input motion components leads to more substantial torsional effects in the bell tower's foundation, as shown in Figure 8.25. Kausel (2006) discusses the Tau Effect identified and coined by *Newmark* in 1969 as a function of the foundation width, L and the shear wave velocity, C_s, as in $\tau = L/C_s$. Since, the width of the tower is 8 meters in both directions, the observed torsional rotations are small and do not lead to any noticeable interruption in the serviceability of the tower.

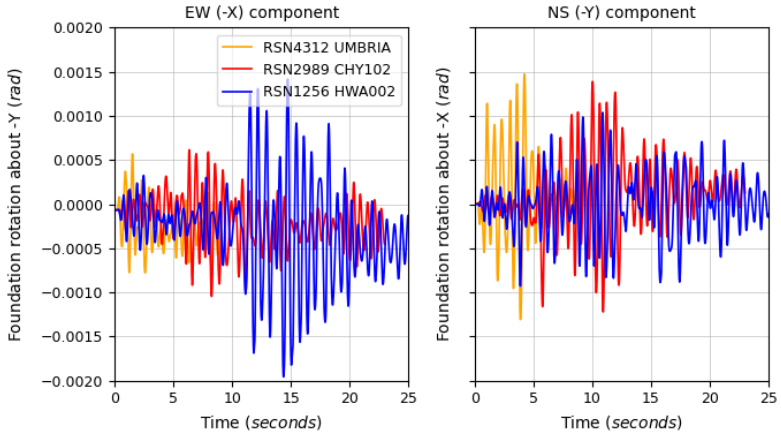

Figure 8.26. (Tower-only-Flat model) Foundation rotation about the X and Y axes computed at the foundation of the nonlinear structure and soil model.

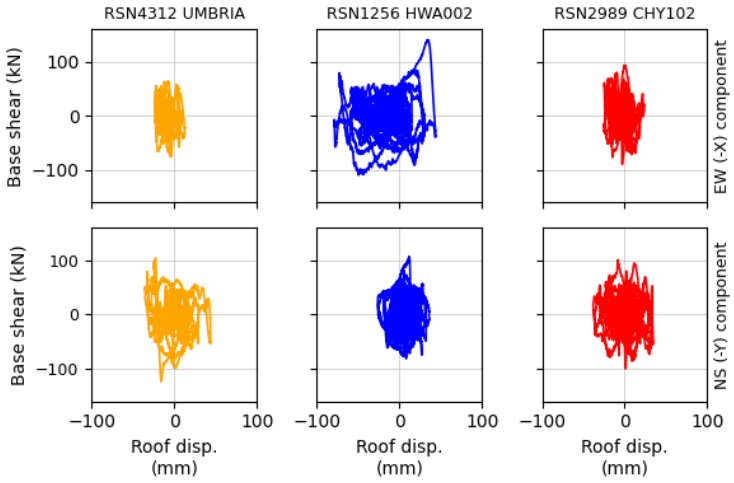

Figure 8.27. (Tower-only-Flat model) Roof displacement versus base shear response for different strong motions.

The base shear-roof displacement response of the bell tower was reduced tremendously as a result of modelling the inelastic rocking mechanism (Figure 8.11). Subsequently, the force demand is further reduced in Figure 8.27, whereas the displacement demand is increased when considering the bell tower-only model. As the adjacent walls are removed, the bell tower can oscillate freely without restriction. Due to the rocking isolation mechanism, foundation rotations increase to accommodate the displacement demand of a softer system. At the same time, the base shear reduces due to the perfectly plastic response exhibited by the foundation soil at the critical state. However, as discussed extensively in Section 8.3, it is crucial to emphasize that the foundation rocking mechanism should not be incorrectly assumed to possess infinite ductility. The perpetual perfectly plastic stress-strain response after reaching the critical state is a limitation of the kinematic hardening model and, thus, a limitation of this study as well. More accurate estimations of the force-displacement capacity can be achieved by using soil models that incorporate a more comprehensive representation of critical state soil mechanics, including strain softening.

To summarize, the effect of the adjacent walls on the dynamic response of the bell tower is discussed in this section. The adjacent walls are removed to isolate the tower-only behaviour, and the bell tower is analyzed again with the same ground motions used in Section 8.3. The key findings of this section are:

1. **Increase in the rocking isolation**: Removal of the adjacent walls decreases the foundation width of the bell tower along the NS direction, triggering a further inelastic response in the foundation soil.
2. **Tower-only versus tower-wall acceleration response**: The tower-only response is concentrated around the fundamental oscillation periods, whereas the amplified frequencies observed in response spectra are wider in the tower-wall model.
3. **Importance of modelling the pounding interaction**: Modeling the interaction between adjacent structures is crucial in the bell tower SSI model for accurately capturing the contribution of the foundation rocking mechanism.
4. **Residual foundation rotations in asymmetrical aggregates**: Increased residual rotations may occur in aggregate masonry buildings if the surrounding adjacent structures are asymmetrical in height, weight, or stiffness.

8.6 THE EFFECT OF THE VERTICAL COMPONENT IN TOTAL STRESS SSI ANALYSES

The effect of the vertical component on structures is an ongoing discussion in the literature. The findings of previous authors on the topic and the significance of the vertical component in the fixed-base bell tower model are discussed in Section 7.7. It is found that, in some cases, increased vertical accelerations might rotate the principal tensile strain planes towards the vertical axis, leading to increased cracking damage. The increase in the damage is closely related to the increase in the magnitude of the principal tensile strains due to the

superposition of the three components of the shaking. At the same time, the crack planes are sensitive to the direction of the principal tensile strain. Some motions in the set are observed to cause 5-7 times larger amplifications in the vertical accelerations recorded at the tower's roof when the three components are applied simultaneously, compared to the roof accelerations recorded as a result of using only the horizontal components of the same motion. It is noted that the motions that created high vertical amplifications embody a later peak vertical acceleration arrival time than the peak horizontal acceleration arrival time, at least in one of the horizontal components. In light of the aforementioned strong tie between the horizontal and vertical structural response, it is concluded that high vertical amplifications might result from prior stiffness loss (damage accumulation) induced by the horizontal actions.

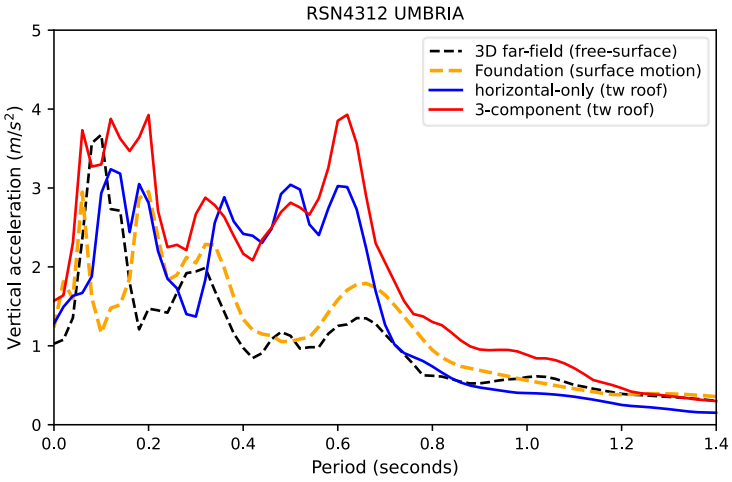

Figure 8.28. Vertical acceleration spectra computed at the tower roof for the two and three components of Umbria motion.

Sections 8.3 and 8.5 discuss the beneficial effects of the foundation rocking mechanism on the bell tower. It is shown that, as a result of modelling the interaction between the foundation and the soil, additional flexibility and energy dissipation are introduced in the system. One of the essential observations in Section 8.3 is that the frequency content of the accelerations that act on the structure significantly changes due to the rocking isolation mechanism present at the foundation level. If triggered, the foundation rocking behaviour is shown to govern the structural vibrations in Sections 6.3, 8.3, 8.4 and 8.5 of this thesis. In the case of the bell tower, the rocking oscillation occurs at a period slightly longer than 0.4 seconds, which is 45% larger than the structural fundamental period of 0.28 seconds. Such a mismatch in the fixed-base and foundation rocking dynamic response range causes a reduction in the high-frequency content of the roof spectrum. In return, low-frequency

oscillations are amplified at the roof of the SSI model, creating a wider and slightly scaled-down version of the fixed-base roof spectra.

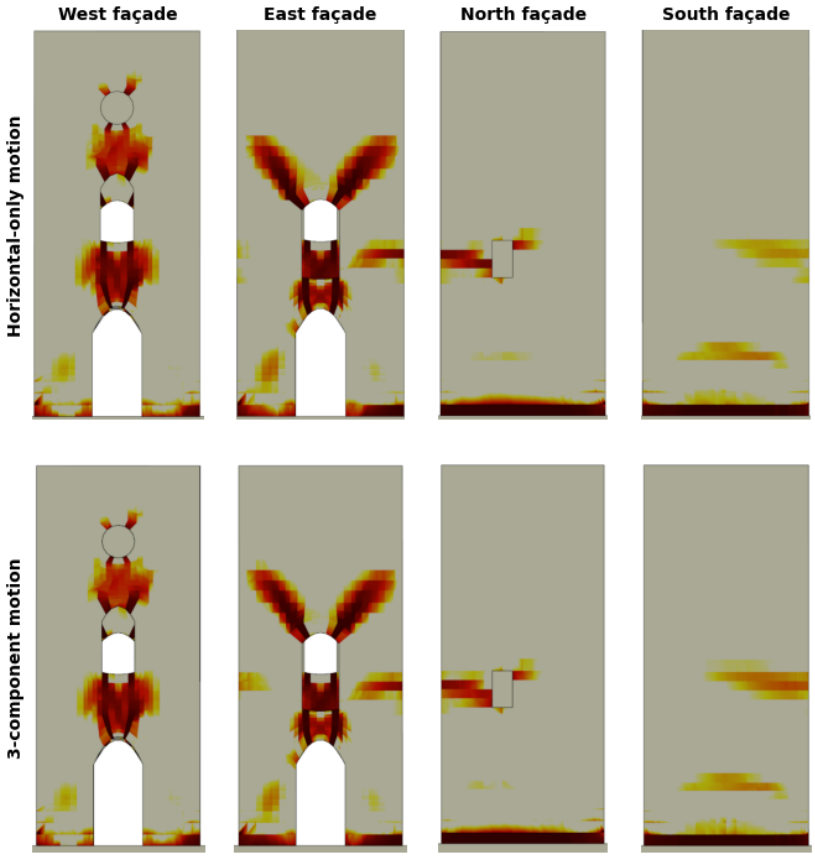

Figure 8.29. The observed cracking damage patterns due to the "Umbria" motion. Comparison of 2 versus 3 component acceleration. The Gauss points having a damage value between 0.5 and 1.0 are shown.

Figure 8.28 shows the response spectra computed on the bell tower's roof. Unlike the fixed-base analyses shown in Figure 7.21, the vertical spectra computed for the two and three-component ground motions are not significantly different. The amplification of the vertical acceleration when the three-component ground motion is applied is very similar to the amplification generated by the two-component motion, especially in the low-period range. Similarly, the difference between the input motion and the roof motions is not as pronounced as in the fixed-base analyses. Amplification in the order of 3-4 times can be seen in Figure 7.21 for the Umbria motion. The higher amplifications observed in the fixed-

base model can be attributed to the reflectivity of the boundary condition of the fixed-base model. In the SSI model, a portion of the waves are returned to the soil medium, whereas the reverberating waves are dissipated by the masonry inelastic response in the fixed-base model. This phenomenon leads to an increased cracking potential in the fixed-base model.

On the other hand, the high-frequency filtering feature of the foundation leads to an additional decrease in vertical acceleration that is transmitted to the structure from the soil. This can be observed as a drop in the low period acceleration range shown in Figure 8.28. As a result, the cracking damage response computed for the Umbria motion is not affected significantly by including the vertical component of the ground motion. However, it should be noted that the presented model focuses on the material-only nonlinear response and ignores any potential effect of the geometric nonlinearities. In future research, modelling of P-delta effects together with damage might cause more critical results. However, geometric nonlinearities are out of the scope of this thesis.

To summarize, this section investigates the effects of vertical accelerations and foundation rocking on the bell tower's dynamic response. Vertical accelerations, when combined with horizontal components, can increase principal tensile strains and cracking damage, with amplifications in roof vertical acceleration up to 5-7 times higher compared to horizontal-only motions. The timing of vertical acceleration peaks, often occurring later than horizontal peaks, suggests that prior damage from horizontal shaking influences vertical responses (Section 7.7). The key findings of this section are as follows:

- The foundation rocking mechanism introduces flexibility and energy dissipation, leading to reduced high-frequency content and amplified low-frequency oscillations at the roof. This results in less vertical acceleration amplification and reduced cracking compared to the fixed-base model.

8.7 THE EFFECT OF GROUND MOTION VARIABILITY ON THE SSI SYSTEM RESPONSE

The effect of the input motion spectral shape on the bell tower SSI system is studied. As indicated by Kausel (2010), the strong dependency of the system response to the changing ground motion characteristics was identified well in advance by Housner and colleagues in the 1950s. The virtual laboratory presented in this study is an optimal candidate for studying the mechanics behind the variability caused by ground motion definition. Even though the computational cost of running a high-fidelity model such as the bell tower is significant, the applied impl-ex integration technique at the material level makes running analyses for multiple ground motion records feasible.

In this section, an earlier version of the bell tower virtual laboratory is studied. Seven ground motion records are selected according to the procedure defined in Section 6.4. The

bell tower-wall SSI model, including the surface topography (Tower-Wall-Topographic model) (shown in Figure 8.30), was analysed. The masonry is modelled using the directionally isotropic DamageTC3D material, unlike the previous sections, in which the ASDConcrete3D with orthotropic strength anisotropy model was used. The soil around the foundation is modelled with the pressure-independent material using the hyperbolic G/Gmax reduction proposed by *Kodner* (Gu et al., 2011) with an undrained strength of 50 kPa.

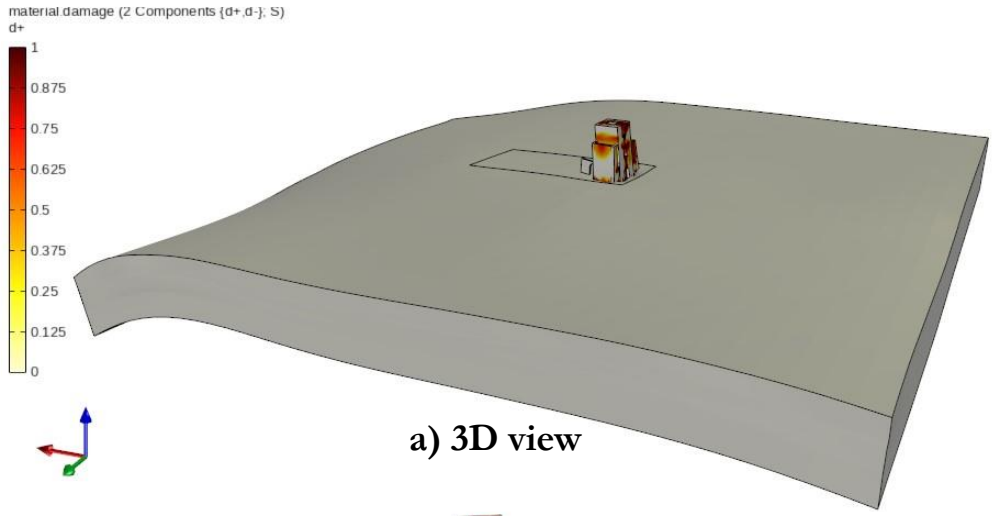

Figure 8.30. 3D illustration of the Tower-Wall-Topographic model. The tensile damage result is shown. The solution in the bottom layer is not monitored to reduce the computational cost.

The ground motion set is selected for the same bedrock properties. However, it is different from the ground motion set used for the rest of the studies discussed in the other sections of this thesis due to the randomness of the ground motion selection process. The AvgSA IM definition to select records is kept the same throughout the versions of the bell tower virtual laboratory, which is defined as the geometric mean of SA from 0.1s to 1.0s with 0.1s intervals. Figure 8.31 depicts the selected ground motion set used in this section. The dispersion match in the selected ground motions in high frequencies is worse than the set shown in Figure 6.11, which is often considered undesirable since it might introduce a frequency-based bias in the distribution of EDPs (Lin et al., 2013). Note the single strongest motion in the set selected by the algorithm to improve the dispersion match in the high frequencies. As the number of requested motions reduces, it becomes harder for the selection algorithm to find records that match the target average and dispersion. Furthermore, the number of strong motions recorded in bedrock conditions is limited in both the NGA and ESM databases. Hence, the resulting recording set is not optimal; however, it presents an acceptable solution for the purpose of this section, which is to study

the possible mechanical aspects of record-to-record differences. The selected records are processed following the procedure described in Section 6.2. Three-component motions are applied at the bottom of the model as force history during the time history analyses.

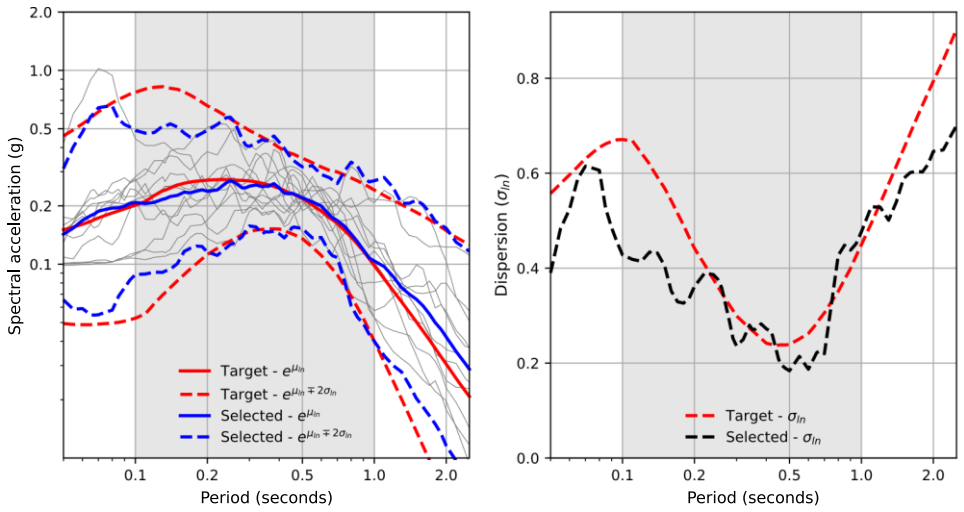

a) Target conditional spectrum (AvgSA) b) Dispersion versus periods

Figure 8.31. The alternative ground motion set selected for outcropping bedrock conditions at the location of the bell tower. AvgSA [0.1 - 1.0 sec].

The resulting foundation settlements are shown in Figure 8.32. Notably, motion RSN789 LOMAP generates the lowest settlement, followed by RSN4083 PARK2004. Together with RSN680 WHITTIER, these motions have the lowest three significant durations in the set (Figure 11.21). Since the settlement is highly sensitive to the duration of the input motion, intuitively, the lowest settlements are obtained for these motions (Karimi & Dashti, 2017; Macedo & Bray, 2018). On the other hand, motions RSN1518 CHICHI and RSN 3925 TOTTORI are the longest strong motions, and they trigger the largest settlement response in the bell tower. In Figure 8.32, the mean settlement is 20.7 mm, with a standard deviation of 2.72 mm. It must be emphasized that since the number of records is not enough to create a statistically significant set, the given standard deviation value does not have any place in any further calculation other than the presented context.

Interestingly, motion RSN680 WHITTIER generates more settlement than motion RSN4083 PARK2004, even though the latter has a longer significant duration. Furthermore, both motions embody very similar frequency content and amplitude in their acceleration response spectra. Therefore, RSN680 WHITTIER induces a strong response in the bell tower along the EW (-X) axis, whereas RSN4083 PARK2004 leads to an equally

high demand along the NS (-Y) axis (Figure 8.33 and Figure 8.34). So, at first glance, the larger settlement caused by the shorter RSN680 WHITTIER might look unintuitive.

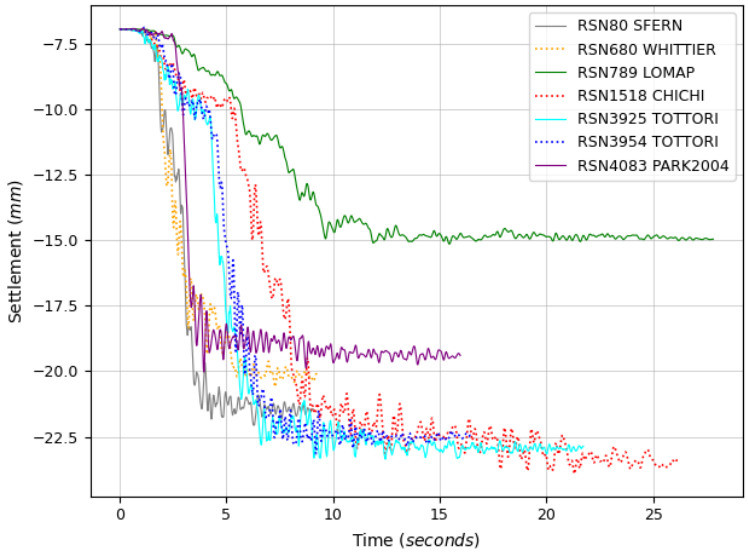

Figure 8.32. (Tower-Wall-Topographic model) Foundation settlement computed for the ground motion set.

However, this peculiarity can be explained by studying the cracking damage patterns, shown in Figure 8.35, induced by each motion. It is noted that the foundation damage induced by RSN680 WHITTIER is significantly more than that induced by RSN4083 PARK2004. In Sections 8.3, 8.4, and 8.5, the consistently increased settlements due to the softening of the foundation material is discussed. Since the damage accumulated at the foundation due to the RSN680 WHITTIER is much higher, the soil around the foundation is allowed to distort more than in the case of RSN4083 PARK2004.

Meanwhile, the RSN4083 PARK2004 motion causes significant damage to the west and east façades of the bell tower, even initiating a mechanism on the east façade due to the convergence of the two upwards propagating cracks at a point near the roof. The localization of the cracking damage emanating from the directionally isotropic masonry behaviour is discussed in Section 7.4. Therefore, in the case of RSN4083 PARK2004, the damage localizes within the large structural crack once it appears. The effect of localization clearly leads to a beneficial effect at the foundation level, decreasing the damage accumulation. The foundation stiffness is conserved, which leads to reduced settlements.

A similar phenomenon is observed in the foundation damage computed as a result of RSN789 LOMAP and RSN80 SFERN motions. As in the case of RSN4083 PARK2004,

RSN80 SFERN favours structural cracking over foundation damage. Even though RSN789 LOMAP motion has a comparable acceleration intensity to RSN4083 PARK2004, it fails to create extensive cracks in the structure since it has a greater energy content in periods longer than the foundation rocking period (Figure 11.19). The exact opposite applies to RSN3954 TOTTORI since it has more energy content in higher frequencies than the foundation rocking period (Figure 11.20). However, since this motion has a significantly longer duration, it causes larger settlements in the bell tower.

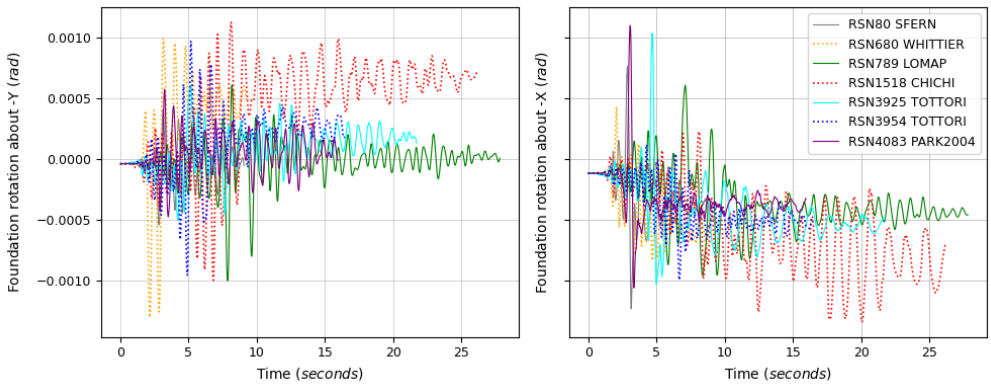

Figure 8.33. (Tower-Wall-Topographic model) Foundation rotation about the X and Y axes computed for the ground motion set.

The foundation rotation results are shown in Figure 8.33. The mean permanent rotation about the -Y axis is 0.00026 radians with a standard deviation of 0.000232 radians. Meanwhile, the average permanent rotation about the -X axis is 0.000546 radians with a standard deviation of 0.000180 radians. Moreover, some torsional rotation is observed in the tower due to the RSN680 WHITTIER motion, shown in Figure 11.18. The significant phase difference in the horizontal components of the RSN680 WHITTIER motion can be seen in Figure 11.21.

The largest rotation response is triggered by the RSN1519 CHICHI motion. Notably, although RSN1519 CHICHI is not the strongest motion overall, its spectral acceleration in the EW (-X) direction peaks at longer periods than the rocking period of the bell tower, contributing to its significant rotational impact. (Figure 11.20). In Figure 8.33, the amplitude of the rotation caused by the RSN1519 CHICHI motion is relatively smaller at the beginning of the analysis compared to other motions such as RSN4083 PARK2004, RSN3954 TOTTORI or RSN680 WHITTIER. However, it has a significantly longer duration than the mentioned records. Later in the analysis, as the damage accumulates in the structure, the inelastic period of the tower shifts and falls into the amplified period ranges by the RSN1519 CHICHI motion. This results in increased foundation rotation,

cracking damage (Figure 8.35) and the base shear-roof displacement response along the EW (-X) direction observed in Figure 8.34.

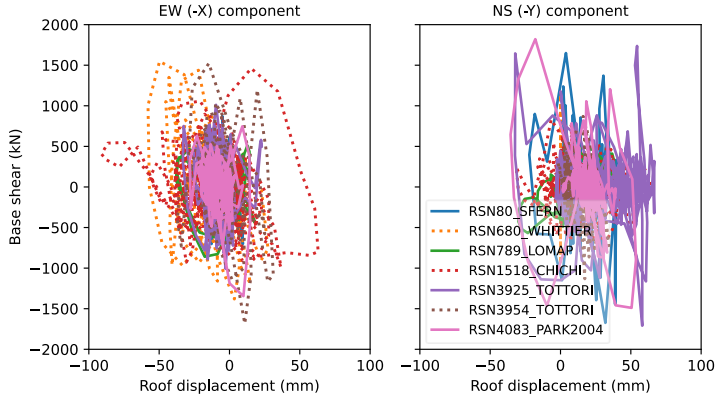

a) Base shear versus roof displacement

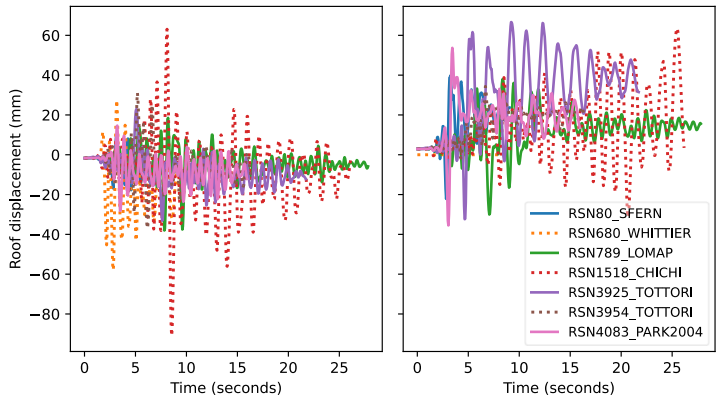

b) Roof displacement history

Figure 8.34. (Tower-Wall-Topographic model) a) Roof displacement versus base shear response, and b) Permanent roof displacements for strong motions.

Interestingly, the motions RSN3954 TOTTORI, RSN680 WHITTIER, and RSN1519 CHICHI lead to the maximum force-displacement demand along the EW (-X) direction, whereas the motions RSN4083 PARK2004, RSN3925 TOTTORI, and RSN80 SFERN lead to increased demand along the NS (-Y) direction of the bell tower. In the cracking damage plots shown in Figure 8.35, motions RSN4083 PARK2004, RSN3925 TOTTORI, and RSN80 SFERN tend to trigger primarily structural damage, whereas the other three motions chiefly induce foundation failure.

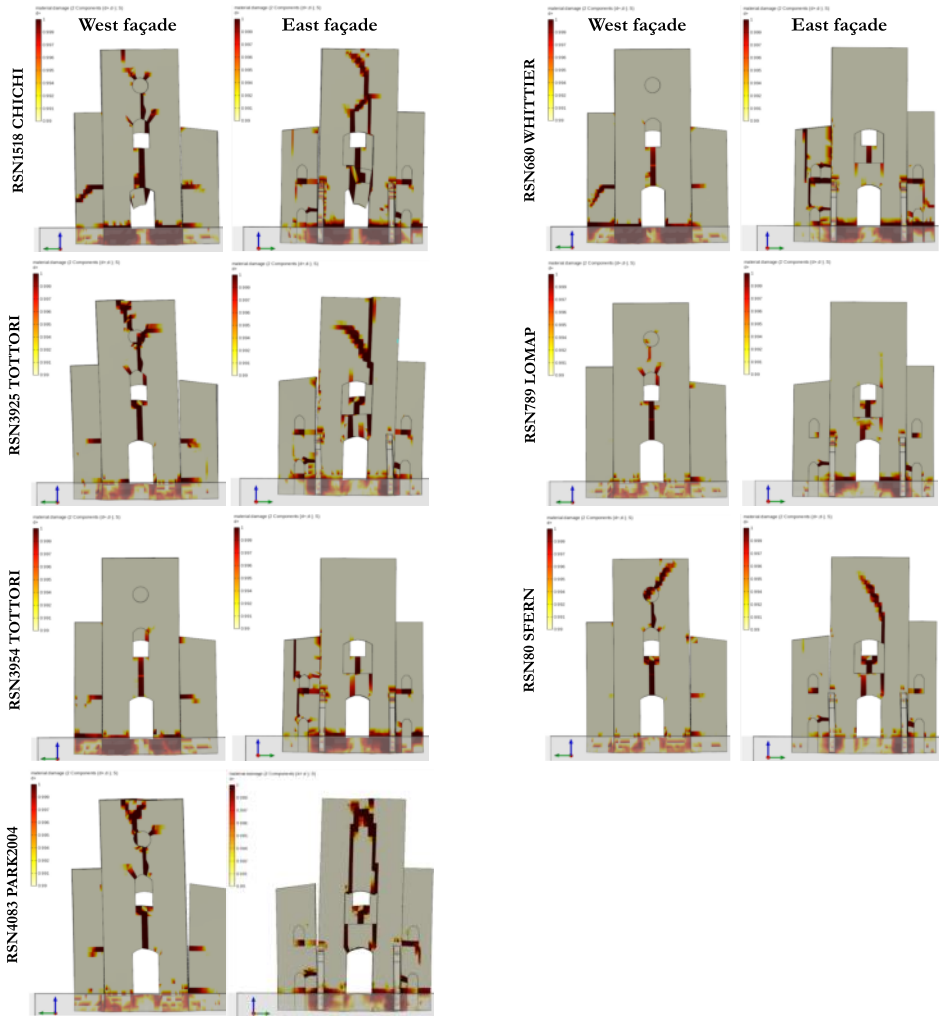

Figure 8.35. (Tower-Wall-Topographic model) Tensile cracking damage patterns computed for the record set. The Gauss points having a damage value between 0.5 and 1.0 are shown.

As an exception, RSN1519 CHICHI motion first softens the structure by inducing foundation damage. Then, once the period of the tower elongates, it matches the primary failure mechanism. This is the underlying mechanism that leads to the increased foundation rocking and force-displacement response observed before.

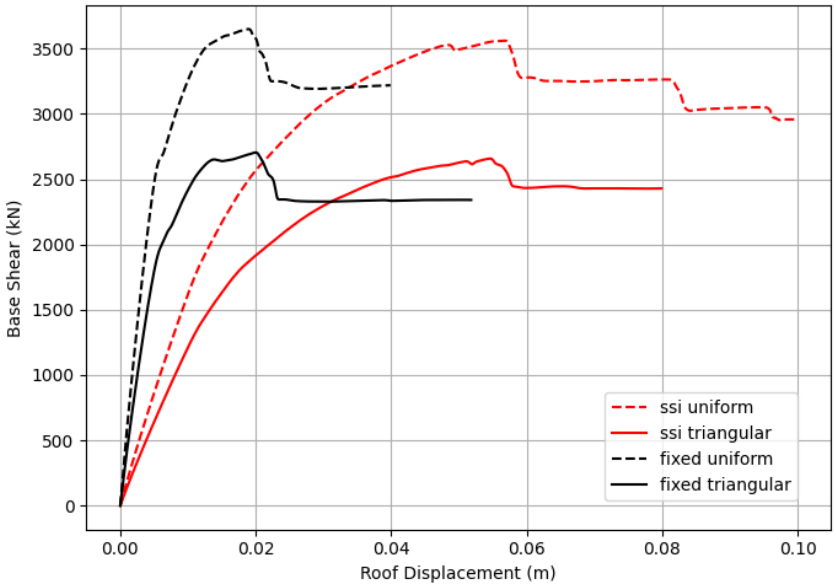

Figure 8.36. Pushover analyses of fixed base versus SSI models. The ductility of the tower increases when the soil is considered, which is crucial in seismic assessment, such as the N2 method.

Finally, the pushover analysis result of the tower is shown in Figure 8.36. The pushover curves are computed according to the uniform and triangular force vector assumptions widely used in the industry in the seismic assessment of structures using static methods such as the N2 method (Fajfar & Gašperšič, 1996) adopted by Eurocode 8. It is worth noting that the dynamic (Figure 8.34) versus static (Figure 8.36) force-displacement responses are considerably different. So much so that comparing the static capacity to the dynamic demand would indicate that the structure is more than capable of counteracting the seismic demand created by all the seven ground motions without attaining significant damage. However, the damage response observed in Figure 8.35 clearly proves otherwise. The discrepancy between the static and dynamic capacity indicates that traditional pushover methods are incapable of capturing the complex response of the bell tower, neither in the fixed base nor the SSI case. Hence, future research might explore the applicability of more advanced nonlinear static analysis techniques in the assessment of masonry tower structures.

To summarize, the study examines the influence of the spectral shape on the seismic response of a bell tower-soil-structure interaction (SSI) system. The bell tower model is subjected to seven ground motion records that are selected to match the conditional mean spectrum computed for the site for the hazard with a return period of 457 years. The masonry is modelled using a directionally isotropic material, while the soil employs a

pressure-independent material model with low undrained strength (50 kPa). The study focuses on understanding how variability in ground motion characteristics affects the structural and foundation response, considering both settlement and rotation effects. The key findings of this section are as follows:

- **Foundation settlements**: The settlement response varies significantly across the motions, with RSN1518 CHICHI and RSN3925 TOTTORI causing the largest settlements due to their long duration, while shorter motions like RSN789 LOMAP result in the least settlement.
- **Foundation rotations**: Despite not being the strongest motion, RSN1519 CHICHI triggers the largest rotational response due to its peculiar spectral shape peaking at longer periods than the bell tower's rocking period.
- **Cracking damage**: Some motions (e.g., RSN680 WHITTIER) induce more masonry foundation damage due to higher accelerations along the strong (EW) direction of the bell tower, while others (e.g., RSN4083 PARK2004) cause significant structural damage, particularly at the façades.
- **Dynamic vs. static response**: The pushover analysis reveals a discrepancy between static and dynamic force-displacement responses, indicating that traditional static analysis methods may not fully capture the complex seismic behaviour of the bell tower.

8.8 SUMMARY AND DISCUSSION

This chapter presents a comprehensive investigation into the dynamic SSI response of the masonry bell tower of St. Maria Maggiore cathedral in Guardiagrele under seismic loading. The results of a detailed finite element model of the bell tower, incorporating site-specific soil conditions and structural characteristics, is presented. The effects of material nonlinearity are examined to assess the impact of foundation rocking and energy dissipation mechanisms on the overall structural response. By considering different ground motions and analysing both linear and nonlinear soil responses, the modifications in the input motion due to foundation rocking and its influence on the damage patterns are discussed.

One of the significant findings is the beneficial role of the foundation rotations in reducing seismic demands. First, the natural frequency of the system is altered due to the soil flexibility at the base, effectively increasing the vibration periods of the tower. Second, the foundation rocking mechanism, termed "rocking isolation," acts as a form of natural seismic isolation, allowing energy dissipation at the foundation soil, reducing the risk of severe structural failure. Plastic processes in the soil leads to a reduction in the accelerations transmitted to the structure, thus mitigating cracking and other forms of damage typically observed in masonry towers.

Another key contribution is the detailed examination of the effect of rate of shear stiffness degradation in the foundation soil on the structural cracking. The study demonstrates that a stiffness reduction in the small strain ranges occurring within the foundation soil results in reduced cracking damage in the bell tower.

Furthermore, the study finds that the accurate modelling of foundation masonry response can be a significant factor in the prediction of residual foundation settlements. Consistently higher foundation settlements are observed when the foundation masonry is allowed to soften during shaking because of cracking damage accumulation in the masonry.

It is worth noting that the assumptions about hydromechanical coupling in modelling both fine-grained and coarse-grained soil behaviour can considerably impact the seismic response in terms of foundation rotation and settlement.

In this thesis, fine-grained soil behaviour was modelled using a nested von Mises type pressure-independent model, which serves as a simplified representation of rapid loading conditions. This approach is applicable to low-permeability, high-plasticity soils under fully saturated conditions. As a result, the model behaviour is strongly dependent on the used undrained shear strength parameter. Incorporating a pressure-dependent model that explicitly simulates pore-pressure buildup during rapid loading would provide a more refined analysis. This approach would offer improved estimation of undrained shear strength, better capture the pressure-dependent strength and stiffness gradients in the soil profile, and more accurately predict the stress-strain response under cyclic loading.

A hydromechanically coupled analysis could yield notable differences in the calculated settlements and rotations. Most notably, the permanent settlement estimates would likely change, as increased undrained shear strength tends to reduce settlements. Moreover, the dynamic nature of shear strength during shaking in a coupled analysis would result in a more nuanced stress-strain response. The findings of Section 8.4 suggest that a stiffer response during the initial stages of shaking can reduce settlement. Additionally, modelling the strength and stiffness gradient more accurately would likely localize settlements and rotations to shallower regions beneath the foundation.

Overall, considering the hydromechanical coupling in fine-grained soil behaviour could have important consequences for some SSI problems and should be studied in more detail in the future. Considering the scope of the studies discussed in this thesis, the simplified total stress model for clays is refined enough to identify the important SSI behaviour trends and mechanisms. Within the scope of this thesis, however, the simplified total stress model for clays sufficiently captures key SSI behaviour trends and mechanisms. Future research could explore more complex scenarios, such as partial saturation, which would require advanced modelling techniques that consider hydromechanical coupling

Finally, the chapter provides insights into the effects of seismic pounding and ground motion variability on the SSI system. When adjacent walls are removed, the rocking isolation mechanism becomes more prominent, reducing the accelerations and thus the overall seismic demand. The chapter also shows that ground motions with longer durations or higher frequency content produce more substantial foundation damage and increased settlements, highlighting the sensitivity of the SSI system to the characteristics of the input motion.

9 CONCLUSIONS

In this chapter, a summary of the thesis work is presented. The principal findings from all sections of the thesis are stated in a concise manner. Finally, an answer to the research question introduced in the introduction chapter of this thesis is provided based on the findings summarized here. The limitations of the thesis work are discussed. Then, the main contributions of the thesis are presented as bullets points focusing on the novelties achieved concerning the direct SSI analysis of masonry tower structures within the scope of this thesis. The thesis work is concluded by compiling several topics to be addressed in future studies, and possible practical implications of the thesis work in the seismic assessment of masonry towers.

KEYWORDS: research outcomes, principal findings, novelties, future research, discussion

9.1 SUMMARY OF THE THESIS

The seismic analysis of masonry towers focusing on the nonlinear soil-structure interaction (SSI) effects is discussed in this thesis. The primary research question focuses on how the degradation of soil stiffness and the nonlinear material behaviour of masonry affect the seismic response of masonry towers. Furthermore, the role of pounding interaction between adjacent structures and wall in the SSI response is considered. In addition, the study seeks an answer to the question whether the rocking isolation mechanism, which has been shown to be effective in reinforced concrete frames, exists in heritage masonry structures. These research objectives are pursued through the development of a comprehensive computational framework, aimed at capturing both structural and geotechnical nonlinearities in seismic assessments.

To achieve these objectives, a virtual laboratory within OpenSees is established, using the STKO pre-processor to model both the bell tower and the underlying soil layers. The virtual laboratory enables the high-fidelity simulation of detailed soil-structure systems under seismic loading, incorporating advanced constitutive models that accurately reflect the nonlinear behaviour of both the masonry and the soil.

To control the computational cost of solving a large SSI boundary value problem, a mixed implicit-explicit (impl-ex) integration scheme is employed, allowing a stable solution even for large time steps. This approach is plays critical for efficiently capturing key phenomena such as cracking in the masonry or dynamic contact nonlinearities. The formulations of a

novel impl-ex contact element as well as pressure dependent multi yield surface constitutive model are given in Chapters 3 and 4.

Another crucial aspect of the presented research is the selection of ground motions using an innovative approach. The seismic input motion set for the analyses is selected using the Conditional Spectrum (CS) method, targeting the spectrum conditioned on the AvgSA suited for the bell tower. It is shown that elaborate intensity measures (IMs) such as the AvgSA which is composed of the geometric mean of a range of frequencies can be tailored to cover the predominant vibration frequencies of a masonry tower structure. Then, 1D free surface site response analyses are conducted using the selected motions to obtain the ground motion set for the fixed base analyses. Ground motion analyses are conducted using 2D and 3D site response models, exploring the effects of topographic amplifications on the acceleration observed at the foundation of the bell tower.

The study proceeds by analysing the bell tower under both fixed-base and SSI conditions. These analyses explore various factors, including the effects of pounding interaction between the bell tower and adjacent structures, as well as the contribution of vertical seismic accelerations. The findings from these simulations reveal critical insights into how different seismic conditions can influence cracking patterns in the masonry and the global response of the SSI system.

The principal findings of the thesis concerning the nonlinear soil-structure interaction of masonry towers are:

1. Intensity measure (IM) selection and frequency range identification

The study proposes that the average spectral acceleration (AvgSA) is a potentially effective intensity measure for the seismic analysis of masonry bell towers. A method for identifying the significant frequency ranges, considering both horizontal and vertical ground motion components, is presented. This approach offers an efficient way to quantify the seismic demands on masonry towers by correlating ground motion characteristics with observed structural responses.

2. Role of material anisotropy in the seismic behaviour of masonry towers

A key finding is the detrimental impact of neglecting the inherent strength anisotropy of the masonry. The analysis shows that ignoring the directional properties of masonry can lead to overestimation of damage and localized cracking patterns due to shaking. Anisotropy significantly influences how energy is dissipated within the structure making it an essential consideration for accurate modelling of the dynamic capacity.

3. Amplification of vertical accelerations

Vertical accelerations, particularly when their peak arrival is delayed relative to horizontal accelerations, can critically affect the seismic response of the tower. The research demonstrates that in some cases, this delayed arrival results in amplified vertical forces, intensifying the tensile cracking damage patters observed in the masonry tower.

4. Rocking isolation mechanism

The presence of a rocking isolation mechanism, previously observed in shallow-founded reinforced concrete (RC) structures by Gazetas (2015), also exists for masonry towers. This mechanism reduces the forces transmitted to the superstructure and helps mitigate damage in the tower structures.

5. Shear stiffness reduction in foundation soil

The shear modulus reduction characteristics of the foundation soil is shown to have significant effect on the cracking damage observed in the tower. As the soil undergoes more shear modulus reduction in small strain ranges, the foundation's capacity to dissipate seismic energy increases, reducing the overall demand on the superstructure.

6. Pounding interactions and cracking damage

The pounding interactions between the bell tower and adjacent walls are shown to significantly contribute to the cracking damage patterns observed in the bell tower. Pounding effects in the fixed-base model led to increased cracking damage and local failure zones in the tower.

7. Stable solution in contact elements

The use of the impl-ex scheme successfully bypasses convergence issues in contact elements, enabling stable simulation of pounding interactions between structural components. This approach controls numerical errors while maintaining computational efficiency, allowing the model to continue past failure points.

8. Cyclic soil behaviour

The impl-ex integration technique effectively captures cyclic soil behaviour, reducing the computational cost induced by Newton-Raphson iterations. For pressure-independent materials, a solution is found after a single iteration, while solution with effective stresses

require two iterations: one iteration for the pressure-dependent material and a second iteration for the pore-pressure degree of freedom.

9.2 CONTRIBUTIONS

The contributions of this thesis are:

- Implementation and formulation of a highly stable implicit-explicit contact-friction element in OpenSees.
- Modelling of the dynamic pounding interactions via contact-friction elements during the seismic analysis of an aggregate masonry church-bell tower complex.
- Implementation and formulation of the implicit-explicit versions of the pressure-independent and pressure-dependent multi-yield soil materials in OpenSees.
- Modelling and preparation of a virtual laboratory in OpenSees for studying the effect of material nonlinearities in dynamic soil-structure interaction of stone masonry towers.
- Demonstrating the technique and advantages of employing implicit-explicit material models in the transient seismic analysis of masonry structures.

9.3 PRACTICAL IMPLICATIONS AND FUTURE RESEARCH

Some of the practical applications for seismic assessment and retrofit of masonry towers might be:

- Modelling of foundation masonry softening

Accurate modelling of the softening behaviour of foundation masonry might be critical for predicting the vertical settlements. The accumulation of cracking damage in the foundation can significantly lead to increased flexibility, which, if not accounted for, could lead to conservative settlement predictions.

- Shear stiffness degradation in the foundation soil

Proper characterisation of the shear stiffness degradation in foundation soil might be essential for the accurate seismic assessment of masonry towers. The predicted cracking damage in the tower structure is highly sensitive to changes in foundation soil stiffness, particularly within small strain ranges. Understanding how the soil stiffness evolves during seismic shaking can improve predictions of tower damage response.

Finally, some of the future research opportunities are:

- Synchronism in seismic response

- Inclusion of geometric nonlinearities

The current analyses exclude geometric nonlinearities, which can result in an underestimation of the tower's structural response, particularly in cases involving large deformations or P-delta effects. Future research should incorporate these geometric nonlinearities to better capture critical failure mechanisms, especially under extreme seismic loads.

- Undrained shear strength with depth

Further research into the variation of undrained shear strength (Su) with depth would be valuable in understanding the foundation's capacity during seismic events, particularly in complex soil profiles.

- Effective stress analyses for undrained conditions

- Response of structured and stiff clays

- Further Application of PDMY02 Implicit-Explicit Integration

The implementation of the pressure-dependent multi-yield (PDMY02) model using implicit-explicit (impl-ex) integration has shown promise in improving computational efficiency. Future studies should extend the application of this model to a wider range of engineering problems and soil types, testing its robustness across different conditions.

10 REFERENCES

Abdulla, K. F., Cunningham, L. S., & Gillie, M. (2017). Simulating masonry wall behaviour using a simplified micro-model approach. *Engineering Structures*, *151*, 349–365. https://doi.org/10.1016/j.engstruct.2017.08.021

Abell, J. A., Crempien, J. G., & Recabarren, M. (2022). ShakerMaker: A framework that simplifies the simulation of seismic ground-motions. *SoftwareX*, *17*, 100911.

Abell, J. A., Orbović, N., McCallen, D. B., & Jeremic, B. (2018). Earthquake soil-structure interaction of nuclear power plants, differences in response to 3-D, 3 × 1-D, and 1-D excitations. *Earthquake Engineering & Structural Dynamics*, *47*(6), 1478–1495. https://doi.org/10.1002/eqe.3026

Abruzzese, D., Miccoli, L., Vari, A., Ferraioli, M., Mandara, A., & Froncillo, S. (2009, June 1). *Dynamic investigations on medieval masonry towers: Seismic resistance and strengthening techniques*. International Conference on Protection of Historical Buildings, Rome, Italy.

Addessi, D., Sacco, E., & Paolone, A. (2010). Cosserat model for periodic masonry deduced by nonlinear homogenization. *European Journal of Mechanics - A/Solids*, *29*(4), 724–737. https://doi.org/10.1016/j.euromechsol.2010.03.001

Adhikary, D. P., Jayasundara, C. T., Podgorney, R. K., & Wilkins, A. H. (2017). A robust return-map algorithm for general multisurface plasticity. *International Journal for Numerical Methods in Engineering*, *109*(2), 218–234. https://doi.org/10.1002/nme.5284

Akan, O. D., & Petracca, M. (2022). *3.1.9.4. ZeroLengthContactASDimplex Element—OpenSees Documentation* [C++]. https://opensees.github.io/OpenSeesDocumentation/user/manual/model/elements/zeroLengthContactASDimplex.html

Amestoy, P. R., Buttari, A., L'Excellent, J.-Y., & Mary, T. (2019). Performance and Scalability of the Block Low-Rank Multifrontal Factorization on Multicore Architectures. *ACM Transactions on Mathematical Software*, *45*(1), 2:1-2:26. https://doi.org/10.1145/3242094

Amestoy, P. R., Duff, I. S., L'Excellent, J.-Y., & Koster, J. (2001). A Fully Asynchronous Multifrontal Solver Using Distributed Dynamic Scheduling. *SIAM Journal on Matrix Analysis and Applications*, *23*(1), 15–41. https://doi.org/10.1137/S0895479899358194

Anastasopoulos, I., Gazetas, G., Loli, M., Apostolou, M., & Gerolymos, N. (2010). Soil failure can be used for seismic protection of structures. *Bulletin of Earthquake Engineering*, *8*, 309–326.

Anastasopoulos, I., Gelagoti, F., Kourkoulis, R., & Gazetas, G. (2011). Simplified Constitutive Model for Simulation of Cyclic Response of Shallow Foundations: Validation against Laboratory Tests. *Journal of Geotechnical and Geoenvironmental Engineering*, *137*(12), 1154–1168. https://doi.org/10.1061/(ASCE)GT.1943-5606.0000534

Anastasopoulos, I., Loli, M., Gelagoti, F., Kourkoulis, R., & Gazetas, G. (2012). Nonlinear soil–foundation interaction: Numerical analysis. *2nd Int. Conf. on Performance-Based Design in Earthquake Geotechnical Engineering*. https://www.academia.edu/download/94123666/TAORMINA_IXA_LOLI_GELAGOTI_KOURKOULIS_2012ROCKANAL.pdf

Ancheta, T. D., Darragh, R. B., Stewart, J. P., Seyhan, E., Silva, W. J., Chiou, B. S.-J., Wooddell, K. E., Graves, R. W., Kottke, A. R., Boore, D. M., Kishida, T., & Donahue, J. L. (2014). NGA-West2 Database. *Earthquake Spectra*, *30*(3), 989–1005. https://doi.org/10.1193/070913EQS197M

Andrade, J. E., Avila, C. F., Hall, S. A., Lenoir, N., & Viggiani, G. (2011). Multiscale modeling and characterization of granular matter: From grain kinematics to continuum mechanics. *Journal of the Mechanics and Physics of Solids*, *59*(2), 237–250. https://doi.org/10.1016/j.jmps.2010.10.009

Andreotti, G., Famà, A., & Lai, C. G. (2018). Hazard-dependent soil factors for site-specific elastic acceleration response spectra of Italian and European seismic building codes. *Bulletin of Earthquake Engineering*, *16*(12), 5769–5800. https://doi.org/10.1007/s10518-018-0422-9

Andrianopoulos, K. I., Papadimitriou, A. G., & Bouckovalas, G. D. (2010). Explicit integration of bounding surface model for the analysis of earthquake soil liquefaction. *International Journal for Numerical and Analytical Methods in Geomechanics*, *34*(15), 1586–1614. https://doi.org/10.1002/nag.875

Angiolilli, M., & Gregori, A. (2020). Triplet Test on Rubble Stone Masonry: Numerical Assessment of the Shear Mechanical Parameters. *Buildings*, *10*(3), Article 3. https://doi.org/10.3390/buildings10030049

Arduino, P. (2014). *Geotechnical Elements and Models in OpenSees Type of Geotechnical Problems that can be solved using OpenSees*. 1–16.

Bahçecioğlu, T. (2011). *Parallel solution of soil-structure interaction problems on pc clusters* [Master Thesis]. https://open.metu.edu.tr/handle/11511/20408

Baker, J. W. (2011). Conditional Mean Spectrum: Tool for Ground-Motion Selection. *Journal of Structural Engineering*, *137*(3), 322–331. https://doi.org/10.1061/(ASCE)ST.1943-541X.0000215

Bartoli, G., Betti, M., & Monchetti, S. (2017). Seismic Risk Assessment of Historic Masonry Towers: Comparison of Four Case Studies. *Journal of Performance of Constructed Facilities*, *31*(5), 04017039. https://doi.org/10.1061/(ASCE)CF.1943-5509.0001039

Bathe, K. J. (2007). Conserving energy and momentum in nonlinear dynamics: A simple implicit time integration scheme. *Computers and Structures*, *85*(7–8), 437–445. https://doi.org/10.1016/j.compstruc.2006.09.004

Bathe, K.-J. (2016). *Finite Element Procedures*. Prentice Hall, Pearson Education, Inc.

Bažant, Z. P., Belytschko, T. B., & Chang, T.-P. (1984). Continuum Theory for Strain-Softening. *Journal of Engineering Mechanics*, *110*(12), 1666–1692. https://doi.org/10.1061/(ASCE)0733-9399(1984)110:12(1666)

Belytschko, T., Liu, W. K., Moran, B., & Elkhodary, K. I. (2014). *Nonlinear Finite Elements for Continua and Structures, 2nd Edition* (2nd Edition).

Belytschko, T., & Mullen, R. (1978). Stability of explicit-implicit mesh partitions in time integration. *International Journal for Numerical Methods in Engineering*, *12*(10), 1575–1586. https://doi.org/10.1002/nme.1620121008

Belytschko, T., Yen, H.-J., & Mullen, R. (1979). Mixed methods for time integration. *Computer Methods in Applied Mechanics and Engineering*, *17–18*, 259–275. https://doi.org/10.1016/0045-7825(79)90022-7

Ben, Z. (2013). *Large-scale Finite Element Simulation of Seismic Soil-Pile foundation-Structure Interaction*. National University of Singapore.

Bielak, J., Loukakis, K., Hisada, Y., & Yoshimura, C. (2003). Domain reduction method for three-dimensional earthquake modeling in localized regions, part I: Theory. *Bulletin of the Seismological Society of America*, *93*(2), 817–824. https://doi.org/10.1785/0120010251

Biondi, S., Camata, G., Candigliota, E., Spacone, E., & Valente, C. (2009, June). *Identificazione strutturale di una torre in muratura per la messa a punto del modello numerico*. XIII Convegno ANIDIS L'Ingegneria Sismica in Italia ANIDIS, BOLOGNA.

Biot, M. A. (1962). Mechanics of Deformation and Acoustic Propagation in Porous Media. *Journal of Applied Physics*, *33*(4), 1482–1498. https://doi.org/10.1063/1.1728759

Boore, D. M. (2010). Orientation-Independent, Nongeometric-Mean Measures of Seismic Intensity from Two Horizontal Components of Motion. *Bulletin of the Seismological Society of America*, *100*(4), 1830–1835. https://doi.org/10.1785/0120090400

Boore, D. M., Stewart, J. P., Seyhan, E., & Atkinson, G. M. (2014). NGA-West2 Equations for Predicting PGA, PGV, and 5% Damped PSA for Shallow Crustal Earthquakes. *Earthquake Spectra*, *30*(3), 1057–1085. https://doi.org/10.1193/070113EQS184M

Boore, D. M., Watson-Lamprey, J., & Abrahamson, N. A. (2006). Orientation-Independent Measures of Ground Motion. *Bulletin of the Seismological Society of America*, *96*(4A), 1502–1511. https://doi.org/10.1785/0120050209

Borja, R. I., & Andrade, J. E. (2006). Critical state plasticity. Part VI: Meso-scale finite element simulation of strain localization in discrete granular materials. *Computer Methods in Applied Mechanics and Engineering*, *195*(37), 5115–5140. https://doi.org/10.1016/j.cma.2005.08.020

Borja, R. I., Sama, K. M., & Sanz, P. F. (2003). On the numerical integration of three-invariant elastoplastic constitutive models. *Computer Methods in Applied Mechanics and Engineering*, *192*(9), 1227–1258. https://doi.org/10.1016/S0045-7825(02)00620-5

Boulanger, R. W., & Ziotopoulou, K. (2022). *PM4SAND (VERSION 3.2): A SAND PLASTICITY MODEL FOR EARTHQUAKE ENGINEERING APPLICATIONS* (Issue July). UNIVERSITY OF CALIFORNIA AT DAVIS.

Bradley, B. A. (2012a). A ground motion selection algorithm based on the generalized conditional intensity measure approach. *Soil Dynamics and Earthquake Engineering*, *40*, 48–61. https://doi.org/10.1016/j.soildyn.2012.04.007

Bradley, B. A. (2012b). Empirical Correlations between Peak Ground Velocity and Spectrum-Based Intensity Measures. *Earthquake Spectra*, *28*(1), 17–35. https://doi.org/10.1193/1.3675582

Bray, J. D., & Dashti, S. (2014). Liquefaction-induced building movements. *Bulletin of Earthquake Engineering*, *12*(3), 1129–1156. https://doi.org/10.1007/s10518-014-9619-8

Bray, J. D., & Macedo, J. (2017). 6th Ishihara lecture: Simplified procedure for estimating liquefaction-induced building settlement. *Soil Dynamics and Earthquake Engineering*, *102*(September), 215–231. https://doi.org/10.1016/j.soildyn.2017.08.026

Bui, H.-G., & Meschke, G. (2020). A parallelization strategy for hydro-mechanically coupled mechanized tunneling simulations. *Computers and Geotechnics*, *120*, 103378. https://doi.org/10.1016/j.compgeo.2019.103378

Bullock, Z., Dashti, S., Karimi, Z., Liel, A., Porter, K., & Franke, K. (2019). Probabilistic Models for Residual and Peak Transient Tilt of Mat-Founded Structures on Liquefiable Soils. *Journal of Geotechnical and Geoenvironmental Engineering*, *145*(2), 04018108. https://doi.org/10.1061/(asce)gt.1943-5606.0002002

Bullock, Z., Dashti, S., Liel, A., Porter, K., & Karimi, Z. (2018). Efficiency, sufficiency, and predictability of intensity measures for predicting the consequences of liquefaction

on buildings. *11th National Conference on Earthquake Engineering 2018, NCEE 2018: Integrating Science, Engineering, and Policy*, *11*, 6778–6788.

Camata, G., Cifelli, L., Spacone, E., Conte, J., & Torrese, P. (2008). Safety analysis of the bell tower of St. Maria Maggiore cathedral in Guardiagrele (Italy). *The 14th World Conference on Earthquake Engineering*, *88*. https://doi.org/10.4203/ccp.88.58

Carydis, P., Castiglioni, C., Lekkas, E., Kostaki, I., Lebesis, N., & Drei, A. (2012). *The Emilia Romagna, May 2012 earthquake sequence. The influence of the vertical earthquake component and related geoscientific and engineering aspects*. *2*.

Cascone, V., Barone, I., & Boaga, J. (2022). Velocity gradients choice affecting seismic site response in deep alluvial basins: Application to the Venetian Plain (Northern Italy). *Journal of Geophysics and Engineering*, *19*(1), 1–13. https://doi.org/10.1093/jge/gxab067

Chandler, H. W. (1985). A plasticity theory without drucker's postulate, suitable for granular materials. *Journal of the Mechanics and Physics of Solids*, *33*(3), 215–226. https://doi.org/10.1016/0022-5096(85)90012-2

Chatzigogos, C. T., Pecker, A., & Salençon, J. (2009). Macroelement modeling of shallow foundations. *Soil Dynamics and Earthquake Engineering*, *29*(5), 765–781. https://doi.org/10.1016/j.soildyn.2008.08.009

Chen, W.-F., & Mizuno, E. (1990). *Nonlinear Analysis in Soil Mechanics: Theory and Implementation*. Elsevier.

Chen, Z., Trombetta, N. W., Hutchinson, T. C., Mason, H. B., Bray, J. D., & Kutter, B. L. (2013). Seismic System Identification Using Centrifuge-based Soil-Structure Interaction Test Data. *Journal of Earthquake Engineering*, *17*(4), 469–496. https://doi.org/10.1080/13632469.2012.762956

Cheng, Z., Dafalias, Y., & Manzari, M. (2013, October 22). *Application of SANISAND Dafalias-Manzari model in FLAC3D*.

Chopra, A. K. (2015). *Dynamics of Structures, Global Edition*. Financial Times Prentice Hall.

Conte, J. P., Elgamal, A., Yang, Z., Zhang, Y., Acero, G., & Seible, F. (2002). Nonlinear Seismic Analysis of a Bridge Ground System. *Proceedings of the 15th ASCE Engineering Mechanics Conference*, *June*, 1–8.

Cosserat, E., & Cosserat, F. (1909). Théorie des Corps déformables. *Nature*, *81*(2072), Article 2072. https://doi.org/10.1038/081067a0

Courant, R., Friedrichs, K., & Lewy, H. (1928). Über die partiellen Differenzengleichungen der mathematischen Physik. *Mathematische Annalen*, *100*(1), 32–74. https://doi.org/10.1007/BF01448839

Cremer, C., Pecker, A., & Davenne, L. (2001). Cyclic macro-element for soil–structure interaction: Material and geometrical non-linearities. *International Journal for*

Numerical and Analytical Methods in Geomechanics, *25*(13), 1257–1284. https://doi.org/10.1002/nag.175

Cremer, C., Pecker, A., & Davenne, L. (2002). Modelling of Nonlinear Dynamic Behaviour of a Shallow Strip Foundation with Macro-Element. *Journal of Earthquake Engineering*, *6*(2), 175–211. https://doi.org/10.1080/13632460209350414

Cubrinovski, M., & Ishihara, K. (1998a). Modelling of Sand Behaviour Based on State Concept. *Soils and Foundations*, *38*(3), 115–127. https://doi.org/10.3208/sandf.38.3_115

Cubrinovski, M., & Ishihara, K. (1998b). State Concept and Modified Elastoplasticity for Sand Modelling. *Soils and Foundations*, *38*(4), 213–225. https://doi.org/10.3208/sandf.38.4_213

Curiel-sosa, J. L., Beg, O. A., & Murillo, J. M. L. (2013). Finite Element Analysis of Structural Instability Using an Implicit/Explicit Switching Technique. *International Journal for Computational Methods in Engineering Science and Mechanics*, *14*(5), 452–464. https://doi.org/10.1080/15502287.2013.784383

Cuthill, E., & McKee, J. (1969). Reducing the bandwidth of sparse symmetric matrices. *Proceedings of the 1969 24th National Conference*, 157–172. https://doi.org/10.1145/800195.805928

Dafalias, Y. F. (1986). Bounding Surface Plasticity. I: Mathematical Foundation and Hypoplasticity. *Journal of Engineering Mechanics*, *112*(9), 966–987. https://doi.org/10.1061/(ASCE)0733-9399(1986)112:9(966)

Dafalias, Y. F., & Manzari, M. T. (2004). Simple Plasticity Sand Model Accounting for Fabric Change Effects. *Journal of Engineering Mechanics*, *130*(6), 622–634. https://doi.org/10.1061/(asce)0733-9399(2004)130:6(622)

D'Ambrisi, A., Mariani, V., & Mezzi, M. (2012). Seismic assessment of a historical masonry tower with nonlinear static and dynamic analyses tuned on ambient vibration tests. *Engineering Structures*, *36*, 210–219. https://doi.org/10.1016/j.engstruct.2011.12.009

Darendeli, M. B. (2001). *Development of a New Family of Normalized Modulus Reduction and Material Damping Curves* [PhD Thesis]. The University of Texas at Austin.

Das, B. M. (2011). *Geotechnical Engineering Handbook*. J. Ross Publishing, Inc.

Dashti, S., Bray, J. D., Pestana, J. M., Riemer, M., & Wilson, D. (2010a). Centrifuge Testing to Evaluate and Mitigate Liquefaction-Induced Building Settlement Mechanisms. *Journal of Geotechnical and Geoenvironmental Engineering*, *136*(7), 918–929. https://doi.org/10.1061/(asce)gt.1943-5606.0000306

Dashti, S., Bray, J. D., Pestana, J. M., Riemer, M., & Wilson, D. (2010b). Mechanisms of Seismically Induced Settlement of Buildings with Shallow Foundations on

Liquefiable Soil. *Journal of Geotechnical and Geoenvironmental Engineering*, *136*(1), 151–164. https://doi.org/10.1061/(asce)gt.1943-5606.0000179

Dashti, S., & Karimi, Z. (2017). Ground Motion Intensity Measures to Evaluate I: The Liquefaction Hazard in the Vicinity of Shallow-Founded Structures. *Earthquake Spectra*, *33*(1), 241–276. https://doi.org/10.1193/103015EQS162M

Dawadi, N., Mahdi Hallal, M., & R. Cox, B. (2024). Two-dimensional Ground Response Analyses at the Delaney Park Downhole Array Site. *Japanese Geotechnical Society Special Publication*, *10*(9), 207–212. https://doi.org/10.3208/jgssp.v10.SS-3-01

di Lernia, A., D'Oria, A. F., Uva, G., & Elia, G. (2024). *ASSESSMENT OF MASONRY TOWERS SEISMIC VULNERABILITY THROUGH NON-LINEAR SSI NUMERICAL MODELLING*. 18th World Conference on Earthquake Engineering, Milan.

Di Michele, F., Cantagallo, C., & Spacone, E. (2020). Effects of the vertical seismic component on seismic performance of an unreinforced masonry structures. *Bulletin of Earthquake Engineering*, *18*(4), 1635–1656. https://doi.org/10.1007/s10518-019-00765-3

Di Michele, F., Spacone, E., Camata, G., Brando, G., Sextos, A., Crewe, A., Mylonakis, G., Diez, M., Dihoru, L., & Varum, H. (2023). Shaking table test and numerical analyses of a full scale three-leaf masonry wall. *Bulletin of Earthquake Engineering*, *21*(10), 5041–5081. https://doi.org/10.1007/s10518-023-01705-y

Di Trapani, F., Di Benedetto, M., Petracca, M., & Camata, G. (2024). Local infill-frame interaction under seismic loads: Investigation through refined micro-modeling. *Engineering Structures*, *315*, 118088. https://doi.org/10.1016/j.engstruct.2024.118088

Drysdale, R. G., Hamid, A. A., & Baker, L. R. (1994). *Masonry structures: Behavior and design*. Prentice Hall. http://books.google.com/books?id=5AFTAAAAMAAJ

Einav, I., & Cassidy, M. J. (2005). A framework for modelling rigid footing behaviour based on energy principles. *Computers and Geotechnics*, *32*(7), 491–504. https://doi.org/10.1016/j.compgeo.2005.10.003

Elgamal, A., & He, L. (2004). VERTICAL EARTHQUAKE GROUND MOTION RECORDS: AN OVERVIEW. *Journal of Earthquake Engineering*, *8*(5), 663–697. https://doi.org/10.1080/13632460409350505

Elgamal, A., Yan, L., Yang, Z., & Conte, J. P. (2008). Three-Dimensional Seismic Response of Humboldt Bay Bridge-Foundation-Ground System. *Journal of Structural Engineering*, *134*(7), 1165–1176. https://doi.org/10.1061/(asce)0733-9445(2008)134:7(1165)

Elgamal, A., Yang, Z., Parra, E., & Ragheb, A. (2003). Modeling of cyclic mobility in saturated cohesionless soils. *International Journal of Plasticity*, *19*(6), 883–905. https://doi.org/10.1016/S0749-6419(02)00010-4

EN 1997-1. (2004). *Eurocode 7: Geotechnical design—Part 1: General rules* (No. Authority: The European Union Per Regulation 305/2011, Directive 98/34/EC, Directive 2004/18/EC). https://eurocodes.jrc.ec.europa.eu/EN-Eurocodes/eurocode-7-geotechnical-design

Fajfar, P., & Gašperšič, P. (1996). The N2 Method for the Seismic Damage Analysis of Rc Buildings. *Earthquake Engineering & Structural Dynamics*, *25*(1), 31–46. https://doi.org/10.1002/(SICI)1096-9845(199601)25:1<31::AID-EQE534>3.0.CO;2-V

Felippa, C. (2000). *A Systematic Approach to the Element-Independent Corotational Dynamics of Finite Elements*.

Felippa, C. A., & Haugen, B. (2005). A unified formulation of small-strain corotational finite elements: I. Theory. *Computer Methods in Applied Mechanics and Engineering*, *194*(21-24 SPEC. ISS.), 2285–2335. https://doi.org/10.1016/j.cma.2004.07.035

Feng, Y. (2017). *Multi-Surface Material Model and Tsinghua Liquefaction Mode*. UC Davis.

Fioravante, V., & Giretti, D. (2016). Unidirectional cyclic resistance of Ticino and Toyoura sands from centrifuge cone penetration tests. *Acta Geotechnica*, *11*(4), 953–968. https://doi.org/10.1007/s11440-015-0419-3

Frederick, C. O., & Armstrong, P. J. (2007). A mathematical representation of the multiaxial Bauschinger effect. *Materials at High Temperatures*. https://www.tandfonline.com/doi/abs/10.1179/096034007X207589

Frohne, J., Heister, T., & Bangerth, W. (2016). Efficient numerical methods for the large-scale, parallel solution of elastoplastic contact problems. *International Journal for Numerical Methods in Engineering*, *105*(6), 416–439. https://doi.org/10.1002/nme.4977

Gajan, S., & Kutter, B. (2007, June 1). *A contact interface model for nonlinear cyclic moment-rotation behavior of shallow foundations*. 4th International Conference on Earthquake Geotechnical Engineering, Thessaloniki, Greece.

Gazetas, G. (2013). Can we design in geotechnics with seismic factors of safety less than 1? *Proceedings of the 15th European Conference on Soil Mechanics and Geotechnical Engineering*, 141–154. https://ebooks.iospress.nl/doi/10.3233/978-1-61499-199-1-141

Gazetas, G. (2015). 4th Ishihara lecture: Soil–foundation–structure systems beyond conventional seismic failure thresholds. *Soil Dynamics and Earthquake Engineering*, *68*, 23–39. https://doi.org/10.1016/j.soildyn.2014.09.012

Gazetas, G. (2019). *59th RANKINE Lecture London, March 2019*.

Gazetas, G., Anastasopoulos, I., Adamidis, O., & Kontoroupi, T. (2013). Nonlinear rocking stiffness of foundations. *Soil Dynamics and Earthquake Engineering*, *47*, 83–91.

Gelagoti, F., Kourkoulis, R., Anastasopoulos, I., & Gazetas, G. (2012a). Rocking isolation of low-rise frame structures founded on isolated footings. *Earthquake Engineering & Structural Dynamics*, *41*(7), 1177–1197.

Gelagoti, F., Kourkoulis, R., Anastasopoulos, I., & Gazetas, G. (2012b). Rocking-isolated frame structures: Margins of safety against toppling collapse and simplified design approach. *Soil Dynamics and Earthquake Engineering*, *32*(1), 87–102. https://doi.org/10.1016/j.soildyn.2011.08.008

Genna, F., & Pandolfi, A. (1994). Accurate numerical integration of Drucker-Prager's constitutive equations. *Meccanica*, *29*(3), 239–260. https://doi.org/10.1007/BF01461438

Gimenes, M., Rodrigues, E. A., Maedo, M. A., Bitencourt, L. A. G., & Manzoli, O. L. (2020). 2D Crack Propagation in High-Strength Concrete Using Multiscale Modeling. *Multiscale Science and Engineering*, *2*(2), 169–188. https://doi.org/10.1007/s42493-020-00049-y

Gu, Q., Conte, J. P., Elgamal, A., & Yang, Z. (2009). Finite element response sensitivity analysis of multi-yield-surface J2 plasticity model by direct differentiation method. *Computer Methods in Applied Mechanics and Engineering*, *198*(30), 2272–2285. https://doi.org/10.1016/j.cma.2009.02.030

Gu, Q., Conte, J. P., Yang, Z., & Elgamal, A. (2011). Consistent tangent moduli for multi-yield-surface J2 plasticity model. *Computational Mechanics*, *48*(1), 97–120. https://doi.org/10.1007/s00466-011-0576-7

Gu, Q., Qiu, Z., & Huang, S. (2015). A modified multi-yield-surface plasticity model: Sequential closest point projection method. *Computers and Geotechnics*, *69*, 378–395. https://doi.org/10.1016/j.compgeo.2015.05.020

Guerrini, G., Senaldi, I., Scherini, S., Morganti, S., Magenes, G., Beyer, K., & Penna, A. (2017). *Material Characterization for the Shaking-Table Test of the Scaled Prototype of a Stone Masonry Building Aggregate*. ANIDIS, Pistoia.

Guidoboni, E., Ferrari, G., Tarabusi, G., Sgattoni, G., Comastri, A., Mariotti, D., Ciuccarelli, C., Bianchi, M. G., & Valensise, G. (2019). CFTI5Med, the new release of the catalogue of strong earthquakes in Italy and in the Mediterranean area. *Scientific Data*, *6*(1), 80. https://doi.org/10.1038/s41597-019-0091-9

Guo, N., & Zhao, J. (2016). Parallel hierarchical multiscale modelling of hydro-mechanical problems for saturated granular soils. *Computer Methods in Applied Mechanics and Engineering*, *305*, 37–61. https://doi.org/10.1016/j.cma.2016.03.004

Gutierrez, J. A., & Chopra, A. K. (1978). A substructure method for earthquake analysis of structures including structure-soil interaction. *Earthquake Engineering & Structural Dynamics*, *6*(1), 51–69. https://doi.org/10.1002/eqe.4290060107

Hallal, M. M., & Cox, B. R. (2023). What Spatial Area Influences Seismic Site Response: Insights Gained from Multiazimuthal 2D Ground Response Analyses at the Treasure Island Downhole Array. *Journal of Geotechnical and Geoenvironmental Engineering*, *149*(1), 04022124. https://doi.org/10.1061/JGGEFK.GTENG-11023

Han, D. J., & Chen, W. F. (1986). Strain-space plasticity formulation for hardening-softening materials with elastoplastic coupling. *International Journal of Solids and Structures*, *22*(8), 935–950. https://doi.org/10.1016/0020-7683(86)90072-7

Harrington, C. C., & Liel, A. B. (2016). Collapse assessment of moment frame buildings, considering vertical ground shaking. *Earthquake Engineering & Structural Dynamics*, *45*(15), 2475–2493. https://doi.org/10.1002/eqe.2776

Helnwein, P. (2001). Some remarks on the compressed matrix representation of symmetric second-order and fourth-order tensors. *Computer Methods in Applied Mechanics and Engineering*, *190*(22), 2753–2770. https://doi.org/10.1016/S0045-7825(00)00263-2

Hendry, A. W. (1990). *Structural Masonry*. Macmillan.

Herle, I., & Gudehus, G. (1999). Determination of parameters of a hypoplastic constitutive model from properties of grain assemblies. *Mechanics of Cohesive-Frictional Materials*, *4*(5), 461–486. https://doi.org/10.1002/(SICI)1099-1484(199909)4:5<461::AID-CFM71>3.0.CO;2-P

Housner, G. W. (1957). Interaction of building and ground during an earthquake. *Bulletin of the Seismological Society of America*, *47*(3), 179–186. https://doi.org/10.1785/BSSA0470030179

Huang, S., Ozcelik, O., & Gu, Q. (2015). A practical and efficient coupling method for large scale soil–structure interaction problems. *Soil Dynamics and Earthquake Engineering*, *76*, 44–57. https://doi.org/10.1016/j.soildyn.2014.12.014

Hughes, T. J. R., Pister, K. S., & Taylor, R. L. (1979). Implicit-explicit finite elements in nonlinear transient analysis. *Computer Methods in Applied Mechanics and Engineering*, *17–18*, 159–182. https://doi.org/10.1016/0045-7825(79)90086-0

Jacob, B. P., & Ebecken, N. F. F. (1994). Towards an adaptive 'semi-implicit' solution scheme for nonlinear structural dynamic problems. *Computers & Structures*, *52*(3), 495–504. https://doi.org/10.1016/0045-7949(94)90235-6

Jefferies, M., & Been, K. (2015). *Soil Liquefaction: A Critical State Approach, Second Edition* (2nd ed.). CRC Press. https://doi.org/10.1201/b19114

Jefferies, M. G. (1993). Nor-Sand: A simle critical state model for sand. *Géotechnique*, *43*(1), 91–103. https://doi.org/10.1680/geot.1993.43.1.91

Jefferies, M., Shuttle, D., & Been, K. (2015). Principal stress rotation as cause of cyclic mobility. *Geotechnical Research*, *2*(2), 66–96. https://doi.org/10.1680/jgere.15.00002

Jeremić, B., & Sture, S. (1997). Implicit integrations in elastoplastic geotechnics. *Mechanics of Cohesive-Frictional Materials*, *2*(2), 165–183. https://doi.org/10.1002/(SICI)1099-1484(199704)2:2<165::AID-CFM31>3.0.CO;2-3

Jirásek, M. (2007). Mathematical analysis of strain localization. *Revue Européenne de Génie Civil*, *11*(7–8), 977–991. https://doi.org/10.1080/17747120.2007.9692973

Jung, D. W., & Yang, D. Y. (1998). Step-wise combined implicit–explicit finite-element simulation of autobody stamping processes. *Journal of Materials Processing Technology*, *83*(1), 245–260. https://doi.org/10.1016/S0924-0136(98)00059-4

Kalkbrenner, P. (2021). *A Machine Learning based Material Homogenization Technique for Masonry Structures*. Universitat Politecnica de Catalunya.

Kallioras, S., Graziotti, F., Penna, A., & Magenes, G. (2022). Effects of vertical ground motions on the dynamic response of URM structures: Comparative shake-table tests. *Earthquake Engineering & Structural Dynamics*, *51*(2), 347–368. https://doi.org/10.1002/eqe.3569

Kanellopoulos, C., Rangelow, P., Jeremic, B., Anastasopoulos, I., & Stojadinovic, B. (2023). *Dynamic Structure-Soil-Structure-Interaction for Nuclear Power Plants* (No. arXiv:2310.10251). arXiv. https://doi.org/10.48550/arXiv.2310.10251

Karimi, Z., & Dashti, S. (2017). Ground Motion Intensity Measures to Evaluate II: the Performance of Shallow-Founded Structures on Liquefiable Ground. *Earthquake Spectra*, *33*(1), 277–298. https://doi.org/10.1193/103015EQS163M

Kastelic, V., Vannoli, P., Burrato, P., Fracassi, U., Tiberti, M. M., & Valensise, G. (2013). Seismogenic sources in the Adriatic Domain. *Marine and Petroleum Geology*, *42*, 191–213. https://doi.org/10.1016/j.marpetgeo.2012.08.002

Kausel, E. (2006). *Fundamental Solutions in Elastodynamics: A Compendium*. Cambridge University Press.

Kausel, E. (2010). Early history of soil–structure interaction. *Soil Dynamics and Earthquake Engineering*, *30*(9), 822–832. https://doi.org/10.1016/j.soildyn.2009.11.001

Kausel, E., Whitman, R. V., Morray, J. P., & Elsabee, F. (1978). The spring method for embedded foundations. *Nuclear Engineering and Design*, *48*(2), 377–392. https://doi.org/10.1016/0029-5493(78)90085-7

Kohrangi, M., Bazzurro, P., & Vamvatsikos, D. (2016). Vector and Scalar IMs in Structural Response Estimation, Part I: Hazard Analysis. *Earthquake Spectra*, *32*(3), 1507–1524. https://doi.org/10.1193/053115EQS080M

Kohrangi, M., Bazzurro, P., Vamvatsikos, D., & Spillatura, A. (2017). Conditional spectrum-based ground motion record selection using average spectral acceleration. *Earthquake Engineering & Structural Dynamics*, *46*(10), 1667–1685. https://doi.org/10.1002/eqe.2876

Kohrangi, M., Vamvatsikos, D., & Bazzurro, P. (2017). Site dependence and record selection schemes for building fragility and regional loss assessment. *Earthquake Engineering & Structural Dynamics*, *46*(10), 1625–1643. https://doi.org/10.1002/eqe.2873

Kondner, R. L. (1963). Hyperbolic Stress-Strain Response: Cohesive Soils. *Journal of the Soil Mechanics and Foundations Division*, *89*(1), 115–143. https://doi.org/10.1061/JSFEAQ.0000479

Kottke, A. R., & Rathje, E. M. (2008). *Technical Manual for Strata* (No. 2008/10). Pacific Earthquake Engineering Research Center, University of California, Berkeley.

Kramer, S. L. (1996). *Geotechnical Earthquake Engineering* (1st edition). Pearson College Div.

Kunar, R. R. (1982). A mixed implicit/explicit procedure for soil-structure interaction. *Nuclear Engineering and Design*, *69*(1), 87–93. https://doi.org/10.1016/0029-5493(82)90283-7

Kwong, N. S., & Chopra, A. K. (2016). Evaluation of the exact conditional spectrum and generalized conditional intensity measure methods for ground motion selection. *Earthquake Engineering & Structural Dynamics*, *45*(5), 757–777. https://doi.org/10.1002/eqe.2683

Lai, C. G., & Martinelli, M. (2013). Soil-Structure Interaction Under Earthquake Loading: Theoretical Framework. In *ALERT Doctoral School 2013 Soil-Structure Interaction* (pp. 3–43). The Alliance of Laboratories in Europe for Research and Technology.

Leong, E. C., & Randolph, M. F. (1992). A model for rock interfacial behaviour. *Rock Mechanics and Rock Engineering*, *25*(3), 187–206. https://doi.org/10.1007/BF01019711

Li, L., Lai, N., Zhao, X., Zhu, T., & Su, Z. (2023). A generalized elastoplastic load-transfer model for axially loaded piles in clay: Incorporation of modulus degradation and skin friction softening. *Computers and Geotechnics*, *161*, 105594. https://doi.org/10.1016/j.compgeo.2023.105594

Lin, T., Harmsen, S. C., Baker, J. W., & Luco, N. (2013). Conditional Spectrum Computation Incorporating Multiple Causal Earthquakes and Ground-Motion Prediction Models. *Bulletin of the Seismological Society of America*, *103*(2A), 1103–1116. https://doi.org/10.1785/0120110293

Liu, W. K., & Belytschko, T. (1982). Mixed-time implicit-explicit finite elements for transient analysis. *Computers & Structures*, *15*(4), 445–450. https://doi.org/10.1016/0045-7949(82)90079-7

Loli, M., Gazetas, G., Knappett, J. A., & Anastasopoulos, I. (2016). Use of micro-pile inclusions to enhance foundation rocking isolation. *Proceedings of the 1st International Conference on Natural Hazards and Infrastructure: Protection, Design, Rehabilitation (ICONHIC 2016), Chania, Greece*. https://www.researchgate.net/profile/Marianna-Loli/publication/334794342_Use_of_Micro-Pile_Inclusions_to_Enhance_Foundation_Rocking_Isolation/links/5d418ce992851cd04695b9ce/Use-of-Micro-Pile-Inclusions-to-Enhance-Foundation-Rocking-Isolation.pdf

Lourenco, P. (1995). *AN ORTHOTROPIC CONTINUUM MODEL FOR THE ANALYSIS OF MASONRY STRUCTURES*. https://doi.org/10.13140/RG.2.2.24379.02081

Lourenco, P. (1998). Experimental and numerical issues in the modelling of the mechanical behaviour of masonry. *Structural Analysis of Historical Constructions II*.

Lourenço, P. B. (1996). *Computational strategies for masonry structures* [PhD Thesis, Delft University of Technology]. https://repository.tudelft.nl/record/uuid:4f5a2c6c-d5b7-4043-9d06-8c0b7b9f1f6f

Lourénço, P. B., De Borst, R., & Rots, J. G. (1997). A plane stress softening plasticity model for orthotropic materials. *International Journal for Numerical Methods in Engineering*, *40*(21), 4033–4057. https://doi.org/10.1002/(SICI)1097-0207(19971115)40:21<4033::AID-NME248>3.0.CO;2-0

Lourenço, P. B., & Rots, J. G. (1997). Multisurface Interface Model for Analysis of Masonry Structures. *Journal of Engineering Mechanics*, *123*(7), 660–668. https://doi.org/10.1061/(ASCE)0733-9399(1997)123:7(660)

Love, E. (2018). *Standard Brick Element—OpenSeesWiki* [Computer software]. https://opensees.berkeley.edu/wiki/index.php/Standard_Brick_Element

Lu, J., Elgamal, A., Law, K. H., & Yang, Z. (2012). *Parallel Computing for Seismic Geotechnical Applications*. 1–6. https://doi.org/10.1061/40803(187)182

Lubliner, J., Oliver, J., Oller, S., & Onate, E. (1989). A Plastic-Damage Model. *International Journal of Solids and Structures*, *25*(3), 299–326. https://doi.org/10.1016/0020-7683(89)90050-4

Luco, N., & Cornell, C. A. (2007). Structure-Specific Scalar Intensity Measures for Near-Source and Ordinary Earthquake Ground Motions. *Earthquake Spectra*, *23*(2), 357–392. https://doi.org/10.1193/1.2723158

Luzi, L., Lanzano, G., Felicetta, C., D'Amico, M. C., Russo, E., Sgobba, S., Pacor, F., & ORFEUS Working Group 5. (2020). *Engineering Strong Motion Database (ESM), version 2.0* (Version 2.0) [Text/html,application/json,image/jpeg,application/vnd.fdsn.mseed,text/plain,application/zip,text/plain,text/xml,application/xml]. Istituto Nazionale di Geofisica e Vulcanologia (INGV). https://doi.org/10.13127/ESM.2

Lv, H., & Chen, S. (2022). Analysis of nonlinear soil-structure interaction using partitioned method. *Soil Dynamics and Earthquake Engineering*, *162*, 107470. https://doi.org/10.1016/j.soildyn.2022.107470

Lysmer, J., & Kuhlemeyer, R. L. (1969). Finite Dynamic Model for Infinite Media. *Journal of the Engineering Mechanics Division*, *95*(4), 859–877. https://doi.org/10.1061/JMCEA3.0001144

Macedo, J., & Bray, J. D. (2018). Key Trends in Liquefaction-Induced Building Settlement. *Journal of Geotechnical and Geoenvironmental Engineering*, *144*(11), 04018076. https://doi.org/10.1061/(ASCE)GT.1943-5606.0001951

Maedo, M. A., Sánchez, M., Fabbri, H., Cleto, P., Guimarães, L. J. N., & Manzoli, O. L. (2021). Coupled Thermo-Hydro-Mechanical Numerical Modeling of Evolving Fractures in Rocks. *Rock Mechanics and Rock Engineering*, *54*(7), 3569–3591. https://doi.org/10.1007/s00603-021-02387-1

Magenes, G., Penna, A., Galasco, A., & Rota, M. (2010). *Experimental Characterisation of Stone Masonry Mechanical Properties*. 8th International Masonry Conference, Dresden.

Manzari, M. T., & Dafalias, Y. F. (1997). A critical state two-surface plasticity model for sands. *Géotechnique*, *47*(2), 255–272. https://doi.org/10.1680/geot.1997.47.2.255

Mašín, D. (2013). *GEO-SLOPE SIGMA/W implementation of hypoplasticity*.

McGann, C. R., & Arduino, P. (2011). *Site Response Analysis of a Layered Soil Column (Total Stress Analysis)—OpenSeesWiki* [OpenSees Examples Manual]. https://opensees.berkeley.edu/wiki/index.php?title=Site_Response_Analysis_of_a_Layered_Soil_Column_(Total_Stress_Analysis)

Mckenna, F., & Fenves, G. L. (2007). *TN-2007-16 Using the OpenSees Interpreter on Parallel Computers*. 1–15.

McKenna, F. T. (1997). *Object-oriented finite element programming: Frameworks for Analysis, Algorithms and Parallel Computing*. University of California, Berkeley.

Mercatoris, B. C. N., Bouillard, Ph., & Massart, T. J. (2009). Multi-scale detection of failure in planar masonry thin shells using computational homogenisation. *Engineering Fracture Mechanics*, *76*(4), 479–499. https://doi.org/10.1016/j.engfracmech.2008.10.003

Mercatoris, B. C. N., & Massart, T. J. (2011). A coupled two-scale computational scheme for the failure of periodic quasi-brittle thin planar shells and its application to masonry. *International Journal for Numerical Methods in Engineering*, *85*(9), 1177–1206. https://doi.org/10.1002/nme.3018

Merritt, R. G., & Housner, G. W. (1954). Effect of foundation compliance on earthquake stresses in multistory buildings*. *Bulletin of the Seismological Society of America*, *44*(4), 551–569. https://doi.org/10.1785/BSSA0440040551

Milosevic, J., Lopes, M., Gago, A. S., & Bento, R. (2013). Testing and modeling the diagonal tension strength of rubble stone masonry panels. *Engineering Structures*, *52*, 581–591. https://doi.org/10.1016/j.engstruct.2013.03.019

Mohammadi, K., M. Hallal, M., Roshankhah, S., & R. Cox, B. (2024). One- and Two-Dimensional Ground Response Analyses: What They Do/Don't Tell about the Site. *Japanese Geotechnical Society Special Publication*, *10*(9), 213–219. https://doi.org/10.3208/jgssp.v10.SS-3-02

Monforte, L., Ciantia, M. O., Carbonell, J. M., Arroyo, M., & Gens, A. (2019). A stable mesh-independent approach for numerical modelling of structured soils at large strains. *Computers and Geotechnics*, *116*, 103215. https://doi.org/10.1016/j.compgeo.2019.103215

Motamedi, M. H., & Foster, C. D. (2015). An improved implicit numerical integration of a non-associated, three-invariant cap plasticity model with mixed isotropic–kinematic hardening for geomaterials. *International Journal for Numerical and Analytical Methods in Geomechanics*, *39*(17), 1853–1883. https://doi.org/10.1002/nag.2372

Mróz, Z. (1967). On the description of anisotropic workhardening. *Journal of the Mechanics and Physics of Solids*, *15*(3), 163–175. https://doi.org/10.1016/0022-5096(67)90030-0

Mróz, Z., & Pietruszczak, St. (1983). A constitutive model for sand with anisotropic hardening rule. *International Journal for Numerical and Analytical Methods in Geomechanics*, *7*(3), 305–320. https://doi.org/10.1002/nag.1610070304

Muthukumar, S., & DesRoches, R. (2006). A Hertz contact model with non-linear damping for pounding simulation. *Earthquake Engineering & Structural Dynamics*, *35*(7), 811–828. https://doi.org/10.1002/eqe.557

Mylonakis, G., & Gazetas, G. (2000). Seismic Soil-Structure Interaction: Beneficial or Detrimental? *Journal of Earthquake Engineering*, *4*(3), 277–301. https://doi.org/10.1080/13632460009350372

Mylonakis, G., Nikolaou, S., & Gazetas, G. (2006). Footings under seismic loading: Analysis and design issues with emphasis on bridge foundations. *Soil Dynamics and*

Earthquake Engineering, *26*(9), 824–853. https://doi.org/10.1016/j.soildyn.2005.12.005

Nie, J.-Y., Zhao, J., Cui, Y.-F., & Li, D.-Q. (2021). Correlation between grain shape and critical state characteristics of uniformly graded sands: A 3D DEM study. *Acta Geotechnica*. https://doi.org/10.1007/s11440-021-01362-y

Nielsen, A. H. (2006). Absorbing Boundary Conditions for Seismic Analysis in ABAQUS. *ABAQUS Users' Conference*, 359–376.

Niemunis, A., & Herle, I. (1997). Hypoplastic model for cohesionless soils with elastic strain range. *Mechanics of Cohesive-Frictional Materials*, *2*(4), 279–299. https://doi.org/10.1002/(SICI)1099-1484(199710)2:4<279::AID-CFM29>3.0.CO;2-8

Noels, L., Stainier, L., & Ponthot, J.-P. (2004). Combined implicit/explicit time-integration algorithms for the numerical simulation of sheet metal forming. *Journal of Computational and Applied Mathematics*, *168*(1), 331–339. https://doi.org/10.1016/j.cam.2003.12.004

Oktiovan, Y. P., Davis, L., Wilson, R., Dell'Endice, A., Mehrotra, A., Pulatsu, B., & Malomo, D. (2023). Simplified Micro-Modeling of a Masonry Cross-Vault for Seismic Assessment Using the Distinct Element Method. *International Journal of Architectural Heritage*, 1–34. https://doi.org/10.1080/15583058.2023.2277328

Oliver, J., Caicedo-Silva, M., Roubin, E., & Hernández, J. (2014). Multi-scale (FE2) analysis of material failure in cement/aggregate-type composite structures. In *Computational Modelling of Concrete Structures—Proceedings of EURO-C 2014* (Vol. 1). https://doi.org/10.1201/b16645-6

Oliver, J., Huespe, A. E., & Cante, J. C. (2008). An implicit/explicit integration scheme to increase computability of non-linear material and contact/friction problems. *Computer Methods in Applied Mechanics and Engineering*, *197*(21–24), 1865–1889. https://doi.org/10.1016/j.cma.2007.11.027

Oliynyk, K., Ciantia, M. O., & Tamagnini, C. (2021). A finite deformation multiplicative plasticity model with non–local hardening for bonded geomaterials. *Computers and Geotechnics*, *137*, 104209. https://doi.org/10.1016/j.compgeo.2021.104209

Oller, S., Car, E., & Lubliner, J. (2003). Definition of a general implicit orthotropic yield criterion. *Computer Methods in Applied Mechanics and Engineering*, *192*(7–8), 895–912. https://doi.org/10.1016/S0045-7825(02)00605-9

Otero, F., Oller, S., & Martinez, X. (2018). Multiscale Computational Homogenization: Review and Proposal of a New Enhanced-First-Order Method. *Archives of Computational Methods in Engineering*, *25*(2), 479–505. https://doi.org/10.1007/s11831-016-9205-0

Özcebe, A. G., Giretti, D., Bozzoni, F., Fioravante, V., & Lai, C. G. (2021). Centrifuge and numerical modelling of earthquake-induced soil liquefaction under free-field conditions and by considering soil–structure interaction. *Bulletin of Earthquake Engineering*, *19*(1), 47–75. https://doi.org/10.1007/s10518-020-00972-3

Ozer, E., Özcebe, A. G., Negulescu, C., Kharazian, A., Borzi, B., Bozzoni, F., Molina, S., Peloso, S., & Tubaldi, E. (2022). Vibration-Based and Near Real-Time Seismic Damage Assessment Adaptive to Building Knowledge Level. *Buildings*, *12*(4), Article 4. https://doi.org/10.3390/buildings12040416

Ozsarac, V., Monteiro, R., & Calvi, G. M. (2023). Probabilistic seismic assessment of reinforced concrete bridges using simulated records. *Structure and Infrastructure Engineering*, *19*(4), 554–574. https://doi.org/10.1080/15732479.2021.1956551

Pagani, M., Monelli, D., Weatherill, G., Danciu, L., Crowley, H., Silva, V., Henshaw, P., Butler, L., Nastasi, M., Panzeri, L., Simionato, M., & Vigano, D. (2014). OpenQuake Engine: An Open Hazard (and Risk) Software for the Global Earthquake Model. *Seismological Research Letters*, *85*(3), 692–702. https://doi.org/10.1785/0220130087

Paolucci, R. (1997). Simplified Evaluation of Earthquake-Induced Permanent Displacements of Shallow Foundations. *Journal of Earthquake Engineering*, *1*(3), 563–579. https://doi.org/10.1080/13632469708962378

Papazoglou, A. J., & Elnashai, A. S. (1996). Analytical and Field Evidence of the Damaging Effect of Vertical Earthquake Ground Motion. *Earthquake Engineering & Structural Dynamics*, *25*(10), 1109–1137. https://doi.org/10.1002/(SICI)1096-9845(199610)25:10<1109::AID-EQE604>3.0.CO;2-0

Pelà, L., Cervera, M., & Roca, P. (2011). Continuum damage model for orthotropic materials: Application to masonry. *Computer Methods in Applied Mechanics and Engineering*, *200*(9), 917–930. https://doi.org/10.1016/j.cma.2010.11.010

Pelà, L., Cervera, M., & Roca, P. (2013). An orthotropic damage model for the analysis of masonry structures. *Construction and Building Materials*, *41*, 957–967. https://doi.org/10.1016/j.conbuildmat.2012.07.014

Peña, F., Lourenço, P. B., Mendes, N., & Oliveira, D. V. (2010). Numerical models for the seismic assessment of an old masonry tower. *Engineering Structures*, *32*(5), 1466–1478. https://doi.org/10.1016/j.engstruct.2010.01.027

Penna, A., Senaldi, I. E., Galasco, A., & Magenes, G. (2016). Numerical Simulation of Shaking Table Tests on Full-Scale Stone Masonry Buildings. *International Journal of Architectural Heritage*, *10*(2–3), 146–163. https://doi.org/10.1080/15583058.2015.1113338

Pérez-Foguet, A., & Armero, F. (2002). On the formulation of closest-point projection algorithms in elastoplasticity—part II: Globally convergent schemes. *International Journal for Numerical Methods in Engineering*, *53*(2), 331–374. https://doi.org/10.1002/nme.279

Petracca, M. (2015). *Computational Multiscale Analysis of Masonry Structures*.

Petracca, M. (2021). *3.1.10.14. ASDShellQ4 Element—OpenSees Documentation documentation* [Computer software]. https://opensees.github.io/OpenSeesDocumentation/user/manual/model/elements/ASDShellQ4.html

Petracca, M. (2022). *3.1.9.23. ASDEmbeddedNode Element—OpenSees Documentation* [C++]. https://opensees.github.io/OpenSeesDocumentation/user/manual/model/elements/ASDEmbeddedNodeElement.html

Petracca, M., Bottini, M., Sallese, L., Marano, C., Di, F., & Camata, G. (2019). Interazione suolo struttura applicato all ' analisi di un ponte autostradale. *Convegno Anidis XVIII*.

Petracca, M., Camata, G., Spacone, E., & Pelà, L. (2022). Efficient Constitutive Model for Continuous Micro-Modeling of Masonry Structures. *International Journal of Architectural Heritage*, *0*(0), 1–13. https://doi.org/10.1080/15583058.2022.2124133

Petracca, M., Marano, C., Camata, G., & Pelà, L. (2021). *Advanced tools for fast micro-modelling of masonry structures*. 1–10. https://upcommons.upc.edu/handle/2117/341795

Petracca, M., Pelà, L., Rossi, R., Oller, S., Camata, G., & Spacone, E. (2016). Regularization of first order computational homogenization for multiscale analysis of masonry structures. *Computational Mechanics*, *57*(2), 257–276. https://doi.org/10.1007/s00466-015-1230-6

Petracca, M., Pelà, L., Rossi, R., Zaghi, S., Camata, G., & Spacone, E. (2017). Micro-scale continuous and discrete numerical models for nonlinear analysis of masonry shear walls. *Construction and Building Materials*, *149*, 296–314. https://doi.org/10.1016/j.conbuildmat.2017.05.130

Petry, S., & Beyer, K. (2015). Cyclic Test Data of Six Unreinforced Masonry Walls with Different Boundary Conditions. *Earthquake Spectra*, *31*(4), 2459–2484. https://doi.org/10.1193/101513EQS269

Plesha, M. E., & Belytschko, T. (1985). A constitutive operator splitting method for nonlinear transient analysis. *Computers & Structures*, *20*(4), 767–777. https://doi.org/10.1016/0045-7949(85)90038-0

Potts, D. M., & Zdravkovic, L. (1999). *Finite Element Analysis in Geotechnical Engineering: Theory*. Thomas Telford.

Poulos, A., & Miranda, E. (2022). Proposal of orientation-independent measure of intensity for earthquake-resistant design. *Earthquake Spectra*, *38*(1), 235–253. https://doi.org/10.1177/87552930211038240

Poulos, H. G., & Davis, E. H. (1974). *Elastic Solutions for Soil and Rock Mechanics*. John Wiley & Sons Inc.

Prevost, J. H. (1982). Nonlinear Transient Phenomena in Elastic-Plastic Solids. *Journal of the Engineering Mechanics Division*, *108*(6), 1297–1311. https://doi.org/10.1061/JMCEA3.0002905

Prevost, J. H. (1989). *DYNA1D: A computer program for nonlinear seismic site response analysis—Technical documentation* (No. NCEER-89-0025). Princeton University.

Prévost, J.-H. (1977). Mathematical modelling of monotonic and cyclic undrained clay behaviour. *International Journal for Numerical and Analytical Methods in Geomechanics*, *1*(2), 195–216. https://doi.org/10.1002/nag.1610010206

Qiu, Z., & Elgamal, A. (2020). Three-Dimensional Modeling of Strain-Softening Soil Response for Seismic-Loading Applications. *Journal of Geotechnical and Geoenvironmental Engineering*, *146*(7), 04020053. https://doi.org/10.1061/(ASCE)GT.1943-5606.0002282

Qiu, Z., Prabhakaran, A., Zhou, Y.-G., & Elgamal, A. (2023). A practical three-dimensional plasticity model for cyclic degradation of soil in earthquake loading applications. *Earthquake Engineering & Structural Dynamics*, *52*(12), 3835–3852. https://doi.org/10.1002/eqe.3951

Regione Abruzzo. (2015, May 15). *Modello digitale del terreno—Risoluzione 10x10 metri*. http://opendata.regione.abruzzo.it/content/modello-digitale-del-terreno-risoluzione-10x10-metri

Regueiro, R. A., & Borja, R. I. (1999). A finite element model of localized deformation in frictional materials taking a strong discontinuity approach. *Finite Elements in Analysis and Design*, *33*(4), 283–315. https://doi.org/10.1016/S0168-874X(99)00050-5

Restrepo Vélez, L. F., Magenes, G., & Griffith, M. C. (2014). Dry Stone Masonry Walls in Bending—Part I: Static Tests. *International Journal of Architectural Heritage*, *8*(1), 1–28. https://doi.org/10.1080/15583058.2012.663059

Roca, P., Cervera, M., Gariup, G., & Pela', L. (2010). Structural Analysis of Masonry Historical Constructions. Classical and Advanced Approaches. *Archives of Computational Methods in Engineering*, *17*(3), 299–325. https://doi.org/10.1007/s11831-010-9046-1

Rodrigues, E. A., Manzoli, O. L., & Bitencourt, L. A. G. (2020). 3D concurrent multiscale model for crack propagation in concrete. *Computer Methods in Applied Mechanics and Engineering*, *361*, 112813. https://doi.org/10.1016/j.cma.2019.112813

Roscoe, K. H. (1970). The Influence of Strains in Soil Mechanics. *Géotechnique*, *20*(2), 129–170. https://doi.org/10.1680/geot.1970.20.2.129

Rosell, L. A. (2010). *Explicit / Implicit Nonlinear Soil Structure Interaction Study of the Bell Tower of Santa Maria Maggiore , Guardiagrele*. Istituto Universitario di Studi Superiori di Pavia.

Rouainia, M., & Muir Wood, D. (2001). Implicit numerical integration for a kinematic hardening soil plasticity model. *International Journal for Numerical and Analytical Methods in Geomechanics*, *25*(13), 1305–1325. https://doi.org/10.1002/nag.179

Sacco, E., & Lebon, F. (2012). A damage–friction interface model derived from micromechanical approach. *International Journal of Solids and Structures*, *49*(26), 3666–3680. https://doi.org/10.1016/j.ijsolstr.2012.07.028

Salvatori, L., Marra, A. M., Bartoli, G., & Spinelli, P. (2015). Probabilistic seismic performance of masonry towers: General procedure and a simplified implementation. *Engineering Structures*, *94*, 82–95. https://doi.org/10.1016/j.engstruct.2015.02.017

Sandia, N. L. (2023). *The Cubit® Geometry and Mesh Generation Toolkit* (Version 16.14) [Computer software]. Sandia National Laboratories. https://cubit.sandia.gov/

Saqib, M., Das, A., & Patra, N. R. (2023). Numerical modeling of pile embedded in crushable sand subjected to earthquake loading. *Acta Geotechnica*. https://doi.org/10.1007/s11440-023-02153-3

Schellekens, J. C. J., & De Borst, R. (1993). On the numerical integration of interface elements. *International Journal for Numerical Methods in Engineering*, *36*(1), 43–66. https://doi.org/10.1002/nme.1620360104

Schofield, A. N., & Wroth, P. (1968). *Critical State Soil Mechanics*. McGraw-Hill.

Schröder, J., & Hackl, K. (Eds.). (2014). *Plasticity and Beyond: Microstructures, Crystal-Plasticity and Phase Transitions* (Vol. 550). Springer. https://doi.org/10.1007/978-3-7091-1625-8

Seifert, T., & Schmidt, I. (2008). Line-search methods in general return mapping algorithms with application to porous plasticity. *International Journal for Numerical Methods in Engineering*, *73*(10), 1468–1495. https://doi.org/10.1002/nme.2131

Senaldi, I., Guerrini, G., Scherini, S., Morganti, S., Magenes, G., Beyer, K., & Penna, A. (2018). *NATURAL STONE MASONRY CHARACTERIZATION FOR THE SHAKING-TABLE TEST OF A SCALED BUILDING SPECIMEN*. 10th International Masonry Conference, Milan.

Senaldi, I., Magenes, G., Penna, A., Galasco, A., & Rota, M. (2014). The Effect of Stiffened Floor and Roof Diaphragms on the Experimental Seismic Response of a Full-Scale Unreinforced Stone Masonry Building. *Journal of Earthquake Engineering*, *18*(3), 407–443. https://doi.org/10.1080/13632469.2013.876946

Sezawa, K., & Kanai, K. (1935). Decay in the Seismic Vibrations of a Structure by Dissipation of their Energy into the Ground. *Proceedings of the Imperial Academy*, *11*(5), 174–176. https://doi.org/10.2183/pjab1912.11.174

Simo, J. C., & Hughes, T. J. R. (1998). *Computational Inelasticity* (Vol. 7). Springer-Verlag. https://doi.org/10.1007/b98904

Simo, J. C., & Taylor, R. L. (1985). Consistent tangent operators for rate-independent elastoplasticity. *Computer Methods in Applied Mechanics and Engineering*, *48*(1), 101–118. https://doi.org/10.1016/0045-7825(85)90070-2

Simpson, B. G., Zhu, M., Seki, A., & Scott, M. (2023). Challenges in GPU-Accelerated Nonlinear Dynamic Analysis for Structural Systems. *Journal of Structural Engineering*, *149*(3), 04022253. https://doi.org/10.1061/JSENDH.STENG-11311

Su, L., Wan, H.-P., Bi, K., Li, Y., Lu, J., Ling, X.-Z., Elgamal, A., & Arulmoli, A. K. (2019). Seismic fragility analysis of pile-supported wharves with the influence of soil permeability. *Soil Dynamics and Earthquake Engineering*, *122*, 211–227. https://doi.org/10.1016/j.soildyn.2019.04.003

Taborda, D. M. G., Zdravković, L., Kontoe, S., & Potts, D. M. (2014). Computational study on the modification of a bounding surface plasticity model for sands. *Computers and Geotechnics*, *59*, 145–160. https://doi.org/10.1016/j.compgeo.2014.03.005

Tabucanon, J., Airey, D., & Poulos, H. (1995). Pile Skin Friction in Sands from Constant Normal Stiffness Tests. *Geotechnical Testing Journal*, *18*(3), 350–364. https://doi.org/10.1520/GTJ11004J

Taciroglu, E., Rha, C., & Wallace, J. W. (2006). A Robust Macroelement Model for Soil–Pile Interaction under Cyclic Loads. *Journal of Geotechnical and Geoenvironmental Engineering*, *132*(10), 1304–1314. https://doi.org/10.1061/(ASCE)1090-0241(2006)132:10(1304)

Tamagnini, C., Castellanza, R., & Nova, R. (2002). Implicit integration of constitutive equations in computational plasticity. *Revue Française de Génie Civil*, *6*(6), 1051–1067. https://doi.org/10.1080/12795119.2002.9692731

Tian, Y., Xie, L., Xu, Z., & Lu, X. (2015). *GPU-Powered High-Performance Computing for the Analysis of Large-Scale Structures Based on OpenSees*. 411–418. https://doi.org/10.1061/9780784479247.051

Tomić, I., & Beyer, K. (2023). Shake-table test on a historical masonry aggregate: Prediction and postdiction using an equivalent-frame model. *Bulletin of Earthquake Engineering*. https://doi.org/10.1007/s10518-023-01765-0

Tomić, I., Penna, A., DeJong, M., Butenweg, C., Correia, A. A., Candeias, P. X., Senaldi, I., Guerrini, G., Malomo, D., & Beyer, K. (2023). Shake table testing of a half-scale stone masonry building aggregate. *Bulletin of Earthquake Engineering*. https://doi.org/10.1007/s10518-023-01810-y

Tu, X., Andrade, J. E., & Chen, Q. (2009). Return mapping for nonsmooth and multiscale elastoplasticity. *Computer Methods in Applied Mechanics and Engineering*, *198*(30), 2286–2296. https://doi.org/10.1016/j.cma.2009.02.014

Uranjek, M., Bosiljkov, V., Žarnić, R., & Bokan-Bosiljkov, V. (2012). In situ tests and seismic assessment of a stone-masonry building. *Materials and Structures*, *45*(6), 861–879. https://doi.org/10.1617/s11527-011-9804-z

Vaculik, J., Griffith, M. C., & Magenes, G. (2014). Dry Stone Masonry Walls in Bending—Part II: Analysis. *International Journal of Architectural Heritage*, *8*(1), 29–48. https://doi.org/10.1080/15583058.2012.663060

Valente, M., & Milani, G. (2016). Non-linear dynamic and static analyses on eight historical masonry towers in the North-East of Italy. *Engineering Structures*, *114*, 241–270. https://doi.org/10.1016/j.engstruct.2016.02.004

Vardoulakis, I. (2019). *Cosserat Continuum Mechanics: With Applications to Granular Media* (Vol. 87). Springer International Publishing. https://doi.org/10.1007/978-3-319-95156-0

Vasconcelos, G., & Lourenço, P. B. (2009). In-Plane Experimental Behavior of Stone Masonry Walls under Cyclic Loading. *Journal of Structural Engineering*, *135*(10), 1269–1277. https://doi.org/10.1061/(ASCE)ST.1943-541X.0000053

Veletsos, A. S., & Nair, V. V. D. (1975). Seismic Interaction of Structures on Hysteretic Foundations. *Journal of the Structural Division*, *101*(1), 109–129. https://doi.org/10.1061/JSDEAG.0003962

Veletsos, A. S., & Wei, Y. T. (1971). Lateral and Rocking Vibration of Footings. *Journal of the Soil Mechanics and Foundations Division*, *97*(9), 1227–1248. https://doi.org/10.1061/JSFEAQ.0001661

von Wolffersdorff, P.-A. (1996). A hypoplastic relation for granular materials with a predefined limit state surface. *Mechanics of Cohesive-Frictional Materials*, *1*(3), 251–271. https://doi.org/10.1002/(SICI)1099-1484(199607)1:3<251::AID-CFM13>3.0.CO;2-3

Vucetic, M., & Dobry, R. (1991). Effect of Soil Plasticity on Cyclic Response. *Journal of Geotechnical Engineering*, *117*(1), 89–107. https://doi.org/10.1061/(ASCE)0733-9410(1991)117:1(89)

Wang, G., & Du, W. (2012). Empirical correlations between cumulative absolute velocity and spectral accelerations from NGA ground motion database. *Soil Dynamics and Earthquake Engineering*, *43*, 229–236. https://doi.org/10.1016/j.soildyn.2012.07.029

Watanabe, K., Pisanò, F., & Jeremić, B. (2017). Discretization effects in the finite element simulation of seismic waves in elastic and elastic-plastic media. *Engineering with Computers*, *33*(3), 519–545. https://doi.org/10.1007/s00366-016-0488-4

Whittaker, A., Atkinson, G., Baker, J., Bray, J., Grant, D., Hamburger, R., Haselton, C., & Somerville, P. (2011). Selecting and Scaling Earthquake Ground Motions for Performing Response-History Analyses. *NIST*. https://www.nist.gov/publications/selecting-and-scaling-earthquake-ground-motions-performing-response-history-analyses

Woessner, J., Laurentiu, D., Giardini, D., Crowley, H., Cotton, F., Grünthal, G., Valensise, G., Arvidsson, R., Basili, R., Demircioglu, M. B., Hiemer, S., Meletti, C., Musson, R. W., Rovida, A. N., Sesetyan, K., Stucchi, M., & The SHARE Consortium. (2015). The 2013 European Seismic Hazard Model: Key components and results. *Bulletin of Earthquake Engineering*, *13*(12), 3553–3596. https://doi.org/10.1007/s10518-015-9795-1

Wolf, J. P. (1998). Simple physical models for foundation dynamics. In Z. Chuhan & J. P. Wolf (Eds.), *Developments in Geotechnical Engineering* (Vol. 83, pp. 1–70). Elsevier. https://doi.org/10.1016/S0165-1250(98)80004-7

Wood, D. M. (1991). *Soil Behaviour and Critical State Soil Mechanics*. Cambridge University Press. https://doi.org/10.1017/CBO9781139878272

Wood, D. M., & Belkheir, K. (1994). Strain softening and state parameter for sand modelling. *Géotechnique*, *44*(2), 335–339. https://doi.org/10.1680/geot.1994.44.2.335

Wu, J. Y., Li, J., & Faria, R. (2006). An energy release rate-based plastic-damage model for concrete. *International Journal of Solids and Structures*, *43*(3), 583–612. https://doi.org/10.1016/j.ijsolstr.2005.05.038

Yang, H., Sinha, S. K., Feng, Y., McCallen, D. B., & Jeremić, B. (2018). Energy dissipation analysis of elastic–plastic materials. *Computer Methods in Applied Mechanics and Engineering*, *331*, 309–326. https://doi.org/10.1016/j.cma.2017.11.009

Yang, Z., & Elgamal, A. (2008). Multi-surface Cyclic Plasticity Sand Model with Lode Angle Effect. *Geotechnical and Geological Engineering*, *26*(3), 335–348. https://doi.org/10.1007/s10706-007-9170-3

Yang, Z., Elgamal, A., & Parra, E. (2003). Computational Model for Cyclic Mobility and Associated Shear Deformation. *Journal of Geotechnical and Geoenvironmental Engineering*, *129*(12), 1119–1127. https://doi.org/10.1061/(ASCE)1090-0241(2003)129:12(1119)

Yoshimura, C., Bielak, J., Hisada, Y., & Fernández, A. (2003). Domain reduction method for three-dimensional earthquake modeling in localized regions, part II: Verification and applications. *Bulletin of the Seismological Society of America*, *93*(2), 825–840. https://doi.org/10.1785/0120010252

Zaghi, S., Martinez, X., Rossi, R., & Petracca, M. (2018). Adaptive and off-line techniques for non-linear multiscale analysis. *Composite Structures*, *206*, 215–233. https://doi.org/10.1016/j.compstruct.2018.08.022

Zhang, Y., Acero, G., Conte, J., Yang, Z., & Elgamal, A. (2004). Seismic Reliability Assessment of a Bridge Ground System. *13th World Conference on Earthquake Engineering*, *August*, Paper No. 2978.

Zhang, Y., Conte, J. P., Yang, Z., Elgamal, A., Bielak, J., & Acero, G. (2008). Two-dimensional nonlinear earthquake response analysis of a bridge-foundation-ground system. *Earthquake Spectra*, *24*(2), 343–386. https://doi.org/10.1193/1.2923925

Zhang, Y., Yang, Z., Bielak, J., Conte, J. P., & Elgamal, A. (2003). Treatment of seismic input and boundary conditions in nonlinear seismic analysis of a bridge ground system. *16th ASCE Engineering Mechanics Conference*.

Zhao, J., Sheng, D., Rouainia, M., & Sloan, S. W. (2005). Explicit stress integration of complex soil models. *International Journal for Numerical and Analytical Methods in Geomechanics*, *29*(12), 1209–1229. https://doi.org/10.1002/nag.456

Zhu, M. (2014). *4.15.15. LayeredShell—OpenSeesPy 3.2.2.9 documentation* [Computer software]. https://openseespydoc.readthedocs.io/en/stable/src/LayeredShell.html

Zucchini, A., & Lourenço, P. B. (2009). A micro-mechanical homogenisation model for masonry: Application to shear walls. *International Journal of Solids and Structures*, *46*(3), 871–886. https://doi.org/10.1016/j.ijsolstr.2008.09.034

Zuccolo, E., O'Reilly, G. J., Poggi, V., & Monteiro, R. (2021). haselREC: An automated open-source ground motion record selection and scaling tool. *Bulletin of Earthquake Engineering*, *19*(14), 5747–5767. https://doi.org/10.1007/s10518-021-01214-w

11 APPENDIX - SUPPLEMENTARY FIGURES

a) Front façade drawing. The bell tower and the side walls (after Rosell, 2010).

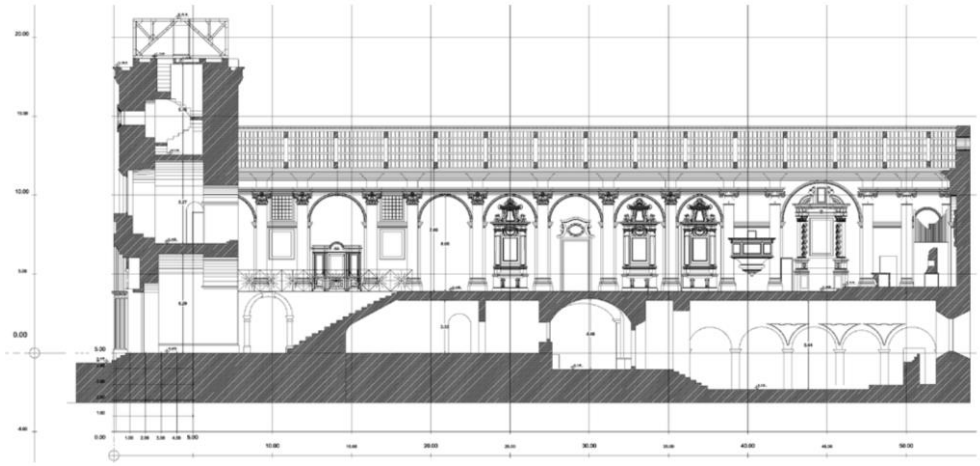

b) Elevation view drawing (after Rosell, 2010).

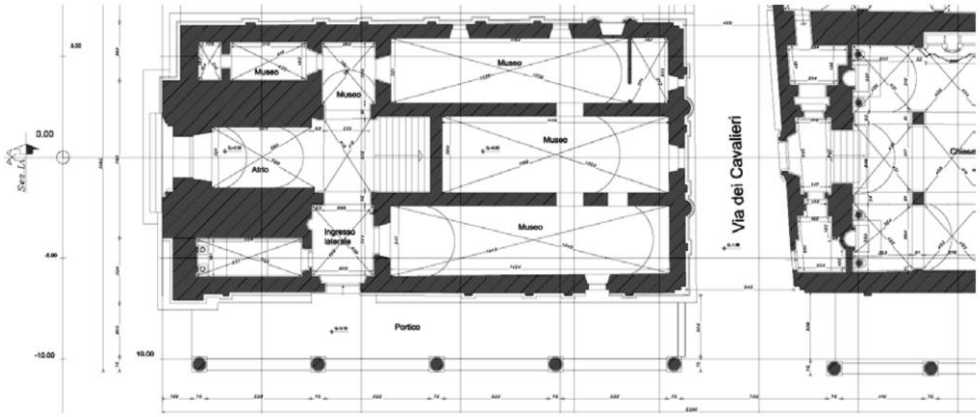

c) Plan view drawing of the bell tower, and the ground level below the church gallery (after Rosell, 2010).

Figure 11.1. Architectural a) front façade, b) elevation and c) plan view drawings of the St. Maria Maggiore church.

Figure 11.2. The Northwest oblique view of the bell tower of St. Maria Maggiore of Guardiagrele. Taken from: https://percorsi.vinidabruzzo.it/tappa/collegiata-di-santa-maria-maggiore-guardiagrele

Figure 11.3. The East façade of the bell tower. Taken from: https://www.viviguardiagrele.it/arte-e-cultura/guardiagrele-religiosa/chiesa-di-santa-maria-maggiore.html

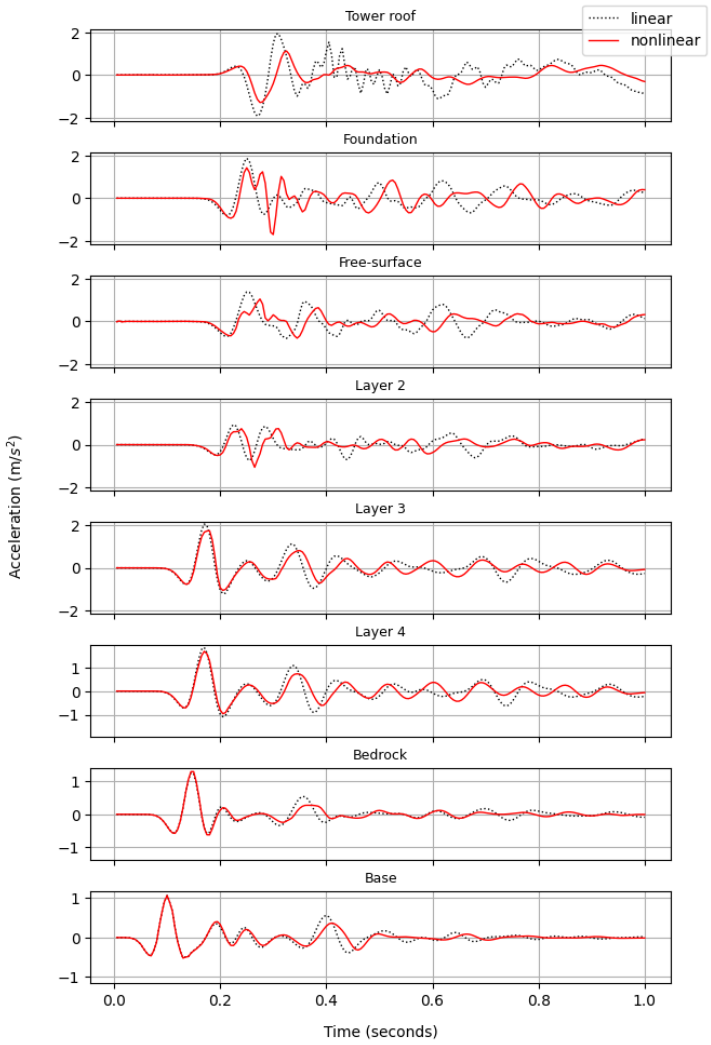

Figure 11.4. Global X direction. 10 Hz Ricker wavelet travelling from the base of the model to the free surface and the tower roof. Base motion includes the returning waves that are reflected from the free surface.

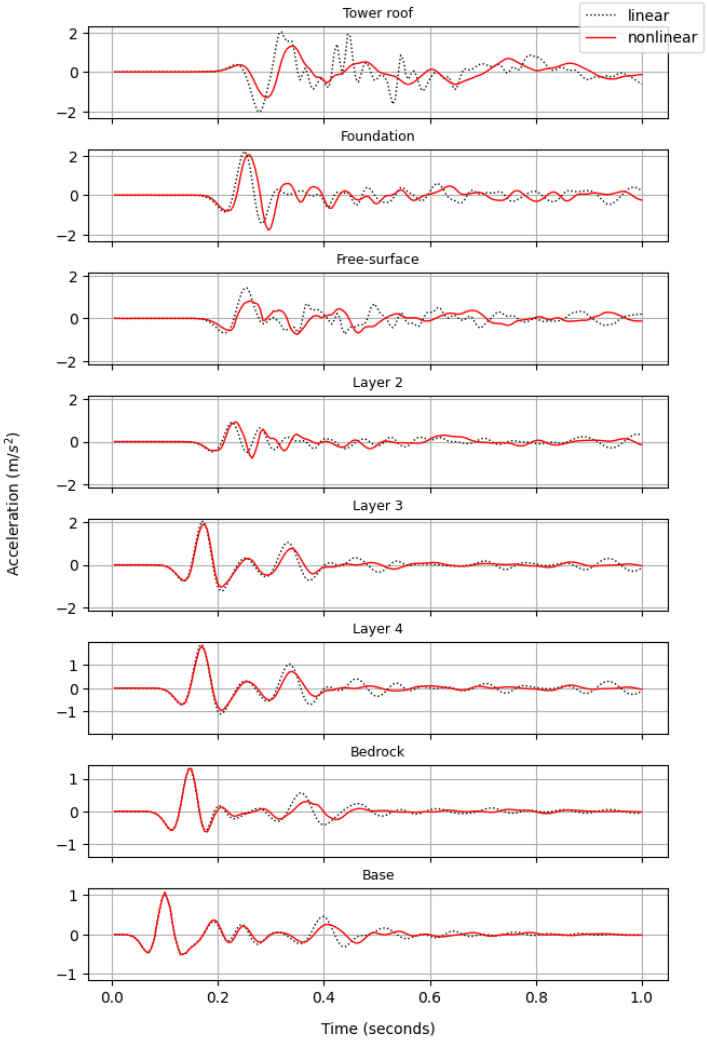

Figure 11.5 Global Y direction. 10 Hz Ricker wavelet travelling from the base of the model to the free surface and the tower roof. Base motion includes the returning waves that are reflected from the free surface.

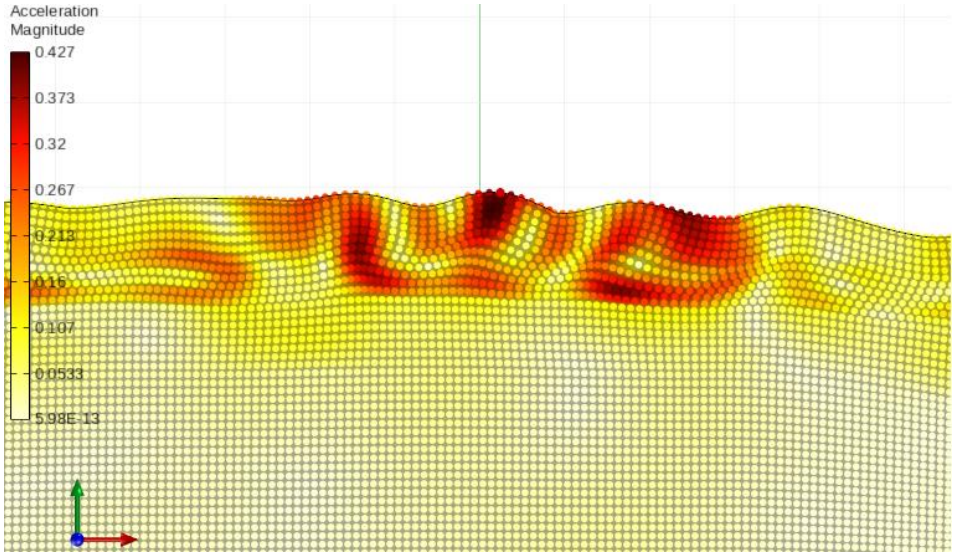

Figure 11.6. 2D Rayleigh wave propagation in the elastic topographic model (Displacement field is amplified by a factor of 1000)

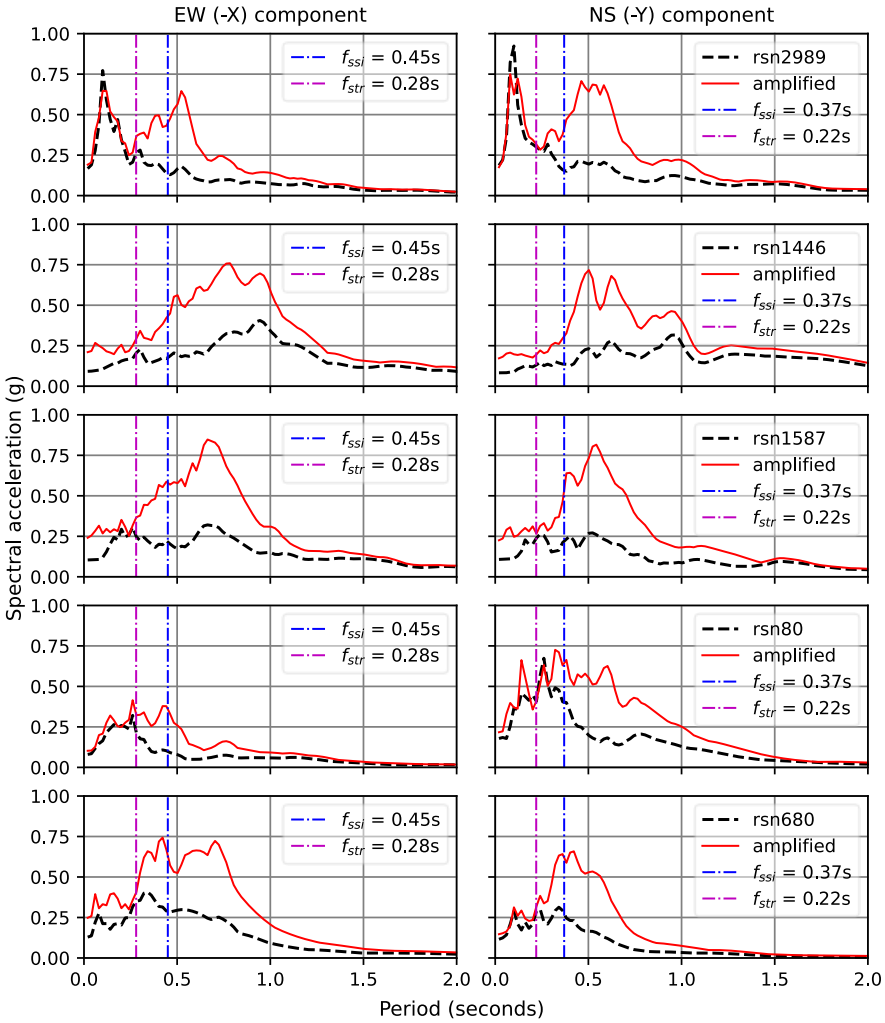

Figure 11.7.Free surface accelerations obtained from nonlinear total stress 1D site response analysis. Part 1.

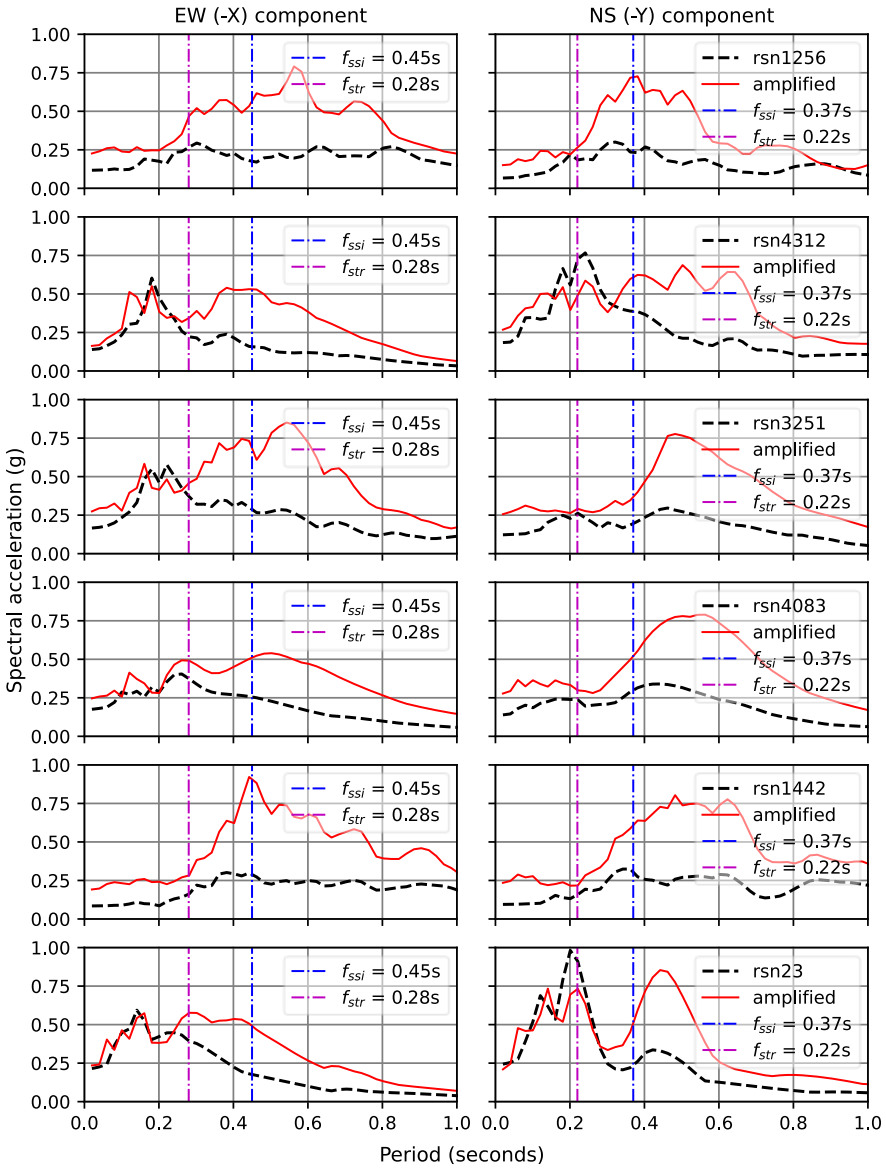

Figure 11.8. Free surface accelerations obtained from nonlinear total stress 1D site response analysis. Part 2.

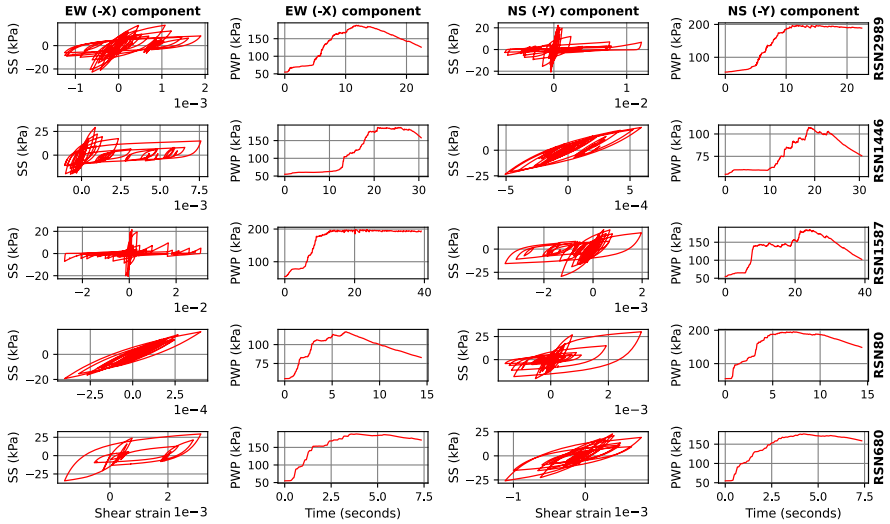

Figure 11.9.Stress-strain and pore pressure evolutions obtained from nonlinear effective stress 1D site response analysis. Part 1.

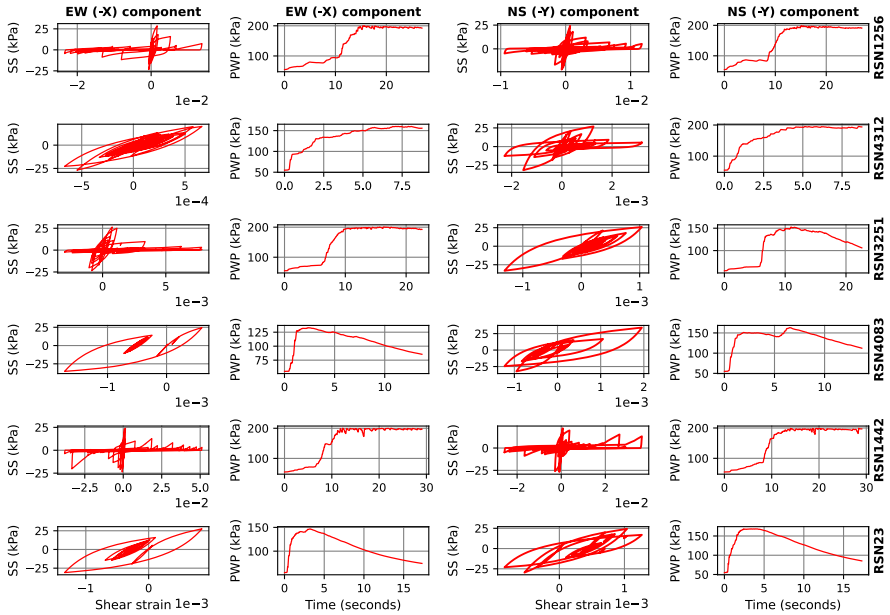

Figure 11.10. Stress-strain and pore pressure evolutions obtained from nonlinear effective stress 1D site response analysis. Part 2.

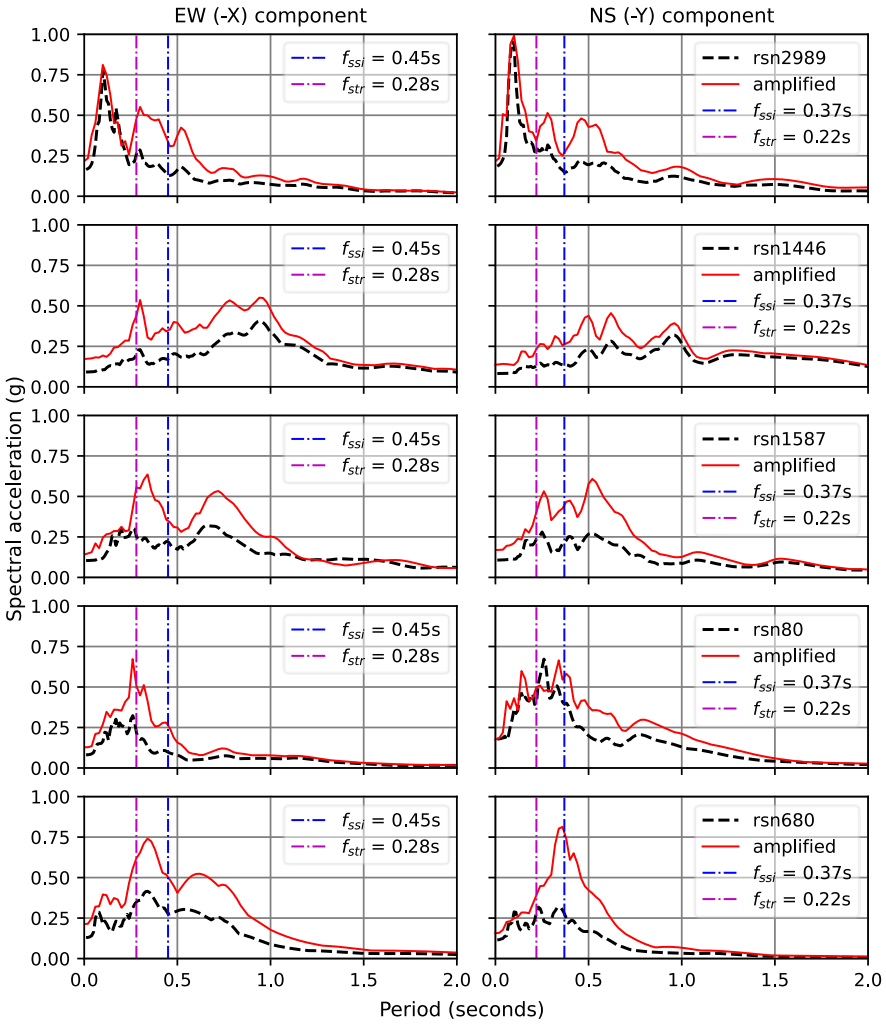

Figure 11.11. Free surface accelerations obtained from nonlinear effective stress 1D site response analysis. Part 1.

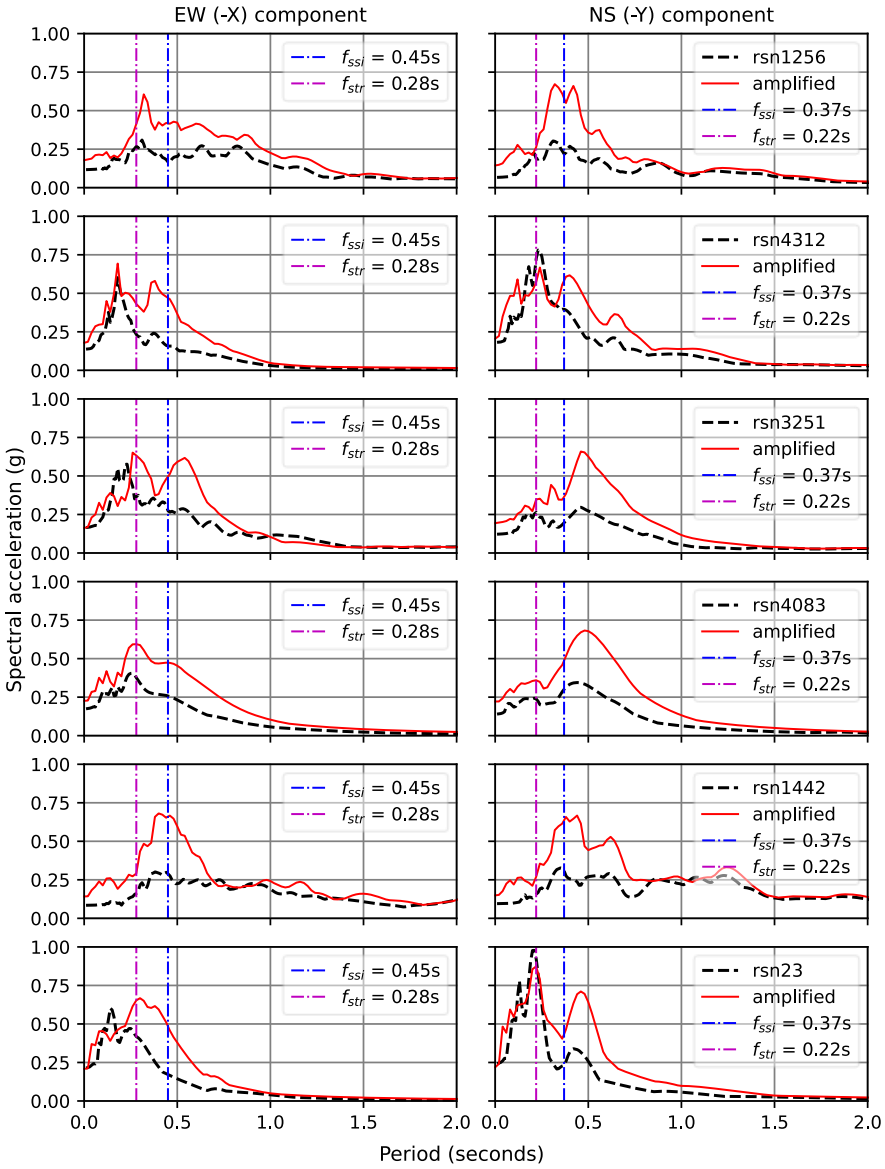

Figure 11.12. Free surface accelerations obtained from nonlinear effective stress 1D site response analysis. Part 2.

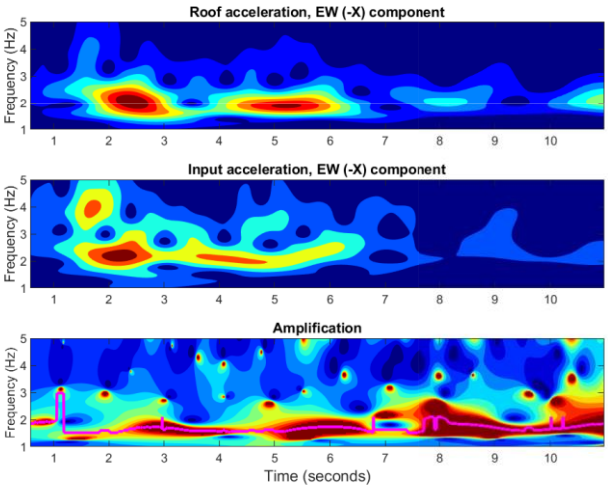

Figure 11.13. Time-frequency response of the bell tower SSI model during Lazio-Abruzzo 1984 strong motion. EW component.

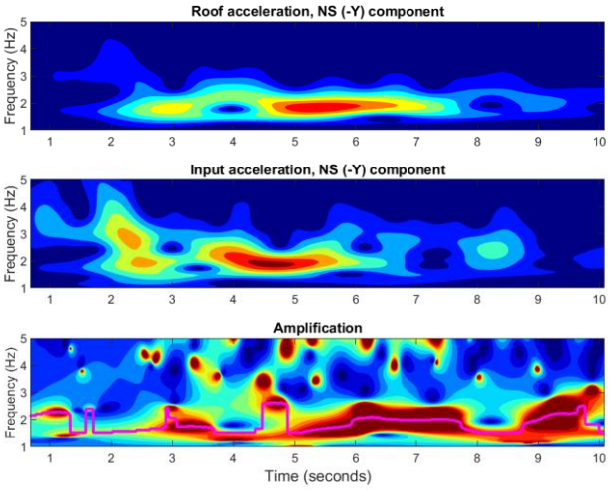

Figure 11.14. Time-frequency response of the bell tower SSI model during Lazio-Abruzzo 1984 strong motion. NS component.

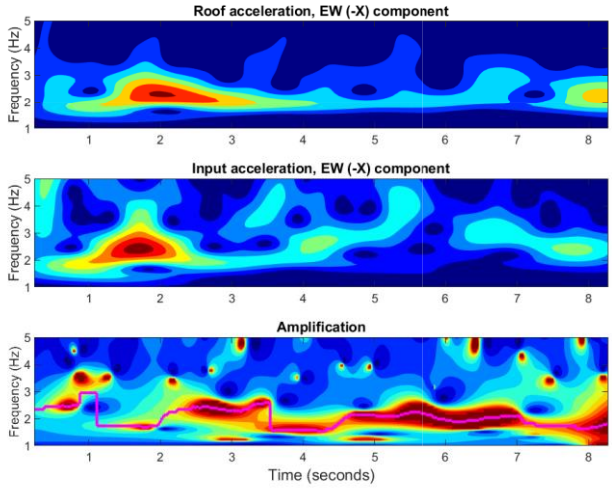

Figure 11.15. Time-frequency response of the bell tower SSI model during RSN4312 UMBRIA strong motion. EW component.

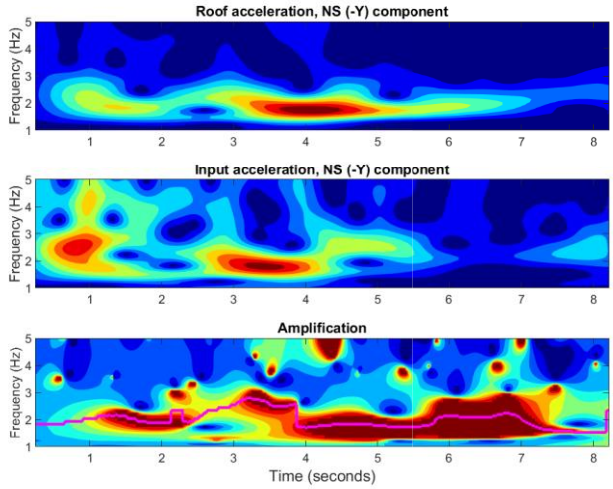

Figure 11.16. Time-frequency response of the bell tower SSI model during RSN4312 UMBRIA strong motion. NS component.

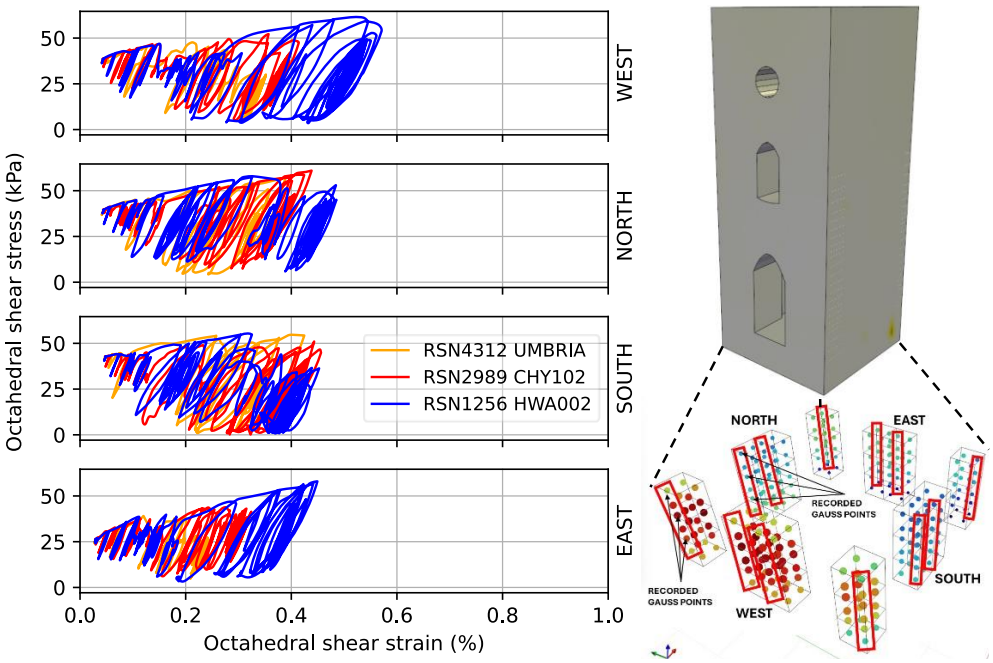

Figure 11.17. (Tower-only-Flat model) Octahedral shear stress-strain response of the soil below the foundation. The topmost Gauss point is plotted.

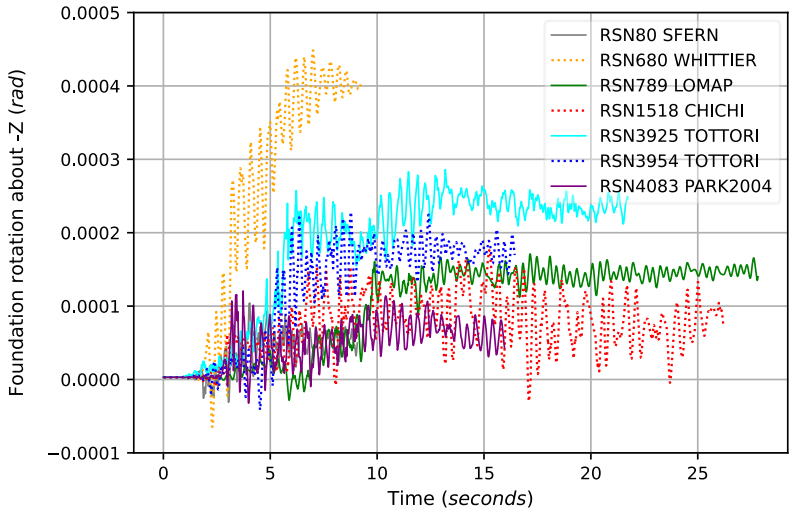

Figure 11.18. (Tower-Wall-Topographic model) Foundation rotation about the Z axis computed for the ground motion set.

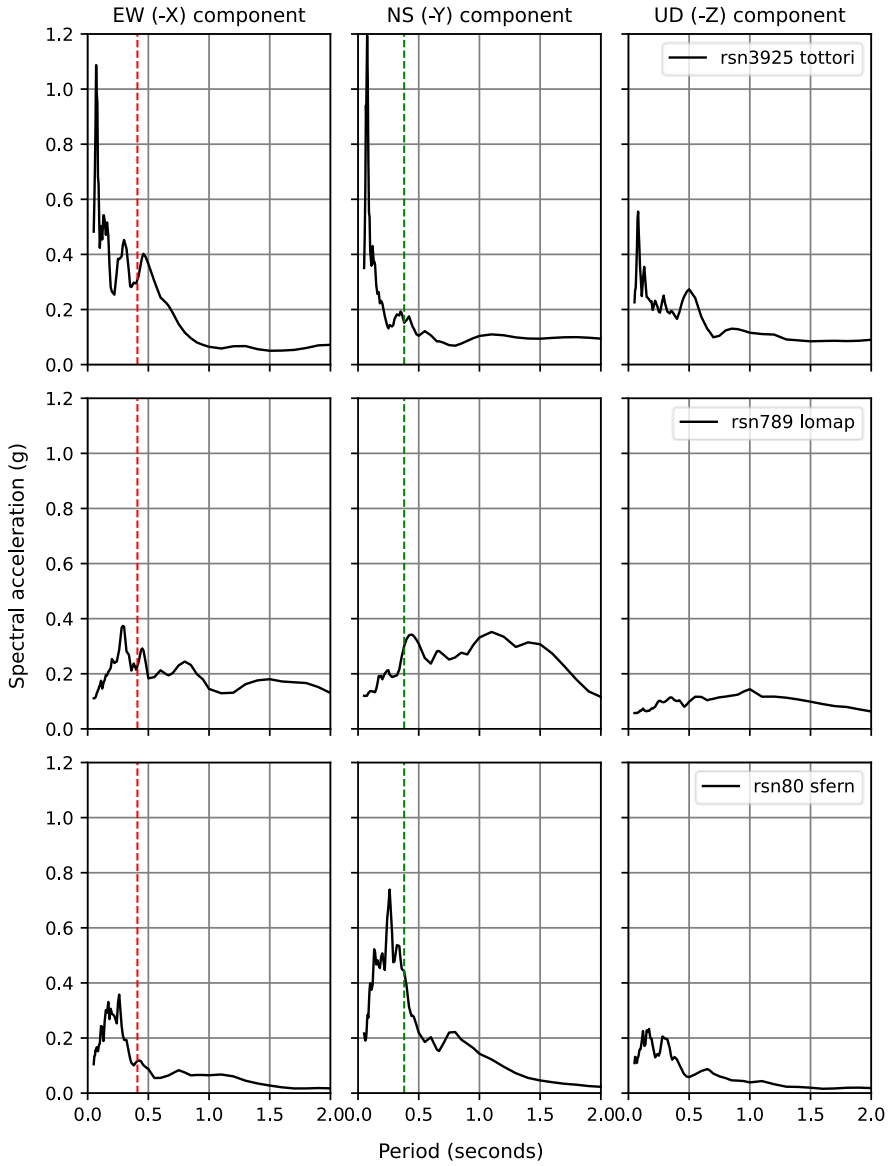

Figure 11.19. Response spectra of the alternative ground motion set at outcropping bedrock. Part 1.

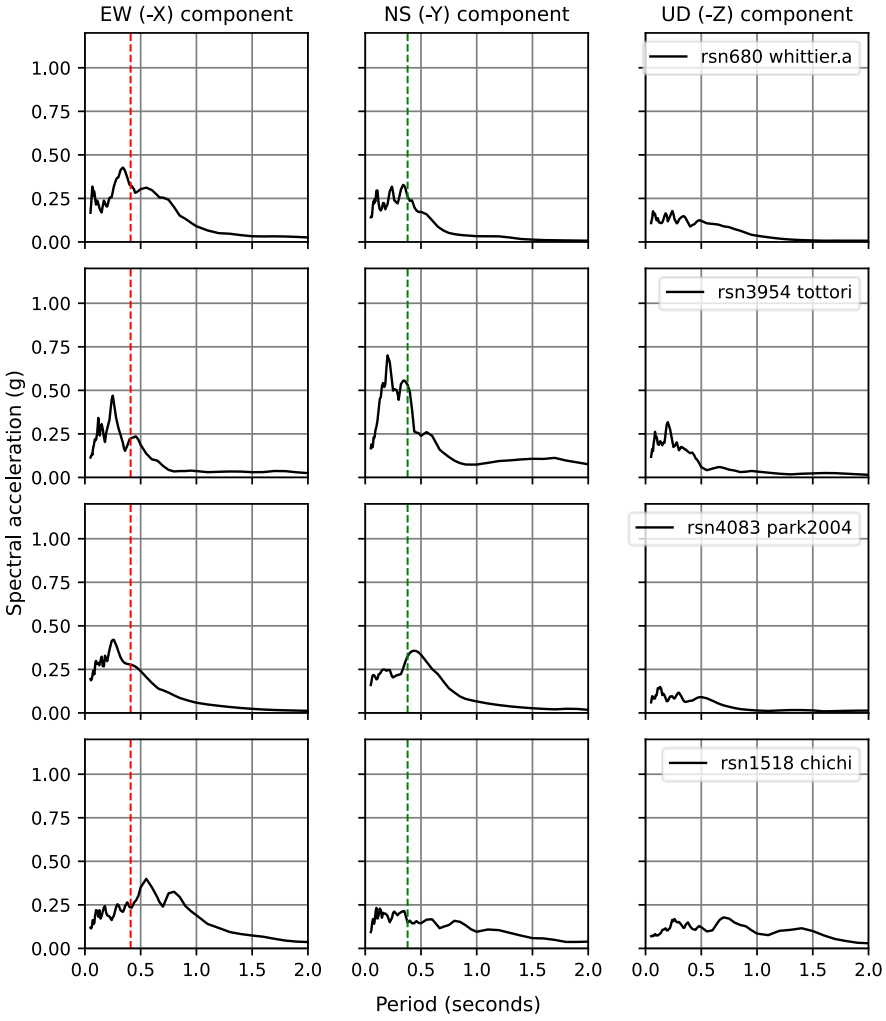

Figure 11.20. Response spectra of the alternative ground motion set at outcropping bedrock. Part 2.

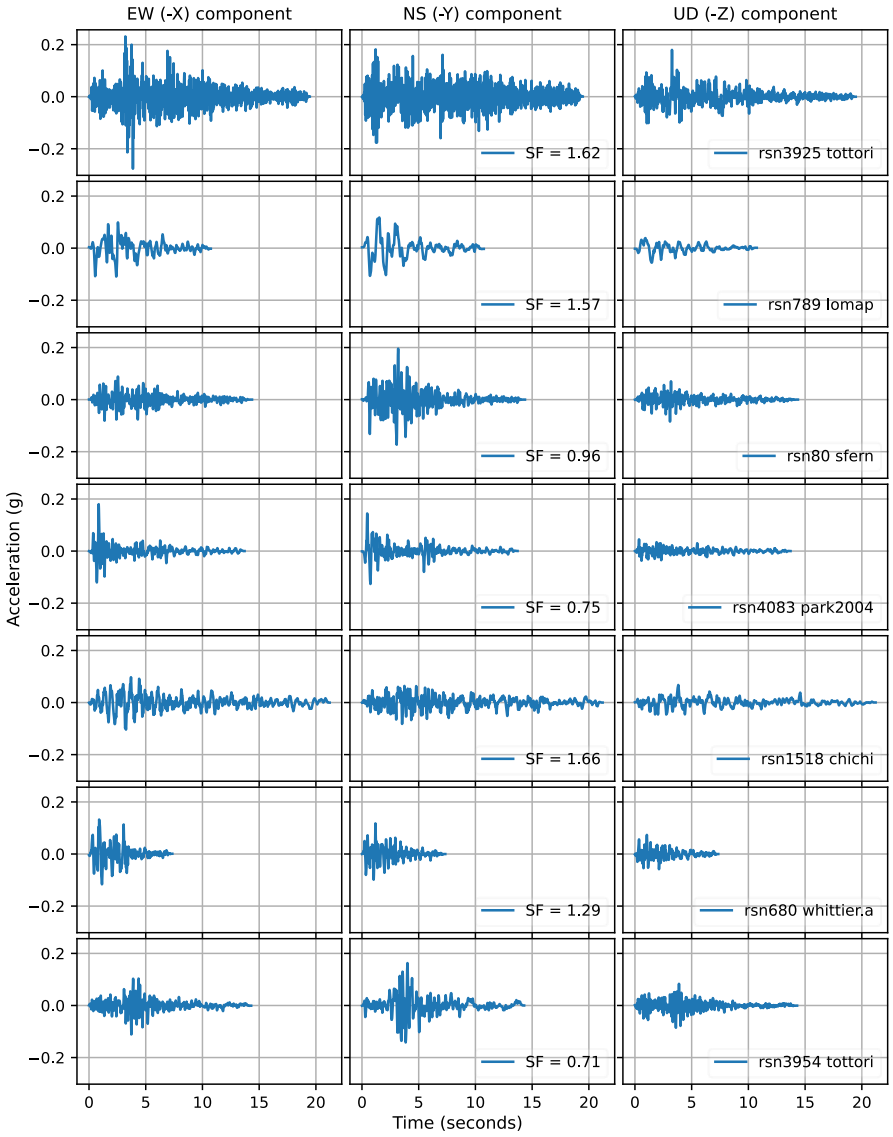

Figure 11.21. Acceleration histories of the alternative ground motion set at outcropping bedrock.